Temperature and Injection Dependent Lifetime Spectroscopy for Defect Characterization in Silicon

Bijaya Babu Paudyal

Centre for Sustainable Energy Systems
College of Engineering and Computer Science
Australian National University
Canberra, Australia

A thesis submitted for the degree of Doctor of Philosophy
of The Australian National University

January 2010

Declaration of originality

I certify that this thesis does not contain any material previously written or published by any other person except where due reference is made. The work in this thesis is my own, except for the contribution made by others as described in Acknowledgements. Part of this work has been already published in four journal articles and three conference proceedings as listed below.

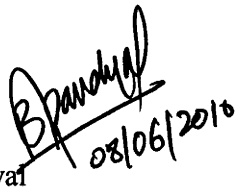

Bijaya Paudyal

1. *The implementation of temperature control to an inductive-coil photoconductance instrument for the range of 0-230°C*, B. B. Paudyal, K. R. McIntosh, D. H. Macdonald, B. S. Richards, and R. A. Sinton, Progress in PV: Res. and Application. 16, 609-613 (2008)
2. *Electron capture cross section of iron-boron pairs in crystalline silicon over the temperature range 0 – 100 °C*, B. B. Paudyal, K. R. McIntosh, and D. H. Macdonald, in 23rd EU PVSEC, Valencia, Spain, p. 1481, September 2008
3. *Generalized procedure to determine the dependence of steady-state photoconductance lifetime on the occupation of multiple defects*, K. R. McIntosh, B. B. Paudyal, and D. H. Macdonald, Journal of Applied Physics 104, 084503 (2008)
4. Erratum: *Generalized procedure to determine the dependence of steady-state photoconductance lifetime on the occupation of multiple defects [J. Appl. Phys. 104, 084503 (2008)]*, K. R. McIntosh, B. B. Paudyal, and D. H. Macdonald, Journal of Applied Physics 106, 029901 (2009)
5. *Temperature dependent carrier lifetime studies on Ti-doped multicrystalline silicon*, B. B. Paudyal, K. R. McIntosh, and D. H. Macdonald, Journal of Applied Physics, 105, 124510 (2009)
6. *Temperature Dependent Electron and Hole Capture Cross Sections of Iron-contaminated Boron-doped Silicon*, B. B. Paudyal, K. R. McIntosh and D. H. Macdonald, 34th IEEE PV specialist conference, Philadelphia, USA, p. 001588, June 2009
7. *Temperature dependent electron and hole capture cross sections of the molybdenum defect in Silicon*, B. B. Paudyal, K. R. McIntosh, D. H. Macdonald and G. Coletti, Proc. 24th EU PVSEC, Hamburg, Germany, p. 981, September 2009
8. *Temperature dependent carrier lifetime studies on Mo in crystalline silicon*, B. B. Paudyal, K. R. McIntosh, D. H. Macdonald and G. Coletti, Accepted in Journal of Applied Physics (2009)

Abstract

This thesis presents a new procedure for the simplification of a carrier lifetime equation to determine the electrical properties of the defects and their temperature dependencies in silicon. The development process of a temperature controlled lifetime measuring instrument and determination of electrical properties of some of the most common metal impurities in silicon are also presented.

Lifetime spectroscopy (LS) is a measurement and analysis technique for defect characterization in semiconductors. LS applies different approaches and conditions to extract some of the defect specific parameters by making one or more other parameters negligible, irrelevant or constant. A new approach in lifetime spectroscopy is proposed for the explicit determination of electrons and holes capture time constants (τ_{n0} and τ_{p0}) at different temperatures, which are used to determine electron and hole capture cross sections σ_n and σ_p). These temperature dependent values of σ_n and σ_p allow the assessment of the effective carrier capture mechanism of the defect and its energy level (E_t).

An inductive coil photoconductance (PC) based carrier lifetime measurement system is found suitable for this work because of its contactless nature and simple operational procedure. Implementation of a temperature control system in a commercially available inductive coil PC based lifetime measurement instrument (WCT-100 from Sinton consulting Inc.) is performed. Calibration and traceability measurements of the developed instrument ensured its operation for the temperature range -150 to 320 °C with ± 6.5% maximum error in measured lifetime.

Three common metallic impurities in silicon, molybdenum (Mo), iron (Fe) and titanium (Ti), are studied using the new lifetime spectroscopy procedure. Study of the Mo defect in silicon depicts excitonic Auger capture (EAC) as an effective capture mechanism for both types of carrier (σ_n and σ_p) and the measured values at room temperature are found consistent with previously reported values measured by other techniques. Fe defects were investigated in boron-doped silicon, where it exists as two types of defects: interstitial iron Fe_i and iron-boron pairs (FeB). Fe_i defects are studied for the temperature range -150 to 320 °C to ensure its dominance on overall recombination. This study of Fe_i defects shows EAC as an effective capture mechanism for σ_n and

multiphonon emission (MPE) for σ_p consistent with previously reported values and mechanisms. FeB pair defects are studied for the temperature range 0 to 90 °C and shows EAC as an effective capture mechanism for σ_n and MPE for σ_p, where the value at room temperature is consistent with previously reported values. Ti defects are studied in multicrystalline silicon to determine σ_n at different temperatures and effective densities of Ti atoms at different positions in the silicon ingot. Temperature dependent values of σ_n show MPE as the effective capture mechanism and the measured effective densities of Ti atoms is then used to calculate the segregation coefficient of Ti in multicrystalline silicon.

Acknowledgements

I would like to thank my supervisor, Dr. Keith McIntosh for his guidance, encouragement, transferring enthusiasm for research, availability for discussion all the time and correcting my writings to give them a better scientific shape. I am equally grateful to my cosupervisor Dr. Daniel Macdonald for his valuable suggestions and guidance during this work. I am thankful to Dr. Bryce Richards, my cosupervisor for his design work in implementing a temperature controlled system in an inductive coil photoconductance measurement system. I am also grateful to Dr. Klaus Weber for being a part of my supervisory panel.

I would like to thank Dr. Ron Sinton, from Sinton Instrument Inc., and Dr. Henry Zou, from Instec Inc., for their valuable suggestions during the development and commissioning phase of the instrument used throughout this work. I am also thankful to the laboratory staff of CSES, Mr. Bruce Condon for his assistance in fixing the electronics problems of the instrument, Mr. James Cotsell for setting up the instrument and making it operable and Mr. Neil Kaines for his guidance in the laboratory and providing tools as required. I am equally grateful to Ms Nina de Caritat for her instruction in operating the dicing saw and cell processing. I am also grateful to Mr. Ben Nash of the mechanical laboratory for his help in finding a thermally stable material suitable for coil housing.

I am thankful to Dr. Bart Greeligs and Dr. Gianluca Coletti from Energy research Centre, Netherlands (ECN), for providing me with the samples for study. I am equally thankful to Dr. Jan Schmidt for his help in finding an error in the photoconductance analysis. I am also thankful to Dr. Dan Dickey of Solecon Laboratories Inc. for his help in performing the conductivity measurements of the calibration wafers.

I am grateful to Dr. Anthony Flynn, of the engineering department at ANU, for editing this thesis and helping me to understand the usage of the English language.

I would like to express my thanks to all of the staff of the Centre for Sustainable Energy System (CSES) and College of Engineering for their help in administrative matters. I am also thankful to the Australian Research Council Linkage Grant between the Australian National University, SierraTherm Production Furnaces, and SunPower Corporation for providing me with conference and scholarship funding.

Finally, I would like to express my deepest thank to my family members and friends for their support and help throughout.

Contents

List of Figures

List of Tables

Chapter 1

Introduction

1.1 Background and motivation

Solar photovoltaic (PV) technology is a renewable means for harnessing the abundant energy from the sun. The popularity of solar PV technology is high not only because it is environmentally friendly, but also because of its lower maintenance requirements. A solar cell is the core element of a PV system which converts incident solar radiation energy into electrical energy. Several types of solar cells are available in the current market, however more than 90% of solar cells fabricated worldwide are made of crystalline silicon. The advantages of crystalline silicon over other types of cells are found in its well suited band gap for PV conversion and its non-toxic nature. Furthermore, crystalline solar cell technology has benefited from well established processing techniques and wide knowledge of silicon as it has been used in semiconductor devices over several decades.

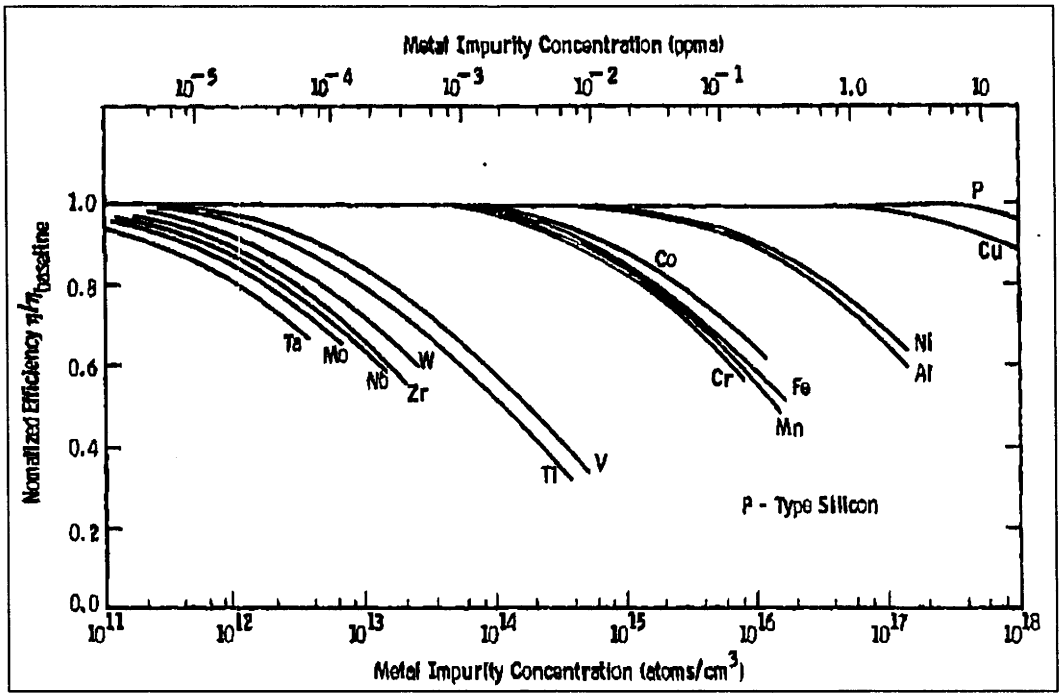

Figure 1.1: Solar cell efficiency versus impurity concentration for 4 Ω cm boron-doped silicon solar cells. Source: Davis *et al.*[1], 1980.

On the other hand solar PV technology is still less commercially competitive in comparison to other established conventional energy sources like thermal or nuclear electricity, because of its high processing or manufacturing cost and low energy conversion efficiency. The most recent and highest conversion efficiency for crystalline silicon solar cell is 25.0% [2], with efficiency of silicon solar cells strongly related to material quality. Contamination by metal impurities during the growth of ingots and the processing of silicon solar cells and their electrical activation during cell operation lowers their efficiency. The improvement of cell efficiency requires the elimination of such electrically active defects, which in turn requires their identification and quantification in order to optimize the processing steps during cell fabrication. Hence the analysis of electrically active defects which is also known as characterization is of special importance as it helps to improve the cell quality and its efficiency. Figures 1.1 and 2.2 depict the effects of various metal impurities on the efficiency of solar cells (screen printed) in boron and phosphorus doped Czochralski-grown single-crystal silicon measured and reported by Davis *et al.*[1].

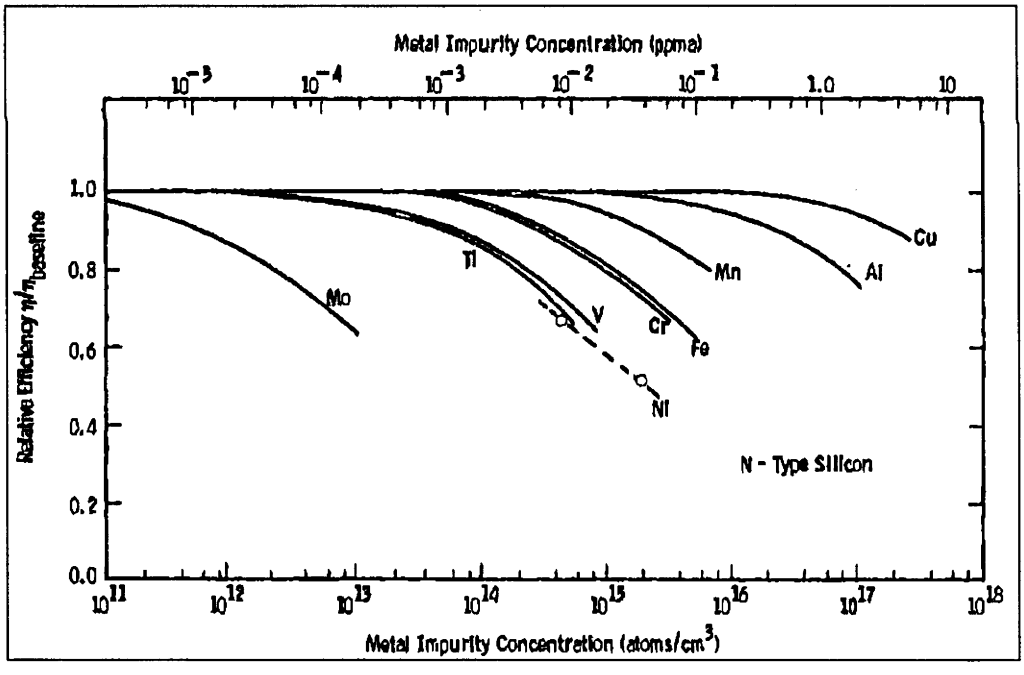

Figure 1.2: Solar cell efficiency versus impurity concentration for 1.5 Ω cm phosphorous-doped silicon solar cells. Source: Davis *et al.*[1], 1980.

The most appropriate parameter used to characterize the material quality of silicon is the recombination lifetime of the generated carriers. The detailed analysis of the dependence of the lifetime on the temperature, injection level or doping concentration is

known as lifetime spectroscopy (LS), and can reveal fundamental properties of the dominant recombination centres. There are several other characterization techniques which are in use for the detection of impurities or which analyse their behaviour in silicon. Deep-Level Transient Spectroscopy (DLTS) [3] is another characterization technique which is accepted as the most sensitive technique for the detection of small concentrations of impurities and analysis of their electrical behaviours. However, experiments have shown that even concentrations of impurities below the detection level of DLTS have a significant effect on the carrier lifetime and hence the efficiency of the solar cells [4, 5]. In this regard lifetime spectroscopy is a highly sensitive and prominent characterization technique for the study of defect parameters.

The importance of minority carrier lifetime is illustrated in Figure 1.3, which depicts the efficiency as a function of minority carrier lifetime for different types of commercially available silicon solar cells at room temperature (300 K). The efficiencies of the solar cells are calculated by using a computer simulation (PC1D) and the respected input parameters of for the simulation is presented in Appendix-A. The parameters used for simulation are just representational, and may vary in real solar cells. Figure 1.3 shows that the efficiency of solar cells increases monotonically with the minority carrier lifetime.

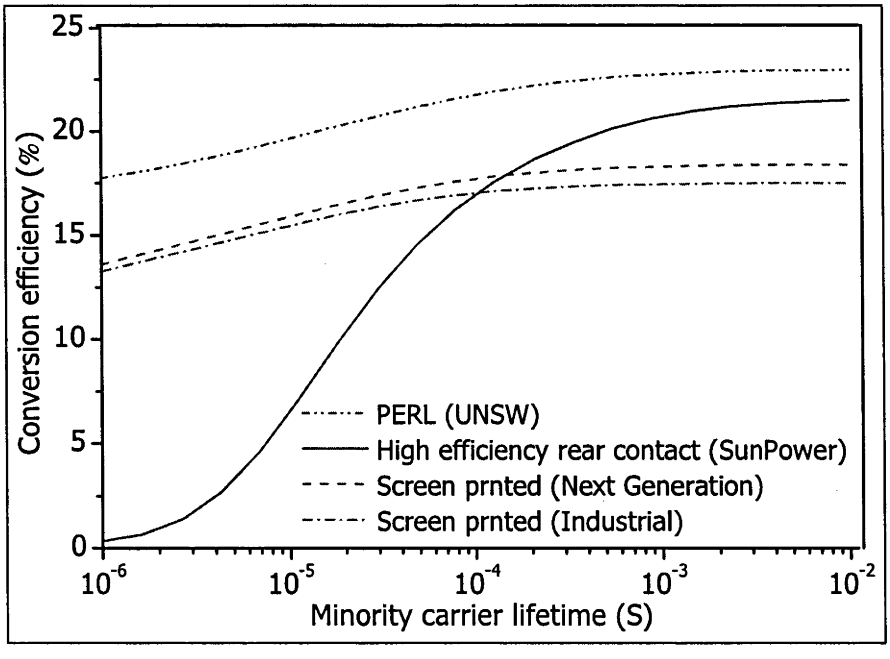

Figure 1.3: Silicon solar cell efficiency versus minority carrier lifetime.

Lifetime spectroscopies are based upon the well known Shockley–Read–Hall theory[6,7] in general and have different approaches in analysis. As different defects have different responses to the carrier injection level or temperature, characterization of single or multiple defects in cells can be performed using lifetime spectroscopy by changing either one or both of the injection level and temperature. Depending upon the nature of analysis, lifetime spectroscopy can be identified with different names. Analysis in which injection density varies is known as injection dependent lifetime spectroscopy (IDLS). Similarly, analysis in which lifetime measurement and analysis is performed at different temperatures is known as temperature dependent lifetime spectroscopy (TDLS) and where both temperature and injection vary is known as temperature and injection dependent lifetime spectroscopy (TIDLS). As TIDLS is a synthesis of TDLS and IDLS, this analysis has the advantages of both techniques, making it a sensitive and versatile technique for defect characterization.

The first TIDLS instrument was developed and tested on aluminium-doped silicon by Schmidt *et al.* [8]. He measured and analysed lifetime data to determine the defect energy level (E_t) and temperature dependence of the capture cross-section (σ_n and σ_p). The measurement device consisted of an inductive-coil PC instrument (WCT-100) from Sinton Consulting Inc[9], with a brass ring capable of heating the sample from 30 °C to 150 °C. A similar setup was used by Diez *et al.*[10, 11] and Brikholz *et al.*[12] for the measurement of E_t, σ_n/σ_p and the defect concentration (N_t) of tungsten and cobalt-contaminated silicon, and the measurement of E_t, σ_n and σ_p, of iron-contaminated boron-doped silicon. TIDLS analysis has been performed over a wider temperature range by Roth *et al.*[13] using a photoluminescence (PL) detector to measure E_t of titanium-contaminated boron-doped silicon, and by Rein *et al.* [14] using a microwave (MW) PC detector to determine E_t and σ_n/σ_p of molybdenum-contaminated silicon. Rein *et al.* [15] combined the temperature-controlled MW detector and inductive-coil PC instruments to characterize recombination in iron-contaminated boron-doped silicon.

Implementation of TIDLS for defect characterization in silicon is growing quickly, however a refinement in analysis and development of an instrument with a wider operating temperatures and injection levels is advantageous in minimizing the ambiguity in findings. First, most of the TIDLS analysis performed so far consider the capture the cross sections or their ratio to be temperature independent for the

simplification of analysis, in spite of most of the carrier capture mechanisms and their ratios in silicon being temperature dependent [16-20]. A variation of TIDLS that accounts for and determines the temperature dependence of σ_n and σ_p or σ_n/σ_p will give a better understanding of carrier recombination and hence defect characterization. Second, TIDLS measurement instruments so far have either narrow operating temperature ranges (30 to 150 °C) [8] or need to use two or more instruments with different measurement techniques[15]. A single instrument with a wide operating range for injection density (Δn) (1×10^{11} to 1×10^{17} cm^{-3}) and temperature (-150 to 300 °C) is desirable for TIDLS measurement.

In this context, this work is dedicated to filling the above mentioned two gaps seen in TIDLS characterization by proposing a new analysis technique which explicitly determines σ_n and σ_p at different temperatures and the development of an instrument suitable for measurements over a wide range of temperatures and injection levels. Moreover, this work also presents the application of the new analysis and the refined instrument to characterize three common impurities in silicon: molybdenum, iron and titanium

1.2 Thesis outline

Chapter 2 discusses the fundamentals of carrier lifetimes, lifetime spectroscopy and their importance in defect characterization in silicon. The first section of this chapter presents the fundamentals behind the different types of carrier recombinations in silicon. The second section presents the derivation of the Shockley–Read–Hall (SRH) lifetime equation, which is followed by a discussion of SRH equation parameters and their dependencies on temperature in section three. Section four discusses the advantages and disadvantages of traditional lifetime spectroscopy and a new analysis technique for the determination of electrical properties of defects in silicon is presented in section five.

Chapter 3 firstly presents a discussion of different types of lifetime measuring instruments available and their suitability for temperature controlled lifetime measurement. It then provides the details of the design and performance of a temperature controlled lifetime measurement instrument suitable for the analysis technique mentioned in Chapter 2, followed by calibration and traceability measurement

in Section three. Finally it presents the effect of input parameters and discusses the uncertainty of results.

Chapter 4 presents a temperature dependent carrier lifetime study of Molybdenum (Mo) defects in silicon, based upon the new TIDLS procedure presented in Chapter 2 and using the instrument developed in Chapter 3. The first section discusses the importance of Mo-defects in silicon and previous work in their characterization. This is followed by a discussion of methodology and sample details and then results and analysis of temperature dependent carrier capture cross sections of Mo-defects in silicon in Section 3. This section also presents the effective capture mechanism of carriers of Mo-defects and assesses its defect energy level.

Chapter 5 presents the characterization of iron-related defects in boron-doped silicon using the above mentioned new characterization procedure. The first section discusses the importance of iron-related defects in silicon and previous characterization work. This is followed by a discussion of characterization methodology and presents sample details for this experiment, followed by the results and discussion of temperature dependent carrier capture cross sections of interstitial iron and iron boron pair defects in silicon, and their effective capture mechanism.

Chapter 6 presents the procedure for and results of characterization of titanium-related defects in multi-crystalline silicon. The first section discusses the importance of Titanium-related defects in silicon and previous characterization work. Section 6.2 discusses methodology and presents sample details for the experiments. Section 6.3 presents the procedure for determining the active defect energy level, which is followed by results and discussion of electron capture cross section and effective capture mechanism in Section 6.4. Section 6.5 presents the lower values of the segregation coefficient of Ti in multicrystalline silicon.

This thesis closes with a conclusion in Chapter 7.

References

[1] J. R. Davis Jr, A. Rohatgi, R. H. Hopkins, P. D. Blais, P. Rai-Choudhury, J. R. McCormick, and H. C. Mollenkopf, "Impurities in silicon solar cells," *IEEE Transactions on Electron Devices,* vol. 27, pp. 677-687, 1980.

[2] M. A. Green, K. Emery, Y. Hishikawa, and W. Warta, "Solar Cell Efficiency Tables (Version 34) " *Prog. Photovolt: Res. Appl,* vol. 17, pp. 320-326, 2009

[3] D. V. Lang, "Deep-level transient spectroscopy: A new method to characterize traps in semiconductors," *Journal of Applied Physics,* vol. 45, pp. 3023-3032, 1974.

[4] S. A. McHugo, H. Hieslmair, and E. R. Weber, "Gettering of metallic impurities in photovoltaic silicon," *Applied Physics A: Materials Science & Processing,* vol. 64, p. 127, 1997-02-15 1997.

[5] S. W. Glunz, S. Rein, J. Y. Lee, and W. Warta, "Minority carrier lifetime degradation in boron-doped Czochralski silicon," *Journal of Applied Physics,* vol. 90, pp. 2397-2404, 2001

[6] W. Shockley and W. T. Read, "Statistics of the Recombinations of Holes and Electrons," *Physical Review,* vol. 87, p. 835, 1952

[7] R. N. Hall, "Electron-Hole Recombination in Germanium," *Physical Review,* vol. 87, p. 387, 1952.

[8] J. Schmidt, "Temperature- and injection-dependent lifetime spectroscopy for the characterization of defect centers in semiconductors," *Applied Physics Letters,* vol. 82, pp. 2178-2180, 2003

[9] www.sintonconsulting.com, December, 2009.

[10] S. Diez, S. Rein, and S. W. Glunz, "Analyzing defects in silicon by temperature and injection dependent lifetime spectroscopy," in *20th EU PVSEC*, Barcelona, Spain, 2005, p. 1216.

[11] S. Diez, S. Rein, T. Roth, and S. W. Glunz, "Cobalt related defect levels in silicon analyzed by temperature- and injection-dependent lifetime spectroscopy," *Journal of Applied Physics,* vol. 101, p. 033710, 2007.

[12] E. B. Jens, B. Karsten, M. Daniel, and S. Jan, "Electronic properties of iron-boron pairs in crystalline silicon by temperature- and injection-level-dependent lifetime measurements," *Journal of Applied Physics,* vol. 97, p. 103708, 2005.

[13] T. Roth, M. Rudiger, S. Diez, T. Trupke, R. A. Bardos, and S. W. Glunz, "Analysing defects by temperature and injection dependent lifetime measurements," in *21st European PVSEC*, Dresden, Germany, 2006.

[14] S. Rein and S. W. Glunz, "Temperature and Injection Dependent Lifetime Spectroscopy (TIDLS): Advanced analysis," in *19th EU PVSEC*, Paris, France, 2004, p. 479.

[15] S. Rein and S. W. Glunz, "Electronic properties of interstitial iron and iron-boron pairs determined by means of advanced lifetime spectroscopy," *Journal of Applied Physics,* vol. 98, p. 113711, 2005.

[16] C. H. Henry and D. V. Lang, "Nonradiative capture and recombination by multiphonon emission in GaAs and GaP," *Physical Review B,* vol. 15, p. 989, 1977.

[17] M. Lax, "Cascade Capture of Electrons in Solids," *Physical Review,* vol. 119, p. 1502, 1960.

[18] J. C. Bourgoin and M. Zazoui, "Carrier capture on defects in multiband semiconductors," *Physical Review B,* vol. 45, p. 11324, 1992.

[19] R. M. Gibb, G. J. Rees, B. W. Thomas, B. L. H. Wilson, B. Hamilton, D. R. Wight, and N. F. Mott, "A two stage model for deep level capture " *Philosophical Magazine,* vol. 36, pp. 1021 - 1034, 1977.

[20] A. Hangleiter, "Nonradiative recombination via deep impurity levels in silicon: Experiment," *Physical Review B,* vol. 35, p. 9149, 1987.

CHAPTER 2

Carrier lifetimes and lifetime spectroscopy

Lifetime spectroscopy is the measurement and analysis of the recombination lifetime of a semiconductor wafer. It is applied as a defect characterization technique in the semiconductor industry and in this thesis. This chapter describes the fundamental principles of the recombination lifetimes and their parameters, and the various existing lifetime spectroscopy techniques and their limitations. Furthermore, this chapter presents a new approach to temperature and injection dependent lifetime spectroscopy (TIDLS).

Section 2.1 introduces three types of recombination mechanisms in semiconductors. Section 2.2 presents the derivation and assumptions of the Shockley–Read–Hall (SRH) recombination equation. Section 2.3 discusses the effect of temperature on the SRH parameters. Section 2.4 presents existing lifetime spectroscopy technique, and finally, Section 2.5 proposes a new analysis approach for the determination of electrical properties of metal impurities in silicon. This new technique will be used for defect characterization in Chapters 4, 5 and 6.

2.1 Carrier generation, recombination and lifetime in semiconductor

2.1.1 Generation and recombination in semiconductors

The process by which the electron-hole pairs are created in silicon is known as generation. The electron moves from the valance band (VB) to the conduction band (CB) by absorbing excitation energy that is equal to or more than the energy difference of the CB and VB. Excitation energy for generation either comes by means of a thermal or an optical (absorption of photons) process. Conversely, recombination is the process by which the generated electron and hole pairs are lost i.e., the transition of an electron from the CB to a hole (an unoccupied state in the VB). Both the generation and recombination processes satisfy conversion of momentum and energy. The rate of recombination is dependent upon the densities of the carriers involved in the process and certain coefficients. These coefficients are dependent upon the physical processes causing recombination and are known as recombination coefficients.

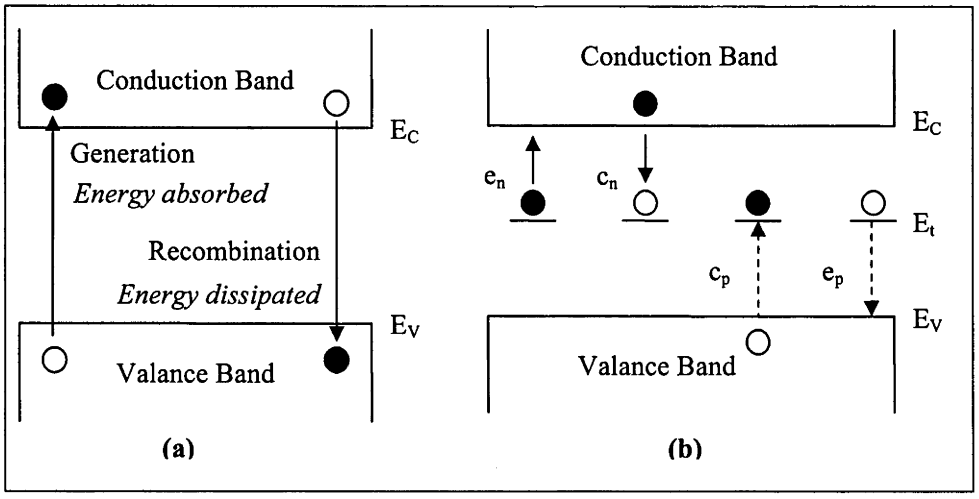

Figure 2.1: Pictorial representation of (a) band to band or intrinsic generation and recombination in silicon, (b) defect assisted generation and recombination in silicon.

Generation and recombination are spontaneous phenomena in silicon. In thermal equilibrium the generation rate (G_0) is equal to the recombination rate (R_0). The product of the electrons (n_0) and holes (p_0) concentrations remains constant at thermal equilibrium and the square root of that product is known as the intrinsic carrier concentration (n_i). When the silicon is subject to optical excitation, generation ($G > G_0$) and recombination ($R > R_0$) both increase and counterbalance each other. Accordingly, the concentrations of electrons (n) and holes (p) also increase above their thermal equilibrium values (n_0 and p_0). When optical excitation is ceased, the excess carrier concentrations ($n - n_0$ and $p - p_0$) decrease at a certain rate (U), which is the difference between the total recombination rate (R) and the equilibrium recombination rate (R_0). For silicon without any trapping defects the excess number of electrons ($\Delta n = n - n_0$) is always equal to the excess numbers of holes ($\Delta p = p - p_0$). Hence during the spontaneous recombination process and in the absence of generation, Δn can be expressed as a function of time $\Delta n(t)$. The recombination rate U is a function of the carrier concentrations, and can be written as $U(\Delta n(t), n_0, p_0)$. Then the time decay of $\Delta n(t)$ can be expressed as

$$\frac{d\Delta n(t)}{dt} = -U(\Delta n(t), n_0, p_0) \tag{2.1}$$

The lifetime of $\Delta n(t)$ is the ratio of $\Delta n(t)$ to its rate of decay ($d\Delta n/dt$) and can be expressed as

$$\tau(\Delta n, n_0, p_0) \equiv \frac{\Delta n(t)}{\frac{d\Delta n(t)}{dt}} = -\frac{\Delta n(t)}{U(\Delta n(t), n_0, p_0)} \tag{2.2}$$

This is the general expression of carrier lifetime in a semiconductor and the solution for $\Delta n(t)$ can be expressed as

$$\Delta n(t) = \Delta n(0) \exp\left(-\frac{t}{\tau}\right) \tag{2.3}$$

where τ is a time constant of the exponential function of $\Delta n(t)$ and known as the lifetime.

The recombination mechanisms in silicon are classified as "intrinsic" and "defect-assisted" on the basis of their character. Intrinsic recombination is also known as band to band recombination and is unavoidable. This is further classified as radiative and Auger recombination [1] on the basis of the nature of the release of the excess energy by the decay of electron-hole pairs. In the defect-assisted recombination process, the number of electron-hole pairs decays by the transition of electrons from the CB to VB through a defect energy level, which lies between the CB and VB. This recombination mechanism is known as Shockley–Read–Hall (SRH) recombination [2, 3]. This recombination mechanism can be avoided theoretically by producing a perfect crystal structure. However in practice SRH recombination is the most dominant recombination process because many defects are introduced either by impurities or lattice defects in the bulk of silicon and by dangling bonds at the surfaces, and by virtue of the fact that radiative recombination is suppressed in crystalline silicon due to its indirect band-gap. This section describes the three processes and presents their expressions and their parameters for all recombination mechanisms mentioned above.

2.1.2 Effective and multiple recombination lifetimes

The three recombination mechanisms occur simultaneously. Each recombination mechanism has its own lifetime and the overall recombination rate is the sum of the individual rates. For a sample which has active radiative (U_{Rad}), Auger (U_{Aug}) and SRH (U_{SRH}) recombination mechanisms, the total recombination rate (U_{Total}) is the sum of these three, expressed as $U_{Total} = U_{Rad} + U_{Aug} + U_{SRH}$. If the lifetimes of these

recombinations are given as τ_{Rad}, τ_{Aug} and τ_{SRH} respectively, then the effective lifetime τ_{Total} can be expressed as

$$\frac{1}{\tau_{Total}} = \frac{1}{\tau_{Rad}} + \frac{1}{\tau_{Aug}} + \frac{1}{\tau_{SRH}} \tag{2.4}$$

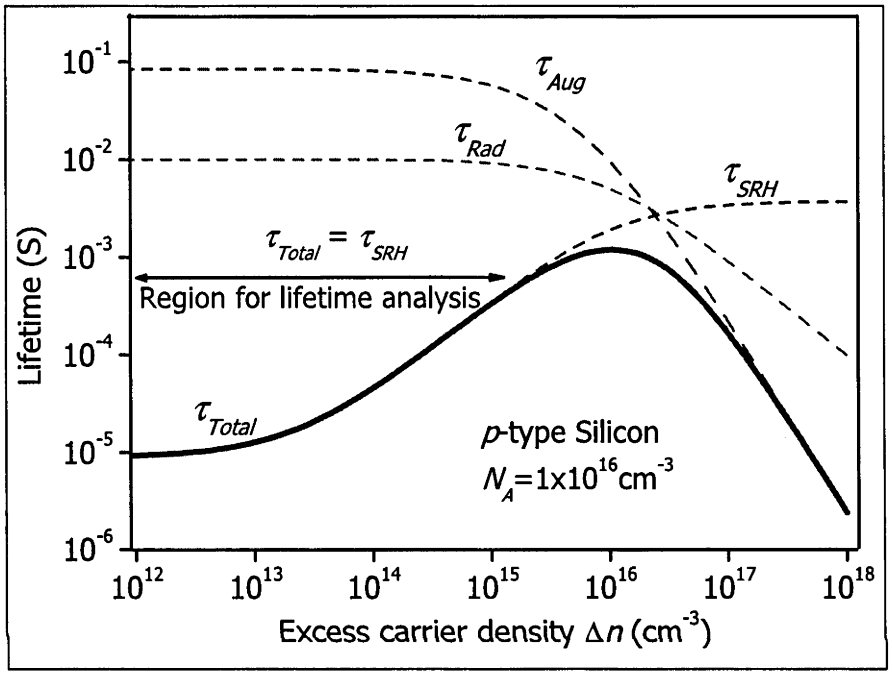

Figure 2.2: Effective lifetime composed of SRH, radiative and Auger terms. Lifetimes are calculated for a typical solar cell at 300 K, doping density, 1×10^{15} cm^{-3} (boron) and impurity density, 5×10^{11} cm^{-3} (titanium).

Figure 2.2 depicts the three lifetimes as a function of Δn and their resultant lifetime (τ_{Total}). This figure plots the lifetimes for a *p*-type silicon with doping density 1×10^{15} cm^{-3} with defect energy level 0.28 eV above the valance band and shows the relative importance of SRH lifetime for a typical silicon solar cell. Coefficients for Auger recombination and radiative recombinations are taken as B = 1×10^{-14} cm^{3}s^{-1} [4] and $C_n = 2.8 \times 10^{-31}$ cm^{6}s^{-1} and $C_p = 9.9 \times 10^{-32}$ cm^{6}s^{-1} [5] respectively. Capture cross section for SRH recombinations are taken as $\sigma_n = 1.92 \times 10^{-14}$ cm^2 and $\sigma_p = 5.3 \times 10^{-17}$ cm^2 [6]. τ_{Rad} and τ_{Aug} are several orders of magnitude higher than τ_{SRH} for low Δn ($< 1 \times 10^{14}$ cm^{-3}). Hence the recombination due to radiative and Auger mechanisms can be neglected in comparison to SRH recombination for these injection ranges. However for high Δn

($> 1\times 10^{16}$ cm^{-3}) τ_{SRH} is often much higher than τ_{Rad} and τ_{Aug}, and so no longer dominates the effective lifetime. Hence for the purpose of defect characterization, analysis of τ_{Total} when equal to τ_{SRH} at lower values of Δn is preferred.

2.1.3 Radiative recombination

Radiative recombination is a process in which an electron in the CB recombines with a hole in the VB by emitting a photon with an energy equal to the band gap. The radiative recombination rate U_{Rad} is a function of the concentration of electrons and holes in the CB and the VB respectively and can be expressed as

$$U_{Rad} = -B\left(n\times p - n_i^2\right) \tag{2.5}$$

where B is a constant. B accounts for the probability of recombination and depends upon the band structure of the semiconductor [4]. Conservation of momentum of carriers must prevail during the recombination process, hence the probability of radiative recombination in a direct-band semiconductor (GaAs) is higher than for the indirect-band semiconductor (Si). The value of B for silicon is 1×10^{-14} cm^{3}s^{-1} and 3×10^{-10} cm^{3}s^{-1} for GaAs [4] at 300 K.

Equation (2.5) is valid for both equilibrium and non-equilibrium conditions, so by replacing $n = n_0 + \Delta n$ and $p = p_0 + \Delta p$ (and assuming $\Delta n = \Delta p$) the recombination rate can be expressed as

$$U_{Rad} = B(n_0 + p_0)\Delta n + B\Delta n^2 \tag{2.6}$$

from which the recombination lifetime can be determined using Equations (2.2)

$$\tau_{Rad} = \frac{\Delta n}{B(n_0 + p_0)\Delta n + B\Delta n^2} = \frac{1}{B(n_0 + p_0 + \Delta n)} \tag{2.7}$$

The radiative recombination lifetime (τ_{Rad}) is inversely proportional to the sum of n_0, p_0 and Δn. For large values of Δn, i.e. $\Delta n >> p_0 + n_0$, τ_{Rad} can be simplified as the inverse of the product of $B \times \Delta n$. However for small Δn, with $\Delta n << p_0 + n_0$ and $p_0 = N_A >> n_0$ for p-type and $n_0 = N_D >> p_0$ for n-type, τ_{Rad} is inversely proportional to the product of B with majority carrier concentration (N_A or N_D). Figure 2.2 shows that

τ_{Rad} switches from inversely-proportional to N_A to inversely-proportional to Δn for $\Delta n \geq N_A$.

This radiative recombination mechanism is dominant in direct-band semiconductors (for example GaAs). However, it has negligible effect in comparison to SRH or Auger recombination mechanisms in an indirect-band semiconductor, i.e in silicon, as seen in Figure 2.2. This thesis is confined to the defect characterization of silicon, so this recombination mechanism has little importance for this work.

2.1.4 Auger recombination

Auger band-to-band recombination is another form of an intrinsic recombination mechanism. In this recombination the excess energy released by annihilation of an electron with a hole is transferred to a third free carrier instead of emitting a photon as in the case of radiative recombination. The Auger recombination rate U_{Aug} is dependent upon the type of third carrier and is also named after it. If the third carrier is an electron in the CB, it is called an electron-electron-hole (*eeh*) recombination event, and if the third carrier is a hole, then the process is called an electron-hole-hole (*ehh*) recombination event. The corresponding recombination rates are expressed as $U_{eeh} = C_n(n^2p - n_0^2p_0)$ and $U_{ehh} = C_p(np^2 - n_0p_0^2)$. Where C_n and C_p are the Auger coefficients of the *eeh* and *ehh* process respectively and the most quoted values are $C_n = 2.8 \times 10^{-31}$ cm^6s^{-1} and $C_p = 9.9 \times 10^{-32}$ cm^6s^{-1} [5]. The net recombination rate can be expressed as

$$U_{Auger} = C_n\left(n^2p - n_0^2p_0\right) + C_p\left(np^2 - n_0p_0^2\right) \tag{2.8}$$

For p-type silicon, $n_0 << p_0$ and Δn, so $n = n_0 + \Delta n$ can be replaced by Δn and any product of n_0 can be neglected. Similarly, for n-type silicon, $p_0 << n_0$ and Δn, so $p = p_0 + \Delta p$ can be replaced by Δn ($\Delta p = \Delta n$) and any product of p_0 can be neglected. Hence the Auger recombination lifetime can be expressed as

$$\tau_{Aug} = \frac{1}{C_p p^2 + C_n p\Delta n} \text{ for } p\text{-type and } \tau_{Aug} = \frac{1}{C_n n^2 + C_p n\Delta n} \text{ for } n\text{-type} \tag{2.9}$$

τ_{Aug} is inversely related to the carrier concentration (N_A, N_D or Δn). For N_A, N_D or Δn greater than 1×10^{17} cm^{-3}, Auger recombination is the dominant mode of recombination and limits the overall recombination lifetime as shown in Figure 2.2.

For samples with N_A or N_D less than 5×10^{18} cm^{-3}, the Auger lifetime is calculated by using the values of C_n and C_p stated above and are found to be larger than the measured values [1]. Hangleiter [7] and Hacker [8] put forward a "coulomb-enhanced Auger recombination" theory to explain this problem. This theory describes the coulombic interactions between electron-electron, electron-hole and hole-hole as the reason for a smaller value of actual Auger lifetime for a lower doping level.

The Auger recombination mechanism is natural and unavoidable in a silicon solar cell and has a significant effect for higher levels of Δn as depicted in Figure 2.2. To avoid the effect of τ_{Aug} in τ_{Eff}, this work concentrates on lifetime analysis in medium and low injection levels ($\Delta n < 1 \times 10^{15}$ cm^{-3}) for defect characterization.

2.1.5 Shockley–Read–Hall recombination

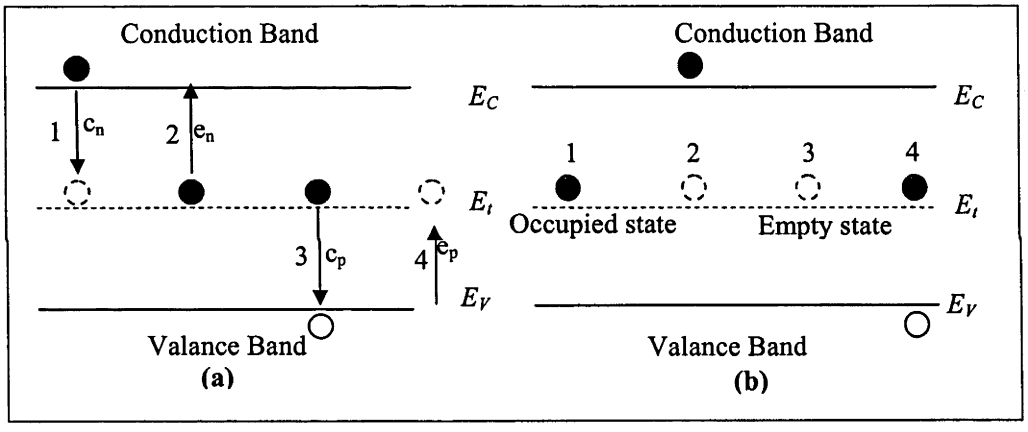

Figure 2.3: (a) State before carrier transaction (b) state after carrier transaction.

This recombination mechanism is named after W Shockley, W T J Read and R N Hall [2, 3], who originally proposed and modelled it. In this recombination process annihilation of the electrons from the CB into the holes in the VB happens through defects. The excess energy of the electron in transition is released in the form of phonons and photons [9]. An electron in the CB makes a first transition to the defect level and then to the hole in the VB, so this is also known as a two-step recombination process. The defects are the intermediate energy level (E_t) within the band-gap of the semiconductor and are created either by dislocation in the crystal structure or due to impurities. Such an intermediate state can be occupied by an electron or by a hole and can interact with the CB and the VB in four ways. An empty defect can capture an

electron from the CB (1) or emit a hole into the VB (4) while a filled defect can emit an electron into the CB (2) or absorb a hole from the VB (3). These four fundamental interactions of the defect energy level are depicted in Figure 2.3. Figure 2.3(a) shows the state before the carrier transaction and Figure 2.3(b) represents after the carrier transaction.

Depending upon the combination of these four fundamental carrier transitions, each defect can behave as a recombination, a generation or a trap centre. The combination of transitions (1) and (3), in which an electron from the CB is captured by an empty defect level, then sees the defect level absorb a hole from the VB which is annihilated by the previously absorbed electron is known as recombination. Conversely, a defect level can emit an electron to the CB (2) and a hole to the VB (4). This process is called generation, where the defect level behaves as a generation centre. The electron and hole captured by the empty defect level may be bounced back to its original level, which is the combination of transition (1) and (2) or (4) and (3). This process is called trapping and the defect level is then known as a trap centre.

2.2 Derivation of the SRH equation and its assumptions

The SRH equation is an essential element of any type of lifetime spectroscopy. The proposed TIDLS for this work is also based upon the SRH equation. This Section presents the derivation of the comprehensive form of the SRH equation and discusses the assumptions necessary to simplify it.

2.2.1 The SRH equation

a. Rate of change of carrier concentrations: The rate of change to electron density in the CB and hole density in the VB can be determined by using their capture and emission rates. The capture rate of electrons (C_n) and holes (C_p) for a defect centre in the lattice of a semiconductor can be expressed as [10]

$$C_n = \sigma_n v_{th} n = c_n n \text{ for electrons and } C_p = \sigma_p v_{th} p = c_p p \text{ for holes} \qquad (2.10)$$

where v_{th} is the thermal velocity of the defect centre, and σ_n and σ_p are the capture cross sections of electrons and holes. The thermal velocity of the defect centre can be thought

of as its movement in relation to carriers which are regarded as immobile. The defect centre sweeps out the volume $\sigma_n \times v_{th}$ on the CB and $\sigma_p \times v_{th}$ on the VB in each second , and captures electrons or holes. If (f_t) is the probability of emission of the electrons by a defect centre in the CB, i.e. the occupation by the electrons, then (1-f_t) is the probability of capture of the electrons. For N_t number of defects with *the same defect energy level*, then the total number of electron emissions is proportional to $N_t \times f_t$ and capture is proportional to $N_t \times (1-f_t)$. Conversely, the total number of hole emissions is proportional to $N_t \times (1-f_t)$ and capture to $N_t \times f_t$. Hence the rate of change of the electrons and holes can be expressed as

$$\frac{dn}{dt} = electron\ emission - electron\ capture = e_n N_t f_t - c_n n N_t (1 - f_t) \tag{2.11}$$

$$\frac{dp}{dt} = hole\ emission - hole\ capture = e_p N_t (1 - f_t) - c_p p N_t f_t \tag{2.12}$$

where e_n and e_p are the emission rate of electrons and holes respectively and can be determined in an expression formed by subjecting Equations (2.11) and (2.12) to an equilibrium condition $dn/dt = 0$ and $dp/dt = 0$. The expression for e_n and e_p are expressed as

$$e_n = c_n n\left(\frac{1-f_t}{f_t}\right) \text{ and } e_p = c_p p\left(\frac{f_t}{1-f_t}\right) \tag{2.13}$$

where n and p are the number of electrons and holes respectively.

b. The occupation probability (f_t) is determined using Fermi-Dirac integral approaches with Boltzmann's statistics for thermal equilibrium with carrier concentrations of n_0 and p_0 [11] in the CB and VB. The expressions for n_0 and p_0 for a Fermi energy level E_f in a *non degenerated semiconductor* are

$$n_0 = N_C \exp\left(-\frac{E_C - E_f}{k_B T}\right) \text{ and } p_0 = N_V \exp\left(-\frac{E_f - E_V}{k_B T}\right) \tag{2.14}$$

where N_C is the state density of electrons in the CB, N_V is the state density of holes in the VB, E_C and E_V are the energy levels of the CB and VB respectively, E_f is the Fermi

energy level, k_B is Boltzamnn's constant and T is temperature, in Kelvin. N_C and N_V are dependent upon the effective masses of the electrons and holes [11]. Hence, the emission rates for equilibrium with a defect energy level E_t can be expressed as

$$e_n = c_n N_C \exp\left(-\frac{E_C - E_t}{k_B T}\right) \quad \text{and} \quad e_p = c_p N_V \exp\left(-\frac{E_t - E_V}{k_B T}\right) \tag{2.15}$$

When the Fermi level coincides with the defect energy level (E_t) the emission rate is equal to the product of capture rates (c_n and c_p) with corresponding equilibrium carrier concentrations n_0 and p_0. However for other conditions the electron and hole concentrations are termed as SRH carrier densities and denoted as n_1 and p_1, which are expressed as

$$n_1 = N_C \exp\left(-\frac{E_C - E_t}{k_B T}\right) \quad \text{and} \quad p_1 = N_V \exp\left(-\frac{E_t - E_V}{k_B T}\right) \tag{2.16}$$

Equation (2.15) can be simplified to Equation (2.17) by using Equations (2.10) and (2.16)

$$e_n = c_n n_1 \text{ and } e_p = c_p p_1 \tag{2.17}$$

Hence the occupation probability of an electron f_t is expressed by equating Equations (2.10) and (2.11) with Equation (2.16) as $dn/dt = dp/dt$, which gives

$$f_t = \frac{c_n n + c_p p_1}{c_n (n + n_1) + c_p (p + p_1)} \tag{2.18}$$

c. Expression for U_{SRH} and τ_{SRH}: Subjecting the value of f_t to either Equations (2.10) or (2.11) and applying $n_1 p_1 = n_i^2$ (Intrinsic carrier concentration), the recombination rate can be expressed as

$$U_{SRH} = \frac{np - n_i^2}{\frac{n + n_1}{c_p N_t} + \frac{p + p_1}{c_n N_t}} = \frac{np - n_i^2}{\tau_{p0}(n + n_1) + \tau_{n0}(p + p_1)} \tag{2.19}$$

where τ_{n0} and τ_{p0} are known as fundamental capture time constants and depend upon the capture cross section (σ), thermal velocity (v_{th}) and defect concentrations (N_t) and are expressed as

$$\tau_{n0} = \frac{1}{N_t \sigma_n v_{th}} \quad and \quad \tau_{p0} = \frac{1}{N_t \sigma_p v_{th}} \tag{2.20}$$

The non equilibrium carrier densities n and p can be replaced by the sum of the carrier densities at thermal equilibrium ($n_0 + p_0$) with the excess carrier densities (Δn and Δp). For *negligible trapping effect of the defect level* $\Delta n = \Delta p$, hence the SRH lifetime can be expressed as

$$\tau_{SRH} \equiv \frac{\Delta n}{U_{SRH}} = \frac{\tau_{p0}(n_1 + n_0 + \Delta n) + \tau_{n0}(p_0 + p_1 + \Delta n)}{n_0 + p_0 + \Delta n} \tag{2.21}$$

2.2.2 Assumptions for SRH lifetime expressions

There are four assumptions made in obtaining the simplified expression for the SRH lifetime expressed in Equation 2.20. In general these assumptions are valid, however they need to be taken into account while using this expression for the ensuing analysis. It is worthwhile to discuss these assumptions as they need to be fulfilled in the lifetime spectroscopy technique used throughout this thesis.

1. Defect levels involved in recombination have the same energy level E_t and are stable.

This assumption is needed to be valid to in order to derive the expression for the rate of change of carrier emission or capture. If the defects have multiple energy levels or are unstable then Equations (2.9) and (2.10) becomes invalid, hence the expression for SRH lifetime becomes invalid. This assumption is valid when a single impurity in silicon dominates the overall recombination process and hence is valid for point defects. However this assumption is not valid for the impurities in precipitate form in bulk or in the surface. Furthermore, the co-existence of multiple defect energy levels is valid for the condition when these defects do not communicate with each other and are treated independently.

2. Non-degenerate semiconductor.

This assumption is part of a condition of the Fermi-dirac distribution which is used during the derivation of SRH lifetime to obtain the thermal equilibrium number of electrons (n_0) and holes (p_0). This assumption is valid in the bulk region of a silicon wafer, however this may not be valid in heavily diffused regions. All analysis in this thesis is performed for defects in the bulk of the silicon, hence this condition is satisfied throughout this work.

3 The defect concentration (N_t) is 'small'

This condition is necessary to ensure that the SRH lifetime reflects the recombination lifetime of the carriers in cases when not all the defects act only as recombination centres. When the defects also act as trapping centres the excess carrier concentrations can become unequal ($\Delta n \neq \Delta p$).

Macdonald *et. al.* [12] presented an analytical expression for the upper limit of N_t above which the standard SRH theory becomes inaccurate to support assumption 3. On the basis of their work, which compared the simplified SRH model with a more general model that accounts for the trapping effect, Macdonald *et. al.* suggest a critical defect density (N_{crit}) which must not be exceeded by the recombination centre density, and which is a function of N_{DOP}, defect energy level E_t and the capture cross sections (σ_n and σ_p). The expression for N_{crit} for a p–type silicon at low level injection is

$$N_{crit}^{LLI} = \frac{[p_0 + p_1] \times [n_1 + (\tau_{n0}/\tau_{p0})(p_0 + p_1)]}{p_0 - (\tau_{n0}/\tau_{p0})p_1} \tag{2.22}$$

This condition is fulfilled in the experiments and analyses performed in this work.

4. The relaxation time of the charge carrier captured is negligibly small in comparison with the average time between two emission processes.

This is yet another condition required to ensure that the defect level behaves as a recombination centre rather than a trap or a generation centre in assumption 3. When the relaxation time of the captured carrier is significant in comparison with two successive emissions, then the defect centre's behaviour are traps rather than recombination centres. The trapping effects of the defect centres cause distortion in excess carrier concentration and Δn becomes unequal to Δp. This results in significant deviation

between actual lifetime and trapping-free SRH lifetime. Relaxation time of the captured charge carrier depends upon temperature [13, 14]. This assumption can be verified by analysing the measured injection dependent carrier lifetime data over a wider range of temperatures.

2.3 Parameters of the SRH equation

Table 2.1: Components of the SRH parameters and their dependencies.

Components of the SRH parameter	**Relationship to SRH parameter**	**Defect Dependent**	**Temp Dependent**
Carrier capture cross sections (σ_n and σ_p)	Capture time constants (τ_{p0} and τ_{n0}) $\sigma_p = (\tau_{p0} \times v_{thp} \times N_t)^{-1}$ for p-type and $\sigma_n = (\tau_{n0} \times v_{thp} \times N_t)^{-1}$ for n-type	√	√
Thermal velocities of carriers (v_{thp} and v_{thn})	Capture time constants (τ_{p0} and τ_{n0}) $v_{thp} = (\tau_{p0} \times \sigma_p \times N_t)^{-1}$ for p-type and $v_{thn} = (\tau_{n0} \times \sigma_n \times N_t)^{-1}$ for n-type	×	√
Impurity doping concentration (N_{DOP})	Equilibrium carrier concentrations $N_{DOP} \approx p_0$ for p-type and $N_{DOP} \approx n_0$ for n-type	×	√
Intrinsic carrier concentration (n_i)	Equilibrium carrier concentrations $n_i^2 \approx n_0 \times N_{DOP}$ for p-type and $n_i^2 \approx p_0 \times N_{DOP}$ for n-type	×	√
Defect concentration (N_t)	Capture time constants (τ_{p0} and τ_{n0}) $N_t = (\tau_{p0} \times \sigma_p \times v_{thp})^{-1}$ for p-type and $N_t = (\tau_{n0} \times \sigma_n \times v_{thn})^{-1}$ for n-type	×	×
Defect energy level (ΔE_t)	SRH carrier densities (p_1 and n_1) $\Delta E_t = -k_B \times T \times ln(p_1/N_V)$ for p-type $\Delta E_t = -k_B \times T \times ln(n_1/N_C)$ for n-type	√	×
State densities of carrier in bands (N_V and N_C)	SRH carrier densities (p_1 and n_1) $N_V = p_1 / \exp(-\Delta E_t / k_B T)$ for p-type and $N_C = n_1 / \exp(-\Delta E_t / k_B T)$ for n-type	×	√

The SRH equation is a combination of four defect specific parameters (τ_{n0}, τ_{p0}, n_1 and p_1), two basic parameters (n_0 and p_0) and the excess carrier density (Δn). These parameters can be expressed as a function of other fundamental parameters of a semiconductor and temperature. A T-dependent model of these parameters and their constituent parameters will be applied during the measurement and analysis of lifetime. This section discusses the adopted models of these parameters and their relation to the more fundamental parameters. Table 2.1 presents the relationship of the constituents of the main SRH parameters, their dependency on defect energy levels and temperatures.

2.3.1 Capture time constant for electrons and holes (τ_{n0} and τ_{p0})

Electron and hole capture time constants (τ_{n0} and τ_{p0}) are dependent upon the respective capture cross sections (σ), thermal velocity (v_{th}) and defect concentrations (N_t). The expression for τ_{n0} and τ_{p0} is presented in Equation (2.20). The parameters of τ_{n0} and τ_{p0} and their constituent parameters are described below.

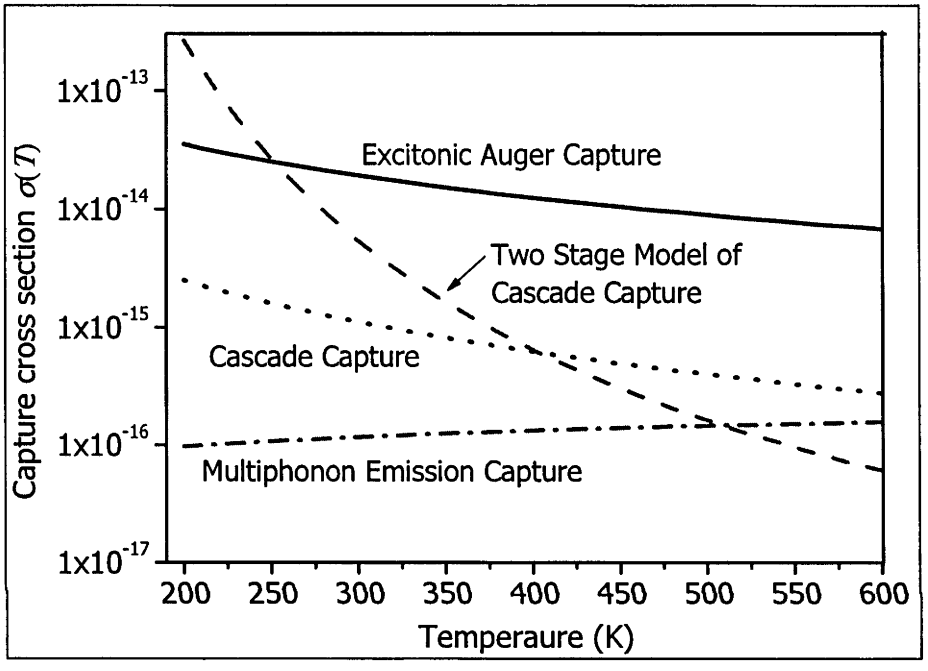

Figure 2.4: Temperature dependencies of different capture mechanisms.

a. Carrier capture cross sections (σ_n and σ_p)

In the SRH recombination process the carrier capture cross sections (σ_n and σ_p) are constituents of fundamental capture time constants τ_{n0} and τ_{p0} as shown in Equations (2.19) and (2.20). The defect centre moves randomly with the thermal velocity v_{th} in the lattice of silicon when we consider a free carrier as a frame of reference, (i. e. mobile defect and a stationary carrier). These movements of the defect centres enable the capture of free carriers in one second within a volume of $\sigma \times v_{th}$. This volume is known as a sweep-out volume and is also known as the fundamental capture rate. The physical area within the sweep-out volume is known as the capture cross section (σ). Capture cross sections are carrier specific and represented as σ_n for electrons and σ_p for holes. Capture cross sections of a particular defect level are dependent upon the effective

capture mechanisms by which they capture the carriers. Three different capture mechanisms have been proposed in which they are categorized on the basis of the energy released during the capture process. The temperature dependency of σ_n and σ_p is decided by the effective capture mechanism they follow. Three capture mechanisms and their thermal models are discussed here.

i. Radiative Capture

In the radiative capture process, excess energy is dissipated in the form of photon emission. This type of capture process is relevant to direct band semiconductors such as GaAs. However in the case of indirect band-gap semiconductors (Si, Ge etc), the radiative capture process is irrelevant [15] for room temperature and above. Furthermore, in the radiative capture process, the energy is dissipated in the form of photons and gives rise to a characteristic line in the emission spectrum corresponding to the depth of the defect in the silicon band gap. In this regard Hangleiter *et. al.* [16] mentioned that most impurities in silicon do not show such deep luminescence in the spectrum and, if shown, they are too weak and not sufficient to explain recombination [17]. The capture cross section size of this mechanism is 10^{-24} to 10^{-22} cm^2 and independent of temperature, i.e. $\sigma(T)$ = constant [18].

ii. Phonon-assisted capture

The capture process in which the energy is dissipated in the form of a phonon is known as phonon-assisted capture. This capture process is modelled as multiphonon emission capture (MPE) [19], cascade capture [20, 21] and a two-stage model of cascade capture [22] depending upon their nature as defect centres.

The cascade capture process was first introduced by Lax [20] in 1960. This capture process assumes that the defect centres possess numbers of closely spaced excited levels below the maximum phonon energy level. Hence a free carrier can be captured by hopping down to each level, releasing its excess energy in the form of one phonon during each step. This step-wise capture of a free carrier is known as cascade capture and is relevant to shallow coulomb attractive centres. The probability of capture by this mechanism decreases with temperature as the reemission of the carrier increases. The

temperature dependence of this capture mechanism is best described with a power law [20] and can be expressed as

$$\sigma(T) = \sigma_0 \times T^{-\alpha} \tag{2.23}$$

where σ_0 is known as the T-dependent pre-factor of the capture cross section and its value lies between 10^{-12} to 10^{-15} cm^2 and the value of temperature exponent α lies between 1 and 4. This capture mechanism is explained for the shallow impurity level which has coulomb attraction, however it does not explain recombination through a deep level defect centre with coulombic attraction [18].

In the MPE capture process the defect energy level crosses the CB by virtue of lattice vibration and captures a free electron. The equilibrium state of the occupied defect level jumps to a new equilibrium state after the capture process. These transitions of occupied defect levels result in the release of energy in a form of localized lattice phonons. A large amount of excess energy is released during the MPE capture process. This capture mechanism is relevant to the defect levels which are near the centre of the band gap, which are also known as deep levels. Furthermore, as MPE capture is the result of lattice vibration, the capture probability increases with temperature and can be expressed as

$$\sigma(T) = \sigma_\infty \times \exp(-E_a / k_B T) \tag{2.24}$$

where σ_∞ is known as T-dependent pre-factor of the capture cross section and its value lie between 10^{-14} and 10^{-15} cm^2 [19]. E_a is known as the activation energy that has to be overcome by the defect level to capture an electron in the CB or a hole in the VB and may lie anywhere between 0 and 0.56 eV (half of band gap).

As a cascade capture mechanism does not account for the capture of a carrier through the deep coulomb attractive centres, Gibb *et al.* [22] suggested a two-stage model of cascade capture in 1977. In this model, it is assumed that a free carrier is first captured by a cascade capture process into a shallow excited level E_1 of the defect centre and then sees transition of the carrier to a deeper ground state by MPE in a subsequent single step. The T-dependence of this model is expressed as Equation (2.25) as the combination of MPE and cascade capture

$$\sigma(T) = \sigma_0 \times T^{-2} \times \exp\left(\frac{E_1 - E_\infty}{k_B T}\right) \tag{2.25}$$

where E_1 is the energy level of the first excited state and E_∞ is the thermal barrier. The capture cross section decreases with increasing temperature for this type of carrier recombination.

iii. Auger capture

The capture process in which excess energy is transmitted to the other free carriers is known as the Auger capture process and it is further divided into two categories, classical and excitonic Auger capture. In the classic Auger capture process two independent free carriers meet at the impurity site and one of the carriers jumps into the defect level while the other receives the excess energy and becomes excited in its respective band. This capture process is less likely to be T-dependent and linearly dependent upon the carrier concentration [23].

Excitonic Auger capture is another type of Auger capture mechanism which considers a free exciton (a bound state of an electron-hole pair) containing a carrier to be captured and another to take over the excess energy when Auger capture occurs. As excitons are the main contributor of this type of recombination and their presence is strongly T-dependent, the capture process is also temperature dependent. For temperatures below 60 K, all carriers are bound as free excitons, hence the capture cross section is not dependent upon temperature. However for temperatures above 60 K, the capture cross section decreases with the increase in temperature, as more excitons become thermally ionized. The T-dependent expression for the excitonic Auger capture can be expressed as [24]

$$\sigma(T) = \sigma_0 \times T^{-\alpha} \quad for \quad T > 60K \tag{2.26}$$

where σ_0 is known as the T-dependent pre-factor of the capture cross section and its value lies between 10^{-12} and 10^{-15} and the value of the temperature exponent α can be any positive value ($\alpha > 0$).

In this regard, detection of an effective or dominating capture mechanism and its T-dependence is crucial to the understanding of the overall recombination in silicon.

Lifetime spectroscopy can be applied to find the effective capture mechanism for a particular defect. This is within the scope of this thesis and will be discussed in detail in Section 2.3.

b. Thermal velocity of the electrons and holes (v_{thn} and v_{thp})

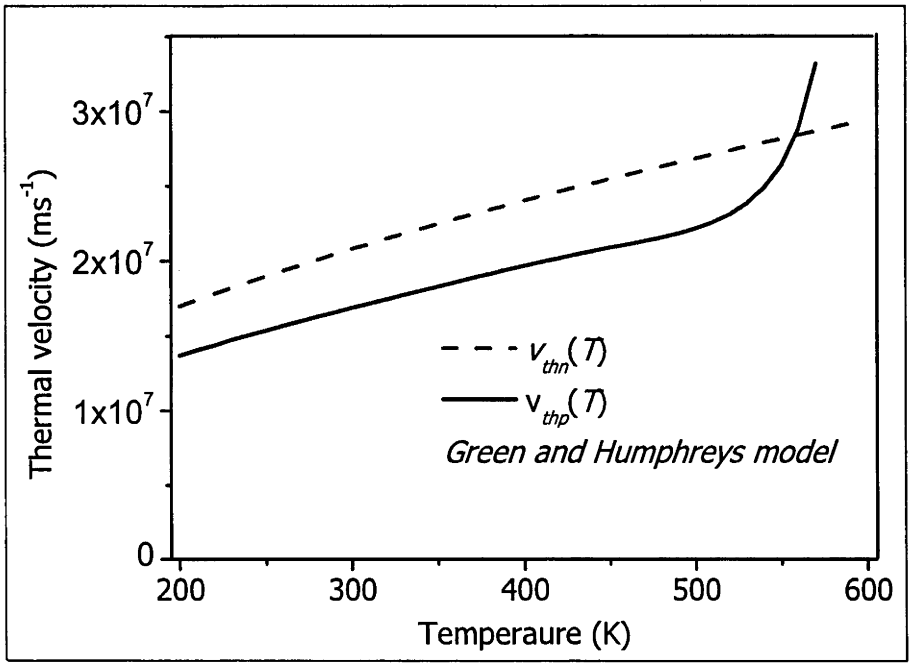

Figure 2.5: Temperature dependence of thermal velocity of electrons $v_{thn}(T)$ and holes $v_{thp}(T)$.

The thermal velocity of the electrons (v_{thn}) and holes (v_{thp}) are constituents of the SRH parameters τ_{n0} and τ_{p0}. Equation (2.20) shows the relationship between thermal velocities and τ_{n0} and τ_{p0}. Thermal velocities of the carriers are their movements in the lattice of the semiconductor when the defect centres are considered as the frame of references. The thermal velocity of electrons differ for a same defect thermal velocity because of the difference in their effective mass. Thermal velocities have a strong dependence on temperature and their average values can be expressed as [25]

$$v_{thn}(T)=\left(\frac{8k_BT}{\pi m^*_{tc}}\right)^{\frac{1}{2}} \text{ for electrons and } v_{thp}(T)=\left(\frac{8k_BT}{\pi m^*_{tv}}\right)^{\frac{1}{2}} \text{ for holes} \qquad (2.27)$$

where m_{tc}^* and m_{tv}^* are the effective masses of electrons in the CB and VB. m_{tc}^* is independent of temperature and can be expressed as [26]

$$m_{tc}^*(T) = \frac{4m_l^*}{\left[1+\left(\frac{m_l^*}{m_t^*}\right)^{\frac{1}{2}} \times \frac{\sin^{-1}\delta}{\delta}\right]^2} \tag{2.28}$$

where $m_l^* = 0.9163 \times m_0$ and is known as a longitudinal effective mass and $m_t^* = 0.1905 \times m_0$ and is known as a transverse effective mass associated with the ellipsoidal constant energy surfaces and $\delta^2 = (m_l^* - m_t^*) / m_l^*$.

$m_{tv}^*(T)$ is strongly dependent upon temperature and can be expressed as [26]

$$m_{tv}^*(T) = a + bT^2 - cT^3 + dT^4 - eT^5 + fT^6 - gT^7 \tag{2.29}$$

where a to g are empirical constants and values are given below.

a	0.3676	d	1.415372×10^{-9}	f	5.410849×10^{-15}
b	1.98738×10^{-5}	e	$-3.919169 \times 10^{-12}$	g	$-2.959797 \times 10^{-18}$
c	-2.588144×10^{-7}				

The Equations (2.28) and (2.29) show that the effective mass of the electrons and holes are T-dependent. The average thermal velocities of each carrier also differ according to their effective masses. Figure 2.5 shows the average thermal velocity of electrons and holes over a temperature range of 200 to 590 K.

c. *Defect concentration (N_t)*

Defect concentration (N_t) is a constituent parameter of the fundamental capture time (τ_{n0} and τ_{p0}) in the SRH equation as shown in Equation (2.20). N_t is the number of defect energy levels within unit volume in the lattice of a semiconductor. Intentional metallic contamination is performed for lifetime spectroscopy experiments to permit the study of the behaviour of particular metal defects. N_t is taken as equal or less than the implant dose if contaminated by the ion implant technique. Metal contamination can also be performed by adding a metallic impurity in the molten state before the crystal growth of silicon. In such a case N_t can be determined by using the technique Neutron Activation Analysis (NAA). LS can also be applied to determine N_t in some conditions, which is

described in Section 2.4. N_t is considered as being independent of temperature and this work makes this assumption throughout.

2.3.2 Equilibrium carrier concentration (n_0 and p_0)

The equilibrium carrier concentrations (n_0 and p_0) are basic parameters in semiconductors. These concentrations can be expressed in terms of Fermi levels (E_F), and can be calculated by using the law of mass action using the doping concentration and intrinsic carrier concentration (n_i)

$$n_0 = N_D \quad and \quad p_0(T) = \frac{n_i^2(T)}{N_D} \qquad \text{for } n\text{-type silicon} \qquad (2.30)$$

$$p_0 = N_A \quad and \quad n_0(T) = \frac{n_i^2(T)}{N_A} \qquad \text{for } p\text{-type silicon} \qquad (2.31)$$

where N_D, N_A are the doping densities and n_i is the intrinsic carrier concentration.

The expressions for n_0 and p_0 show that minority carrier concentrations are T-dependent but not the majority carriers. These expressions are based upon the assumptions of impurity depletion and negligible intrinsic conduction, which are valid for a certain temperature range near room temperature. However at sufficiently low temperature the available thermal energy is not enough for thermal ionisation of all dopant atoms, so the assumption of impurity depletion becomes invalid. On the other hand at sufficiently high temperatures, $n_i(T)$ becomes comparable to N_A or N_D and so there will be significant intrinsic conduction.

So for p-type semiconductors Rein *et al.* [18] present the T-dependent expression for $p_0(T)$ as

$$p_0(T) = f_A(T) \times N_A \text{ for T} < 350 \text{ K}$$

$$p_0(T) = \frac{1}{2} \times \left[N_A + \sqrt{N_A^2 + 4n_i^2(T)} \right] \text{ for T} \geq 350 \text{ K} \qquad (2.32)$$

where $f_A(T)$ is known as the ionization degree, which is a function of temperature, acceptor concentration and acceptor energy level (E_A), and can be expressed as

$$f_A(T) = \frac{-1+\sqrt{1+2\times C(T;N_A,E_A)}}{C(T;N_A,E_A)} \tag{2.33}$$

$$\text{where, } C(T;N_A,E_A) = \frac{4N_A}{N_V(T)}\exp\left(\frac{E_A - E_V}{k_B T}\right) \tag{2.34}$$

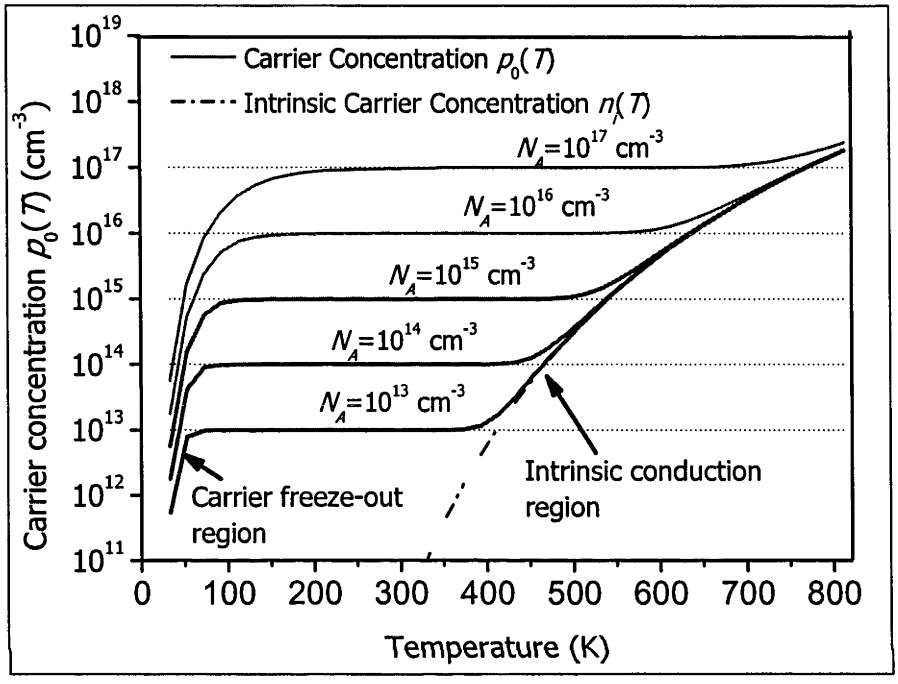

Figure 2.6: Temperature dependence of the majority carrier concentration $p_0(T)$ of p-type silicon for different doping densities N_A.

Equation (2.31) has been used throughout this work for the determination of $p_0(T)$ and $n_0(T)$ for p-type silicon by assuming that all dopant atoms are ionized. For n-type silicon $n_0(T)$ is assumed to be less affected by a lack of impurity depletion at low temperatures and Equation (2.30) is valid, however $n_0(T)$ is affected by intrinsic conduction at higher temperatures. Figure 2.6 depicts how $p_0(T)$ is affected by intrinsic conduction at higher temperatures and by a lack of depletion of impurities (freeze out) at low temperatures.

a. Intrinsic carrier concentration (n_i)

The intrinsic carrier concentration (n_i) is the number of carriers (electrons in the CB and holes in the VB) present in an undoped or intrinsic semiconductor. Intrinsic carriers are generated by thermal agitation and are T-dependent. At thermal equilibrium in an un-

doped semiconductor the number of electrons (n_0) in the CB is equal to the number of holes (p_0) in the VB, so the condition $n_0 = p_0 = n_i$ is valid. A doped semiconductor does not satisfy this condition however in thermal equilibrium the product of n_0 and p_0 is equal to the square of n_i satisfying the law of mass action

$$n_0(T) \times p_0(T) = n_i^2(T) \tag{2.35}$$

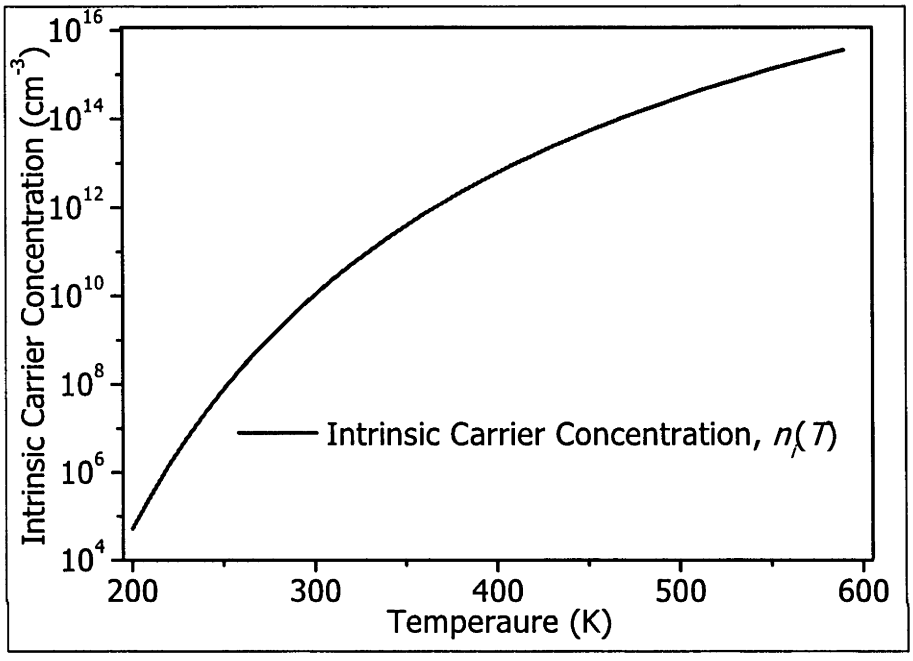

Figure 2.7: Temperature dependence of intrinsic carrier concentration $n_i(T)$.

n_i is not an explicit parameter of the SRH equation, however it affects n_0 and p_0. n_i can be expressed as [11]

$$n_i(T) = \sqrt{N_C N_V} \exp\left(-\frac{E_g}{2kT}\right) \tag{2.36}$$

where N_C and N_V are the effective densities of states in the CB and VB respectively. Figure 2.7 depicts the variation of n_i with temperature.

b. Effective density of states (N_C and N_V)

The effective state density (N_C and N_V) affect n_i and therefore n_0 and p_0. N_C and N_V also affect n_1 and p_1 as seen in Equations (2.42) and (2.43). A T-dependent model for N_C and N_V reported by Green *et al.* [25] is used in this work, which is expressed as

$$N_C(T) = 2.541\times10^{19}\left(-\frac{m_e^*(T)}{m_0}\right)^{\frac{3}{2}}\times\left(\frac{T}{300}\right)^{\frac{3}{2}} \tag{2.37}$$

$$N_V(T) = 2.541\times10^{19}\left(-\frac{m_h^*(T)}{m_0}\right)^{\frac{3}{2}}\times\left(\frac{T}{300}\right)^{\frac{3}{2}} \tag{2.38}$$

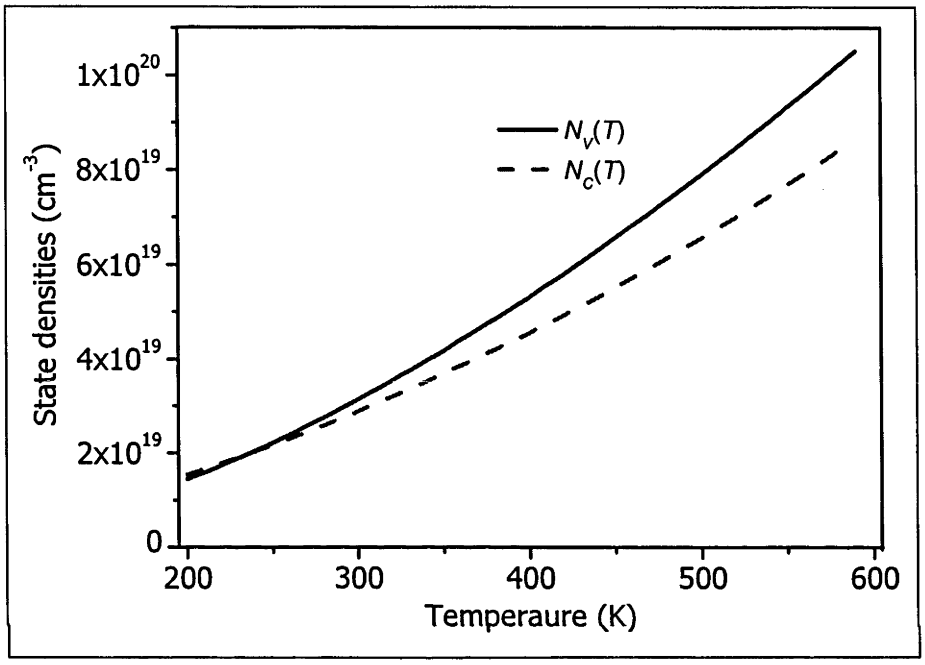

Figure 2.8: Temperature dependence of state densities $N_C(T)$ and $N_V(T)$.

where $m_e^*(T)$ and $m_h^*(T)$ are the effective masses of electrons and holes respectively and their temperature dependence is discussed next. Figure 2.8 depicts the temperature dependence of N_C and N_V in graphical form.

b. 1 Effective mass of electrons and holes (m^*_e and m^*_h)

The effective mass of electrons is expressed as the function of band gap by Green *et al.* [25] and expressed as

$$m_n^*(T) = 6^{\frac{2}{3}}\left[\left(0.1905\times\frac{E_g(0)}{E_g(T)}\right)^2\times0.9163\right]^{\frac{1}{3}} m_0 \tag{2.39}$$

where $m_0 = 9.81 \times 10^{-31}$ kg and is known as a rest mass of electrons, E_g (0) = 1.170 eV and is known as zero-point energy gap of silicon and $E_{gap}(T)$ is the band gap of the silicon.

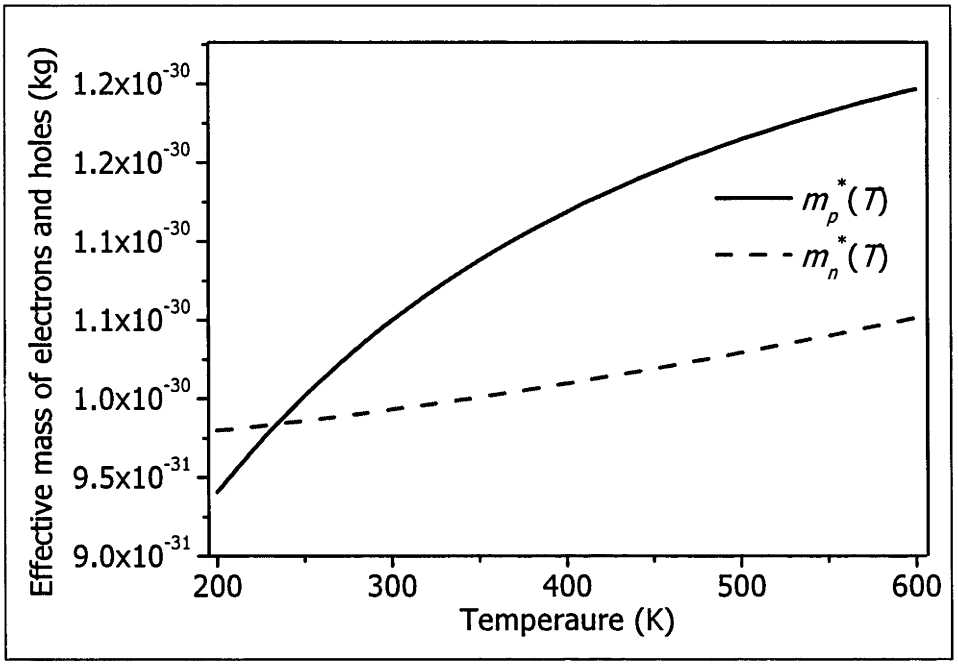

Figure 2.9: Temperature dependence of the effective mass of electrons $m^*_n(T)$ and holes $m^*_p(T)$ in silicon

Similarly, the effective mass of holes in silicon can be expressed as [25]

$$m_p^*(T) = \left[\left(\frac{a + bT + cT^2 + dT^3 + eT^4}{1 + fT + gT^2 + hT^3 + iT^4}\right)^2\right]^{\frac{2}{3}} m_0 \qquad (2.40)$$

where a to i are empirical constants and their values are given below.

a =	0.4435870	d =	0.1263218×10^{-5}	g =	0.2286895×10^{-3}
b =	0.3609528×10^{-2}	e =	0.3025581×10^{-8}	h =	0.7469271×10^{-6}
c =	0.1173515×10^{-3}	f =	0.4683382×10^{-2}	i =	0.1727481×10^{-8}

The effective masses of electrons and holes are depicted in Figure 2.9. The effective mass of electrons is dependent upon the band gap of the silicon E_g, and is discussed next.

b.2 Band gap in silicon (E_g)

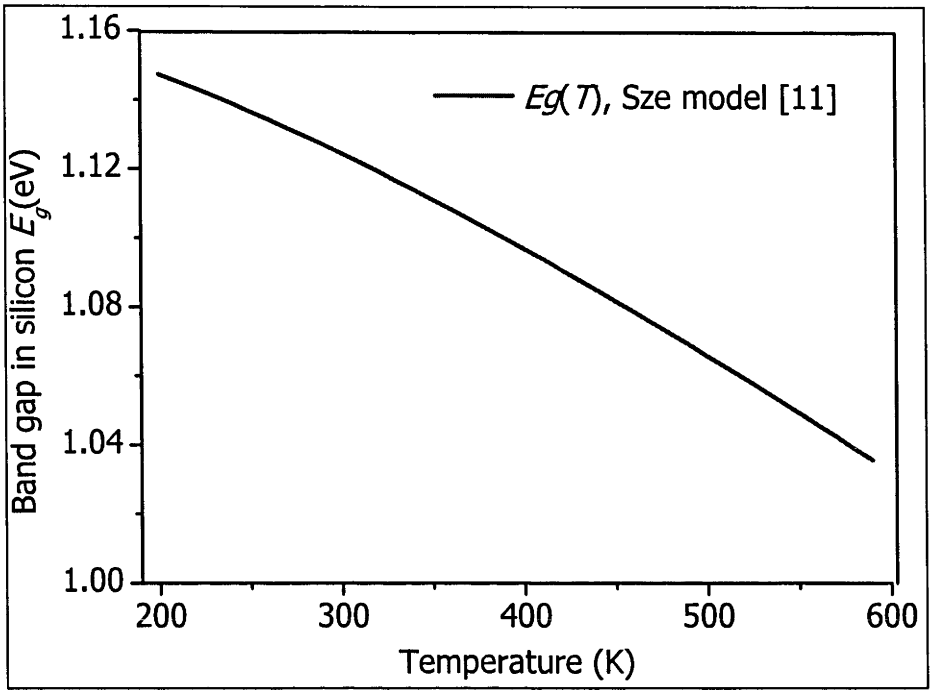

Figure 2.10: Temperature dependence of the energy band gap $E_g(T)$ in silicon.

The band gap (E_g) in highly pure silicon is considered as 1.12 eV at room temperature and normal atmospheric pressure [11]. However, E_g decreases with doping density (N_{DOP}) and increases with temperature. The variation of E_g with temperature is expressed as Equation (2.32) and is valid for the temperature range 0 – 1000 K where,

$$E_g(T) = E_g(0) - \frac{\alpha T^2}{T + \beta} \tag{2.41}$$

and $\alpha = 4.73 \times 10^{-4}$ eV/K and is known as the temperature coefficient, $\beta = 636$ K and is known as the temperature offset and $E_g(0) = 1.170$ eV [11]. The variation of E_g with temperature is depicted in Figure 2.10.

2.3.3 SRH carrier concentrations (n_1 and p_1)

SRH carrier concentrations (n_1 and p_1) are statistical factors and have important roles in the SRH equation. These are dependent upon respective densities of states (N_C and N_V), defect energy level (E_t) and temperature. n_1 and p_1 satisfy the law of mass action so the

product of n_1 and p_1 is equal to the square of n_i. The T-dependent expressions of n_1 and p_1 are presented in Equations (2.42) and (2.43) [2, 3] while the graphical representation is depicted in Figure 2.11 for the specific case of interstitial Fe in silicon.

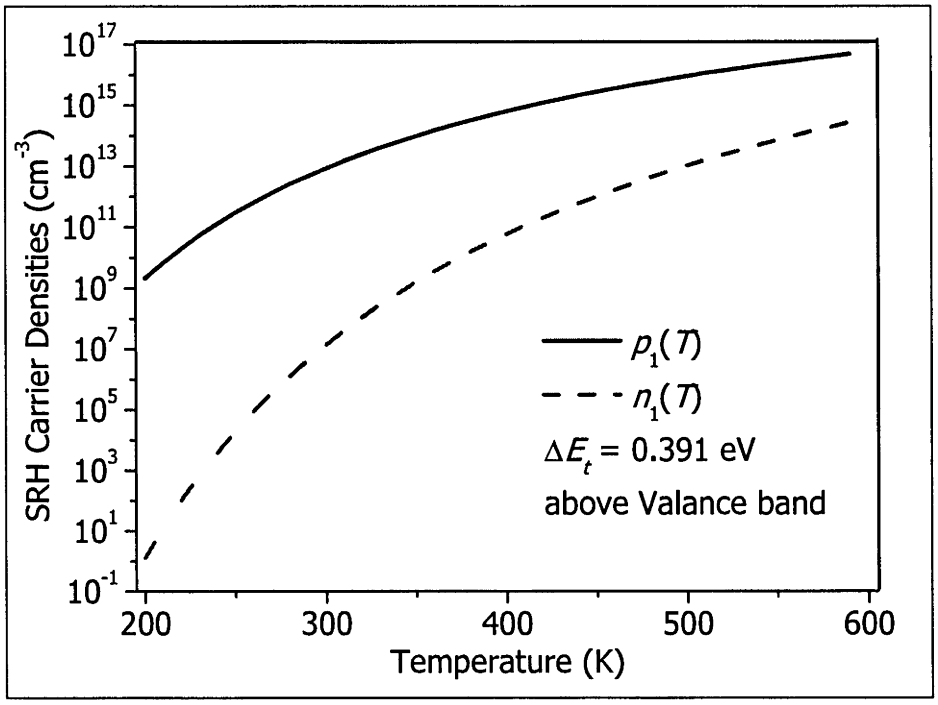

Figure 2.11: Temperature dependence of SRH carrier densities, $n_1(T)$ and $p_1(T)$ for an interstitial iron (Fe_i) defect in silicon.

$$n_1(T) = N_C(T)\left(-\frac{E_C - E_t}{k_B T}\right) \tag{2.42}$$

$$p_1(T) = N_V(T)\left(-\frac{E_t - E_V}{k_B T}\right) \tag{2.43}$$

where $k_B = 8.6174 \times 10^{-5}$ eV and is known as Boltzmann's constant.

2.3.4 Other parameters of the SRH equation

Excess carrier concentration (Δn), doping concentration (N_{DOP}) and Boltzmann's constant (k_B) are independent of temperature while the defect energy level (E_t) is assumed to be independent of temperature throughout this work. Figure 2.12 depicts p_0, p_1, n_0, n_1 and n_i for different E_t and temperatures in 1.0 Ω cm, p-type silicon.

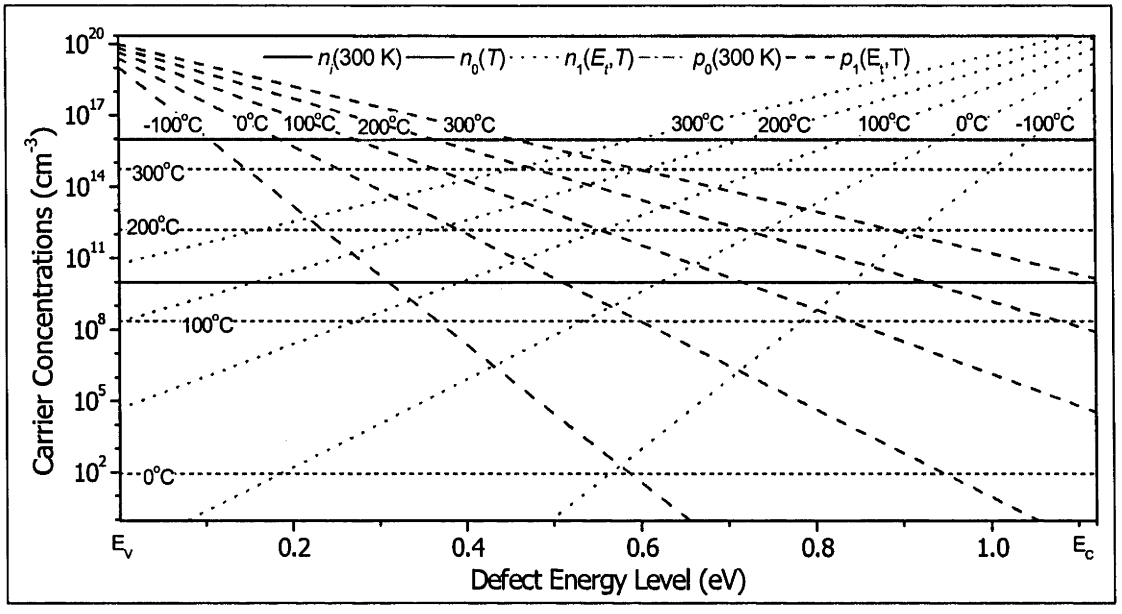

Figure 2.12: Carrier concentrations (p_0, p_1, n_0, n_1 and n_i) for different E_t and temperatures in 1.0 Ω cm, p-type silicon.

2.4 Lifetime Spectroscopy

Lifetime spectroscopy (LS) is a measurement and analysis technique for the characterization of defects in semiconductors. Apart from the better sensitivity of LS compared with DLTS as described in Chapter 1, LS uses the recombination process itself to analyse the recombination properties of defect centres, giving a better picture of those defects in semiconductors. The approach of LS is to fit the SRH Equation (2.19) to experimentally determined lifetime data (τ_{SRH}) at different values of Δn, N_{DOP}, T etc. This permits to determine one or more of the four defect specific parameters, τ_{n0}, τ_{p0}, n_1 and p_1, that are related to the more fundamental parameters, σ_n, σ_p, N_t and E_t, as described in Section 2.2.

The SRH equation describes the lifetime as a function of the seven parameters τ_{n0}, τ_{p0}, n_1, p_1, n_0, p_0 and Δn. These parameters are the functions of ten other parameters, σ_n, v_{thn}, σ_p, v_{thp}, N_t, E_t, N_C, N_V, n_i, and N_{DOP}, and most of them (σ_n, σ_p, v_{thn}, v_{thp}, N_C, N_V, n_i and N_{DOP}) are T-dependent. In this regard, the measured SRH lifetime (τ_{SRH}) at different Δn is not enough to solve the SRH equation in order to determine the four defect specific

parameters mentioned above. LS applies different approaches and conditions to extract some of the defect specific parameters by making one or more other parameters negligible, irrelevant or constant. Based upon these approaches and conditions LS are named accordingly. The first type is injection-dependent lifetime spectroscopy (IDLS) in which the lifetime for different values of Δn is analysed considering other parameters being negligible, irrelevant or constant. Temperature-dependent lifetime spectroscopy (TDLS) is the second type in which the lifetime at different temperatures is used to determine E_t. Finally, temperature and injection-dependent lifetime spectroscopy (TIDLS) performs analysis at different Δn and T. These different LS techniques have specific advantages, applications and limitations which are discussed in this section.

2.4.1 Evolution of Lifetime Spectroscopy

The first systematic LS was applied in 1990 by Kirino *et al.* [27] followed by Shimura *et al.* [28]. They applied a Laser Microwave-DLTS system (LM-DLTS), which was T-dependent and identified as TDLS to determine E_t of Na, Cr, Fe, Co, Ni, Cu, W and Au in silicon. In 1991 Ferenczi *et al.* [29] put forward IDLS theory and applied it to defect characterization of Fe-contaminated silicon. Later Bleichner *et al.* [30] used injection-dependent lifetime data obtained from different measurement techniques to study the recombination centre associated with a vacancy-oxygen complex. Since then, IDLS has been applied for the characterization of a boron-oxygen complex in Czochralski silicon by Schmidt *et al.* [31, 32].

Similarly, Walz *et al.*[38] in 1996, Keskitalu *et al.* [39] in 1998, Ahrenkiel *et al.* [43] in 2000 and Macdonald *et al.*[40] in 2001 applied IDLS for determination of properties of interstitial iron and iron-boron pair defect centers in silicon. In 2003 Schmidt *et al.* combined TDLS with IDLS known as TIDLS [41] for the first time to determine E_t and the ratio of a capture cross section (σ_n/σ_p) for Al defects in silicon. Since then TIDLS has been employed by other researchers for defect characterization of other metal impurities in silicon. In this regard, this section discusses the basis of assumptions, potential and limitations of TDLS, IDLS and TIDLS. Table 2.2 depicts some of the lifetime spectroscopies applied in the past by researchers, together with the measurement techniques applied to the measured and calculated parameters.

Table 2.2: Evolution of lifetime spectroscopy.

Researcher and Year	Technique	Measured parameters	Calculated parameters
Kirino and Simura 1990 [27, 28]	LM-DLTS for TDLS	$\tau(T, t)$	E_t for Na, Cr, Fe, Co, Ni, Cu, W and Au
Hayamizu *et al.* 1991[33]	LM-DLTS for TDLS	$\tau(T)$	E_t of FeB
Daio *et al.* 1994 [34]	LM-PC TDLS	$\tau(T, t)$	Study of meta stable surface recombination centres
Kaniyava *et al.* 1995 [35]	DLTS for TDLS	$\tau(T)$, $\tau(N_t)$	E_t of FeB
Ichimura *et al.* 1998 [36]	PC TDLS	$\tau(T)$	Temperature dependence of lifetime study in *p* and *n*-
Ferenczi *et al.* 1991 [29]	MW-PC IDLS	τ_{HLI} and τ_{LLI}	Detection of dominant impurity in silicon
Horanyi *et al.* 1996 [37]	MW-PC IDLS	$\tau(defect)$ and $\tau(proc.)$	Distinction of effect of Al, Cr, and Fe defects in silicon
Bleichner *et al.* 1996 [30]	FS-IDLS	$\tau(T)$ and $\tau(\Delta n)$	$v_n\sigma_n$, $v_p\sigma_p$ and E_t of oxygen complex
Schmidt *et al.* 1998 [31]	PC-IDLS	$\tau(\Delta n)$ and $\tau(t)$	$\sigma_p(B_iO_i)$
Schmidt *et al.* 1999 [32]	PC-IDLS	$\tau(\Delta n)$ and $\tau(t)$	E_t and σ_n/σ_p of boron-oxygen complex
Walz *et al.* 1995 [38]	SPV- Elymat	SPV, $\tau(\Delta n, N_A, N_t)$	E_t of FeB pairs in silicon
Keskitalo *et al.* 1998 [39]	DLTS-TIDLS	$\tau(\Delta n, T)$	Effects of oxygen related complexes in silicon
Macdonald *et al.* 2001 [40]	PC-IDLS	$\tau(\Delta n)$	E_t, σ_n and σ_p for FeB pairs in silicon
Schmidt *et al.* 2003 [41]	PC-TIDLS	$\tau(\Delta n, T)$	E_t and σ_n/σ_p of Al in silicon
Rein *et al.* 2005 [42]	MW-PC, TIDLS	$\tau(\Delta n, T)$	E_t and σ_n/σ_p of Fe_i and E_t, σ_n and σ_p of FeB

2.4.2 Preliminary simplification of the SRH equation

The SRH theory is the basis of the LS mentioned above and also the basis of this work. Simplification of the SRH equation, subjecting different conditions and assumptions, helps to understand the defect characterization potential and restrictions of LS. The SRH equation for *p*-type silicon is presented in this section and an analogous simplification for *n*-type presented in Appendix B.1. A detectible effect of of Δn on τ_{SRH} is one of the requisites for sensitive LS. In practice, higher values of τ_{p0} in comparison to τ_{n0} for many common impurities makes τ_{SRH} less sensitive to Δn in *n*-type silicon and LS becomes difficult. As a consequence, almost all results published using the

application of LS analysis have performed experiments on p-type silicon. The simplified SRH equation mentioned in Section 2.1.3 is re-stated here.

$$\tau_{SRH} = \frac{\tau_{p0}(n_1 + n_0 + \Delta n) + \tau_{n0}(p_0 + p_1 + \Delta n)}{n_0 + p_0 + \Delta n} \tag{2.44}$$

In p-type silicon $n_0 << p_0$ and $n_0 << n_1$ for a certain temperature range (the temperature range is dependent upon N_A and E_t) which is presented in a tabular and graphical form in Appendix-B.2 so Equation (2.44) can be written as

$$\tau_{SRH}^{p} = \frac{\tau_{p0}(n_1 + \Delta n) + \tau_{n0}(p_0 + p_1 + \Delta n)}{p_0 + \Delta n} \tag{2.45}$$

We then impose a condition known as low-level injection (LLI), where the excess carrier concentration $\Delta n << p_0$ and n_1, and τ_{SRH} can be written as

$$\tau_{SRH}^{LLI,p} = \tau_{p0}\frac{n_1}{p_0} + \tau_{n0}\left(1 + \frac{p_1}{p_0}\right) \tag{2.46}$$

This expression can be subjected to two different conditions depending upon the location of E_t in the band gap of the silicon. If we consider E_t in the upper half of the band gap (UBGH), then $p_0 >> p_1$ hence the expression (2.46) can be re-written as

$$\tau_{SRH}^{LLI,p} = \tau_{p0} \times \frac{n_1}{p_0} + \tau_{n0} \tag{2.47}$$

Similarly, if we consider E_t in the lower half of the band gap (LBGH), then $p_0 >> n_1$ so the first part of expression (2.46) can be neglected and re-written as

$$\tau_{SRH}^{LLI,p} = \tau_{n0}\left[1 + \frac{p_1}{p_0}\right] \tag{2.48}$$

2.4.3 Injection-dependent lifetime spectroscopy (IDLS)

The objective of all lifetime spectroscopy is to determine the electrical properties of one or more defects in silicon wafers using parameterization of the SRH equation. As

mentioned in the previous section, the SRH equation gives the SRH lifetime as a function of seven main variables, (τ_{n0}, τ_{p0}, n_1, p_1, n_0, p_0 and Δn), which are also the functions of other parameters. Hence achieving a solution from a single IDLS curve is almost impossible. In this regard, several attempts have been made to solve the SRH equation by changing only one or two variables and keeping those remaining constant. LS which applies variable injection density (Δn) as a function of lifetime with or without other variables to determine one or more variable in the SRH equation is known as IDLS. Walz *et al.* [38] applied IDLS with variable doping density (N_{DOP}) samples to determine E_t, σ_p and σ_n of iron-boron pairs (FeB) in silicon. As they changed doping densities (N_{DOP}) in different samples and made the SRH equation fit, the technique is known as N_{DOP}-IDLS.

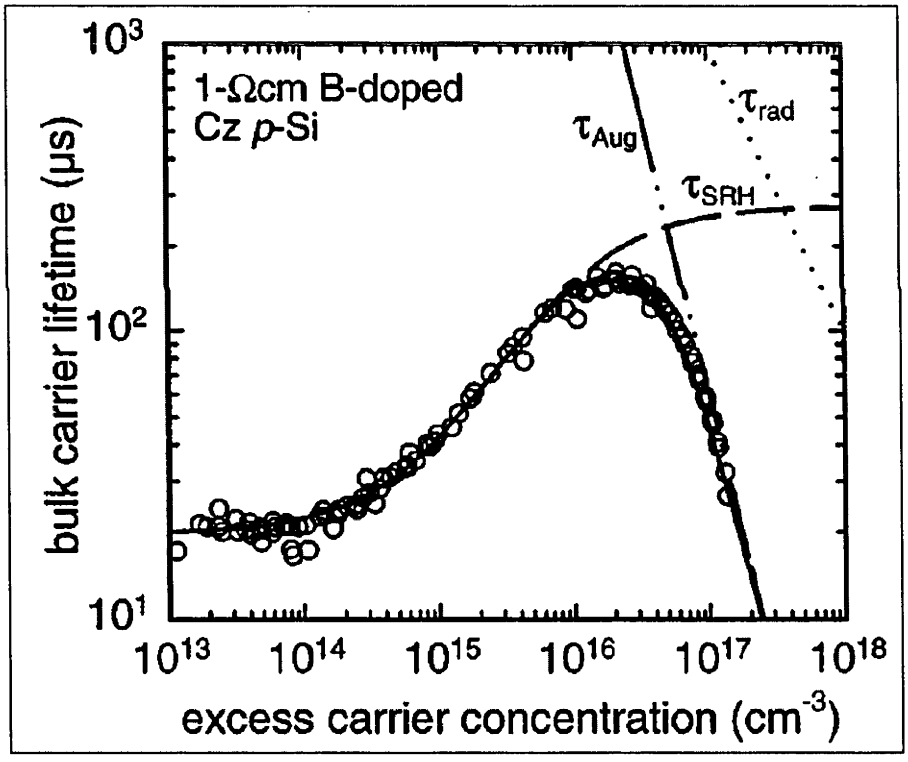

Figure 2.13: IDLS analysis of 1 Ωcm boron-doped silicon, Source: Schmidt *et al.* [31], 1998.

Schmidt *et al.* [31] applied IDLS to determine σ_p of suspected boron-oxygen (B_iO_i) pairs in boron-doped Czochralski silicon. They applied light to the samples which increased the number of B_iO_i defects (N_t), hence they fit the SRH equation for different

Δn with known values of variable defect concentration N_t. Their SRH equation fit is depicted in Figure 2.13. Later in 1999, Schmidt *et al.* [32] applied IDLS with different doping densities (N_{DOP}) samples (1 – 31 Ω cm) and different levels of impurity densities (N_t) by the use of a similar light degradation technique and measured E_t of the B_iO_i pairs and the electron/hole capture time constant ratio (τ_{p0} / τ_{n0}).

IDLS was performed by different researchers [18] for the characterization of the most common defects in silicon. However, IDLS has its own short-comings and restrictions which are discussed below.

Effect of minority carrier trapping (MCT) and depletion region modulation (DRM)

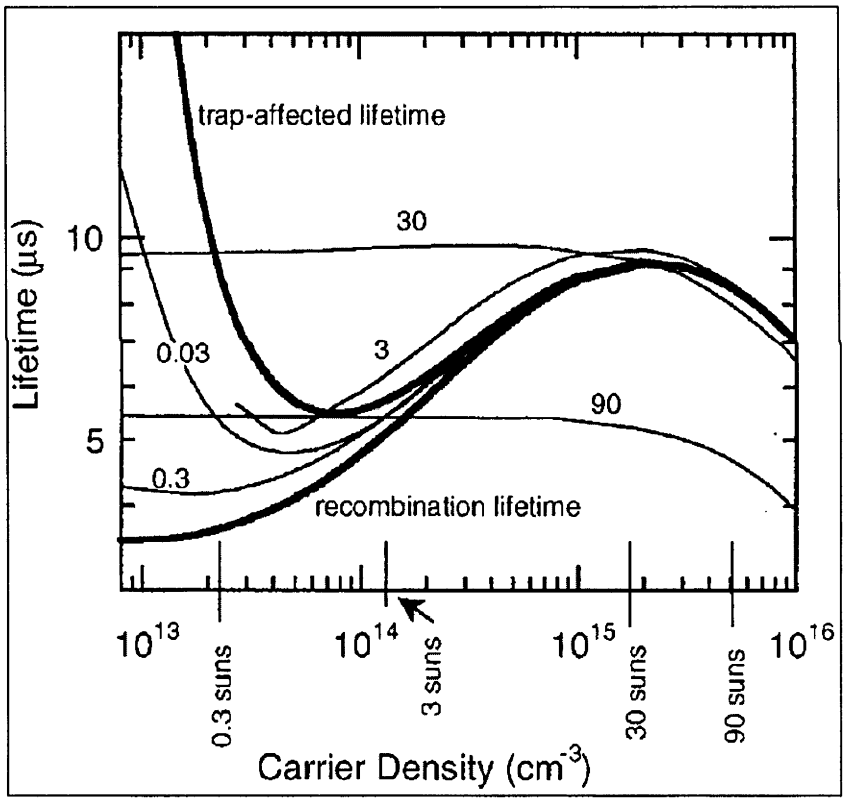

Figure 2.14: The effect of MCT trapping in the lifetime at LLI, Source: Macdonald *et al.* [45], 2001.

IDLS compares the measured τ_{SRH} as a function of Δn in different conditions of other known parameters for defect characterization. The measurement or extraction of pure τ_{SRH} is a fundamental requirement for IDLS analysis, with this analysis requiring reliable

measurement techniques for τ_{SRH} over the whole injection range. τ_{SRH} measurement for LLI may be completely affected if additional minority carrier trapping centres (MCT) [44] are present in silicon. These trapping centers do not contribute to recombination but only capture minority carriers and their effect dominates in LLI region, showing artificially high values of carrier lifetime. The effect of trapping in the lifetime at LLI is depicted in Figure 2.14. Such influence of MCT in τ_{SRH} measurement at LLI may be reduced by applying different techniques [45], however it is difficult to ensure that the measurements are absolutely free from MCT.

The second type of error associated while measuring lifetime at LLI, using photoconductance technique [46] for a particular type of wafer, is depletion region modulation (DRM) [47]. The DRM effect in measurements gives an apparent recombination lifetime much greater than the true lifetime at LLI. Hence, in both cases, a proper method of extracting pure SRH lifetime from the apparent lifetime is necessary.

MCT and DRM affect all three types of LS as they are sample specific. IDLS utilizes injection-dependent lifetime only at a particular temperature in contrast to TDLS and TIDLS. This makes IDLS more susceptible to these effects as the small effects are difficult to notice visually in a single set of injection-dependent lifetime curve, but may still affect the analysis. On the other hand TDLS and TIDLS require measurements at several temperatures where the effects of MCT and DRM can be noticed more easily. Furthermore, the effect of MCT can be nullified at higher temperatures in TDLS and TIDLS but it is not possible for IDLS at room temperature.

On the other hand, the net measured lifetime at high level injection (HLI) Δn is affected by the intrinsic recombination lifetime according to Equation (2.4). In the HLI condition, τ_{SRH} needs to be extracted from measured lifetime by deducting τ_{RAD} and τ_{AUG}. Hence, knowledge of Auger and Radiative recombination lifetime parameters is crucial for IDLS analysis at HLI. Furthermore, IDLS analysis for multiple defects in silicon decreases and becomes not possible as the number of parameters increase with the number of defects. These increasing number of defect parameters increases ambiguity in the analysis [18] and hence in the findings.

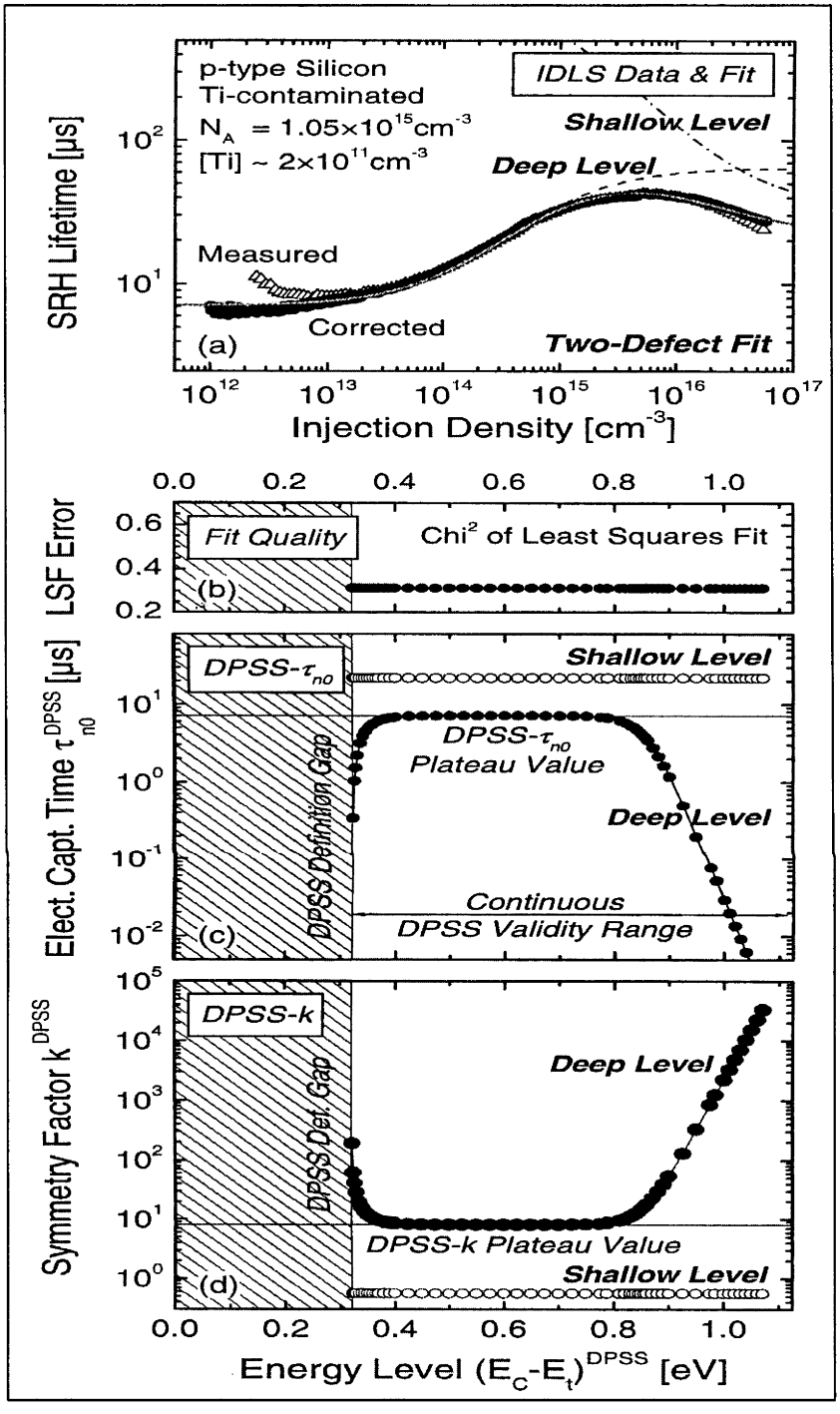

Figure 2.15: DPSS analysis of titanium impurity in silicon, Source: Rein *et al.* [18], 2005

Considering the problems associated with IDLS, Rein *et al.* [18] propose a novel subsidiary analysis tool for IDLS, which is known as defect parameter solution surface (DPSS). In DPSS, the authors considered the ratio of fundamental capture time (τ_{p0} / τ_{n0}

= k) as a constant. The expression (2.44) can then be re-expressed for LLI, where $\Delta n << p_0$ and n_1 as

$$\tau_{SRH}^{LLI} = \tau_{n0}\left[\left(\frac{p_0 + p_1}{p_0 + n_0}\right) + k\left(\frac{n_0 + n_1}{p_0 + n_0}\right)\right] \tag{2.49}$$

Similarly for High level injection (HLI) where $\Delta n >> p_0$ and n_1, the expression (2.44) can be re-expressed as

$$\tau_{SRH}^{HLI} = \tau_{n0}(1 + k) \tag{2.50}$$

The difference between τ_{SRH} for HLI and LLI can be expressed as a function of three unknown parameters (E_t, τ_{n0} and k)

$$\Delta\tau_{SRH}^{LLI} = \tau_{SRH}^{HLI} - \tau_{SRH}^{LLI} = \tau_{n0}\left[\left(\frac{n_0 - p_1}{p_0 + n_0}\right) + k\left(\frac{p_0 - n_1}{p_0 + n_0}\right)\right] \tag{2.51}$$

DPSS determines three unknowns, k, τ_{n0} and E_t, by solving the Equations (2.50) and (2.51) or their combinations which considers other SRH parameters fixed for analysis purposes. Figure 2.15 depicts the DPSS analysis of titanium defects in silicon. The detail of equation solving procedures is yet to be disclosed. Furthermore, authors [48] reported more than one solution for E_t for the same defect which in some cases is non-consistent with E_t when measured by other established techniques like DLTS [6]. This analysis can be performed by considering three variables, τ_{n0}, τ_{p0} and E_t rather than considering a third variable k. The third variable k was chosen by the author for simplification purposes.

2.4.4 Temperature-dependent lifetime spectroscopy (TDLS)

TDLS is considered as an independent method for the determination of E_t and was reportedly first applied by Kirino *et al.* [27] in 1990. Unlike IDLS, TDLS analysis applies the measured lifetime at a particular Δn in LLI so the Equation (2.46) is applicable. Furthermore, the simplification of TDLS is performed in two different conditions depending upon the location of E_t in the band gap. The stepwise

simplification of the SRH equation for E_t in UBGH is described here and the analogous final expression for E_t in LBGH is stated.

For E_t in UBGH, the Equation (2.47) is valid and when consider that the ratio of capture cross sections, $\sigma_n(T) / \sigma_p(T)$ is equal to the ratio of the fundamental capture times $\tau_{p0}(T)/\tau_{n0}(T) = k$, this implies $v_{thn}(T) = v_{thh}(T)$ and k is not T-dependent. The negative consequence of this assumption is an invalid result of energy levels reported by Roth *et al.* [48], which is explained later in this section. If this assumption is valid, Equation (2.47) can be written as

$$\tau_{SRH}^{LLI}(T) = \tau_{n0}(T)\left(1 + k\frac{n_1(T)}{p_0(T)}\right) \tag{2.52}$$

As, $n_1(T)$ is the dependent effective density of the conduction band according to Equation (2.33) and N_C can be expressed as

$$N_C(T) = N_C^{300K}\left(\frac{T}{300K}\right)^{1.5} \tag{2.53}$$

where, $N_C{}^{300K}$ is the SRH state density in the conduction band at 300 K.

Similarly, the thermal velocity expressed in Equation (2.27) can be re-expressed as

$$v_{th}(T) = v_{th}^{300K}\left(\frac{T}{300K}\right)^{0.5} \tag{2.54}$$

where $v_{th}{}^{300K}$ is the thermal velocity of electrons at 300 K.

According to Equations (2.20) and (2.54) $\tau_{n0}(T)$ can be re-expressed as

$$\tau_{n0}(T) = [N_t \sigma_n v_{th}(T)]^{-1} = \tau_{n0}^{300K}\left(\frac{T}{300K}\right)^{-0.5} \tag{2.55}$$

where $\tau_{n0}{}^{300K}$ is the fundamental capture time for electrons at 300 K.

In the temperature range in which impurity depletion is valid (temperature between freeze out and intrinsic conduction) p_0 equals N_A, and is independent of temperature. So for a sufficiently low temperature (which depends upon N_A and E_t) $n_1(T)/p_0$ can be neglected and the LLI-SRH lifetime is equal to $\tau_{n0}(T)$. However for sufficiently high temperatures $n_1(T)/p_0$ becomes dominant and the term $\tau_{n0}(T)$ in Equation (2.52) can be neglected. Hence using Equations (2.52), (2.53) and (2.55) the SRH-LLI lifetime can be written as,

$$\tau_{SRH}^{LLI}(T) = \tau_{n0}(T) k \frac{n_1(T)}{p_0} \quad \alpha \quad T \times \exp\left(-\frac{E_C - E_t}{k_B T}\right) \tag{2.56}$$

This shows that the SRH lifetime is a combination of a linear and an exponential function of temperature. This expression can be written as

$$\ln\left[\frac{\tau_{SRH}^{LLI}(T)}{T}\right] = const - \frac{E_C - E_t}{k_B T} \tag{2.57}$$

Similarly, for the condition when the defect energy lies in LBGH, the ratio $p_1(T)/p_0(T)$ dominates temperature dependence in the Equation (2.50). Hence by applying the temperature dependence of $N_V(T)$, $v_{th}(T)$ and $\tau_{p0}(T)$ as being analogous to Equation (2.53), (2.54) and (2.55). $\tau_{SRH}(T)$ for sufficiently high temperatures ($\geq 200\,^{\circ}C$), can be expressed assuming $v_{thn}(T) = v_{thh}(T)$

$$\ln\left[\frac{\tau_{SRH}^{LLI}(T)}{T}\right] = const - \frac{E_t - E_V}{k_B T} \tag{2.58}$$

Hence the slope of the plot of expressions (2.57) and (2.58) are only dependent upon E_t. Figure 2.16 depicts TDLS analysis for the determination of E_t in Arrhenius plot form. This figure illustrates that $\tau_{SRH}(T)$ starts to rise significantly after a certain temperature known as the onset temperature (T_{onset}) which is dependent upon Δn to a large extent and less dependent upon N_A or N_D. This significant rise of $\tau_{SRH}(T)$ with temperature is known as the Arrhenius rise and continues until the temperature (T_{IC})

where the intrinsic conduction begins. T_{IC} is dependent upon the doping density N_A or N_D.

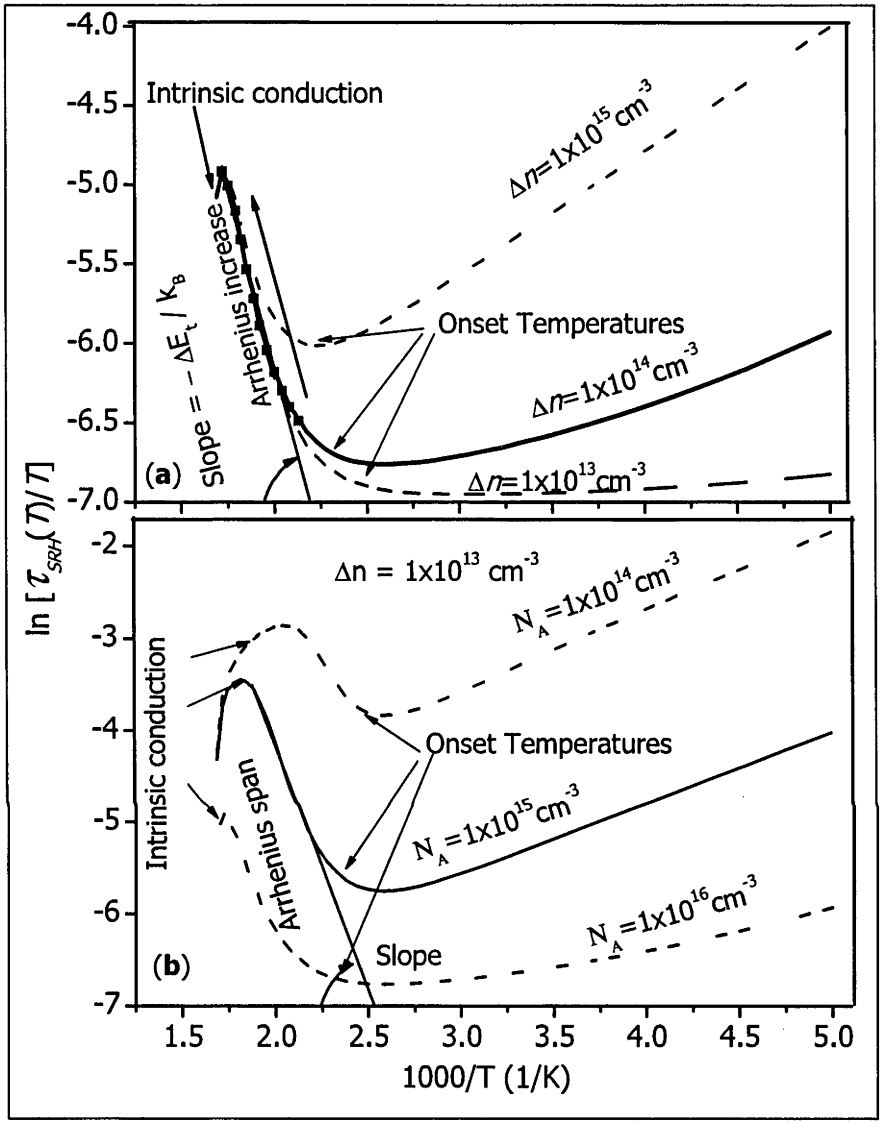

Figure 2.16: Arrhenius plots for TIDLS analysis depicting onset temperature (T_{onset}) for Arrhenius rise in lifetime, Arrhenius span and the temperature for intrinsic conduction (T_{IC}). (a) Depicts the Δn dependence of T_{onset} for p-type wafer with $N_A = 1 \times 10^{16}$ cm^{-3}. (b) Depicts the N_A dependence of T_{IC} for $\Delta n = 1 \times 10^{13}$ cm^{-3}. Both plots consider the defect energy level $E_t = 0.28$ eV

Limitation and drawbacks of TDLS

TDLS analysis is in principle a relatively straight forward measurement of the slope of the Arrhenius rise, revealing the energy levelE_t, and is not influenced by other T-

dependent defect parameters. Furthermore, the determination of E_t is possible from a T-dependent carrier lifetime measurement of a single wafer. The slope of the Arrhenius span is the same whether the plot is according to Equations (2.57) or (2.58). Hence TDLS gives the depth of E_t but does not provide any information about the band gap half in which the defect is situated. The accuracy of the measured E_t is dependent upon the slope of the Arrhenius span which needs to be determined by approximation of T_{onset} and T_{IC}. Hence the accuracy in locating T_{onset} and T_{IC} on Arrhenius introduces error in the E_t determination. Furthermore, the slope of the Arrhenius span is different with Δn as shown in Figure 2.16(b), hence the location of the true low level injection is crucial to this analysis.

In addition, TDLS assumes that the fundamental capture ratio, $k = \tau_{p0}(T) / \tau_{n0}(T)$, is independent of temperature. The temperature independence of k is only valid when electron and hole capture follows the same mechanism with exactly the same T-dependent parameters (see Section 2.2.1.a) and such a situation has not been reported for silicon. An inconsistent result for E_t for a titanium defect (E_C – 0.49 eV) in silicon, reported by Roth *et al.* [48], can be taken as an example which was not detected by DLTS [6].

2.4.5 Temperature and injection-dependent lifetime spectroscopy (TIDLS)

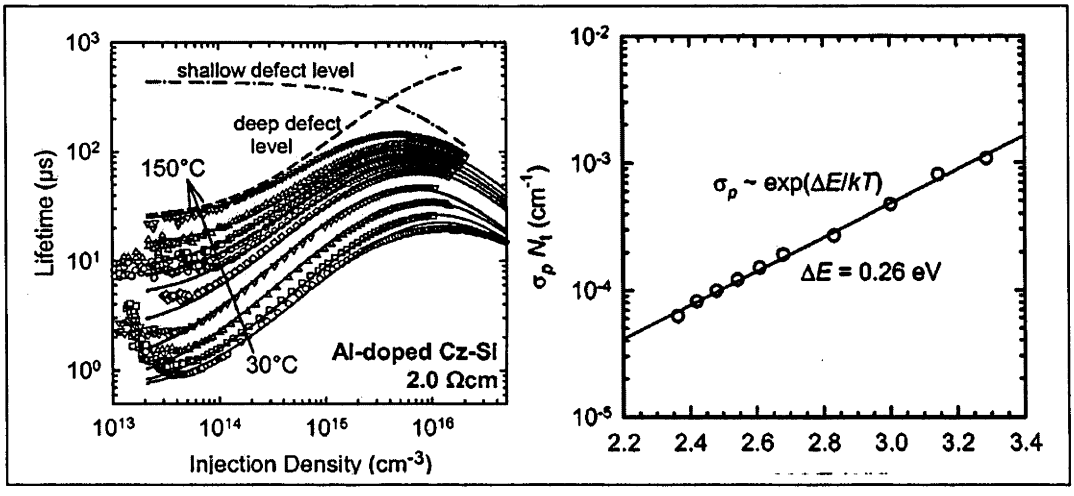

Figure 2.17: Measured lifetime data and temperature dependence of $\sigma_p \times N_t$ of the deep-level centre in Al-doped CZ–Si as determined from TIDLS analysis (open circles) Source: Schmidt *et al.* [41].

TDLS and IDLS have their own advantages and short comings as motioned in previous sections. The lifetime spectroscopy in which lifetime measurements are taken for various Δn, at different temperatures and analyzed for a defect characterization is known as temperature and injection-dependent lifetime spectroscopy (TIDLS). In this context, TIDLS can be treated as an expansion of IDLS, where the temperature is considered as a variable and other SRH parameters as fixed or irrelevant.

The first TIDLS instrument was developed and tested on Al-doped silicon by Schmidt *et al.* [41] in 2003. They analysed their data to determine the defect energy E_t and temperature dependence of the capture cross-section ratio σ_n / σ_p. Measured data and results obtained by Schmidt *et al.* is depicted in Figure 2.17. The measurement device consisted of an inductive-coil PC instrument (WCT-100) from Sinton Consulting Inc [46] with a brass ring capable of heating the sample from 30 °C to 150 °C.

Since then various TIDLS experiments have been performed by different researchers using different experimental set ups in order to characterize the common defects in silicon. Diez *et al.* [52] and Brikholz *et al.* [53] applied a similar setup used by Schmidt *et al.* [40], for the measurement of E_t, σ_n / σ_p and the trap density N_t of tungsten- and cobalt-contaminated silicon, and the measurement of E_t, σ_n and σ_p of iron-contaminated boron-doped silicon. TIDLS analyses have been performed over a wider temperature range by Roth *et al.* using a photoluminescence (PL) [17] detector to measure E_t of titanium-contaminated boron-doped silicon, and by Rein *et al.* using a microwave PC detector to determine E_t and σ_n / σ_p of molybdenum-contaminated silicon [54]. Rein *et al.* have also combined temperature-controlled microwave-detector and inductive-coil PC instruments to characterize recombination in iron-contaminated boron-doped silicon [42].

TIDLS has the potential to overcome the shortcomings of TDLS and IDLS. However all the analysis described above is based upon the assumption that $\sigma_n / \sigma_p = k$ is independent of temperature, which is not always valid. As mentioned in Section 2.2.1, σ_n and σ_p can follow a different capture mechanism and k becomes strongly T-dependent. Figure 2.18 depicts $\sigma_n(T) / \sigma_p(T)$ based upon the T-dependent model of σ_n and σ_p as determined by various researchers for some common impurities in silicon.

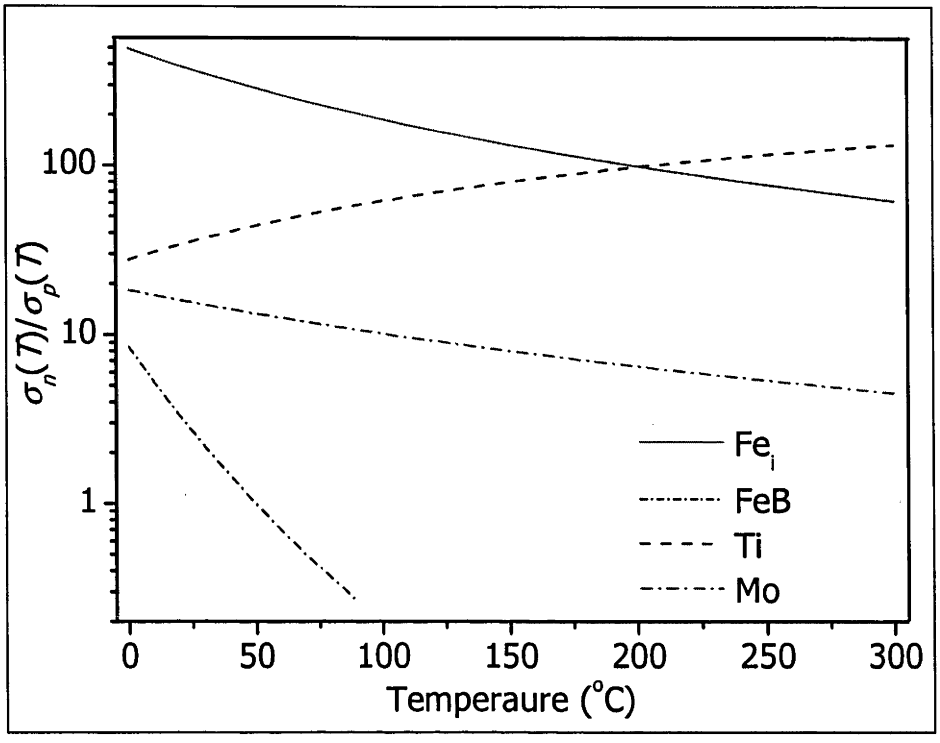

Figure 2.18: Temperature dependence of capture cross section ratios for most common types of impurities in silicon: Sources [6, 49-51]

In this regards IDLS, TDLS and TIDLS analyses applied so far for the defect characterization of silicon are not free of ambiguity. Section 2.5 presents and discusses the theoretical aspects of an unambiguous method of TIDLS analysis for the determination of τ_{n0} and τ_{p0} of a defect in silicon explicitly, which can later be used to determine σ_n and σ_p with known values of Nt and v_{th}. The proposed analysis is implemented for defect characterization later in this thesis.

2.5 New TIDLS analysis for T-dependent σ_n, and σ_p

Lifetime spectroscopy is a proven technique for defect characterization in the silicon industry. Traditionally, LS has been applied to determine the defect energy level (E_t) by assuming the capture cross sections σ_n and σ_p or their ratio (σ_n / σ_p) are constant with temperature, an assumption which is unlikely to be true. This section presents a new approach in TIDLS analysis which independently determines $\sigma_n(T)$ and $\sigma_p(T)$. This

analysis makes E_t irrelevant or assumes it independent of temperature, which is more realistic than assuming σ_n and σ_p as T-independent in traditional Lifetime spectroscopy. These T-dependent σ_n and σ_p can be used to determine the effective carrier capture mechanism in the recombination process and to determine the T-dependent expression for σ_n / σ_p.

Similar to other Lifetime spectroscopy analyses the proposed approach is based upon the simplification of SRH lifetime Equation (2.21). This can be further simplified by neglecting one or more SRH parameters. Most of the SRH parameters are dependent upon carrier concentration and temperature. In this regard, the value of a SRH parameter is considered negligible if its value is less than one percent of another parameter (when summed).. Depending upon the doping type and location of E_t in the band gap of silicon, SRH simplification is explained in four ways.

2.5.1 E_t in lower band gap half (LBGH)

In this condition, a p-type wafer can be considered where three assumptions can be made for the simplification of the SRH equation.

A: Negligible $n_0(T)$

$n_0(T)$ can be neglected in comparison to $p_0(T)$ for p-type silicon for a certain temperature range and doping density, N_A. Figure 2.19 depicts the temperature region for which $n_0(T)$ can be neglected for different values of N_A. The simplified SRH equation can be re-written as

$$\tau_{SRH} = \frac{\tau_{no}(p_1 + p_0 + \Delta n) + \tau_{po}(n_1 + n_0 + \Delta n)}{(p_0 + \Delta n)} \tag{2.59}$$

B: Negligible $[n_1(T) + n_0(T)]$

$n_1(T)$ is sufficiently low when E_t lies in the LBGH. Similarly $n_0(T)$ is sufficiently low for a certain range of temperature for a given value of N_A. Figure 2.19 shows the temperature region for different values of E_t below which $n_1 + n_0 < 0.01 \times \Delta n = 0.0001 \times p_0$, and $p_1 = 0.01 \times p_0$. Hence the SRH equation can be further simplified as

$$\tau_{SRH} = \frac{\tau_{no}(p_1 + p_0 + \Delta n) + \tau_{po}(\Delta n)}{(p_0 + \Delta n)} \tag{2.60}$$

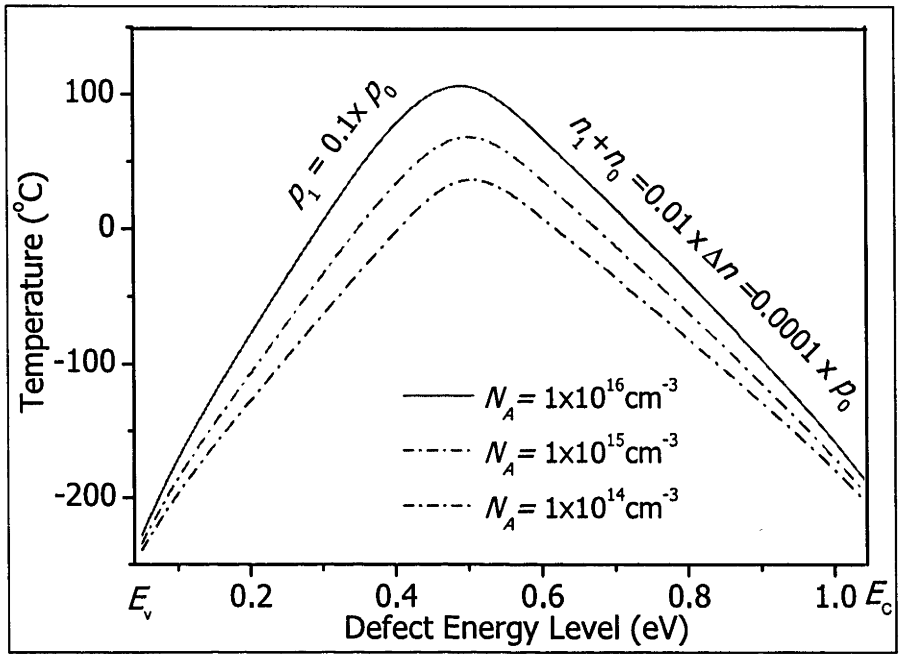

Figure 2.19: Temperature below which $n_1 + n_0 = 0.01 \times \Delta n = 0.0001 \times p_0$, and $p_1 = 0.01 \times p_0$ as a function of E_t for p-type silicon of three doping densities (N_A).

C: Low level injection $p_0 >> \Delta n$

For LLI, Δn can be removed from the denominator and the first part of the numerator in Equation (2.60), and can be re-expressed as

$$\tau_{SRH}(T) \times p_0(T) = \tau_{no}(T) \times [p_1(T) + p_0(T)] + \tau_{po}(T) \times (\Delta n) \tag{2.61}$$

Hence for a particular temperature and Δn range, when conditions A, B and C are satisfied, a plot of $\tau_{SRH}(T) \times p_0(T)$ versus Δn gives a slope corresponding to $\tau_{p0}(T)$ and an offset as $\tau_{n0}(T) \times \{p_1(T) + p_0(T)\}$. As $p_1(T)$ can be calculated for a known E_t and $p_0(T)$ from N_A and temperature, so $\tau_{n0}(T)$ can be calculated from the intercepts of the plot. Finally, $\sigma_{p0}(T)$ and $\sigma_{n0}(T)$ can be calculated from $\tau_{p0}(T)$ and $\tau_{n0}(T)$ using known values of $v_{thp}(T)$, $v_{thn}(T)$ and N_t according to Equation (2.20). Figure 2.20 depicts the condition for a 1 Ω cm p-type wafer with $E_t - E_V = 0.28$ eV at 300 K.

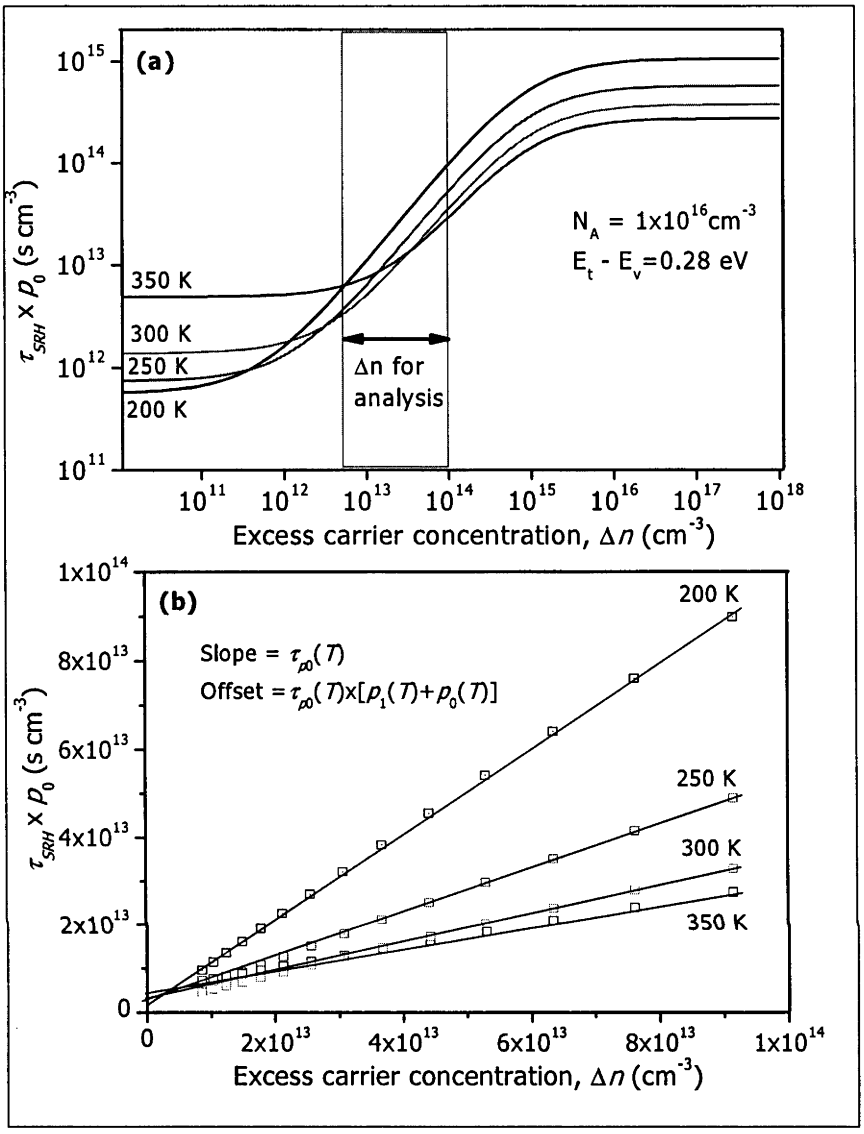

Figure 2.20: TIDLS analysis on a 1 Ω cm p-type wafer with $E_t - E_V = 0.28$ eV. (a) Depicts lifetime times doping density at different temperatures (b) depicts plot for selective injection range suitable for the determination of $\tau_{n0}(T)$ and $\tau_{p0}(T)$.

The simplified SRH expression in Equation (2.61) can be further simplified for a low temperature when $p_1(T) << p_0(T)$ and re-expressed as

$$\tau_{SRH}(T) = \tau_{no}(T) + \frac{\tau_{po}(T)}{p_0(T)} \times \Delta n \tag{2.62}$$

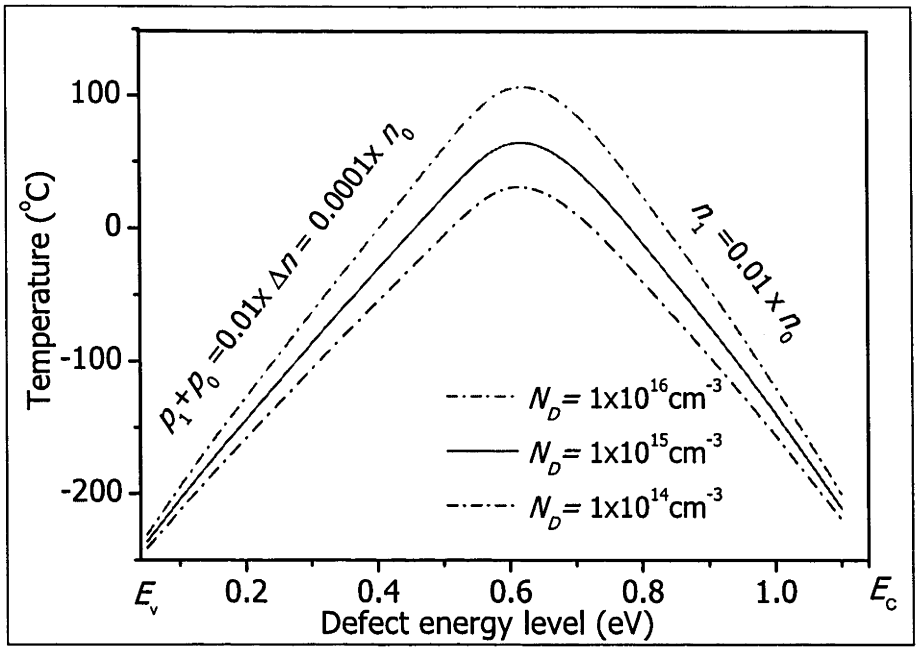

Figure 2.21: Temperatures below which $p_1 + p_0 = 0.01 \times \Delta n = 0.0001 \times n_0$, and $n_1 = 0.01 \times n_0$ as a function of E_t for p-type silicon of three doping densities (N_A).

Figure 2.21 depicts the temperature below which the assumptions are valid for n-type silicon with various N_D and E_t. Minimum temperatures for this type of analysis of n-type silicon are presented in tabular form in appendix-B. This simplification procedure is analogous to an n-type wafer with a defect in the LBGH and can be expressed as

$$\tau_{SRH}(T)\times n_0(T) = \tau_{no}(T)\times\Delta n + \tau_{no}(T)\times p_1(T) + \tau_{po}(T)\times n_0(T) \qquad (2.63)$$

2.5.2 E_t in upper band gap half (UBGH)

Simplification of the SRH equation for a p-type wafer can be performed by considering three different situations when E_t lies in UBGH.

A: Negligible $n_0(T)$

$n_0(T)$ can be neglected in comparison to $p_0(T)$ irrespective of the location of E_t for p-type silicon for a certain temperature range. Hence Equation (2.59) is valid for this case.

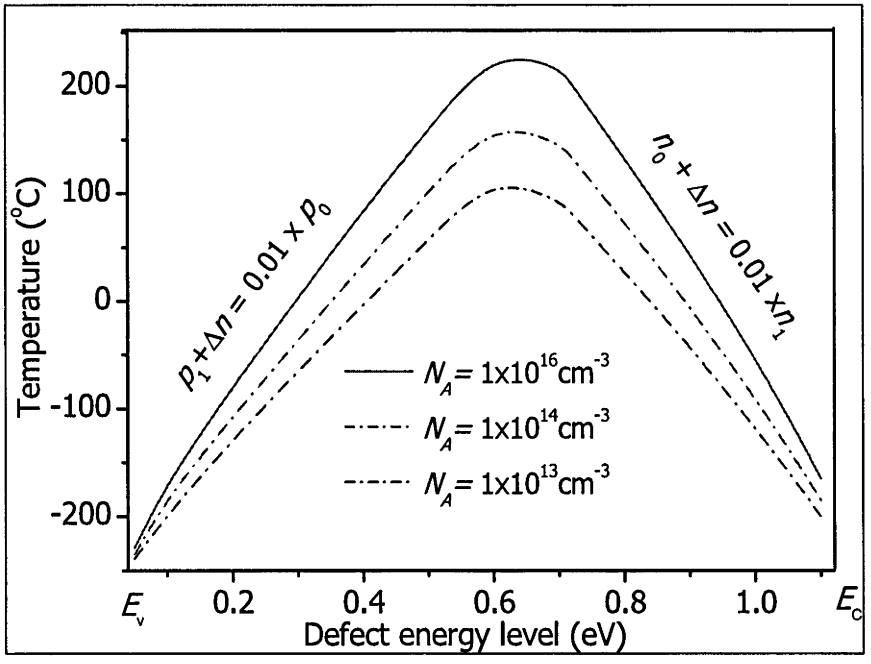

Figure 2.22: Temperatures below which $p_1 + \Delta n = 0.01 \times p_0$ and $n_0 + \Delta n = 0.01 \times p_0$ as a function of E_t for p-type silicon of three doping densities (N_A).

B: Negligible $p_1(T)$ and $n_0(T)$

$p_1(T)$ is sufficiently small in comparison to $p_0(T)$ and $n_0(T)$ is negligible in comparison with $n_1(T)$ when E_t lies in UBGH for a certain range of temperatures. Equation (2.59) can be further simplified as

$$\tau_{SRH} = \frac{\tau_{no}(p_0 + \Delta n) + \tau_{po}(n_1 + \Delta n)}{(p_0 + \Delta n)} \tag{2.64}$$

C: Low level injection $p_0(T), n_1(T) >> \Delta n$

For LLI, Δn can be removed from the denominator and numerator in the simplified SRH Equation (2.64) and can be re-expressed as

$$\tau_{SRH}(T) = \tau_{no}(T) + \frac{\tau_{po}(T)}{p_0(T)} \times n_1(T) \tag{2.65}$$

hence for a particular temperature and Δn range, when conditions A, B and C satisfy the values of $\tau_{p0}(T)$ and $\tau_{n0}(T)$, can be determined by solving two equations for different N_A

and using the known values of $p_0(T)$ and $n_1(T)$. Finally, $\sigma_{p0}(T)$ and $\sigma_{n0}(T)$ can be calculated from $\tau_{p0}(T)$ and $\tau_{n0}(T)$ using known values of $\nu_{thp}(T)$, $\nu_{thn}(T)$ and N_t according to expression (2.20). Figure 2.22 shows the temperature region for different values of E_t below which the conditions, $p_1 + \Delta n < 0.01 \times p_0$ $n_0 + \Delta n < 0.01 \times n_1$ and $n_0 + \Delta n < 0.01 \times p_0$ are satisfied, where Δn is less than $0.01 \times p_0$.

This simplification procedure of the SRH equation is analogous to an n-type wafer and Figure 2.23 depicts the temperatures below which $p_1 + p_0 = 0.01 \times \Delta n = 0.0001 \times n_0$ as a function of E_t for n-type silicon of three doping densities (N_D). The simplified SRH equation for the n-type wafer with a defect in UBGH can be expressed as

$$\tau_{SRH}(T) \times n_0(T) = \tau_{no}(T) \times \Delta n + \tau_{po}(T)[n_1(T) + n_0(T)] \tag{2.66}$$

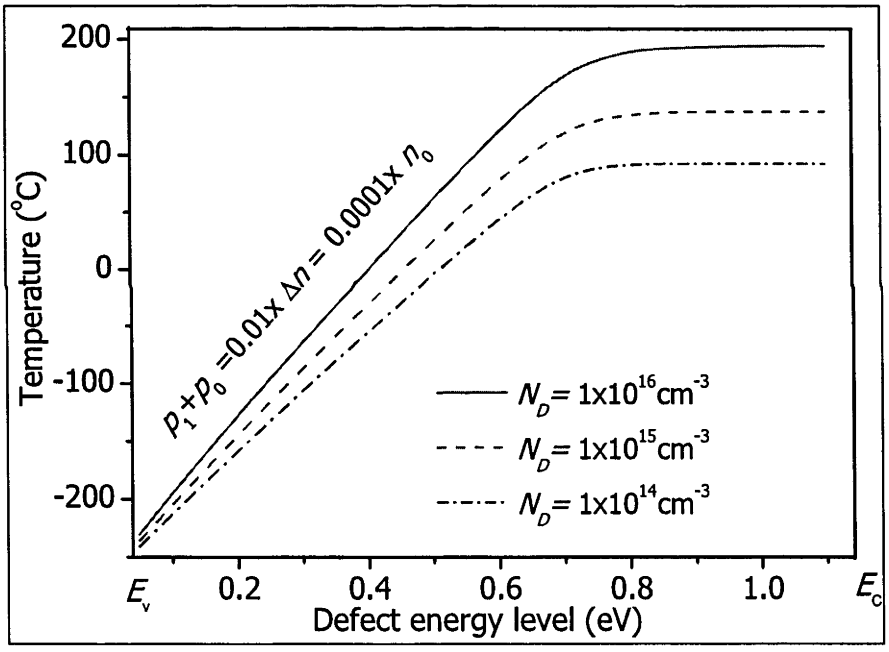

Figure 2.23: Temperatures below which $p_1 + p_0 = 0.01 \times \Delta n = 0.0001 \times n_0$ as a function of E_t for n-type silicon of three doping densities (N_D).

The simplified SRH expression in Equation (2.66) can be further simplified for a low temperature region, when $n_1(T) << n_0(T)$

$$\tau_{SRH}(T) = \tau_{po}(T) + \frac{\tau_{no}(T)}{n_0(T)} \times \Delta n \tag{2.67}$$

In all four cases LLI is not mandatory as the Equations (2.60), (2.64) and corresponding analogous expressions for n-type can also be solved for $\tau_{p0}(T)$ and $\tau_{n0}(T)$ with injection-dependent measured lifetime data for a given temperature. However, this LLI condition makes the SRH equation more simple and reduces the measurement errors in $\tau_{p0}(T)$ and $\tau_{n0}(T)$.

The excess carrier density, Δn, for TIDLS analysis is dependent upon the doping type, doping density, E_t and Temperature. Appendix-C summarizes the suitable Δn and T ranges for TIDLS measurement for different values of doping density and E_t, for p and n-types of silicon.

2.6 Chapter summary

The SRH recombination mechanism and its equation have been used in lifetime spectroscopy for defect characterization of silicon. Derivation of the SRH equation is possible with the help of different assumptions and those assumptions need to be fulfilled during the implementation of the SRH equation in lifetime spectroscopy. Most of the parameters of the SRH equation are T-dependent and can be described by one or more thermal models reported by various researchers. A good thermal model of such parameters ensures better results from T-dependent lifetime spectroscopies like TDLS and TIDLS.

Traditional lifetime spectroscopies (IDLS, TDLS and TIDLS) have various strengths and weaknesses in defect characterization of silicon. It was found that these traditional techniques are unable to determine T-dependent values for σ_n and σ_p explicitly. A new approach to lifetime spectroscopy is proposed for the explicit determination of T-dependent values of σ_n and σ_p of a defect in silicon and assessment of the effective carrier capture mechanism and defect energy level (E_t).

It is concluded that the traditional lifetime spectroscopies are not sufficient to explicitly measure T-dependent σ_n and σ_p and a new procedure for lifetime spectroscopy is proposed to overcome the shortcomings. A new T-controlled lifetime measurement instrument is required to test the new procedure proposed in this Chapter. Chapter 3 will discuss the experimental development of such a T-controlled lifetime measurement instrument.

References

[1] A. G. Aberle, *Crystalline silicon solar cells: advanced surface passivation and analysis.* Kensington, Sydney: Centre for Photovoltaic Engineering, Univ. of NSW, 1999.

[2] W. Shockley and W. T. Read, "Statistics of the Recombinations of Holes and Electrons," *Physical Review,* vol. 87, p. 835, 1952.

[3] R. N. Hall, "Electron-Hole Recombination in Germanium," *Physical Review,* vol. 87, p. 387, 1952.

[4] R. J. Nelson and R. G. Sobers, "Minority-carrier lifetimes and internal quantum efficiency of surface-free GaAs," *Journal of Applied Physics,* vol. 49, pp. 6103-6108, 1978.

[5] J. Dziewior and W. Schmid, "Auger coefficients for highly doped and highly excited silicon," *Applied Physics Letters,* vol. 31, pp. 346-348, 1977.

[6] K. Graff, *Metal impurities in silicon-device fabrication*: Springer-Verlag New York, 1995.

[7] A. Hangleiter and R. Häcker, "Enhancement of band-to-band Auger recombination by electron-hole correlations," *Physical Review Letters,* vol. 65, p. 215, 1990.

[8] R. Hacker and A. Hangleiter, "Excitonic band-to-band Auger recombination in silicon," in *Eighteenth International Conference on the Physics of Semiconductors*, 1986, p. 907.

[9] M. Rüdiger, T. Trupke, P. Würfel, T. Roth, and S. W. Glunz, "Influence of photon reabsorption on temperature dependent quasi-steady-state photoluminescence lifetime measurements on crystalline silicon," *Applied Physics Letters,* vol. 92, p. 222112, 2008.

[10] D. K. Schroder, "Semiconductor Material and Device Characterization, Jonn Wiley & Sons," *Inc. Copyright,* 1990.

[11] S. M. Sze and K. K. Ng, *Physics of semiconductor devices*: Wiley-Interscience, 2007.

[12] D. Macdonald and A. Cuevas, "Validity of simplified Shockley-Read-Hall statistics for modelling carrier lifetimes in crystalline silicon," *Phys. Rev. B,* vol. 67, p. 075203, 2003.

[13] J. A. Hornbeck and J. R. Haynes, "Trapping of minority carriers in silicon. I. p-type silicon," *Physical Review,* vol. 97, pp. 311-321, 1955.

[14] K. R. McIntosh, B. B. Paudyal, and D. H. Macdonald, "Generalized procedure to determine the dependence of steady-state photoconductance lifetime on the occupation of multiple defects," *Journal of Applied Physics,* vol. 104, p. 4503, 2008.

[15] M. A. Green, *Silicon solar cells: advanced principles & practice*: Centre for Photovoltaic Devices and Systems Sydney, 1995.

[16] A. Hangleiter, "Experimental proof of impurity Auger recombination in silicon," *Physical Review Letters,* vol. 55, p. 2976, 1985.

[17] P. Rosenits, T. Roth, W. Warta, S. Reber, and S. W. Glunz, "Determining the excess carrier lifetime in crystalline silicon thin-films by photoluminescence measurements," *Journal of Applied Physics,* vol. 105, p. 053714, 2009.

[18] S. Rein, *Lifetime spectroscopy: a method of defect characterization in silicon for photovoltaic applications*: Springer, 2005.

[19] C. H. Henry and D. V. Lang, "Nonradiative capture and recombination by multiphonon emission in GaAs and GaP," *Physical Review B (Solid State),* vol. 15, pp. 989-1016, 1977.

[20] M. Lax, "Cascade capture of electrons in solids," *Physical Review,* vol. 119, pp. 1502-1523, 1960.

[21] M. Lannoo and J. Bourgoin, *Point defects in semiconductors II*: Springer-Verlag New York, 1983.

[22] R. M. Gibb, G. J. Rees, B. W. Thomas, B. L. H. Wilson, B. Hamilton, D. R. Wight, and N. F. Mott, "V. A two stage model for deep level capture," *Philosophical Magazine,* vol. 36, pp. 1021-1034, 1977.

[23] A. Hangleiter and R. Häcker, "Excitonic band-to-band Auger recombination in silicon," 1987, pp. 907–910.

[24] A. Hangleiter, "Nonradiative recombination via deep impurity levels in semiconductors: The excitonic Auger mechanism," *Physical review. B, Condensed matter,* vol. 37, p. 2594, 1988.

[25] M. A. Green, "Intrinsic concentration, effective densities of states, and effective mass in silicon," *Journal of Applied Physics,* vol. 67, p. 2944, 1990.

[26] R. G. Humphreys, "Valence band averages in silicon: Anisotropy and non-parabolicity," *J. Phys. C(Solid State Phys.),* vol. 14, pp. 2935-2942, 1981.

[27] Y. Kirino, A. Buczkowski, Z. J. Radzimski, G. A. Rozgonyi, and F. Shimura, "Noncontact energy level analysis of metallic impurities in silicon crystals," *Applied Physics Letters,* vol. 57, pp. 2832-2834, 1990.

[28] F. Shimura, T. Okui, and T. Kusama, "Noncontact minority-carrier lifetime measurement at elevated temperatures for metal-doped Czochralski silicon crystals," *Journal of Applied Physics,* vol. 67, pp. 7168-7171, 1990.

[29] G. Ferenczi, T. Pavelka, and P. Totto, "Injection level spectroscopy: a novel non-contact contamination analysis technique in silicon," *Japanese journal of applied physics. Pt. 1, Regular papers & short notes,* vol. 30, pp. 3630-3633, 1991.

[30] H. Bleichner, P. Jonsson, N. Keskitalo, and E. Nordlander, "Temperature and injection dependence of the Shockley–Read–Hall lifetime in electron irradiated n type silicon," *Journal of Applied Physics,* vol. 79, p. 9142, 1996.

[31] J. Schmidt, C. Berge, and A. G. Aberle, "Injection level dependence of the defect-related carrier lifetime in light-degraded boron-doped Czochralski silicon," *Applied Physics Letters,* vol. 73, p. 2167, 1998.

[32] J. Schmidt and A. Cuevas, "Electronic properties of light-induced recombination centers in boron-doped Czochralski silicon," *Journal of Applied Physics,* vol. 86, p. 3175, 1999.

[33] Y. Hayamizu, T. Hamaguchi, S. Ushio, T. Abe, and F. Shimura, "Temperature dependence of minority carrier lifetime in iron diffused p type silicon wafers," *Journal of Applied Physics,* vol. 69, p. 3077, 1991.

[34] H. Daio, A. Buczkowski, and F. Shimura, "Lifetime Study of Metastable Surface Recombination Centers in n Type Silicon Wafers," *Journal of The Electrochemical Society,* vol. 141, p. 1590, 1994.

[35] A. Kaniava, A. L. P. Rotondaro, J. Vanhellemont, U. Menczigar, and E. Gaubas, "Recombination activity of iron related complexes in silicon studied by temperature dependent carrier lifetime measurements," *Applied Physics Letters,* vol. 67, p. 3930, 1995.

[36] M. Ichimura, H. Tajiri, T. Ito, and E. Arai, "Temperature dependence of carrier recombination lifetime in Si wafers," *Journal of The Electrochemical Society,* vol. 145, p. 3265, 1998.

[37] T. S. Horanyi, P. Tüttõ, and C. Kovacsics, "Identification Possibility of Metallic Impurities in p Type Silicon by Lifetime Measurement," *Journal of The Electrochemical Society,* vol. 143, p. 216, 1996.

[38] D. Walz, J. P. My, and G. Kamarinos, "On the recombination behaviour of iron in moderately boron-doped p-type silicon," *Applied Physics A: Materials Science & Processing,* vol. 62, pp. 345-353, 1996.

[39] N. Keskitalo, P. Jonsson, K. Nordgren, H. Bleichner, and E. Nordlander, "Temperature and injection dependence of the Shockley–Read–Hall lifetime in electron-irradiated p-type silicon," *Journal of Applied Physics,* vol. 83, p. 4206, 1998.

[40] D. Macdonald, A. Cuevas, and J. Wong-Leung, "Capture cross sections of the acceptor level of iron–boron pairs in p-type silicon by injection-level dependent lifetime measurements," *Journal of Applied Physics,* vol. 89, p. 7932, 2001.

[41] J. Schmidt, "Temperature-and injection-dependent lifetime spectroscopy for the characterization of defect centers in semiconductors," *Applied Physics Letters,* vol. 82, p. 2178, 2003.

[42] S. Rein and S. W. Glunz, "Electronic properties of interstitial iron and iron-boron pairs determined by means of advanced lifetime spectroscopy," *Journal of Applied Physics,* vol. 98, p. 113711, 2005.

[43] R. K. Ahrenkiel, B. M. Keyes, and S. Johnston, "Injection level lifetime spectroscopy of impurities in semiconductors," *Surface Engineering(UK),* vol. 16, pp. 54-60, 2000.

[44] D. H. Macdonald and A. Cuevas, "Trapping of minority carriers in multicrystalline silicon," *Applied Physics Letters,* vol. 74, p. 1710, 1999.

[45] D. Macdonald, R. A. Sinton, and A. Cuevas, "On the use of a bias-light correction for trapping effects in photoconductance-based lifetime measurements of silicon," *Journal of Applied Physics,* vol. 89, p. 2772, 2001.

[46] R. A. Sinton and A. Cuevas, "Contactless determination of current–voltage characteristics and minority carrier lifetimes in semiconductors from quasi steady state photoconductance data," *Applied Physics Letters,* vol. 69, p. 2510, 1996.

[47] P. J. Cousins, D. H. Neuhaus, and J. E. Cotter, "Experimental verification of the effect of depletion-region modulation on photoconductance lifetime measurements," *Journal of Applied Physics,* vol. 95, p. 1854, 2004.

[48] T. Roth, M. Rüdiger, W. Warta, and S. W. Glunz, "Electronic properties of titanium in boron-doped silicon analyzed by temperature-dependent photoluminescence and injection-dependent photoconductance lifetime spectroscopy," *Journal of Applied Physics,* vol. 104, p. 074510, 2008.

[49] B. B. Paudyal, K. R. McIntosh, and D. H. Macdonald, "Temperature dependent electron and hole capture cross section of iron-contaminated boron-doped silicon" in *34 IEEE PV specilalist conference* Philadelphia, USA, 2009.

[50] B. B. Paudyal, K. R. McIntosh, and D. H. Macdonald, "Temperature dependent carrier lifetime studies on Ti-doped multicrystalline silicon," *Journal of Applied Physics,* vol. 105, p. 4510, 2009.

[51] B. B. Paudyal, K. R. McIntosh, D. H. Macdonald, and G. Coletti, "Temperature dependent electron and hole capture cross section of the molybdenum defect in silicon " in *24th European PV conference* Hamburg, Germany, 2009.

[52] S. Diez, S. Rein, T. Roth, and S. W. Glunz, "Cobalt related defect levels in silicon analyzed by temperature-and injection-dependent lifetime spectroscopy," *Journal of Applied Physics,* vol. 101, p. 033710, 2007.

[53] J. E. Birkholz, K. Bothe, D. Macdonald, and J. Schmidt, "Electronic properties of iron-boron pairs in crystalline silicon by temperature-and injection-level-dependent lifetime measurements," *Journal of Applied Physics,* vol. 97, p. 103708, 2005.

[54] S. Rein, S. Diez, and S. W. Glunz, "Temperature and Injection Dependent Lifetime Spectroscopy (TIDLS): Advanced analysis," in *19th European PVSEC* Paris, 2004.

CHAPTER 3

Lifetime measurement and instrument development

Lifetime spectroscopy requires an instrument for recombination lifetime measurement. This work implements a new approach to lifetime spectroscopy, which is based upon injection and temperature in order to characterize defects in silicon solar cells. An instrument capable of measuring recombination lifetimes for a wide range of injection levels and temperatures is a fundamental requisite for this work. This Chapter discusses various recombination lifetime measurement techniques and their suitability for this work. Furthermore, it explains the implementation of temperature control in the photoconductance (PC) based lifetime measuring instrument which is used for testing the theory presented in Chapter 2.

This Chapter discusses the dynamics of carrier recombination applied by lifetime measurement techniques and their technical details in Section 3.1. Section 3.1 further discusses the operating regime of each measurement technique for wider injection and temperature ranges. Following that, the development of a temperature control system in a PC lifetime measurement device will be discussed in Section 3.2. Section 3.3 deals with the temperature dependent calibration of the developed T-controlled PC system. Finally, the accuracy of the developed measurement system and error analysis of results is presented in Section 3.4.

3.1 Measurement techniques

Recombination lifetime measurement techniques are based upon the recombination dynamics of generated carriers. Optical generation of carriers via the illumination of a semiconductor wafer is the most common practice. Xenon light or light emitting diodes (LED) are used as illuminating sources. Depending upon the illumination state of the optical source before and during the measurement, the lifetime analysis is classified as transient, steady state, or quasi-steady-state (QSS), (a generalised analysis combines all three). This section discusses the general principle of lifetime measurement and the technical details of three different types of lifetime measuring techniques, namely, the

Micro-wave (MW) and Inductive-coil photoconductance (PC) and Photoluminescence techniques.

3.1.1 General principle

Lifetime analysis is based upon the continuity equation for excess carrier concentrations (Δn) [1]

$$\frac{\partial \Delta n(x,t)}{\partial t} = G_{bulk}(x,t) - U_{bulk}(t,x) + \frac{1}{q}\frac{dJ_n(x,t)}{dx} \tag{3.1}$$

where G_{bulk} and U_{bulk} are the generation and recombination rates in the bulk of the semiconductor, q is the elementary charge and J_n is the electron current density. For uniform generation and zero surface recombination, the electrical field within the sample is zero, so the carrier concentration is spatially uniform throughout the wafer. In such circumstances, the last term (known as the transport term) on the right-hand side of Equation (3.1) vanishes and the expression can be re-arranged as

$$U_{bulk}(t,x) = \frac{\partial \Delta n}{\partial t} - G_{bulk}(t,x) \tag{3.2}$$

The basic expression for lifetime described in Equation (2.2) can be substituted by U (t,x) from the Equation (3.1) [2] and the effective lifetime (τ_{Eff}) can be expressed as

$$\tau_{Eff} = \frac{\Delta n(t)}{G(t) - \frac{\partial \Delta n(t)}{\partial t}} \tag{3.3}$$

Equation (3.3) is the general expression for effective lifetime (τ_{eff}) and can be simplified for transient and steady state analyses. During transient measurement the test wafer is illuminated by a sharp pulse of light before Δn(t) is measured in the dark ($G \equiv 0$). Hence the expression for transient measurement can be expressed as a reduced version of Equation (3.3)

$$\tau_{Eff} = -\frac{\Delta n(t)}{\frac{\partial \Delta n(t)}{\partial t}} \tag{3.4}$$

Practical limitations mean that the decay time of the illumination source can never be precisely zero. As a result, the transient analysis is only valid when the recombination lifetime is significantly longer than the decay time of the light source. This work requires the lifetime measurement of silicon wafers with various impurities which have a recombination lifetime as low as 2μs. Transient analysis is thus deemed unsuitable for this work, since the flash decay time of our apparatus is not suitable for transient measurement of lifetimes below 100 microseconds..

Steady state analysis is another type of lifetime analysis. In this case, the illumination is kept constant so that the rate of change of excess carrier concentration is negligible. Equation (3.3) can be re-written as

$$\tau_{eff} = \frac{\Delta n(t)}{G(t)} \tag{3.5}$$

A practical limitation also applies to steady state analysis. The test wafer needs to be kept under constant illumination during measurement, which causes heating, hence the true steady state lifetime is difficult to measure. In order to overcome this problem, Sinton *et al.* [3] proposed another technique known as quasi-steady-state (QSS). In the QSS technique the illumination intensity is slowly reduced to zero over a relatively long interval of time (several milliseconds) so that the decay rate is significantly higher than the recombination lifetime of the test wafer. This method is applied throughout Chapters 4 – 6.

An accurate measurement of $\Delta n(t)$ and $G(t)$ for the wafer under test is therefore essential for the determination of effective lifetime in this work. The generation rate can be easily measured by a reference cell. There are several techniques available for the determination of $\Delta n(t)$. Photoconductance (PC) measurement is the first type of technique which measures the change in photoconductance of the wafer under test to determine $\Delta n(t)$. Micro-wave (MW) and Inductive-coil techniques are based upon PC measurement techniques. A second type of measurement technique is based on photoluminescence (PL) in which a photon flux of radiative recombination is detected and used to determine $\Delta n(t)$. Other techniques such as DLTS are also used to determine

$\Delta n(t)$, however these techniques are not contactless. The following describes in detail the three most used contactless techniques for lifetime measurement. It then focuses on the suitability for implementation of temperature control for a wider range of Δn and temperature measurements.

3.1.2 Micro-wave photoconductance

The Microwave (MW) photoconductance technique was first applied by Ramsa *et. al* [4] in 1959. They measured the minority carrier recombination lifetime in Germanium. The experimental arrangement of a typical MW photoconductance technique is shown in Figure 3.1. An MW signal generated by a wave meter is regulated by the klystron and attenuator. A regulated signal is passed through the line section which consists of a squeeze section, a wave detector and a wave indicator for the measurement of wave ratios. The MW signal is passed through the semiconductor sample and the reflected power is measured with a tuned diode detector followed by an amplifier which is converted to Δn via calibration.

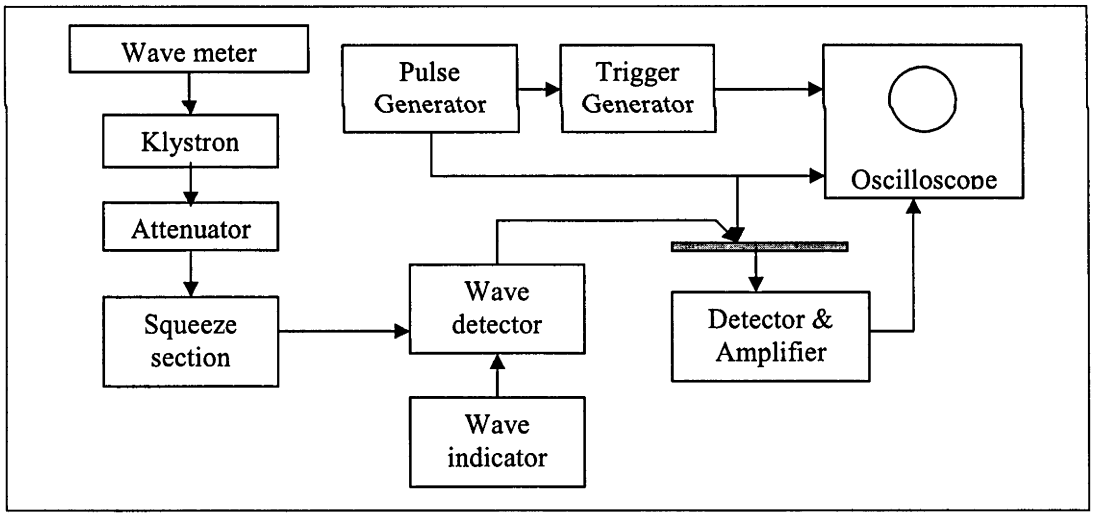

Figure 3.1: Apparatus for a microwave lifetime measurement system.

The electrodeless (Optical) method is a commonly used version of the MW technique for minority carrier lifetime measurement in semiconductors. In this method, carrier injection in the semiconductor is performed by a light pulse and detection is via MW absorption. Figure 3.2 depicts the system used for lifetime measurement with the optical method.

With the MW-PC technique, variation in sample photoconductance ($\Delta\sigma$) is determined by the MW reflectance [5] of the test wafer after optical injection of carriers. The measured $\Delta\sigma$ is then converted to average excess carrier density (Δn_{av}) as

$$\Delta n_{av}(t) = \frac{\Delta\sigma(t)}{q(\mu_n + \mu_p)W} \tag{3.6}$$

where μ_n and μ_p are the carrier mobilities, q is the elementary charge and W is the width of the sample. The recombination lifetime of the carrier is determined from the asymptotic decay of Δn_{av} by transient analysis as stated in Equation (3.4).

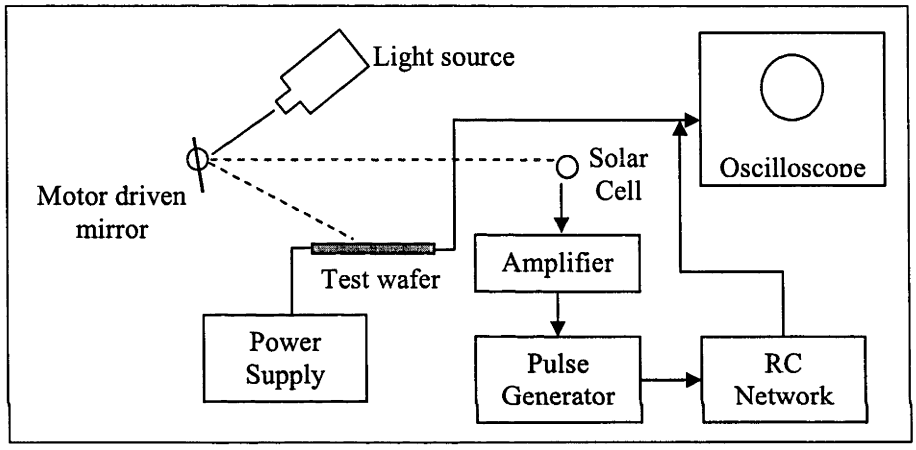

Figure 3.2: Optical method for a microwave lifetime measurement system.

The MW technique is not suitable for absolute lifetime measurements at a higher carrier density (Δn_{av}), if knowledge of the injection level is required, as is the case in this work [6]. This MW signal has a highly non-linear dependence on the photoconductance for higher values of Δn_{av}. As a result, lifetime measurements at higher Δn_{av} are usually performed with the application of a steady-state bias light.

Application of a bias light in order to measure recombination lifetime at higher Δn_{av} is not straight forward. Firstly, the measured lifetime with a bias light is a differential lifetime rather than actual lifetime [7]. It is necessary to measure the differential lifetime with a bias light over the whole injection range and to integrate the resultant data in order to determine the actual injection level. Again, as the actual carrier density also depends upon the carrier lifetime, the integration procedure has to be performed iteratively. Furthermore, the MW reflectivity signal does not give the information about

the absolute magnitude of excess carrier density, so the bias light has to be calibrated each time in order to calculate the background generation rate in the sample.

This work requires the measurement of carrier lifetime over a wide injection and temperature range. Since the MW-PC measurement system has some restrictions and limitations for the higher injection measurement and is more complex than the other contactless techniques (Inductive coil PC, discussed next), this technique is less suitable for our purpose.

3.1.3 Inductive-coil photoconductance

The use of an inductive-coil is another type of photoconductance (PC) based technique employed for recombination lifetime measurements in semiconductor wafers. This is a contactless technique which does not require the preparation of a special sample dedicated for measurement, i.e. with contacts. The fundamental approach of this technique involves the generation of carriers by optical energy, changing the conductance ($\Delta\sigma$) of the test wafer and the measurement of $\Delta\sigma$ by using a magnetically coupled inductive-coil. $\Delta\sigma$ is then converted to Δn which is used to calculate τ_{eff}.

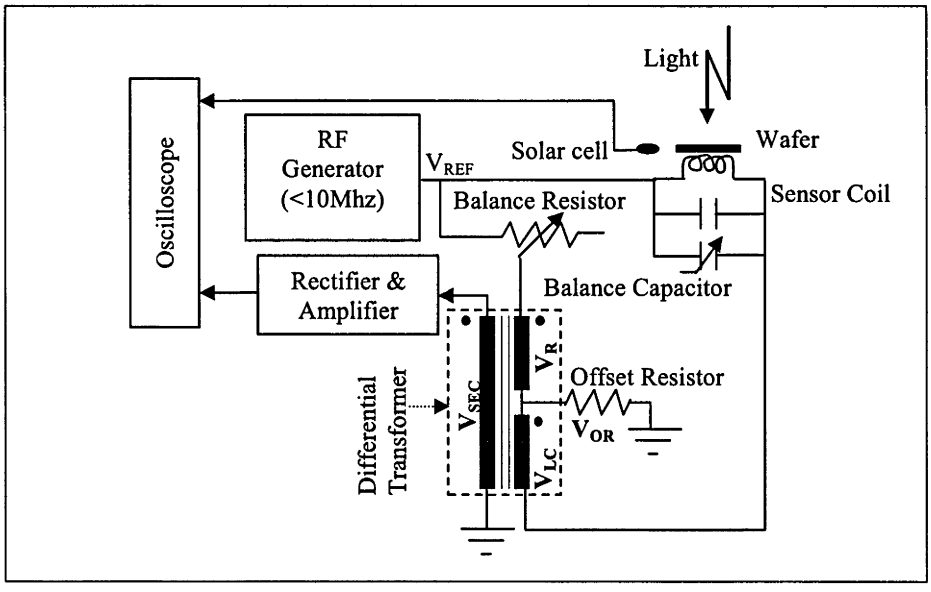

Figure 3.3: Inductive-coil photoconductance measurement system.

The inductive-coil PC based lifetime measurement technique was first used by Gabriel L. Miller *et al.* [8]. A patent registered in 1981 in the name of Miller *et al.* as a United

States Patent with a title of "Method and apparatus for the contactless monitoring carrier lifetime in semiconductor materials" is the first recorded evidence of this technique. In his experiment, Miller *et al.* used a test wafer which was electromagnetically coupled into the tuned inductance-capacitance resonant circuit. The test wafer was then illuminated with a low frequency square wave modulated light source which changed the conductance of the test wafer by optically generating a number of carriers. The difference in the voltage across the resonant circuit between the period of illuminating and non-illuminating indicated the number of generated carriers. Miller also suggested using the difference between the current (ΔI) flowing into the circuit between the period of illumination and non-illumination of the wafer and converting ΔI to a generated carrier concentration (Δn). The measured Δn can be converted to lifetime by employing Equations (3.3), (3.4) or (3.5) as required. The prototype developed by Miller allowed lifetime resolution of 0.1 μs, with 0.4 s of measurement time.

Kane and Swanson [9] used a technique similar to that used by Miller *et al.* to measure the emitter saturation current. However, the light source used by Kane *et al.* was different to that used by Miller and the calculation procedure was revised. A flash lamp with a single pulse was used by Kane *et al.* and the change in conductivity ($\Delta\sigma$) of the wafer was measured after switching the light off. This technique thereby applied the transient photoconductance decay technique seen in Equation (3.4). The apparatus was improved by addition of the quasi-static flash and analysis, and commercialized by Sinton *et al.* [3]. A simple block diagram of the inductive-coil photoconductance measurement system is depicted in Figure 3.3.

An inductive-coil lifetime measurement system consists of a light source to illuminate the test wafer. A radio frequency generator is connected to the sensor coil that maintains a current-flow through the coil and creates a magnetic field around it. The test wafer when positioned adjacent to the coil is electromagnetically coupled with the coil. When the test wafer is illuminated with a pulse of light, the wafer generates excess electrons and holes (Δn) that change the conductance (σ) of the wafer. The change in σ alters the impedance of the sensor coil (Z_L). This in turn, alters the overall impedance (Z_{LC}) of the parallel inductive-capacitive (LC) circuit and alters the voltage drop across the coil. This change in the voltage of the LC circuit (V_{LC}) alters the voltage at the lower end of the primary winding in the differential transformer as shown in Figure 3.3. As there is a

change in V_{LC}, the balance in the primary windings of the transformer (V_R - V_{LC} = 0) no longer prevails. This changes the output of the transformer to V_{SEC} = k_{TR} x (V_R - V_{LC}), where, k_{TR} is the transformation ratio of the transformer. V_{SEC} is then rectified and amplified and read as the output voltage V_{out} and ΔV_{out} is calculated. ΔV_{out} is then converted to the change in conductivity ($\Delta\sigma$) by using calibration coefficients (discussed in Section 3.3). $\Delta\sigma$ is then converted to Δn as per Equation (3.6) and to the effective lifetime (τ_{eff}) by using Equations (3.3), (3.4) or (3.5) as required. The generation rate $G(t)$ is measured by using a solar cell located adjacent to the sensor coil. The output voltage of the solar cell is converted to the generation rate $G(t)$ by using a calibration factor.

The inductive-coil PC technique measures the carrier injection level directly from the voltage output of the LC circuit and does not require device simulation. Furthermore, this technique is applicable for lifetime measurement for a wider injection range in comparison with the MW PC technique and there is no need to integrate the measured lifetime for a higher injection range as in MW PC. Again, there is no need for a bias light setting and calibration for each individual measurement for a higher carrier density in contrast to MW PC. In this regard, the inductive-coil PC technique is simpler and more accurate, and is therefore applied in this work.

3.1.4 Photoluminescence

Photoluminescence (PL) is another technique used for the measurement of carrier lifetime in semiconductors wafer. Unlike MW and Inductive-coil PC measurement techniques, PL detects a signal which is proportional to the product of minority and majority carrier concentrations rather than their sum. During the measurement a test wafer is illuminated with an appropriate light source for excess carrier generation. Some of the generated electron-hole pairs recombine via the radiative recombination mechanism (mentioned in Chapter 2), emitting a photoluminescence (PL) photon. A detector placed underneath the sample detects the number of emitted photons. The generation rate $G(t)$ is detected by a reference solar cell as shown in Figure 3.4. The signal measured by PL detector can be expressed as

$$I_{PL} = A_i B(T, \Delta n)\, n\, p \qquad (3.7)$$

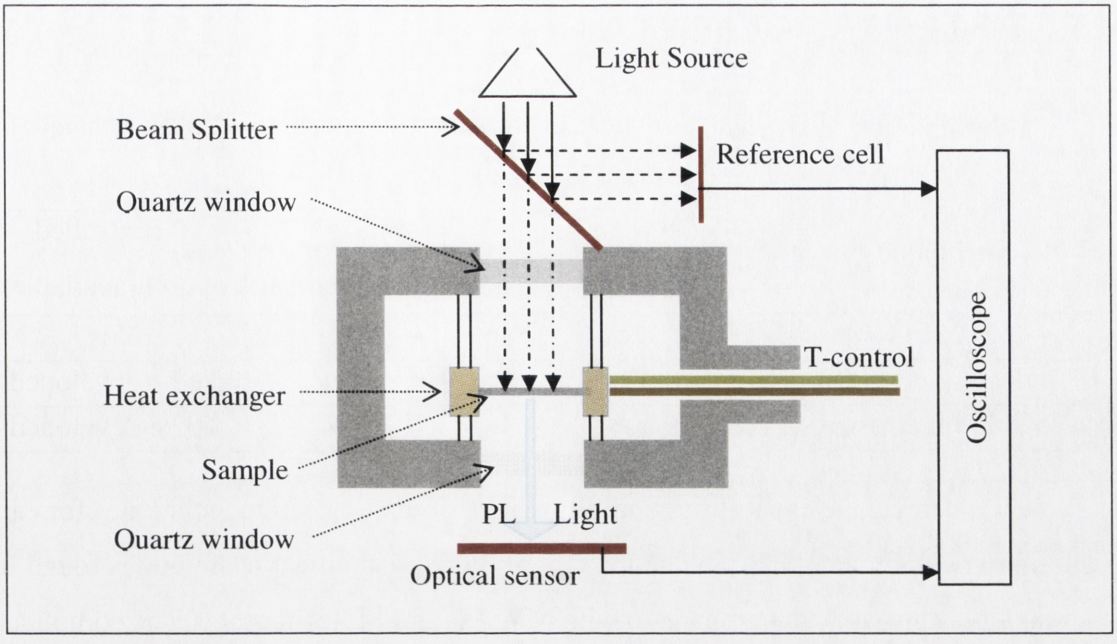

Figure 3.4: T-controlled photoluminescence measurement system.

where A_i is a proportionality constant, B is a coefficient of radiative recombination which is dependent upon Δn, T, n and p. For p-type silicon $p = N_A + \Delta n$ and $n = \Delta n$ and for n-type silicon $n = N_D + \Delta n$ and $p = \Delta n$, where N_A and N_D are the respective doping densities. Hence for p-type silicon Equation (3.7) can be re-expressed as

$$I_{PL} = A_i B(T, \Delta n)(N_A + \Delta n)\Delta n \tag{3.8}$$

This is a quadratic equation of a variable Δn, hence $\Delta n(t)$ can be determined by its solution as

$$\Delta n(t) = -\frac{N_A}{2} + \left(\frac{N_A^2}{4} + \frac{I_{PL}}{A_i B(T, \Delta n)}\right)^{\frac{1}{2}} \tag{3.9}$$

Once $\Delta n(t)$ is calculated, the effective lifetime (τ_{eff}) can be determined by equations (3.3), (3.4) or (3.5) by using the measured value of generation rate $G(t)$ when required.

The coefficient for radiative recombination B is not constant for $\Delta n > 1 \times 10^{15}$ cm^{-3}. The measured value of Δn and hence τ_{eff} will be erroneous for $\Delta n > 1 \times 10^{15}$ cm^{-3}. Hence the PL technique for lifetime measurement is only accurate for the value of Δn less than 1×10^{15}cm^{-3} according to Trupke *et al.* [10].

3.1.5 Suitable measurement techniques

Table 3.1: Capabilities and restrictions of contactless lifetime measurement techniques (as of March 2006).

Technique	Suitable Δn Range			Fast measurement	T-controlled option (available)
	Low	Medium	High		
MW PC	Yes	Yes	No	No	Yes
Inductive-coil PC	Yes	Yes	Yes	Yes	To be developed
Photoluminescence	Yes	Yes	No	Yes	To be developed

Table 3.1 depicts the capabilities and limitations of three different techniques for carrier lifetime measurement [11]. The inductive-coil PC measurement technique is found most suitable for this work in comparison with MW PC and PL technology. The complication associated with the MW technique for higher injection level measurement was explained in Section 3.1.1. Similarly PL technology requires adjustment in the radiative constant for an injection range higher than 1×10^{15} cm^{-3} [11]. Inductive-coil PC measurement has been accepted as a reliable technique for lifetime measurement by several research institutes throughout the world [12]. On the basis of these facts, the inductive-coil PC technique was selected as the measurement technique for this work.

The inductive-coil PC technique for temperature dependent lifetime measurement has been employed by Schmidt *et al.* [13] and Rein *et al.*[5, 14]. The measurement device consisted of an inductive-coil PC instrument (WCT-100) from Sinton Consulting Inc [12] with a brass ring capable of heating the sample from 30 °C to 150 °C. This temperature range is relatively small for the purpose of this work. Hence an inductive-coil PC measurement instrument capable of measuring a wide range of temperatures (-150 to 350 °C) was designed in order to measure the electrical properties of various defects as mentioned in Chapter 2.

3.2 Instrument development

The implementation of temperature control to an inductive-coil PC measurement system was a pre-requisite for this work as there was no such system available. The WCT-100 instrument from Sinton Consulting Inc [12] and a custom designed version of HCS-302 from INTEC Inc. [15] were selected as the PC measurement system and the temperature control stage. This section describes the development of a temperature controlled PC

measurement system and its operating range and condition. Furthermore, this section discusses the accuracy of measurement of the controlled temperature of the wafer and its effects in measured lifetime.

3.2.1 Description of existing systems

a. PC measurement instrument (WCT-100)

WCT-100 is a trade name of an inductive coil PC measurement system of Sinton Consulting Inc and there are more than 200 such systems in use throughout the world [12]. The system has a Xenon flash lamp as a light source which is powered by an adapter with a battery. Each battery is capable of providing 400 Watts per second. The flash has four user selectable operating modes i.e. automatic, manual, stroboscopic and TTL (with optional adapters for TTL camera control). For lifetime measurement purposes, the manual mode is preferred as pulse duration must be adjusted to suit the type of analysis mentioned in Section 3.1.1.

The PC sensor coil remains inside the main cabinet of the WCT-100 adjacent to the top surface where the test sample resides during calibration and measurement. The sample acts as the core for the sensor coil and change in wafer conductance is finally calculated as lifetime. The detail of calculation is discussed in Section 3.3. The coil is powered by a radio frequency generator of 8 Mhz frequency. The sensor coil is a part of a parallel inductor-capacitor (LC) circuit which has one fixed capacitor and one variable capacitor. The variable capacitor can be tuned externally to match the impedance of the LC circuit at the beginning of the measurement. This impedance matching process is known as balancing. The parallel LC circuit is connected to the upper-primary winding of a differential transformer. The lower-primary winding of the transformer is connected to the RF generator with a variable resistor (R) which is accessible externally by a resistor knob. Hence, during the process of balancing, the voltage in the upper and lower winding of the differential transformer should be equal so that the voltage output of the secondary winding is zero (minimum).

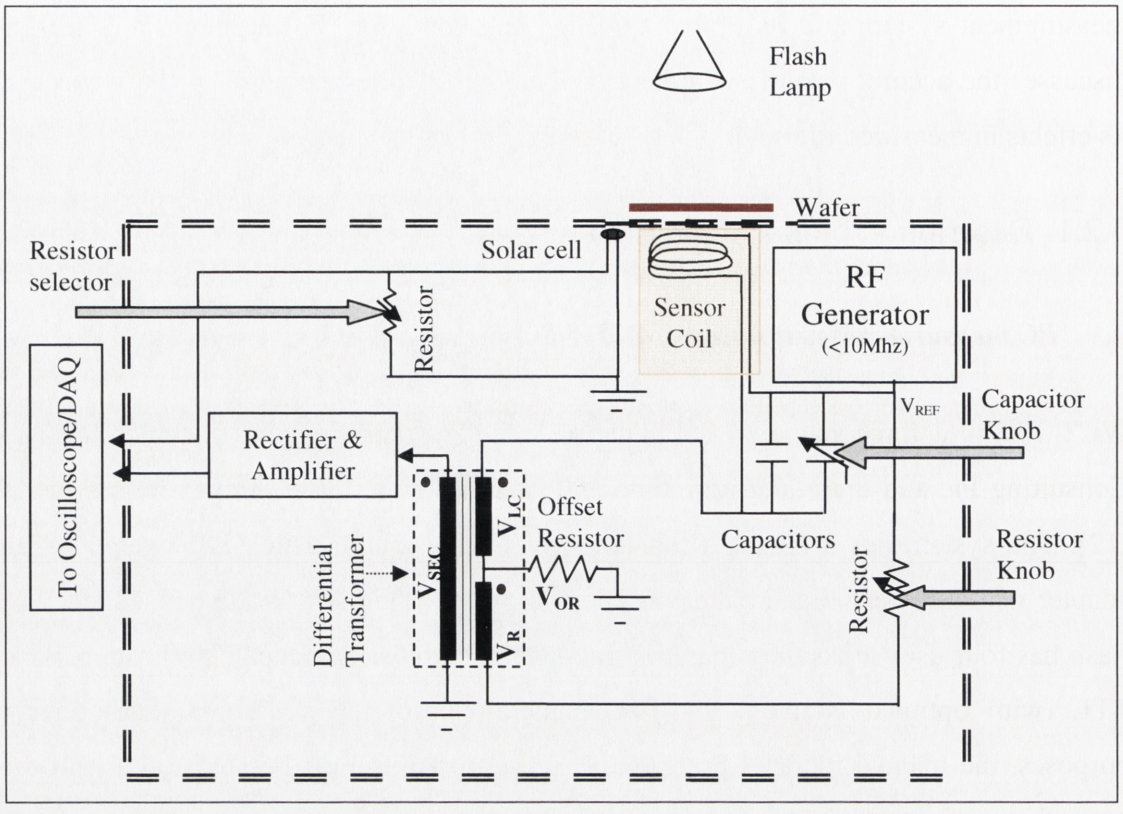

Figure 3.5: Schematic view of WCT-100, depicting external interfaces balancing resistor and capacitor, test wafers and data acquisition to the oscilloscope.

The output terminal of the secondary winding of the differential transformer is connected to a signal conditioning unit which consists of a rectifier and an amplifier. The output signal of the amplifier is then fed to an oscilloscope or a PC for analysis and recording. The WCT-100 also has a light sensor made of a silicon solar cell. This cell is located next to the test sample location so it can measure the same light intensity that is falling on the wafer under test. The cell is connected in parallel to a variable resistor, which can be controlled externally. Appropriate selection of this parallel resistor moves the solar cell into the region of output current that exhibits linear correlation with the incident light intensity. A schematic diagram of a typical WCT-100 is depicted in Figure 3.5.

b. Heating and cooling stage (HCS-302)

'HCS-302' is the trade name of a temperature control stage produced by INSTEC Inc [15]. It was originally designed to provide a temperature controlled environment for optical microscopy. Figure 3.7 shows the HCS-302 with and without its outer cover.

The stage temperature of the HCS-302 can be adjusted to between -190 and 400 °C. Heating in the stage is achieved via a resistive element controlled by a platinum resistive temperature detector (RTD) and the control stage known as STC-200. The STC-200 can also control a liquid nitrogen pump (LN2P) which is employed for the cooling of the HCS-302. Furthermore, the STC-200 has the capacity to control a water pump which becomes active when the stage temperature exceeds 100 °C. This pump circulates water within the outer frame of the stage to prevent conduction of heat to the rest of the system. The test sample is covered by two inner and outer covers. Both covers are made of aluminium and have a central quartz window for optical access to the test sample. The inner cover is attached to the sample stage with four pin screws whereas the outer cover is attached to the outer frame with four thumb screws. The outer cover also has an inlet for dry nitrogen to facilitate demisting of the quartz window.

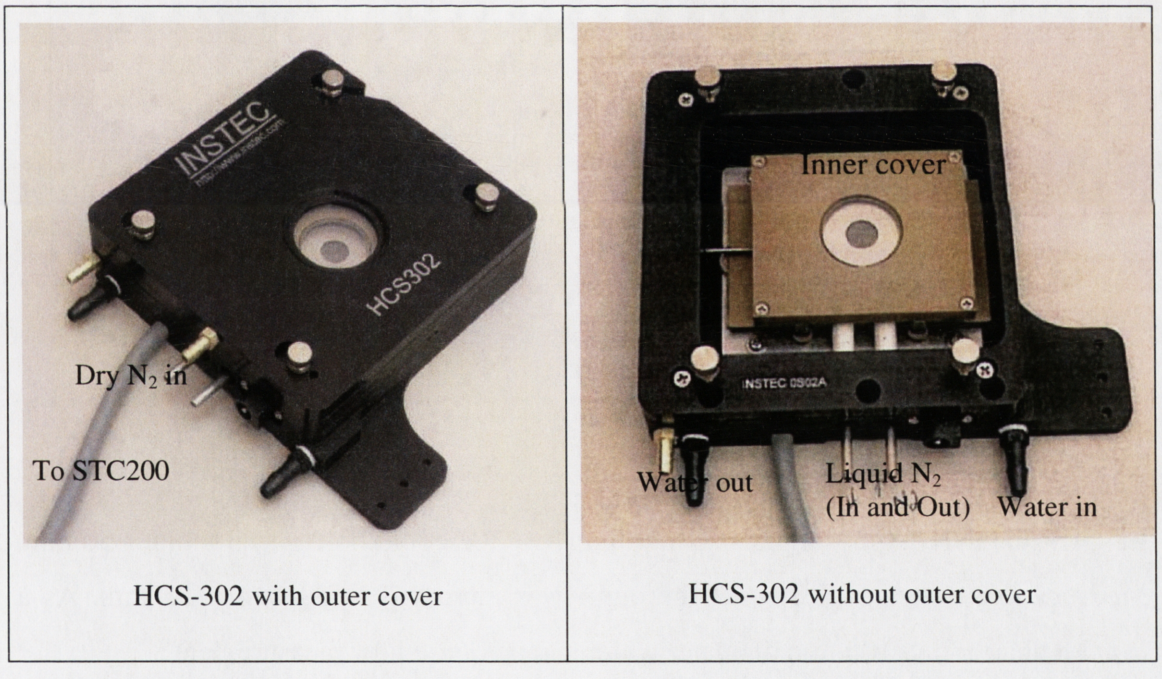

HCS-302 with outer cover

HCS-302 without outer cover

Figure 3.6: Pictorial view of HCS-302.

The physical and operating specifications of HCS-302 and its control were found to be compatible with the WCT-100 and suitable for incorporation into a T-controlled lifetime measurement instrument. However, both systems required modification before they could be combined.

3.2.2 Modifications to the existing systems and their effects

The HCS-302 was designed for optical-thermal microscopy. The sample holding stage and optical windows on its covers (inner and outer) were small and not sufficient for lifetime measurement purposes. In the assumed T-controlled lifetime measurement system, the test sample is required to be concurrently housed within the HCS-302 and close to the sensor coil of the WCT-100. In order to fulfil this requirement the following changes were made in both components.

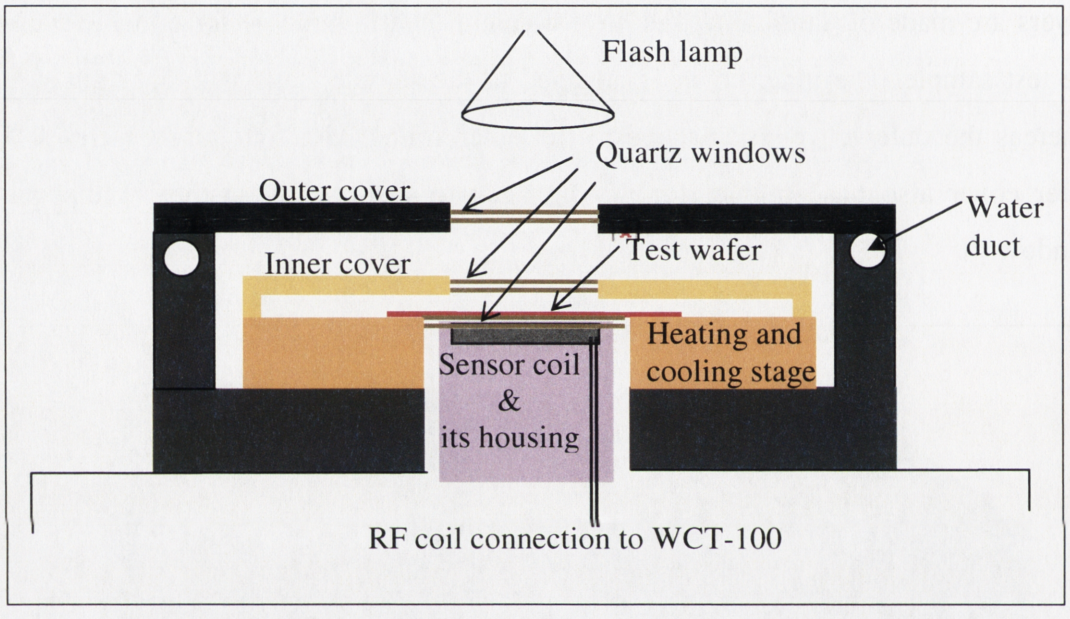

Figure 3.7: Schematic view of the HCS-302 with raised coil of the WCT-100.

a. Sample holding stage of HCS-302

Initially, the maximum sample size that the HCS-302 could hold was 38 mm × 50 mm. Modifications were made so that this limit was increased to 50 mm × 55 mm. As a result a quarter of a 100 mm diameter wafer can be housed for measurement.

b. Apertures in outer and inner covers of HCS-302

The apertures of the outer and inner covers were 5 mm diameter. This was not sufficient to illuminate the test wafer for PC measurement. Hence, the apertures on both covers were increased to 20 mm. Both apertures were fitted with quartz windows for the optimal transmission of light during measurements.

c. Rear aperture of HCS-302

The diameter of the rear aperture was increased to 22 mm from its original size of 5 mm in order to house the sensor coil inside the temperature controlled HCS-302 stage. The larger size rear aperture facilitates the housing of a larger diameter sensor coil in the WCT-100, increasing the sensitivity of lifetime measurements. However the larger rear aperture of the HCS-302 decreases the thermal stability of the stage. The aperture diameter of 22 mm was found to be optimum.

d. Sensor coil of WCT-100

The diameter of the sensor coil of the WCT-100 was reduced to 16 mm from its original size of 20 mm so that it could be fitted within the rear aperture of the HCS-302. The diameter of the sensor coil has a positive correlation with the sensitivity of the coil, so we attempted to make the reduction as small as possible by increasing the HCS-302 rear aperture. The test sample fits inside the inner cover of the HCS-302 and the sensor coil should be located within close proximity (< 2mm) of it. The sensor coil is housed inside the groove of a ceramic solid cylinder (18mm dia.), which is a non-magnetic and high thermal stability material inserted into the HCS-302 via the rear aperture. The upper part of the coil housing, where the coil is found, is situated within 2 mm of the sample surface of the HCS-302. The positioning of the HCS-302 with the WCT-100 is depicted in Figure 3.7.

3.2.3 Complete system and its operating regime

A block diagram of the integrated system is depicted in Figure 3.8. It contains a flash light system controlled by a computer program (Microsoft Excel or MATLAB). The sensor coil of the WCT-100 is housed inside a ceramic cylinder and inserted into the T-controlled stage. The HCS-302 is temperature-controlled by the STC-200. The STC-200 activates the resistive heating arrangement inside the stage for heating and activates the liquid nitrogen pump (LN2P) for cooling. When the STC-200 activates the LN2P, it starts to pump liquid nitrogen from the thermal flask via the stage. The STC-200 also controls a submersible water pump, which is submerged in a bucket of de-ionized water. The submerged pump operates when the temperature of the stage becomes higher than

100 °C and circulates waters within the channel in the outer frame of the stage. This water circulation prevents the spread of heat from the stage to the rest of the WCT-100 system.

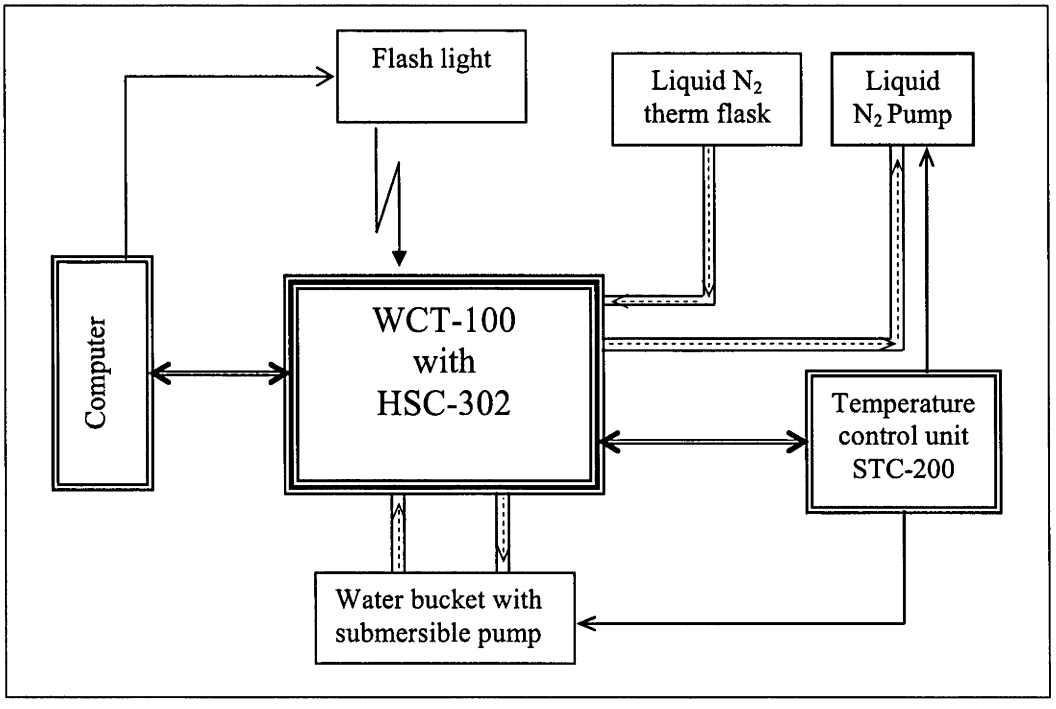

Figure 3.8: T-controlled inductive coil PC based lifetime measurement system.

The temperature of the stage can be controlled between -190 to 400 °C. The desired temperature can be input to the STC-200 manually. The sample should be placed inside the inner cover on the top of the stage. Inner and outer covers provide better thermal stability for the sample by reducing convection heat loss or gain from its surroundings. The STC-200 displays the stage temperature rather than the wafer temperature. Hence the temperature of the wafer may be different from the temperature shown on the display of the STC-200.

The temperature of the sample under test should be stable before the taking of measurements. Thermal stabilization of the sample depends primarily upon the stage temperatures. Increased stabilization time (>5 min) is expected for higher or lower stage temperatures than when at room temperature. Once the wafer temperature becomes stable, measurements can be taken.

3.2.4 Temperature deviation and thermal calibration

a. Deviation of wafer temperature (T_W) with stage temperature (T_S)

The HCS-302 has its temperature sensor (RTD) inside the stage and the STC-200 shows the temperature on its display accordingly. The real temperature of the wafer needs to be measured separately by some other means. However, a correlation between wafer temperature (T_W) and stage temperature (T_S) is useful while setting T_S for a required T_W.

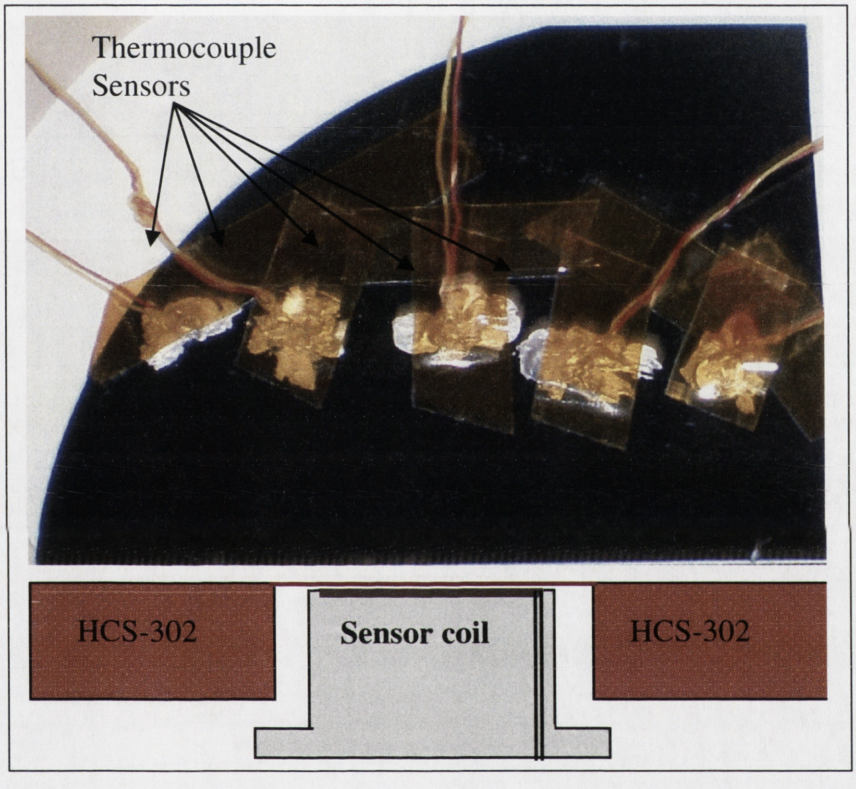

Figure 3.9: Positioning of test wafer with thermocouple sensors (top view) in HCS-302 (cross sectional view).

Experiments were performed to find the correlation between T_W and T_S. The thermocouple sensors were attached to a wafer under test at uniform distances of one cm and the sample was placed on the HCS-302. Sensors were attached to the wafer by silver conductive paste for better thermal conduction. Figure 3.9 depicts the positions of the thermocouples in a quarter of a 10 cm diameter wafer and its position above the HCS-302. The average value of the thermocouple readings were taken as T_W and plotted as a function of T_S as shown in Figure 3.10.

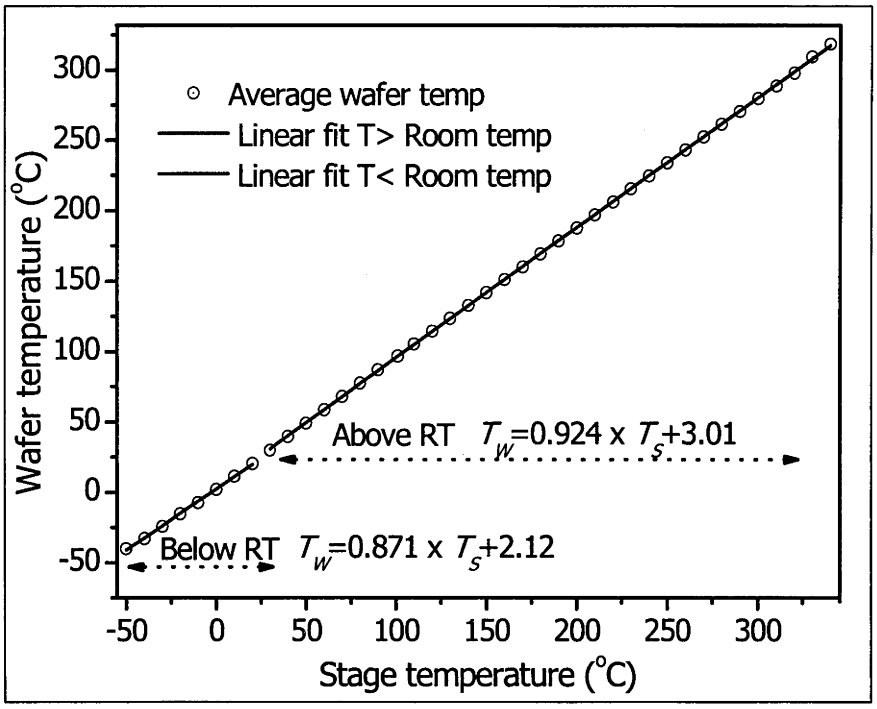

Figure 3.10: Correlation between wafer and stage temperatures.

T_W is found to be higher than T_S for temperatures below room temperature (RT) and lower than T_S when the temperature exceeds RT. The correlations between T_W and T_S are determined separately for each of two temperature regions. The linear correlations between T_S and T_W are

$$T_W = 0.871 \times T_S + 2.12, \text{ for } T_S < \text{RT} \tag{3.10}$$

$$T_W = 0.924 \times T_S + 3.01, \text{ for } T_S > \text{RT} \tag{3.11}$$

Hence, these correlation equations should be use to set the temperature T_S for the required T_W.

b. Temperature deviation within the wafer

The HCS-302 implements conductive mechanisms to heat and cool the wafer. The wafer is normally placed freelyon the top surface, so a non-uniform air layer between HCS and wafer can not be avoided. Furthermore, the HCS has the rear aperture (22 mm dia.) for the sensor coil at its centre, which further reduces the uniformity of temperature distribution within the wafer. Non-uniformity of temperature distribution cannot be avoided in practice in this type of instrument arrangement. However, the

accurate measurement of temperature deviation (T_{DEV}) within the wafer is essential for the determination of confidence levels and the errors for the results obtained with this instrument.

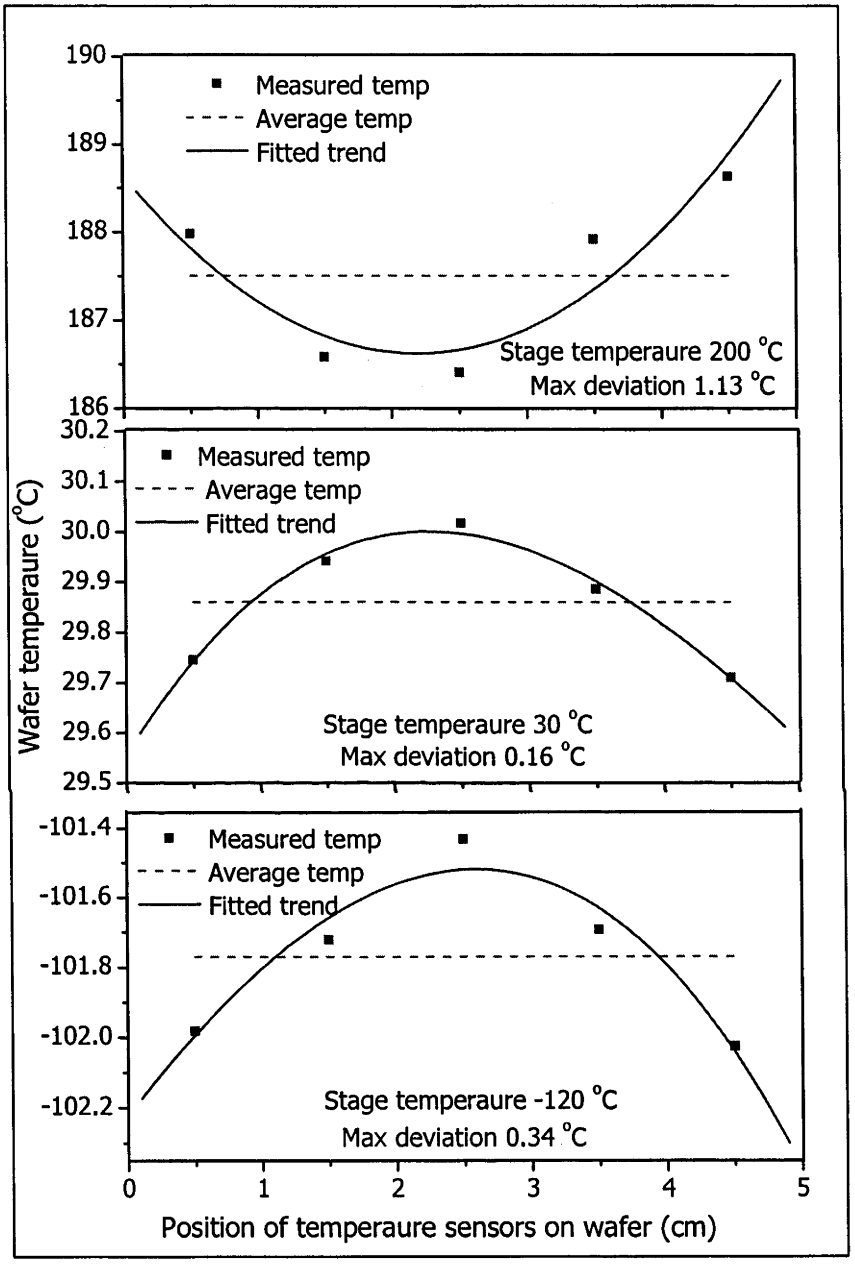

Figure 3.11: Temperature deviation within the wafer for -120, 30 and 200 °C stage temperatures (T_S).

The experimental setup previously used for determination of the correlation between T_W and T_S was used for the determination of T_{DEV} within the wafer over the temperature range -120 to 300 °C. T_{DEV} is plotted in Figure 3.12 for a T_S of -120, 30 and 200 °C for a mono crystalline silicon wafer with thickness 410 μm. Figure 3.11 shows that the wafer

has a minimum temperature at its centre for the $T_S > RT$ and a maximum temperature when $T_S < RT$. T_{DEV} is found to increase as T_W deviates from RT. T_{DEV} is determined as a function of T_W for later use during the calculation of errors in obtained results. The measured T_{DEV} was better explained for three temperature regions. The first region (A) is below RT (-120 to 20 °C), for which T_{DEV} decreases with an increase in temperature. T_{DEV} is represented as a linear function of T_W and may be expressed as Equation (3.12). The second region (B) starts from RT and extends to 100 °C, for which T_{DEV} remains almost constant between 0.1 to 0.2 °C. The third region (C) is above 100 °C, for which the T_{DEV} is represented by a quadratic function of T_W as described in Equation (3.13)

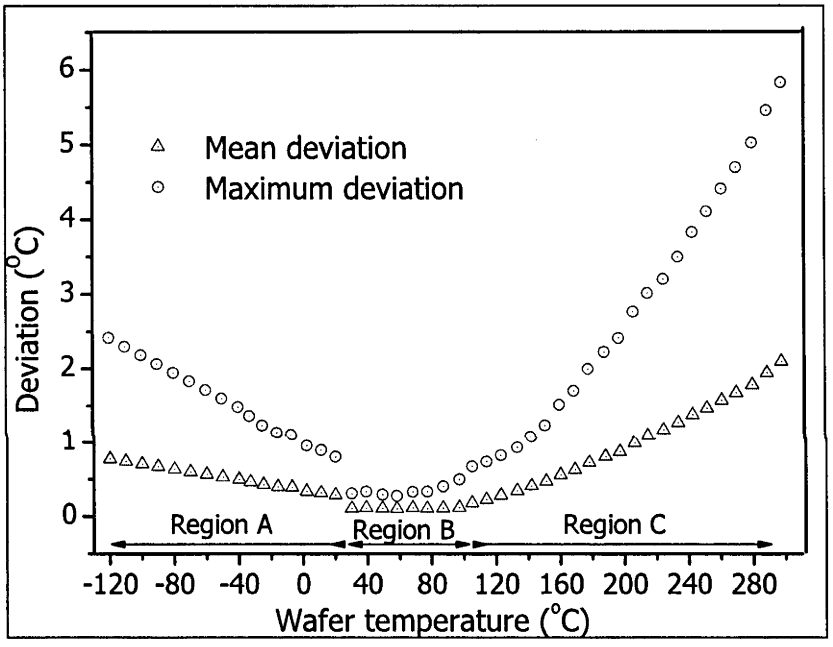

Figure 3.12: Temperature deviation within the test wafer.

$$T_{DEV} = -3.4\times10^{-3}\times T_S + 0.351, \text{ for } T_S < \text{RT} \quad (3.12)$$

$$T_{DEV} = 2\times10^{-5}\times T_S^{\,2} + 1.75\times10^{-3}\times T_S - 0.234, \text{ for } T_S > 100\,^{\circ}\text{C} \quad (3.13)$$

3.3 Calibration and measurement

The test wafer is located at the core of the sensor coil and illuminated with a flash light in the inductive-coil PC measurement instrument. The light flash increases the excess carrier density (Δn) in the test wafer which, in turn, changes its conductance. This

change in conductance ($\Delta\sigma$) alters the inductance (L) of the sensor coil which is processed and finally presented as the carrier lifetime (τ). This section discusses the step-wise signal-flow in the instrument during calibration and measurement. The validity of calibration and measurement is discussed for various ranges of temperatures and doping densities.

3.3.1 Lifetime measurement of inductive-coil PC system

The conductance (σ) of a silicon wafer can be expressed as a function of carrier densities and their mobilities

$$\sigma = q(\mu_n \times n + \mu_p \times p) \tag{3.14}$$

where n and p are the numbers of electrons and holes and μ_n and μ_p are respective mobilities. μ_n and μ_p are temperature and carrier concentration dependent and will be discussed in Section 3.3.2. The carrier concentrations p and n for a p-type silicon can be expressed as

$$p = N + \Delta n, \text{ and } n = \frac{n_i^2}{N} + \Delta n \tag{3.15}$$

where N is the net doping $N = |N_A - N_D|$. In equilibrium or dark conditions ($\Delta n = 0$), σ_0 therefore relates to N as

$$\sigma_0 = q\left[\mu_{p0} N + \mu_{n0} \frac{n_i^2}{N}\right] \tag{3.16}$$

where μ_{n0} and μ_{p0} are the mobilities of electrons and holes for respective concentrations in the dark. When the wafer is illuminated by a light flash, the hole density increases to $(N + \Delta p)$ and electrons to $[n_i^2/(N + \Delta n)]$, where $\Delta n = \Delta p$ when we assume the wafer is without trapping centres. Hence the conductance σ_L can be expressed as

$$\sigma_L = q\left[\mu_{pL}(N + \Delta n) + \mu_{nL}\left(\frac{n_i^2}{N} + \Delta n\right)\right] \tag{3.17}$$

where μ_{nL} and μ_{pL} are the mobilities of electrons and holes for respective concentrations in illuminated conditions.

The PC measurement technique should first determine N from a measurement of σ_0 and then Δn from a measurement of σ_L with the known values of μ_{n0}, μ_{p0}, μ_{nL} and μ_{pL} using Equation (3.16). This process of calculating Δn by using σ_0, σ_L, N μ_{n0}, μ_{p0}, μ_{nL} and μ_{pL} is made simpler by determining the excess conductance ($\Delta\sigma$) directly from the measured excess voltage (ΔV) using calibration coefficients as mentioned in Section 3.3.3. By combining Equations (3.15) and (3.16), $\Delta\sigma$ can be expressed as

$$\Delta\sigma = \sigma_L - \sigma_0 = q\left[(\mu_{pL} + \mu_{nL})\Delta n + (\mu_{pL} - \mu_{p0})N + (\mu_{nL} - \mu_{n0})\frac{n_i^2}{N}\right] \qquad (3.18)$$

This can be further simplified with the help of two assumptions which make the second and third terms of Equation (3.17) negligible in comparison to the first term. The first assumption is $\mu_p = \mu_{pl} = \mu_{p0}$, which is valid for low values of N but increasingly invalid for higher values. The second assumption is $N >> n_i$ which is valid at room temperature for $N >> 10^{12}$ cm^{-3} (but increasingly invalid as the temperature rises due to the subsequent rise in n_i.) The benefit of these assumptions is that Δn can be determined from $\Delta\sigma$ (and therefore ΔV) without knowledge of N, and with just the sum of the mobilities, rather than individual expressions for μ_p and μ_n as

$$\Delta\sigma = q(\mu_{pL} + \mu_{nL})\Delta n \qquad (3.19)$$

These assumptions are routinely employed in lifetime analysis and must also be valid during the process of calibration, which will be discussed in Section 3.3.3.

How does the instrument work?

The illumination of the wafer changes its conductance ($\Delta\sigma$) due to the increased numbers of carriers. The change in conductance ($\Delta\sigma$) of the wafer alters the inductance of the coil (L_M), which alters the impedance (Z_L) of the coil as

$$Z_L = k_L(\omega L_M)^2\sigma \qquad (3.20)$$

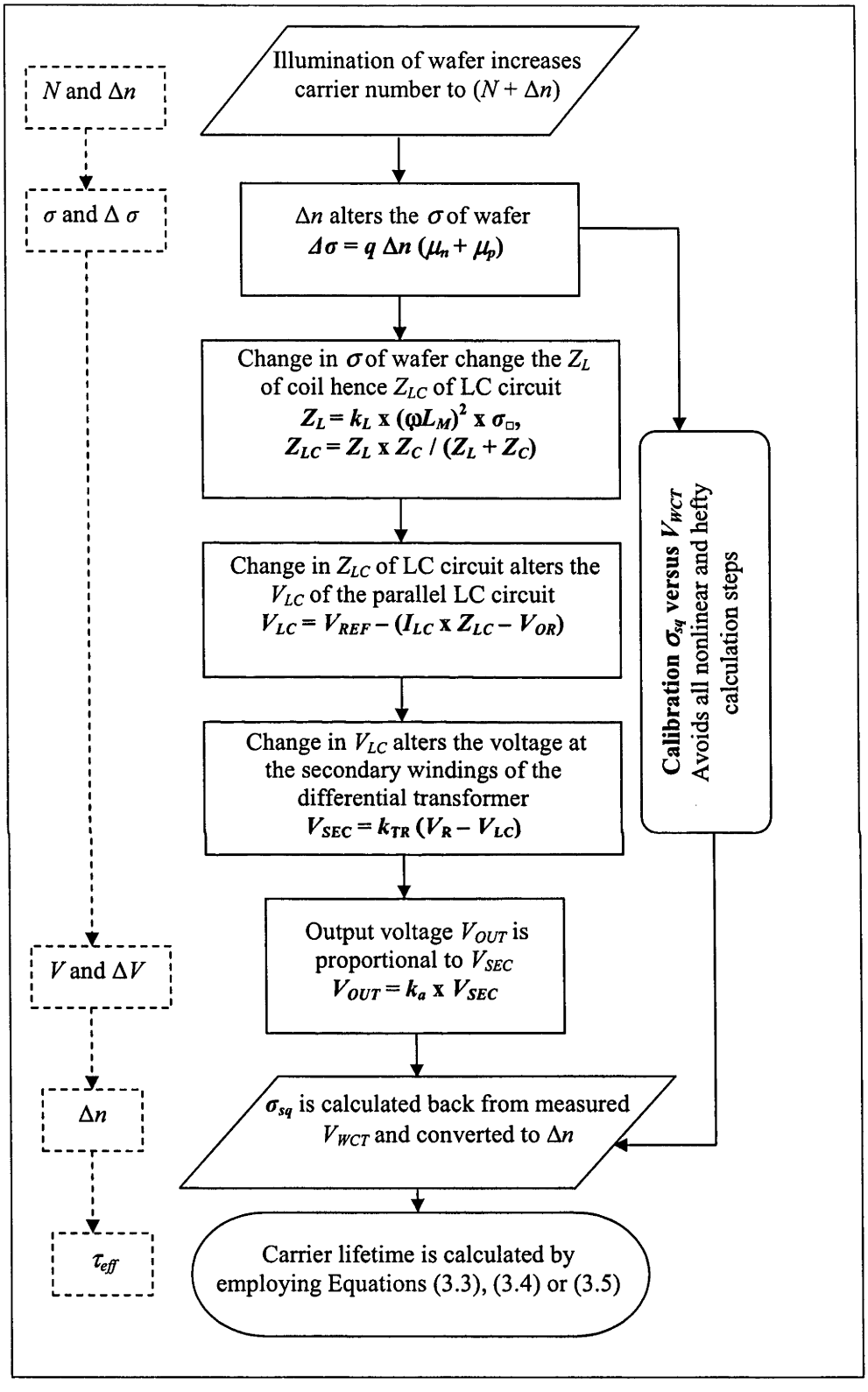

Figure 3.13: Signal flow diagram in inductive-coil PC measurement instrument with calibration bypass.

where k_L is a constant dependent upon the physical dimension of the coil and ω is the frequency of the system. Referring to Equation (3.20), a change in Z_L alters the value of overall impedance (Z_{LC}) of the parallel LC circuit as

$$Z_{LC} = {Z_L \times Z_C}/{Z_L + Z_C} \tag{3.21}$$

where Z_C is the capacitive impedance of the parallel LC circuit. This change in Z_{LC} alters the voltage drop (V_{LC}) across the LC circuit which engenders an imbalance in the primary winding of the differential transformer. An imbalance of the primary winding changes the output of the secondary winding (V_{SEC}) according to,

$$V_{SEC} = k_{TR}(V_R - V_{LC}) \tag{3.22}$$

where k_{TR} is the transformation ratio of the differential transformer and V_R is the voltage of the upper primary winding.

V_{SEC} of the differential transformer is then fed to the rectification and amplification unit and finally to the output voltage (V_{OUT}), which is fed to the oscilloscope or data acquisition card,

$$V_{OUT} = k_a \times V_{SEC} \tag{3.23}$$

where k_a is the amplification factor. Figure 3.13 depicts the signal flow chart in the inductive-coil PC measurement instrument.

The instantaneous value of change to conductivity $\Delta\sigma(t)$ of the wafer under test is calculated from the measured V_{OUT} and then converted to $\Delta n(t)$. The change rate of carrier density $\partial(\Delta n) / \partial t$ is determined and the effective lifetime is calculated by using Equation (3.3), (3.4) or (3.5) as required. The physical parameters (k_L, k_{TR} and k_a) of Equations (3.20) to (3.23) are required in order to calculate $\Delta\sigma(t)$ from measured V_{OUT}. These parameters are difficult to obtain accurately and are sensitive to the vibration and displacement of the instrument. Hence obtaining and using accurate values of these physical parameters for the calculation of $\Delta\sigma$ from measured V_{OUT} is tedious. An alternative method of calculating $\Delta\sigma$ from measured V_{OUT} uses the pre-determined

correlation coefficients between V_{OUT} and $\Delta\sigma$. The process of determining correlation coefficients between V_{OUT} and $\Delta\sigma$ is known as the calibration of the inductive-coil PC measurement instrument and is discussed in Section 3.3.3.

$\Delta\sigma$ is related to Δn and mobilities (μ_n and μ_p) as described in Equation (3.18) or in simplified form in Equation (3.19). μ_n and μ_p are also dependent upon carrier densities. Hence Δn should be calculated from measured $\Delta\sigma$ by an iterative procedure using a relevant carrier-density-dependent mobility model [16-20]. Further, μ_n and μ_p are strongly dependent upon temperature. As this work involves T-dependent measurement of effective lifetime, the appropriate carrier-density and T-dependent mobility model is essential for calibration as well as for measurement purposes. The next section will discuss temperature and doping-dependent mobility models.

3.3.2 Temperature and carrier-density-dependent mobilities

Carrier mobilities have a significant influence in a PC based lifetime measurement process. The effects of carrier mobilities are crucial for T-dependent lifetime measurements because both μ_n and μ_p have strong dependency on temperature. Accurate values for carrier mobilities are essential during determination of Δn from the output voltage signal (V_{OUT}). With this in mind a summary of temperature and carrier-density-dependence on mobilities and a review of reported mobility models [16-20] is presented.

The overall mobility of a carrier in silicon is determined by three kinds of scattering mechanisms to which carriers are subjected while under thermal agitation. Lattice, defect and carrier-carrier scattering are possible mechanisms. Each scattering mechanism is responsible for particular mobility components and can be distinguished [17]. The overall mobility is the function of these three types of mobilities is seen as

$$\mu_{toatl}(T) = f[\mu_L(T), \mu_I(T), \mu_{ccs}(T)] \tag{3.24}$$

where μ_L, μ_I μ_{ccs} represents the lattice, impurity and carrier-carrier scattering mobilities of carriers.

Lattice scattering of carriers is caused by acoustic and optical phonons [21]. The mobility component of this scattering is known as lattice mobility (μ_L) and has strong dependence upon temperature. The generalized expression for μ_L is

$$\mu_L(T) = \mu_{L0}\left(\frac{T}{300}\right)^{-\alpha} \tag{3.25}$$

where μ_{L0} is a T-independent pre-factor and α is an exponent of the T-dependent function. The value of α is dependent upon the type of impurity. Mobility models suggested by Dorkel *et al.*, Arora *et al.* and Klassen *et al.* have a fixed values for α whereas Regiaani *et al.* [20] suggest a T-dependent function, $\alpha = \gamma + c(T/300)$.

Defect scattering of carriers comprises crystal defect, impurity and alloy scattering components. Among these three, impurity scattering dominates. Most reported models neglect crystal defects and alloy scattering in comparison with impurity scattering. Defect scattering mobility is also termed impurity scattering mobility or simply impurity mobility (μ_I). In general, μ_I is found to increase with temperature and decrease with doping concentration (N_{DOP}) and can be expressed as

$$\mu_I(T) = \frac{AT^{3/2}}{N}\left[\ln\left(1+\frac{BT^2}{N}\right) - \frac{BT^2}{N+BT^2}\right]^{-1} \tag{3.26}$$

where N is the concentration of ionized dopants and A and B are physical parameters which depend upon the nature of the carriers. Klassen *et al.* [18, 19] presented two different forms of the expression for impurity mobility for majority and minority carriers. However, in either case, μ_I is found to increase with temperature and decrease with doping concentration.

Table 3.2: Specifications of most commonly used carrier mobility models

Mobility model	As a function	Temp range	Accuracy claim
Dorkel *et al.* [17]	T, $N_{A/D}$, Δn, n and p	200 to 600 K	±3% for 250 to 500 K and ≥ ±10% for 200 to 600 K
Arora *et al.* [16]	T, n and p	250 to 500 K	≥ ±10% for 250 to 500 K
Regiaani *et al.* [20]	T, $N_{A/D}$, n and p	300 to 700 K	Not claimed
Klassen *et al.* [18, 19]	T, $N_{A/D}$, Δn, n and p	200 to 500 K	Not claimed

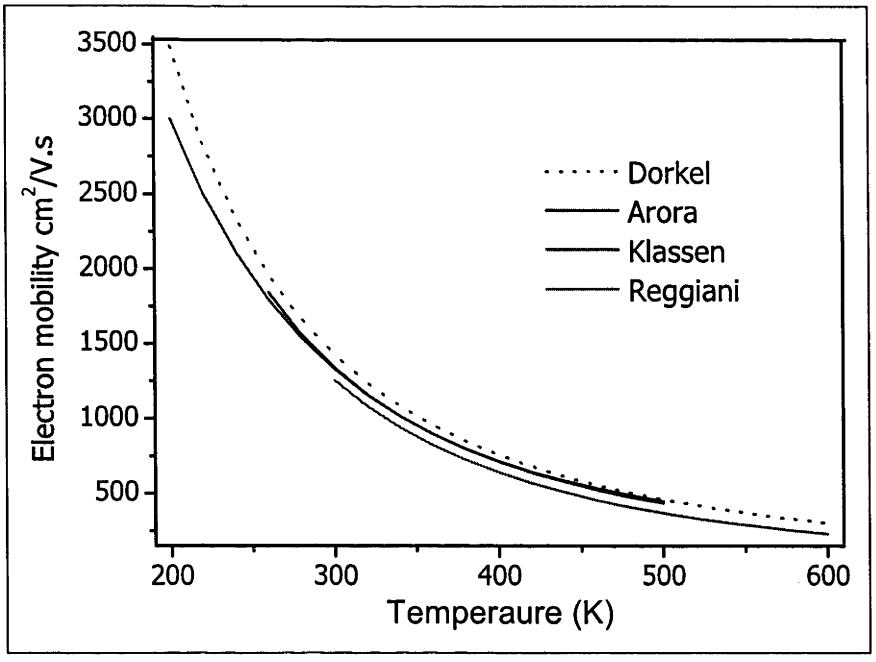

Figure 3.14: Electron mobility for 1 Ω cm boron-doped silicon.

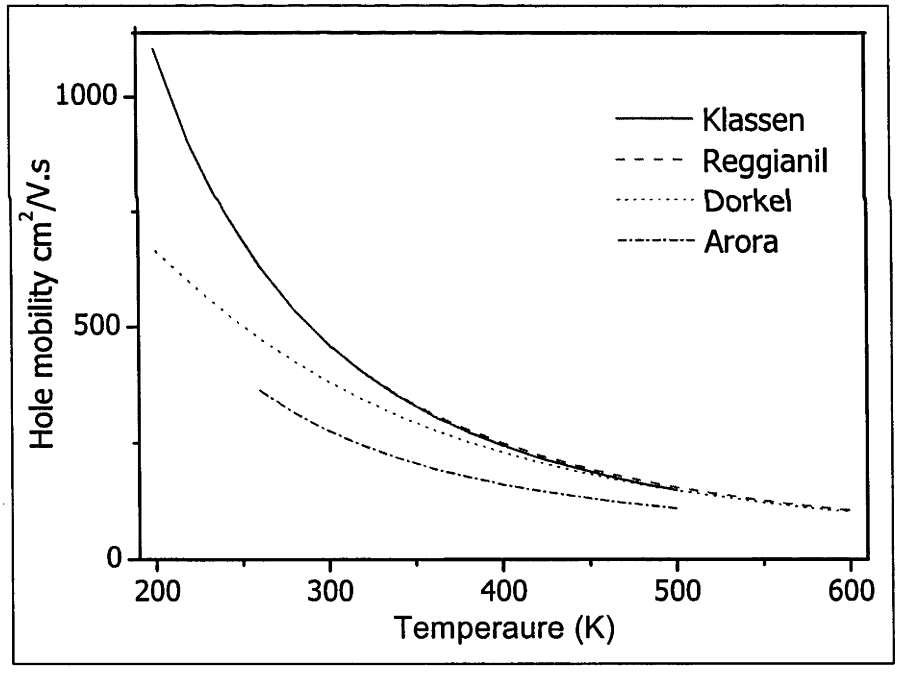

Figure 3.15: Hole mobility for 1 Ω cm boron-doped silicon.

Carrier-carrier scattering is another type of scattering. It is responsible for the carrier-carrier scattering mobility (μ_{ccs}) component. This type of mobility becomes very influential when carriers of both types are at high concentrations. Like μ_l, μ_{ccs} is directly proportional to temperature and inversely proportional to the carrier numbers (n and p). The generalized expression for μ_{ccs} can be expressed as

$$\mu_{CCS}(T) = \frac{2\times10^{17}T^{3/2}}{\sqrt{pn}}\left[\ln\left\{1+8.28\times10^{8}T^{2}(pn)^{-1/3}\right\}\right]^{-1} \tag{3.27}$$

The specifications of four widely used mobility models [16-20] are presented in Table 3.2. Electron and hole mobilities are depicted as a function of temperature in Figures 3.14 and 3.15.

The mobility model reported by Reggiani *et al.* is preferred for this work as this is the only model which is valid for the upper limit of the temperatures (> 320 °C), which is required for this work. However, this model does not account for the scattering mobilities due to excess carriers (Δn). Hence this model is only suitable when $\Delta n << N_{DOP}$. This condition has been fulfilled while measuring and analysing the lifetime at higher values of Δn throughout this work. Furthermore, the effect of Δn scattering mobility on overall mobility was mapped at room temperature by comparing mobilities calculated from the Klassen *et al.* [18, 19] model which accounts for Δn in scattering mobilities. The Reggiani [20] model is formulated as

$$\mu(N_D,N_A,T) = \mu_0(N_D,N_A,T) + \frac{\mu_L(T)-\mu_0(N_D,N_A,T)}{1+\left(\frac{N_D}{C_{r1}(T)}\right)^{\alpha_1}+\left(\frac{N_D}{C_{r1}(T)}\right)^{\alpha_2}} - \frac{\mu_1(N_D,N_A,T)}{1+\left(\frac{N_D}{C_{s1}(T)}+\frac{N_D}{C_{s1}(T)}\right)^{-2}} \tag{3.28}$$

where $\mu_L(T)$ is the lattice mobility given as

$$\mu_L(T) = \mu_{\max}\left(\frac{T}{300}\right)^{-\gamma+c(T/300)} \tag{3.29}$$

$\mu_0(N_D, N_A, T)$ and $\mu_1(N_D, N_A, T)$ are the carrier mobility modulators and given as

$$\mu_0(N_D,N_A,T) = \frac{\mu_{0d}N_D+\mu_{0a}N_A}{N_D+N_A} \quad and \quad \mu_1(N_D,N_A,T) = \frac{\mu_{1d}N_D+\mu_{1a}N_A}{N_D+N_A} \tag{3.30}$$

all the parameters of expressions (3.23), (3.24) and (3.25) are presented in Table 3.3.

Table 3.3: Parameters of Reggiani's mobility model

Parameters	Phosphorous	Boron	Unit
μ_{max}	1141	470	$cm^2/V.s$
c	0.07	0.00	------
γ	2.45	2.16	------
μ_{0d}	$62.2 \times T^{-0.7}$	$90.0 \times T^{-1.3}$	$cm^2/V.s$
μ_{0a}	$132.0 \times T^{-1.3}$	$44.0 \times T^{-0.7}$	$cm^2/V.s$
μ_{1d}	$48.6 \times T^{-0.7}$	$28.2 \times T^{-2.0}$	$cm^2/V.s$
μ_{1a}	$73.5 \times T^{-1.25}$	$73.5 \times T^{-0.8}$	$cm^2/V.s$
C_{r1}	$8.50 \times 10^{16} \times T^{3.65}$	$1.30 \times 10^{18} \times T^{2.2}$	cm^{-3}
C_{r2}	$1.22 \times 10^{17} \times T^{2.65}$	$2.45 \times 10^{17} \times T^{3.1}$	cm^{-3}
C_{s1}	4.00×10^{20}	$1.10 \times 10^{18} \times T^{6.2}$	cm^{-3}
C_{s2}	7.00×10^{20}	6.10×10^{20}	cm^{-3}
α_1	0.68	0.77	------
α_2	0.72	0.719	------

3.3.3 Calibration of the inductive-coil PC measurement instrument

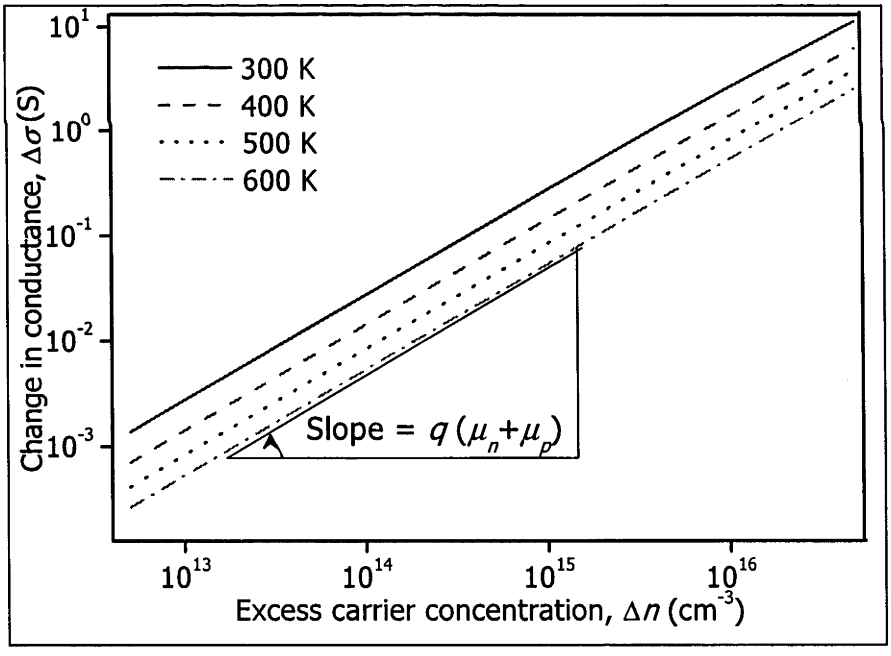

Figure 3.16: Correlation between Δn and $\Delta\sigma$ for different temperatures. $\Delta\sigma$ is calculated by using Equations (3.14) and (3.15).

The calibration of the inductive-coil PC instrument is the process of finding correlation factors between the output voltage (V_{OUT}) and the conductivity (σ) of the wafers. Such correlation avoids the necessity of the determination of instrument specific parameters

shown in Equations (3.15) to (3.18) in calculating $\Delta\sigma(t)$ from measured V_{OUT}. The most common approach to calibration is to record V_{OUT} for a variety of wafers with known σ, the data is then fit linearly or to a parabola as

$$\sigma = a \times V_{OUT}^{\ 2} + b \times V_{OUT} + c \tag{3.31}$$

where a, b and c are correlation coefficients and $a = 0$ for a linear calibration.

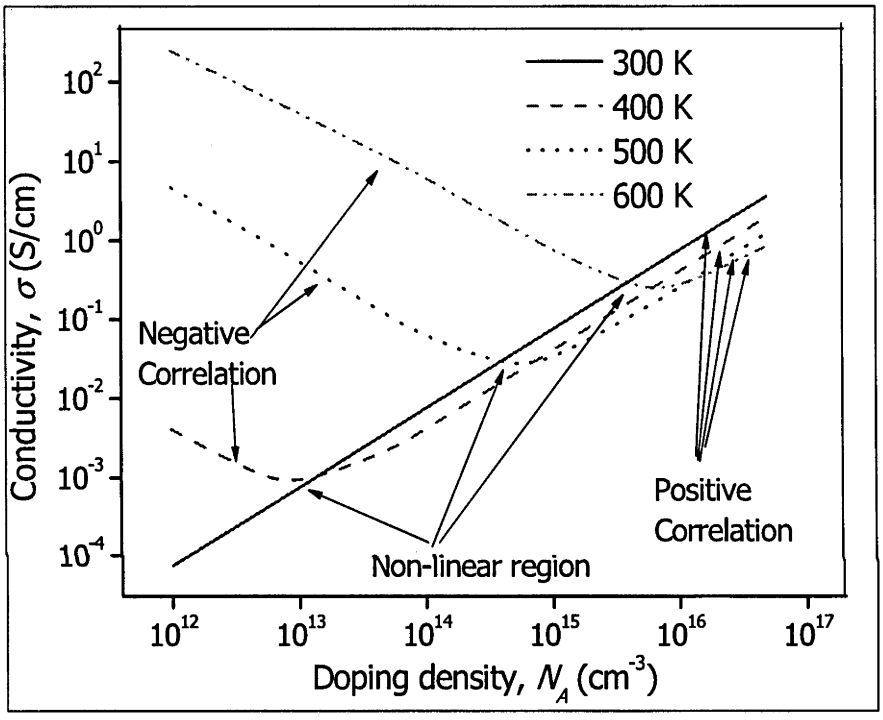

Figure 3.17: Correlation of σ with N_A for p-type wafers at 300, 400, 500 and 600 K.

Wafers with a wide range of doping densities (N_A or N_D) are selected for calibration. These calibration wafers should have conductivity data with high precision to allow greater accuracy in measurements. The four point probe measurement technique [22] is the most common type of conductivity mapping technique used in silicon wafers. However, this technique has poor accuracy for lower conductivity (< 0.01 S/cm) wafers. The calibration process involves the placement of wafers above the sensor coil of the instrument. The corresponding V_{OUT} is recorded and the correlation between V_{OUT} and σ is determined. The corresponding value of N_A or N_D of the calibration wafers according to σ is then used to determine the relation between carrier concentrations and V_{OUT}. As

discussed in Section 3.3.1, these assumptions must be valid during the calibration. Both assumptions are made to ensure a positive correlation of N with σ as Δn to $\Delta\sigma$.

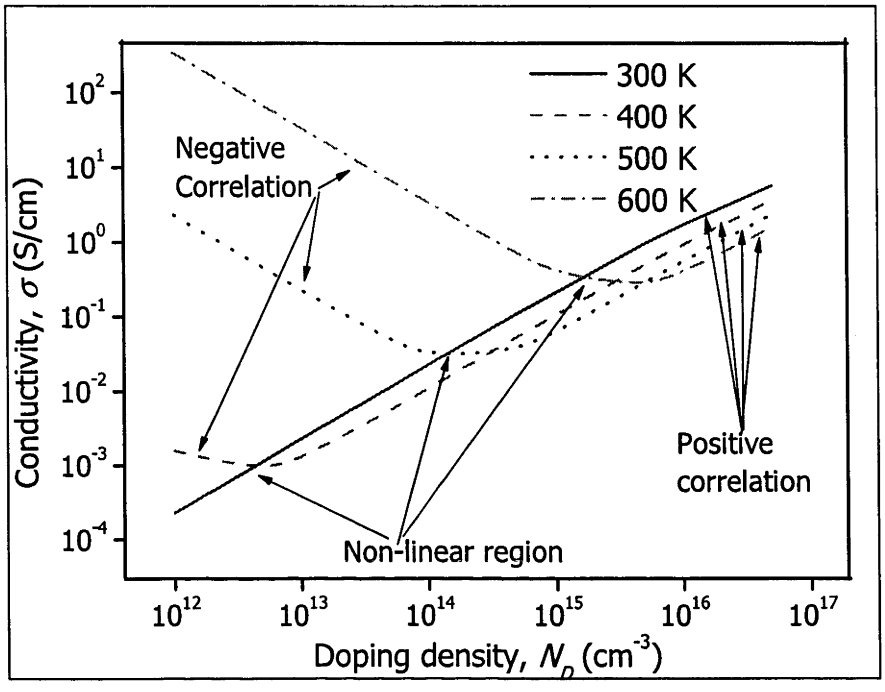

Figure 3.18: Correlation of σ with N_D for n-type wafers at 300, 400, 500 and 600 K

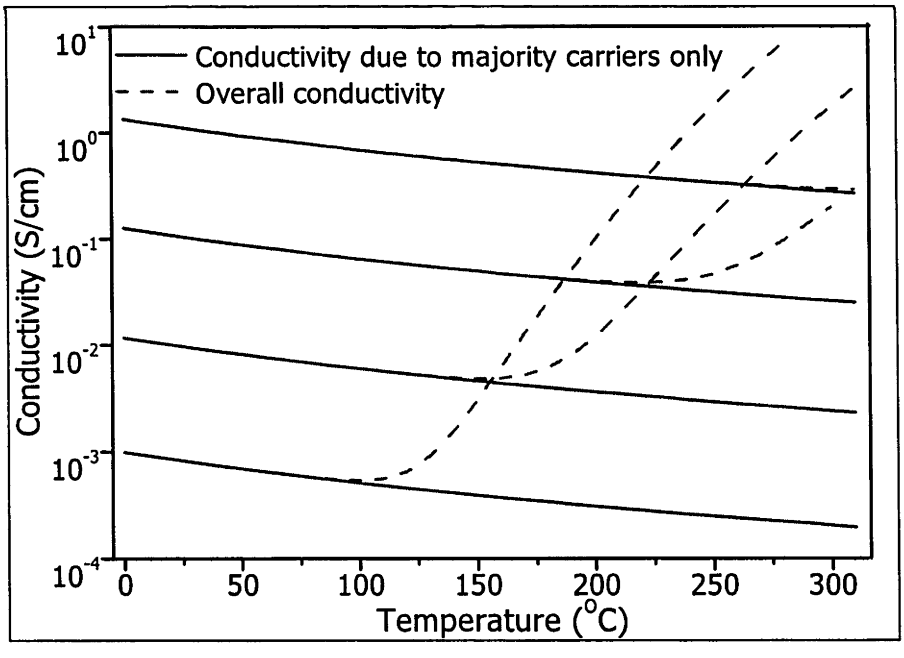

Figure 3.19: Conductivity of p-type silicon due to the majority carriers and both carriers for different temperatures, depicting how the minority carriers dominate overall conductivity at higher temperatures (> T_{max}).

A positive correlation between N_A or N_D with σ ensures a simpler calculation of Δn from measured $\Delta\sigma$. Equation (3.15) shows a positive correlation between Δn and $\Delta\sigma$, which is plotted in Figure 3.16 for different temperatures. T-dependent carrier mobilities, $\mu_n(T)$ and $\mu_p(T)$ are calculated using the model suggested by Reggiani *et. al.* [20]. N_A or N_D also have positive correlation with σ for the wafer having $\sigma \geq 10^{-4}$ S at RT. However, at higher temperatures (> 100 °C) positive correlation does not occur for lower conductivity wafers. Figures 3.17 and 3.18 depict the correlation of N_A or N_D with σ for p and n-type wafers.

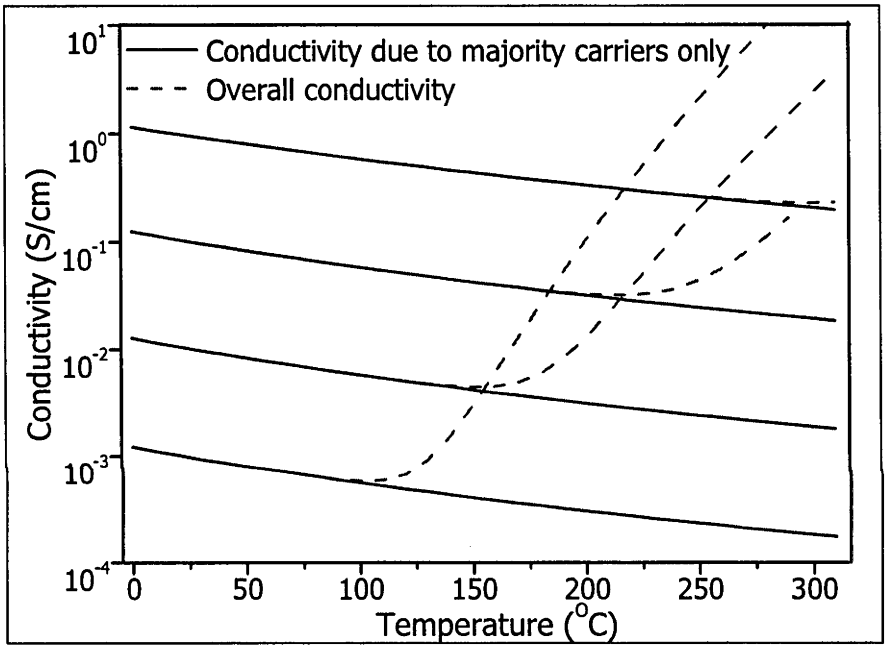

Figure 3.20: Conductivity of n-type silicon due to the majority carrier and both carriers for different temperatures, depicting how the minority carrier dominates overall conductivity at higher temperatures (> T_{max}).

A non-linear region appears in conductivity versus doping density plots at a certain temperature, as shown in Figures 3.17 and 3.18. This nonlinearity occurs above a certain temperature, T_{max}, when the overall conductivity of the wafer becomes less than the conductivity due to the majority carriers, i.e. the third term in Equation (3.18) became significant. T_{max} is below 100 °C for low conductivity (< 10^{-3} S/cm) wafers and increases with the conductivity of the wafer. Figures 3.19 and 3.20 depict the conductivity due to the majority carrier only and overall conductivity for p and n-type silicon for temperatures 0 to 300 °C. T-dependent carrier mobilities, $\mu_n(T)$ and $\mu_p(T)$, are

calculated using the model suggested by Reggiani *et. al.* [20]. Minority carrier densities are calculated by using Equation (2.35) where $n_i(T)$ is calculated by Equation (2.36).

The measured V_{OUT} for wafer temperatures greater than T_{max} should not be used for calibration. Table 3.4 shows the T_{max} of the wafers with their conductivity at room temperature (27 °C). T_{max} is determined as the temperature at which the product of the minority carrier concentration with its mobility within 1 % of the product of the majority carrier concentration with its mobility.

Table 3.4: Maximum temperature (T_{max}) for different conductivity of wafers (at 300 K) below which the minority carrier has a negligible contribution to overall conductivity of the wafer.

Conductivity (S cm^{-1})	*p*-type		*n*-type	
	N_A (cm^{-3})	T_{max} (°C)	N_D (cm^{-3})	T_{max} (°C)
10	2.3×10^{17}	458.00	8.1×10^{16}	429.00
1	1.5×10^{16}	312.00	5.1×10^{15}	300.00
0.1	1.4×10^{15}	224.00	4.5×10^{14}	217.00
0.01	1.3×10^{14}	158.00	4.4×10^{13}	156.00
0.001	1.1×10^{13}	105.00	4.2×10^{12}	107.00
0.0001	1.4×10^{12}	70.00	1.1×10^{11}	49.00

Calibration of the system is performed with a variety of wafers with conductivity from 0.1 to 100 Siemens. The resistivities of these wafers were measured using four point probe measurements and spreading resistance analysis. In four-point probe measurements, each data point has been derived from a statistical analysis of over 2000 current-voltage measurements. Probe configuration switching was used to correct for any variations in probe spacing and for any current crowding due to wafer-edge effects. For spreading resistance analysis, the reduced data have been obtained by comparing measured values with measurements on standard bulk samples of known resistivity and appropriate crystal orientation.

The conductivity of a wafer is dependent upon its width and expressed as Siemens per unit of width (S/cm). The calibration and measurement wafer has a different shape and width, making exact calculation of conductivity difficult. Furthermore, it is not necessary that the entire area of the wafer is magnetically linked with the sensor coil of the PC measurement instrument during calibration and measurement. The conductivity of the wafer needs to be width independent. In this regard, the term "sheet conductance"

(σ_{sq}) is introduced, which is independent of width of the wafer and can be obtained by multiplying the conductivity of the wafer by its width. Hence one Siemens square (σ_{sq}) is the conductivity of one unit area of the silicon wafer and can be expressed as

$$\sigma_{sq} = \sigma \times W \tag{3.32}$$

The specifications of the calibration wafers are presented in Table 3.5 with the maximum temperature (T_{max}) for which assumption (2) is valid and the V_{OUT} of the respective wafers for different temperatures. The sensor coil is housed inside the heating stage and heating or cooling of the coil according to the stage temperature can not be avoided. Hence calibration was performed for the entire operating temperature range (0 – 310 °C) of the instrument in order to ensure any changes in the physical parameters mentioned in expressions (3.16) to (3.19) are accounted for.

Table 3.5: Calibration wafer details and their corresponding V_{OUT} for selected temperatures, data in bold italic corresponds to the negative conductivity as shown in Figure 3.21

Wafer	N_A (cm^{-3})	Width (μm)	T_{max} (° C)	V_{OUT} (V) (30 ° C)	V_{OUT} (V) (100 ° C)	V_{OUT} (V) (200 ° C)	V_{OUT} (V) (300 ° C)
A	1.84×10^{13}	517	118	0.038	0.020	***0.023***	***0.028***
B	1.70×10^{15}	525	236	0.100	0.063	0.012	***0.018***
C	3.80×10^{15}	543	265	0.150	0.105	0.030	***0.035***
D	1.50×10^{16}	245	321	0.286	0.183	0.073	0.020
E	3.10×10^{16}	336	356	0.598	0.388	0.202	0.105
F	3.30×10^{16}	289	359	0.503	0.340	0.170	0.089
G	5.90×10^{16}	297	390	0.827	0.550	0.301	0.612

The value of V_{OUT} recorded for sample (A) for 200 °C and samples (A), (B) and (C) for 300 °C can not be used for the calibration purpose as these temperatures are above T_{max} of the respective wafers. Figure 3.21 (a) depicts the correlation between $\sigma_{sq}(T)$ and V_{OUT} at 30 °C. The correlation is expressed in linear and quadratic forms as

$$\sigma = -0.247 \times V_{OUT}^{\ 2} + 1.253 \times V_{OUT} - 0.049 \text{ for quadratic fit and} \tag{3.33}$$

$$\sigma = 1.473 \times V_{OUT} - 0.081 \text{ for linear fit.} \tag{3.34}$$

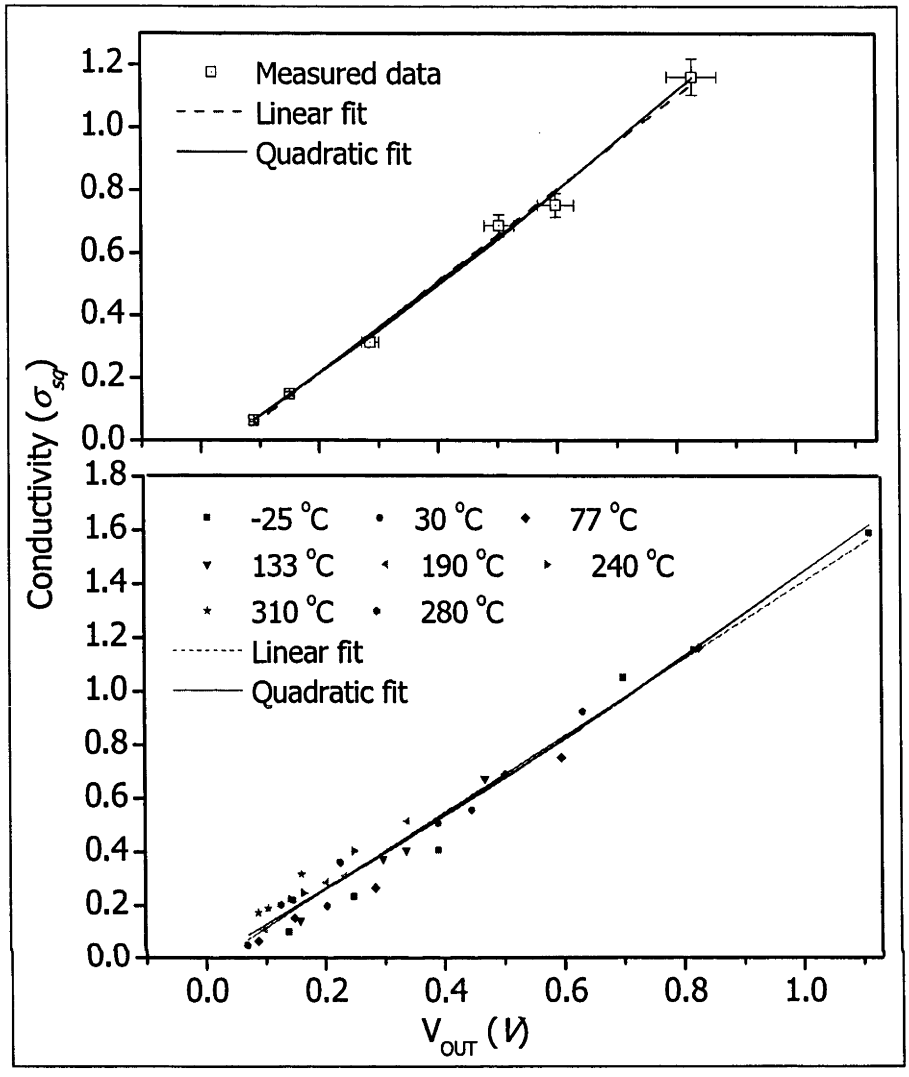

Figure 3.21: Correlation of wafer sheet conductivity (σ_{sq}) to V_{OUT} for (a) 30 °C, (b) at different temperatures.

The temperature of the wafers varies when the stage is operating at increased or decreased temperature, depending on shape and size. This makes it difficult to achieve V_{OUT} for the same temperature in all wafers at higher or lower than room temperature. Figure 3.22 (b) depicts the correlation between $\sigma(T)$ and V_{OUT} for the temperatures -25 to 310 °C. The correlation between $\sigma(T)$ and V_{OUT} determined at 30 °C is found to be valid for the entire temperature range. The linear and quadratic fit has errors of 3% and 2.8% error for 95% confidence interval.

The coefficients of the expressions (*a*, *b* and *c*) are subject to change by physical displacement or vibration of the instrument. Frequent re-calibration of the system helps to maintain measurement precision.

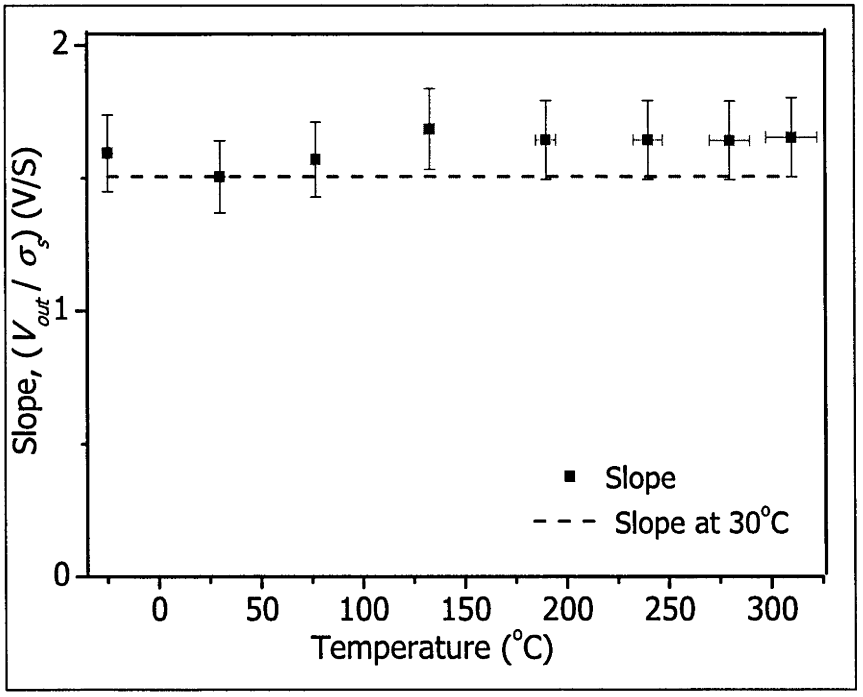

Figure 3.22: Slope of the plot V_{OUT} Vs σ_{sq} for different temperatures.

Figure 3.22 depicts the slope of the plot (V_{out} Vs σ_{sq}) for temperatures -25 to 310 °C. The slope does not show any trend with temperature and is within the error of the measurements (7%).

3.4 Uncertainties in measurement

The inductive-coil PC based instrument measures the carrier lifetime of the wafer under test on the basis of the parameters of the test wafer and the different models adopted. The accuracy of the measured data is dependent upon the accuracy of the test wafer parameters and the error associated with the employed physical models. Furthermore, the precision of the instrument is also vital in obtaining better accuracy in measured data. Detailed assessment of error associated in the results of the device is presented in Appendix D. This section lists the input and model parameters with their typical errors and corresponding error associated with lifetime measurement. Table 3.6 presents the

typical uncertainty of the above mentioned parameters to three types of lifetime analysis.

Table 3.6: Effect of typical errors in different parameters on overall lifetime measurements.

Parameters	Typical error (%)
Wafer thickness (W)	±2.5
Mobility (μ_n and μ_p)	±5
Intrinsic carrier concentration (n_i)	±5
Calibration factors (a, b)	±3
Reference voltage (V_{ref})	±2
Temperature	±2
Measured injection density (Δn)	±6.4
Measured lifetime $\tau_{eff}(G)$ (s)	±7.5
Measured lifetime $\tau_{eff}(QSS)$ (s)	±6.0
Measured lifetime $\tau_{eff}(Tr)$ (s)	±0.0

a. Wafer thickness (W): The thickness of the wafer (test and calibration) is used to calculate $\Delta\sigma_{Sq}$ and Δn. The measured Δn is divided by W to calculate τ_{eff}, hence the uncertainty inherited by W of the test-wafers cancel out. However, the uncertainty inherited by W of the calibration wafer transfers uncertainty on the calibration factor.

b. Mobility (μ_n and μ_p): The sum of the carrier mobilities ($\mu_n + \mu_p$) used to calculate Δn from conductivity of the wafers (test and calibration) and τ_{eff} is calculated from Δn. Hence the uncertainty inherited by the carrier mobility model will transfer to the measured τ_{eff}. As carrier mobilities are also the function of Δn, error in Δn is convoluted. However for the region $\Delta n < 10^{15}\,cm^{-3}$, the effect of Δn on carrier mobilities is less significant. Furthermore, carrier mobilities also depend upon temperature hence the uncertainty associated with T is also transferred to carrier mobilities and then to measured lifetime.

c. Intrinsic carrier concentration (n_i): n_i is used to calculate the minority carrier concentration which is then used to calculate the base conductivity of the wafer. Hence

the uncertainty associated with the adopted model for n_i will be transferred to measured lifetime.

d. Calibration factors (a, b): Calibration factors are determined by linear or quadratic fit of the measured V_{out} with the known conductance (σ_{sq}) as discussed in Section 3.3. Hence the error in such fit of the data (V_{out} Vs σ_{sq}) introduces error in calculated Δn from measured voltage (ΔV_{out}).

e. Temperature (T): Carrier mobilities and intrinsic carrier concentration are the function of temperature. Hence uncertainty in T introduces error to μ and n_i and finally to measured lifetime.

f. Reference voltage (V_{ref}): Reference voltage (V_{ref}) of the reference cell is used to calculate the generation rate $G(t)$ of the test wafer. Hence the error associated with V_{ref} is transferred to measured lifetime.

Appendix D discusses the effect of the above mentioned parameters in three different types of lifetime measurements.

3.5 Chapter summary

In this Chapter, three types of contactless lifetime measurement techniques which have potential for T-controlled lifetime measurement are discussed. The inductive-coil PC measurement instrument is selected for the implementation of the T-controlled stage on the basis of its simplicity and popularity. A T-controlled stage, HCS-302, was selected and custom-designed to be implemented with a modified version of an inductive-coil PC measurement instrument, WCT-100. The modifications to the original systems (HCS-302 and WCT-100) are discussed in Section 3.2.2.

HCS-302 can hold the test wafer from -190 to 400 °C, however the designed T-controlled lifetime measurement system is tested from -150 to 340 °C. The temperature of the test wafer (T_W) is found lagging behind the stage temperature (T_S) displayed in the system and the temperature gradient within the wafer is noted and discussed in Section 3.2.4.

A correlation is made between output voltage (V_{OUT}) of the inductive-coil PC measurement system and the conductivities ($\sigma_{\square}$) of the wafers as determined for the temperature -25 to 310 °C. These correlation factors (calibration coefficients) are found to be unaffected by changes to wafer temperature. The detail of the calibration process is discussed in Section 3.3.

Uncertainties in the measured parameters are assessed on the basis of input and model parameters required and discussed in Section 3.4. A detailed explanation of uncertainties is further discussed in Appendix D. Wafer thickness, calibration factors, reference voltage and temperature are the entered parameters whose uncertainties are transferred to measured lifetime, whereas mobility and intrinsic carrier concentrations are the T-dependent models, which transfer their uncertainties to the measured lifetime.

This Chapter completes the development and commissioning of a T-controlled lifetime measurement instrument suitable for testing the new procedure of lifetime spectroscopy as discussed in Chapter 2. Chapters 4, 5 and 6 will use this instrument for lifetime measurement at different temperatures on intentionally metal-contaminated silicon wafers.

References

[1] S. M. Sze and K. K. Ng, *Physics of semiconductor devices*: Wiley-Interscience, 2007.

[2] H. Nagel, C. Berge, and A. G. Aberle, "Generalized analysis of quasi-steady-state and quasi-transient measurements of carrier lifetimes in semiconductors," *Journal of Applied Physics,* vol. 86, p. 6218, 1999.

[3] R. A. Sinton and A. Cuevas, "Contactless determination of current–voltage characteristics and minority carrier lifetimes in semiconductors from quasi steady state photoconductance data," *Applied Physics Letters,* vol. 69, p. 2510, 1996.

[4] A. P. Ramsa, H. Jacobs, and F. A. Brand, "Microwave techniques in measurement of lifetime in germanium," *Journal of Applied Physics,* vol. 30, p. 1054, 1959.

[5] S. Rein, *Lifetime spectroscopy: a method of defect characterization in silicon for photovoltaic applications*: Springer Verlag, 2005.

[6] M. Schöfthaler and R. Brendel, "Sensitivity and transient response of microwave reflection measurements," *Journal of Applied Physics,* vol. 77, p. 3162, 1995.

[7] R. Brendel and M. wolf, "Differential and actual surface recombination velocity," in *13th EC PVSC*, Nice, France, 1995, p. 428.

[8] G. L. Miller, "Method and apparatus for the contactless monitoring carrier lifetime in semiconductor materials." vol. 4286215, U. S. Patent, Ed. USA: Bell Telephone Laboratories, Inc, 1981.

[9] R. M. S. D. E Kane, "Measurement of Emitter Saturation Current by a Contactless Photoconductivity Decay Method," in *Proc. 18th IEEE photovoltaics Specialist Conference*, 583 ed, 1985, pp. 578-583.

[10] T. Trupke, R. A. Bardos, F. Hudert, P. Würfel, J. Zhao, A. Wang, and M. A. Green, "Effective excess carrier lifetime exceeding 100 milliseconds in float zone silicon determined from photoluminescence," in *19th European Photovoltaic Solar Energy Conference*, Paris, France, 2004, p. 758.

[11] T. Roth, M. Rudiger, S. Diez, T. Trupke, R. A. Bardos, and S. W. Glunz, "Temperature and injection dependent photoluminescence lifetime spectroscopy," in *21st European photovoltaic solar energy conference* Dresden, Germany, 2006, p. 593.

[12] WWW.sintonconsulting.inc, 2009.

[13] J. Schmidt, "Temperature-and injection-dependent lifetime spectroscopy for the characterization of defect centers in semiconductors," *Applied Physics Letters,* vol. 82, p. 2178, 2003.

[14] S. Rein and S. W. Glunz, "Electronic properties of interstitial iron and iron-boron pairs determined by means of advanced lifetime spectroscopy," *Journal of Applied Physics,* vol. 98, p. 113711, 2005.

[15] www.instec.com/, 2009.

[16] N. D. Arora, J. R. Hauser, and D. J. Roulston, "Electron and hole mobilities in silicon as a function of concentration and temperature," *IEEE Transactions on Electron Devices,* vol. 29, pp. 292-295, 1982.

[17] J. M. Dorkel and P. Leturcq, "Carrier mobilities in silicon semi-empirically related to temperature, doping and injection level," *Solid-State Electron,* vol. 24, pp. 821–825, 1981.

[18] D. B. M. Klaassen, "A unified mobility model for device simulation--II. Temperature dependence of carrier mobility and lifetime," *Solid-state electronics,* vol. 35, pp. 961-967, 1992.

[19] D. B. M. Klaassen, "A unified mobility model for device simulation--I. Model equations and concentration dependence," *Solid-state electronics,* vol. 35, pp. 953-959, 1992.

[20] S. Reggiani, M. Valdinoci, L. Colalongo, M. Rudan, G. Baccarani, A. D. Stricker, F. Illien, N. Felber, W. Fichtner, and L. Zullino, "Electron and hole mobility in silicon at large operatingtemperatures. I. Bulk mobility," *IEEE Transactions on Electron Devices,* vol. 49, pp. 490-499, 2002.

[21] L. Elstner, "The temperature dependence of the defect electron mobility in silicon crystals " *Phys status solidi,* vol. 17, pp. 139-150, 1966.

[22] D. K. Schroder, *Semiconductor material and device characterization*: Wiley-interscience, 2006.

CHAPTER 4

Molybdenum in silicon

Molybdenum (Mo) is a transition metal and a potential source of contamination in silicon devices[1]. Mo remains in interstitial form within the lattice structure of silicon and creates an electrically active defect. Such defects act as recombination centres which reduce the lifetime of the generated carrier and hence the efficiency of the solar cells. Electrical properties of such defects are important for the study of performance and to optimize or design an efficient solar cell and other semiconductor devices.

A significant number of Mo atoms ($0.64 - 4.6 \times 10^{13}$ cm^{-3}) was measured by Istratov *et al.* [2] in commercially available multicrystalline silicon solar cells by neutron activation analysis (NAA) techniques in 2004. These cells were prepared by using sheet, cast and ribbon technology. Davis *et al.* [3, 4] presented the correlation between the concentration of various metallic impurities to the conversion efficiency of solar cells in his paper in 1980 as presented in Figures 1.1 and 1.2. The Mo concentration measured by Istratov *et al.* is sufficient to reduce the efficiency of solar cells by one third. Furthermore, Davis *et al.* reported that Mo is the second most effective impurity after Tantalum (Ta) for the reduction of the efficiency of silicon solar-cells.

Mo defects have a capture cross sections ratio in the range 13 – 28 at room temperature [1, 5, 6] and are ideal for testing the new approach of TIDLS proposed in Section 2.5 for determination of T-dependent carrier capture cross sections of Mo defects in silicon. Furthermore, this Chapter presents a novel approach to assess the defect energy level (E_t) of Mo defects in silicon from the measured $\sigma_n(T)$.

Section 4.1 discusses the Mo defect in silicon and its effects on device performance and summarises the previous work performed in determining the electrical properties of the Mo defect in silicon. Section 4.2 explains the details of the sample and the methodology for determination of $\sigma_n(T)$ and $\sigma_p(T)$. Section 4.3 presents the results of $\sigma_n(T)$ and $\sigma_p(T)$ of Mo defects in silicon and discusses a possible capture mechanism. Finally, Section 4.4 presents a novel procedure to assess E_t of a Mo defect by using the T-dependent trend of measured $\sigma_n(T)$.

4.1 Mo defects in silicon

Mo belongs to the 4d transition metal group in the periodic table. Even though the elements in the 4d group have low diffusivity, Mo atoms can diffuse into the silicon wafer during the expitaxial or plasma etching process [1]. Mo reacts strongly with oxygen by forming an oxide. Oxygen is excluded during the high temperature reduction process but Mo remains in the bulk. Thus Mo can be observed in an expitaxial wafer or in the processed wafer after plasma etching. The heat shield of the Cz pullers are another potential source of Mo contamination in Cz silicon as identified by Jester *et al.* [7]. It is believed that Mo neither appears in precipitate form nor forms pairs with other impurities [1]. Mo appears in the lattice of silicon and forms electrically active defects. Such defects reduce the lifetime of the generated carrier and hence reduce the conversion efficiency of solar cells.

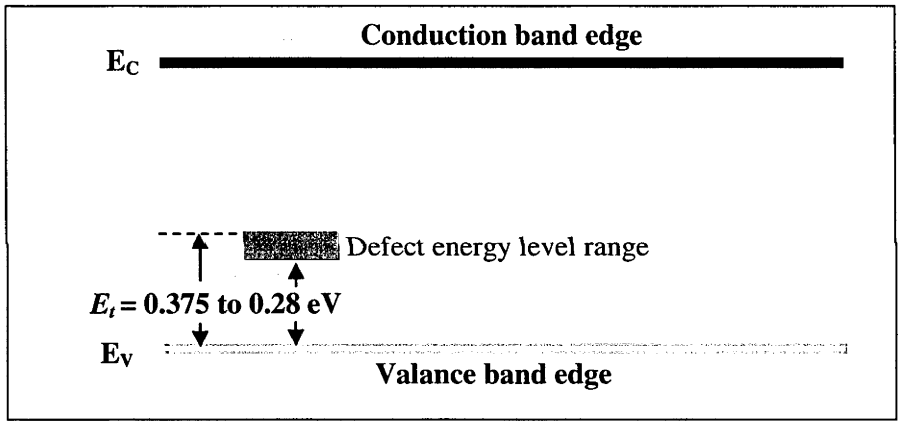

Figure 4.1: A band diagram of silicon depicting the defect energy level of Mo.

In 1995, Graff[1] summarised published information about the electrical properties of Mo in silicon, principally based on deep level transient spectroscopy (DLTS). Interstitial Mo was found to introduce a single defect energy level (E_t) that is donor-like and exists at 0.28 ± 0.01 eV above the valance band edge of silicon (E_V) with hole and electron capture cross sections $\sigma_p = 6.0 \times 10^{-16}$ cm^2 and $\sigma_n = 1.60 \times 10^{-14}$ cm^2 respectively. In addition to those studies, Rohatgi *et al.* [4] applied DLTS coupled with dark and illuminated I-V measurements and concluded the defect energy to be $E_t = E_V + 0.30$ eV. Hamaguchi *et al.* [8] applied DLTS and optical-DLTS to investigate the Mo-related defects in silicon and reported $E_t = E_V + 0.31$ eV. Similarly Pettersson *et al.* [9] applied Junction Space Charge Techniques (JSCT) and found $E_t = E_V + 0.298$ eV. More

recently, Rein *et al.*[5, 6] applied a combination of temperature and injection-dependent lifetime spectroscopy to determine $E_t = E_V + 0.317 \pm 0.05$ eV and the ratio of the capture cross sections $\sigma_n/\sigma_p = 13 \pm 3$. Furthermore, they concluded that both σ_p and σ_n have a dependence on temperature $T^{-1.5}$, where it was assumed that the temperature dependence of σ_n/σ_p was constant. Table 4.1 summarises these published results on the interstitial Mo defect in silicon. Figure 4.1 depicts the Mo defect in silicon in band a diagram.

Table 4.1: Reported results of the electronic properties of Mo related defects in silicon.

σ_n (cm^2)	σ_p (cm^2)	σ_n/σ_p (at 27 °C)	E_t (eV)	Reference and Technique
$4.21 \times 10^{-8} \times T^{-2.95}$	$7.60 \times 10^{-8} \times T^{-1.07}$	11 ± 2	$E_v + 0.375 \pm 0.04$	This work,
1.6×10^{-14} (at 27 °C)	6.0×10^{-16} (at 27 °C)	26.67	$E_v + 0.28$	[1], Average
NA	NA	NA	$E_v + 0.30$	[4], DLTS
NA	NA	NA	$E_v + 0.31$	[8], DLTS
NA	NA	NA	$E_v + 0.298$	[9], JSCT
7.8×10^{-15} (at 27 °C)	NA	13 ± 3	$E_v + 0.317$	[5, 6], TIDLS

4.2 Sample detail and methodology

A silicon ingot was grown with the pedestal growth technique and boron-doped with a resistivity of 1.8 Ω cm. The ingot was intentionally contaminated by adding 2800 ppma of Mo in the silicon melt [10]. A Mo concentration of 2×10^{13} cm^{-3} was determined by Neutron Activation Analysis (NAA) on the section of the ingot studied here, as described in detail elsewhere [10]. If all of the Mo atoms are interstitial and active, this gives an upper limit to N_t of 2×10^{13} cm^{-3}, however only a factor (f_{act}) of those Mo atoms act as recombination centers [1]. The experiment was performed on a silicon sample sliced from the ingot. The wafer was subjected to a phosphorus diffusion step, to remove unintended fast-diffusing impurities such as Fe, which may otherwise affect the lifetime. The diffused layers were then removed by chemical polishing, followed by cleaning and a Plasma-Enhanced Chemical Vapour Deposition (PECVD) process, an SiN_x layer optimised for surface passivation as described by Coletti *et al.* [11]. The average width of the sample was 285 microns.

Mo forms a donor level in the lower half of the silicon band gap. A boron-doped silicon with Mo impurity satisfies the conditions for the simplification of the SRH equation as

mentioned in Section 2.5.1, therefore Equation (2.61) is valid. Equation (2.61) requires E_t to calculate $p_1(T)$, however at very low temperatures, when thermal generation is negligible, i.e. $p_1(T) << p_0(T)$, Equation (2.61) is further simplified as

$$\tau_{SRH}(T) = \tau_{no}(T) + \frac{\tau_{po}(T)}{p_0(T)} \times \Delta n \tag{4.1}$$

Table 4.2: Temperature for which the assumptions $(n_1 + n_0) < 0.01 \times \Delta n$ and $p_1 < 0.01 \times p_0$ is valid for analysis.

E_t	$n_1(T) + n_0(T) << \Delta n$	$p_1(T) << p_0(T)$	References
E_V + 0.28 eV	$T \leq 160$ °C	$T \leq 0$ °C	Graff [1]
E_V + 0.30 eV	$T \leq 158$ °C	$T \leq 10$ °C	Rohatgi *et al.* [4]
E_V + 0.317 eV	$T \leq 155$ °C	$T \leq 18$ °C	Rein [5, 6]

At temperatures where Equation (4.1) is valid, the slope of a plot of τ_{SRH} against Δn gives τ_{p0}/p_0 and the intercept gives τ_{n0}. Hence σ_n and σ_p can be calculated using the measured slope and the intercept of a linear plot of τ_{SRH} against Δn for different temperatures by using Equation (2.20) and an effective capture mechanism can be inferred from the temperature dependence of $\sigma_n(T)$ and $\sigma_p(T)$ [12-14].

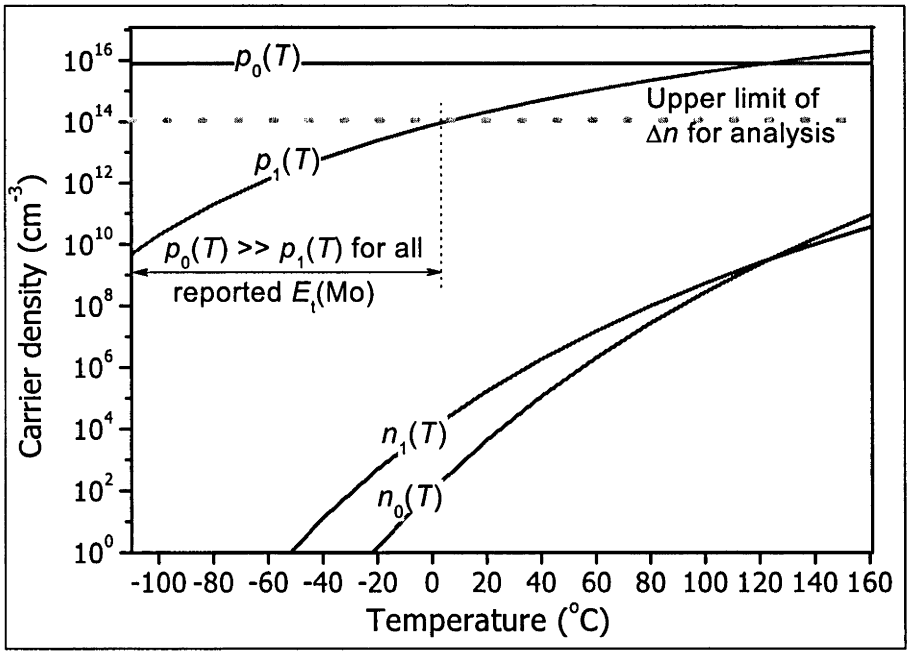

Figure 4.2: Carrier densities (n_1, p_1, n_0 and p_0) for $E_t = E_V + 0.28$ eV for Mo defect shows 0 °C as the most conservative temperature at which Equation (4.1) becomes valid.

When $\Delta n < 2.5 \times 10^{14}$ cm^{-3}, the above mentioned conditions of Equations (2.60) and (4.1) are satisfied. The carrier densities (n_1, p_1, n_0 and p_0) and Δn for the analysis are depicted in Figure 4.2 for the defect energy level of E_V + 0.28 eV in silicon. This graph shows $n_1 + n_0 << 1 \times 10^{14}$ cm^{-3} for temperatures less than 160 °C and $p_1 << p_0$ for temperatures less than 0 °C. Table 4.2 depicts the temperature ranges for which the assumption $(n_1 + n_0) << \Delta n$ and $p_1 << p_0$ is valid for different reported values of E_t, where we require the negligible value to be no more than 1% of the significant value. In this work, the most conservative upper limit of temperature is chosen for subsequent analysis.

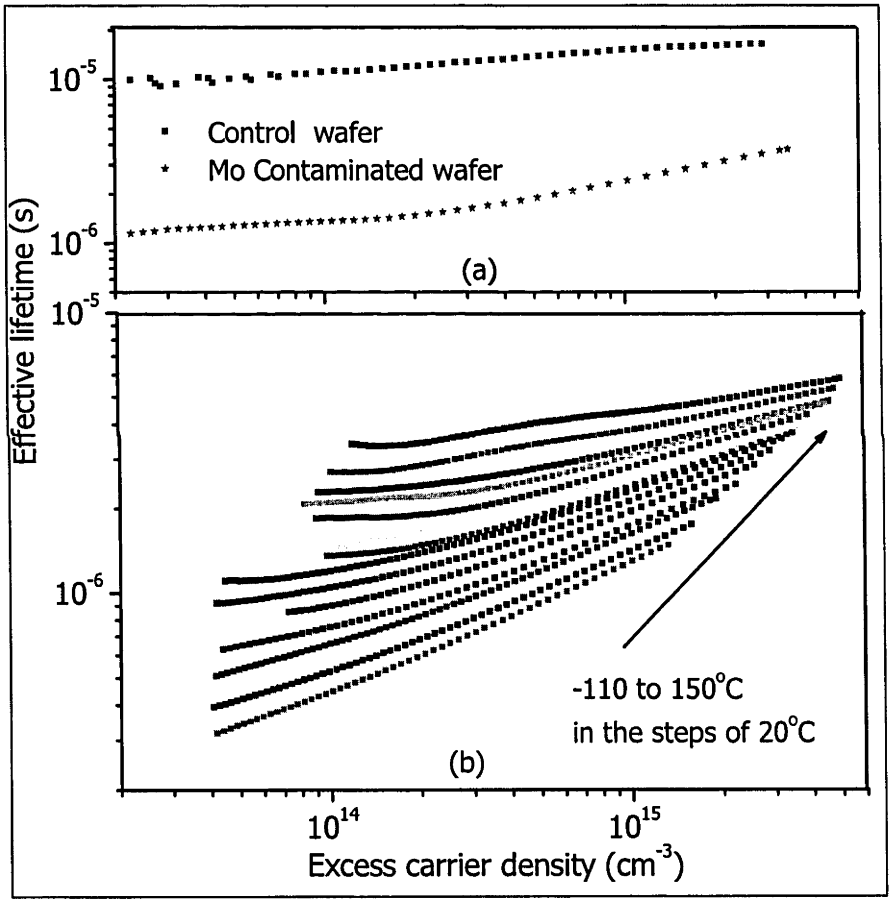

Figure 4.3: (a) Injection-dependent lifetime of Mo-contaminated and control wafers at room temperature. (b) Injection-dependent lifetime for temperatures -110 to 150 °C in intervals of 20 °C.

$n_0(T)$ was determined by using the doping density (N_A) and the T-dependent intrinsic carrier concentration, $n_i(T)$ [15]. Freeze-out of the boron atoms can be taken into account at low temperatures (< 77 °C) by adopting the T-dependent model of $p_0(T)$

suggested by Ashcroft and Mermin [16]. Table 4.2 presents (T_{low}) for different E_t for the selected sample. Taking the most conservative value (0 °C) as T_{low}, $\tau_{n0}(T)$ is determined for -110 to 0 °C only. $\tau_{p0}(T)$ is determined for the entire temperature range (-110 to 150 °C) as it can be calculated from the slope of the plot (τ_{SRH} Vs Δn) which is valid for any temperature in Equations (2.61) or (4.1). T-dependent models for v_{thn} and v_{thp} reported by Green *et al.* [15] were employed to calculate σ_n and σ_p using Equation (2.20).

Experimental

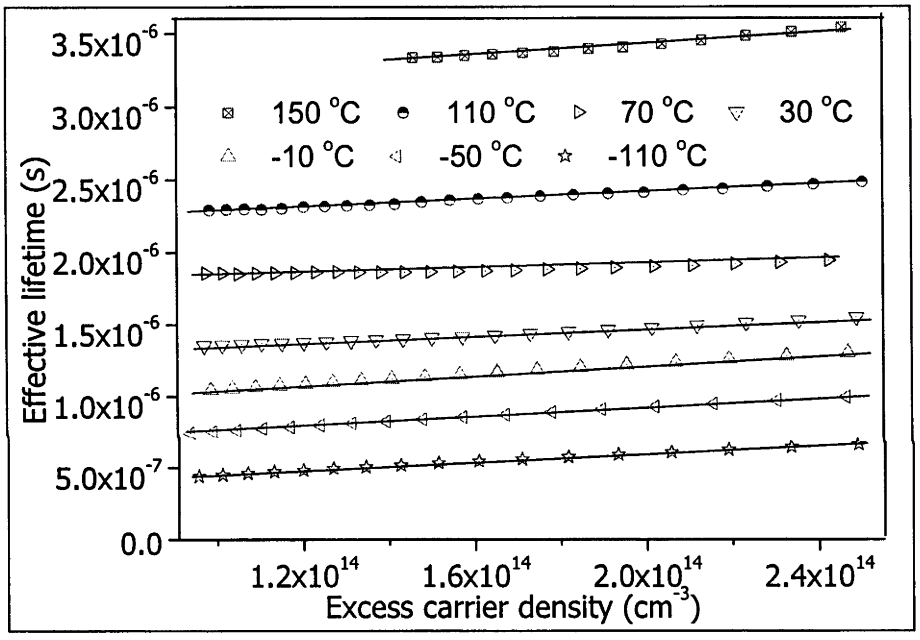

Figure 4.4: Lifetime plot and linear fit of Mo-doped (1.8 Ohm cm) wafer for the selected injection range (1×10^{14} - 2.0×10^{14} cm^{-3}).

Lifetime measurements were performed on a temperature controlled inductive coil photoconductance based instrument, described in Chapter 3. Figure 4.3 (a) depicts the injection-dependent lifetime data for a Mo-contaminated wafer and a control wafer at room temperature. The effective lifetime (τ_{eff}) in a Mo-contaminated wafer was found to be less by an order of magnitude than the control wafer, which ensures the Mo-defects are dominating recombination centres. Figure 4.3 (b) depicts the injection-dependent lifetime for temperatures -110 to 150 °C in intervals of 20 °C. Typical injection-dependent lifetime plots, from –110 to 150 °C in steps of 40 °C over the Δn range chosen for analysis, are depicted in Figure 4.4.

4.3 Capture cross sections of Mo in silicon

$\sigma_p(T)$ of Mo in silicon

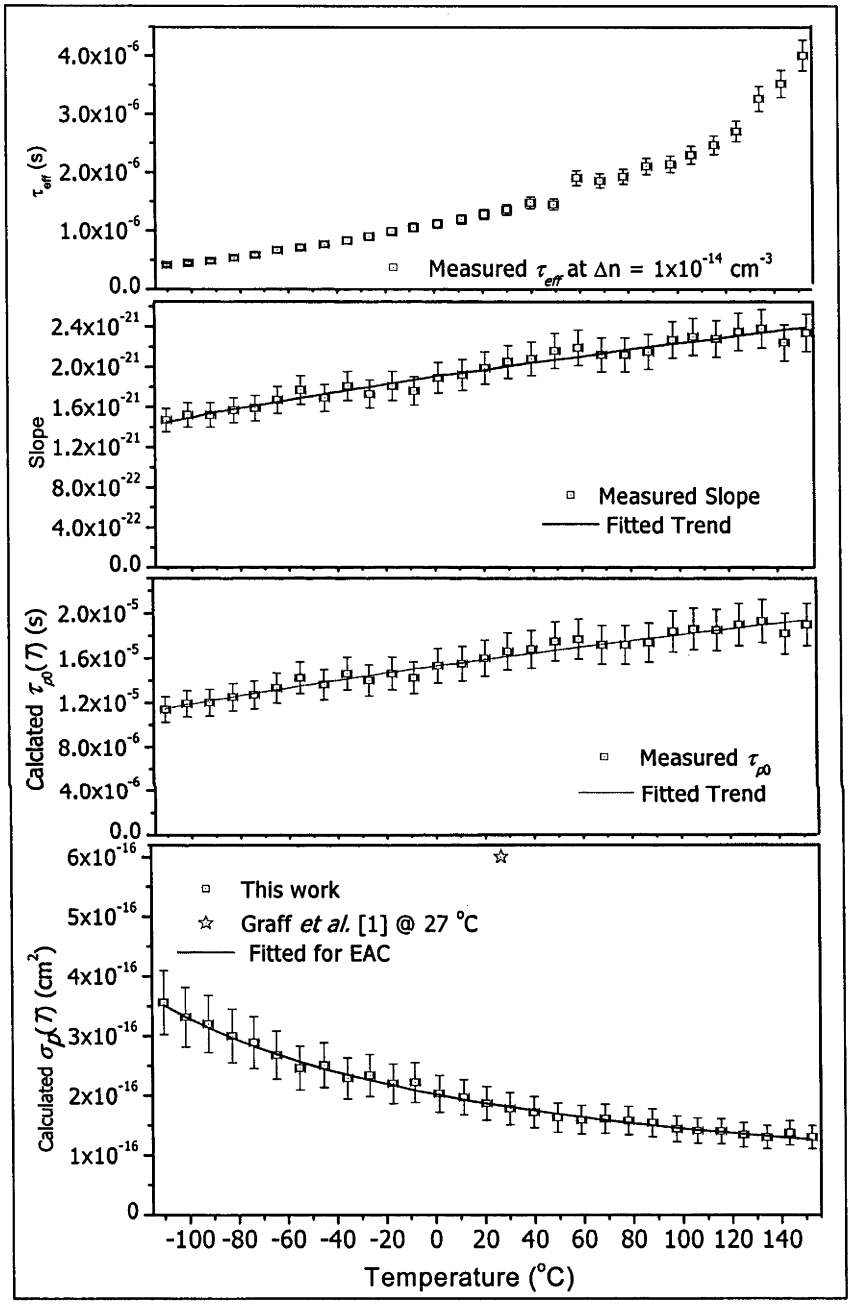

Figure 4.5: Measured τ_{eff} at $\Delta n = 1 \times 10^{-14}$cm^{-3}, slope of the plot (τ_{eff} Vs Δn over the range $1 - 2.5 \times 10^{14}$ cm^{-3}), calculated τ_{p0} and σ_p as a function of temperature(T).

The τ_{eff} of the test wafer at low level injection ($\Delta n < 2.2 \times 10^{14}$ cm^{-3}) was found to increase with temperature. Measured τ_{eff} at Δn 1×10^{14} cm^{-3} and the slope of the plot (τ_{eff}

Vs Δn for the range $1 - 2.5 \times 10^{14}$ cm^{-3}), calculated for τ_{p0} and σ_p when $f_{act} = 1$ over the temperature range –110 to 150 °C, is depicted in Figure 4.5. The measured value of σ_p decreases with temperature over the entire temperature range. This eliminates the possibility that hole capture occurs via multiphonon emission (MPE) in which σ_p increases with temperature [12]. We also rule out cascade capture as a possible capture mechanism because it is only relevant to shallow coulomb attractive defect centres [14]. This leaves excitonic Auger capture (EAC)[13] as the most likely mechanism for the capture of holes by the Mo defect.

The temperature dependence of σ under EAC is governed by the equation $\sigma = \sigma_0 T^{\alpha}$, where σ_0 and α are independent of temperature. The line in Figure 4.5 is a fit of this equation to the experimental data, where $\sigma_0 = 6.1 \pm 0.8 \times 10^{-14}$ cm^{-2} and $\alpha = -1.07 \pm 0.05$. The uncertainty in these values represents a 95% confidence interval from an error-weighted least-square fit to the experimental data.

The above calculation assumes 100% of the Mo atoms are electrically active, however this may not be valid if, for example, precipitation occurs [1]. In the case where only a fraction (f_{act}) of Mo atoms are electrically active, the temperature dependence of the hole capture cross section is therefore

$$\sigma_p(T) = \frac{1}{f_{act}}\left(6.05 \pm 0.8 \times 10^{-14}\right) T^{-(1.07 \pm 0.05)} \qquad (4.2)$$

Thus, σ_0 is inversely proportional to f_{act} while α is independent of f_{act}. If the fraction of electrically active impurities were $f_{act} = 0.3$, then σ_p becomes consistent with the DLTS value reported by Graff at room temperature [1]. We note that a fractional activation of Mo atoms does not alter the conclusion that EAC is the most likely capture mechanism of holes.

$\sigma_n(T)$ of Mo in silicon

The electron capture cross section $\sigma_n(T)$ was first determined for the temperature range -110 to 0 °C by implementing Equation (5), which does not require E_t. σ_n is also found to decrease monotonically and like σ_p, it can be best described by an EAC mechanism. The EAC fit of the measured σ_n gives

$$\sigma_n(T) = \frac{1}{f_{act}}\left(4.21 \pm 0.4 \times 10^{-8}\right) T^{-(2.95 \pm 0.02)} \tag{4.3}$$

Figure 4.6 depicts measured τ_{eff} at $\Delta n = 1 \times 10^{14}$ cm^{-3}, an intercept of the plot (τ_{eff} Vs Δn for the range 1 – 2.5 $\times 10^{14}$ cm^{-3}), calculated τ_{n0} and the calculated $\sigma_n(T)$ when $f_{act} = 1$ over the temperature range –110 to 150 °C. When $f_{act} = 0.3$, σ_n extrapolated to room temperature is consistent with Rein's value of σ_n/σ_p multiplied by Graff's value of σ_n, and when $f_{act} = 0.15$, σ_n is consistent with Graff's value of σ_n.

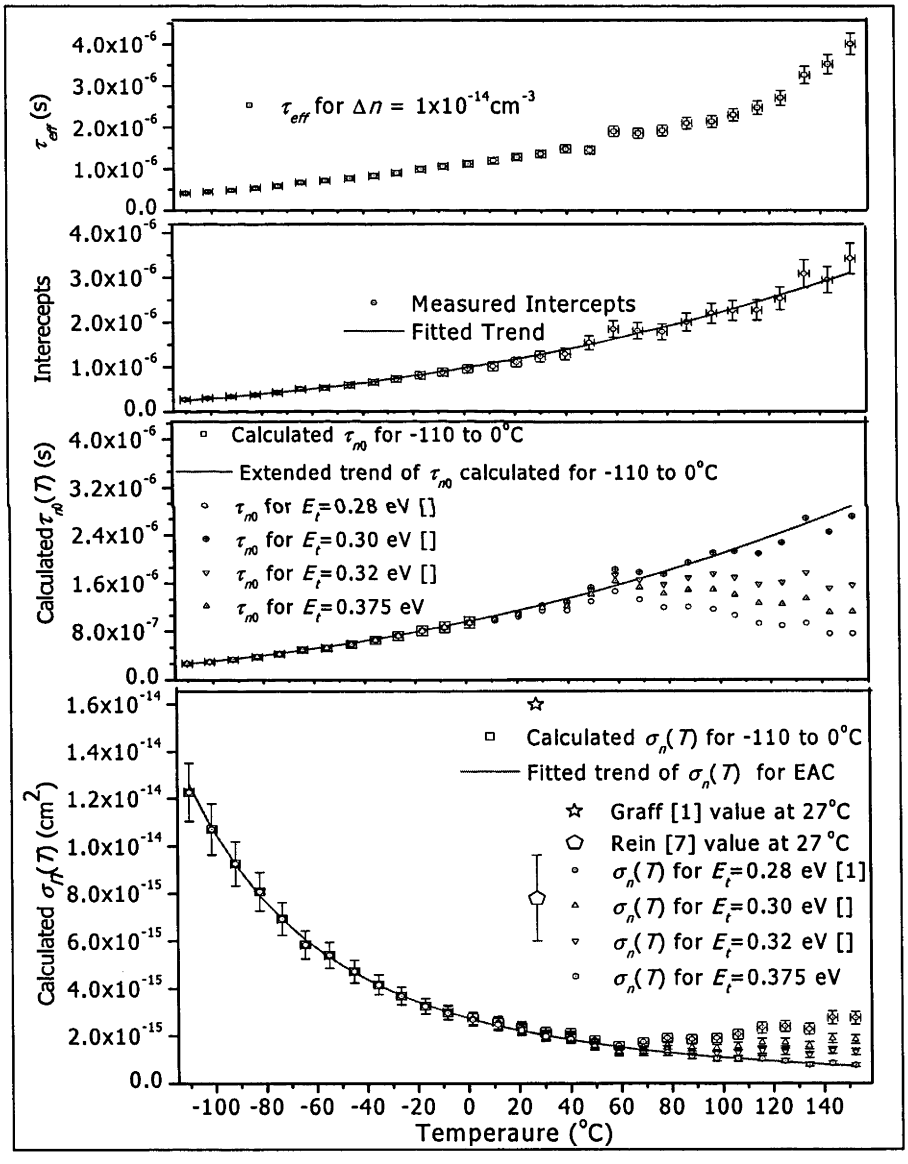

Figure 4.6: Electron capture cross section for Mo in silicon fitted with excitonic Auger capture mechanism and other previously published values at RT.

4.4 Assessing E_t of Mo in Silicon

The extended trend of $\sigma_n(T)$ determined above is then compared with the calculated $\sigma_n(T)$ for the temperate range 0 to 150 °C. $\sigma_n(T)$ for the temperature range 0 to 150 °C is calculated according to Equation (2.61) by using E_t reported by various researchers [1, 4, 5] to calculate $p_1(T)$ and $n_1(T)$. Figure 4.7 depicts the calculated $\sigma_n(T)$ for reported E_t and the best fit for EAC according to Equation (4.3). The corresponding E_t for the best fit $\sigma_n(T)$ is found as $E_V + 0.375 \pm 0.03$ eV which is deeper than the previously reported values [1, 4, 7].

The Mo defect has an effect comparable to the Tantalum (Ta) defect in reducing the efficiency of a silicon solar cell [3] and the efficiency of such a solar cell has a positive correlation with the carrier lifetime [17]. The carrier lifetime is a function of E_t and σ for a defect assisted recombination mechanism [18, 19]. Ta has $\sigma_n(-23\ ^\circ\text{C}) > 3.9 \times 10^{-15}$ cm^2 and $E_t = E_C - 0.58$ eV [1] for a donorlike defect in silicon. Since σ_n of Ta is comparable to Mo, a deeper E_t for Mo is expected than the reported values for a comparable recombination effect of Mo in silicon similar to Ta. Furthermore, an exponential rise in carriers' lifetimes, known as Arrhenius rise, should be observed in an injection-dependent lifetime plot of a silicon wafer at different temperatures (see Figure 4.3), at a low injection level at temperatures around 100 – 120 °C for $E_t < E_V + 0.35$ eV [5]. Figure 4.3 depicts a gradual rise rather than an Arrhenius rise of the carriers' lifetime for injection level $\Delta n \leq 1\times10^{14}$ cm^{-3} up to 150 °C which justifies a deeper E_t for Mo defect than those reported in the literature [1, 4, 5].

4.5 Capture cross section ratio

Figure 4.7 plots the ratio of the capture cross sections (σ_n/σ_p) over the temperature range, -110 to 150 °C. The symbols in Figure 4.7 plot the data assuming $E_t = E_v + 0.375$ eV, and the error bars combine the uncertainty in the measurement with the uncertainty in E_t. The figure shows that σ_n/σ_p decreases with temperature, even though both carriers are best described by the same capture mechanism (EAC). The data agrees well with the values reported by Rein *et al.*[5,6] at room temperature. The uncertainty due to any partial activation of Mo atoms in silicon (represented by f_{act} in Equations (4.2) and (4.3)) cancels in the calculation of σ_n/σ_p. However the uncertainty in

σ_n/σ_p increases at higher temperatures (> 0 °C) due to the uncertainty in σ_n associated with the uncertainty in E_t.

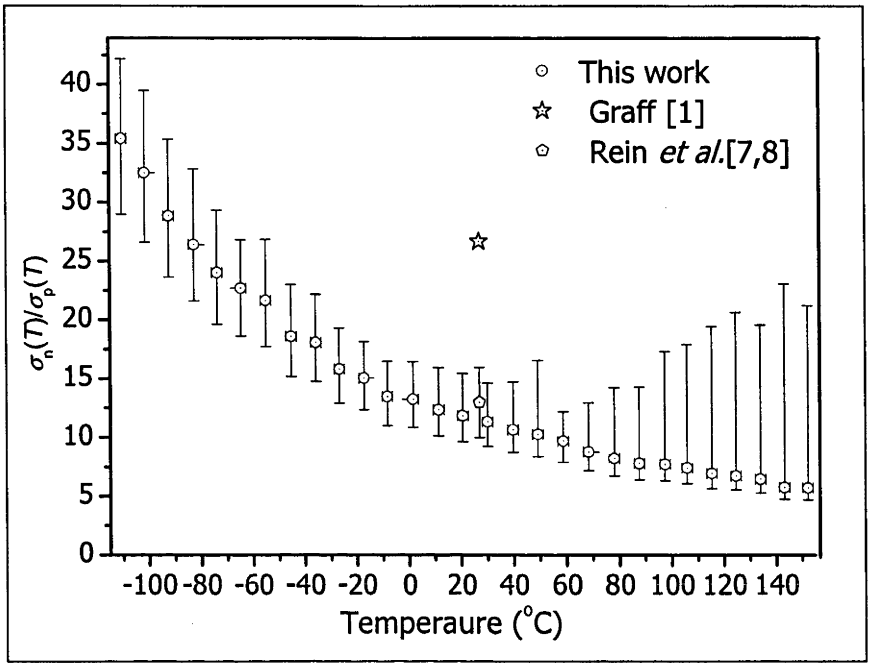

Figure 4.7: Capture cross section ratio of Mo defects in silicon at different temperatures.

4.6 Chapter summary

The T-dependent trend of σ_n and σ_p of Mo defects in silicon were determined by applying a new analysis procedure of SRH lifetime as mentioned in Chapter 2. T-dependent SRH lifetimes were measured by using the inductive coil technique mentioned in Chapter 3. T-dependent expressions for σ_n and σ_p of Mo in silicon were determined independently for the temperature range –110 to 150 °C. The T-dependent trends of both σ_n and σ_p are best represented by the excitonic Auger capture mechanism, giving the minimum values of the coefficients $\sigma_{0min} = 4.21 \pm 0.4 \times 10^{-8}$, $6.05 \pm 0.8 \times 10^{-14}$ cm^2 and the T-exponents α = 2.95±0.2 and 1.07±0.05. The energy level of an interstitial Mo defect in silicon is accessed as 0.375 ± 0.03 eV above the valance band of silicon, by considering a EAC as a only possible single capture mechanism for the temperature range mentioned above.

References

[1] K. Graff, *Metal impurities in silicon-device fabrication*: Springer-Verlag Berlin, 1995.

[2] A. A. Istratov, T. Buonassisi, R. J. McDonald, A. R. Smith, R. Schindler, J. A. Rand, J. P. Kalejs, and E. R. Weber, "Metal content of multicrystalline silicon for solar cells and its impact on minority carrier diffusion length," *Journal of applied physics,* vol. 94, p. 6552, 2003.

[3] J. R. Davis, A. Rohatgi, R. H. Hopkins, P. D. Blais, P. Rai-Choudhury, J. R. McCormick, and H. C. Mollenkopf, "Impurities in silicon solar cells," *IEEE Transactions on Electron Devices,* vol. 27, pp. 677-687, 1980.

[4] A. Rohatgi, R. H. Hopkins, J. R. Davis, R. B. Campbell, and H. C. Mollenkopf, "The impact of molybdenum on silicon and silicon solar cell performance," *Solid-State Electronics,* vol. 23, pp. 1185-1190, 1980.

[5] S. Rein, *Lifetime spectroscopy: a method of defect characterization in silicon for photovoltaic applications*: Springer Verlag, 2005.

[6] S. Rein, S. Diez, and S. W. Glunz, "Temperature-and injection-dependent lifetime spectroscopy (T-IDLS): Advanced analysis," in *Proc. 19 th EC PVSEC* Paris, France, 2004, pp. 219–22.

[7] T. Jester, "Molybdenum contamination during Cz crysteal growth: Heat shield, Discussion on R & D challenges n Si-PV," in *13th workshop on crystalline silicon solar cell materials and processes* Vali, Colorado, 2003.

[8] T. Hamaguchi and Y. Hayamizu, "Deep level associated with molybdenum in silicon," *Japanese Journal of Applied Physics,* vol. 30, pp. 1837-1839, 1991

[9] H. Pettersson, H. G. Grimmeiss, L. Tilly, K. Schmalz, K. Tittelbach, and H. Kerkow, "Electrical and optical properties of molybdenum and tungsten related defects in silicon," *Semiconductor Science and Technology,* vol. 6, pp. 237-242, 1991.

[10] G. Coletti, L. J. Geerligs, P. Manshanden, C. Swanson, S. Riepe, W. Warta, J. Arumughan, and R. Kopecek, "Impact of iron and molybdenum in mono and multicrystalline float-zone silicon solar cells," in *Solid State Phenomena* 2008, p. 15.

[11] G. Coletti, R. Kvande, V. D. Mihailetchi, L. J. Geerligs, L. Arnberg, and E. J. Øvrelid, "Effect of iron in silicon feedstock on p-and n-type multicrystalline silicon solar cells," *Journal of applied physics,* vol. 104, pp. 104913-104913, 2008.

[12] C. H. Henry and D. V. Lang, "Nonradiative capture and recombination by multiphonon emission in GaAs and GaP," *Physical Review B,* vol. 15, pp. 989-1016, 1977.

[13] A. Hangleiter, "Nonradiative recombination via deep impurity levels in semiconductors: The excitonic Auger mechanism," *Physical Review B,* vol. 37, pp. 2594-2604, 1988.

[14] M. Lax, "Cascade capture of electrons in solids," *Physical Review,* vol. 119, pp. 1502-1523, 1960

[15] M. A. Green, "Intrinsic concentration, effective densities of states, and effective mass in silicon," *Journal of applied physics,* vol. 67, p. 2944, 1990

[16] N. W. Ashcroft and N. D. Mermin, "Solid State Physics. 1976," *Saunders College, Philadelphia,* 1976.

[17] B. Ohnesorge, R. Weigand, G. Bacher, A. Forchel, W. Riedl, and F. H. Karg, "Minority-carrier lifetime and efficiency of Cu (In, Ga) Se solar cells," *Applied Physics Letters,* vol. 73, p. 1224, 1998.

[18] W. Shockley and W. T. Read, "Statistics of the recombinations of holes and electrons," *Physical Review,* vol. 87, pp. 835-842, 1952

[19] R. N. Hall, "Electron-hole recombination in germanium," *Physical Review,* vol. 87, pp. 387-387, 1952.

CHAPTER 5

Iron and iron-boron pairs in silicon

Iron (Fe) is a one of the common impurities in silicon solar cells. The dissolved Fe in silicon creates electrically active defect energy levels which act as recombination centres. The electrical properties of these defects are important for the study of the silicon solar cell and the optimization or of design an efficient solar cell. This Chapter discusses the different types of iron related defects and the measurement of their electrical properties.

Section 5.1 discusses Fe related defects in silicon and summaries the previously reported results of their electrical properties. Detail of samples and methodologies used to implement the novel TIDLS technique for the determination of the T-dependent values of carrier capture cross section of interstitial iron ($\sigma_n(Fe_i)$ and $\sigma_p(Fe_i)$) and iron-boron pairs ($\sigma_n(FeB)$ and $\sigma_p(FeB)$), is discussed in Section 4.2. Section 4.3 presents the results of T-dependent expressions for $\sigma_n(Fe_i)$, $\sigma_p(Fe_i)$, $\sigma_n(FeB)$ and $\sigma_p(FeB)$. This section also discusses the effective capture mechanism of Fei and FeB pairs in silicon.

5.1 Iron and its defects in silicon

Silicon can be contaminated by iron, (Fe), during the crystal growth and fabrication process. Fe is located at the middle of 3d transition metals, which indicates that it diffuses moderately within the silicon atoms at room temperature. The diffusivity of Fe increases rapidly above 100 °C [1] so Fe can be dissolved and forms electrically active defects even during annealing at low temperatures [2]. Once dissolved in silicon, Fe remains in either interstitial sites or in a precipitate form, but Fe in a substitutional form is not stable in silicon [3]. The precipitated Fe in silicon contributes to increased leakage currents and reduced breakdown resistance, which eventually reduces device performance [2]. Fe dissolved in interstitial lattice sites (Fe_i) of silicon is electrically active and affects recombination in silicon and reduces the performance of solar cells. Fe_i in silicon becomes electrically active and exhibits a donor energy level (Fei^+) in the lower half of the band gap.

In addition, Fe_i also has a double donor level (Fe_i^{++}) below the valance band of silicon which is not electrically active as it is outside the band gap of silicon.

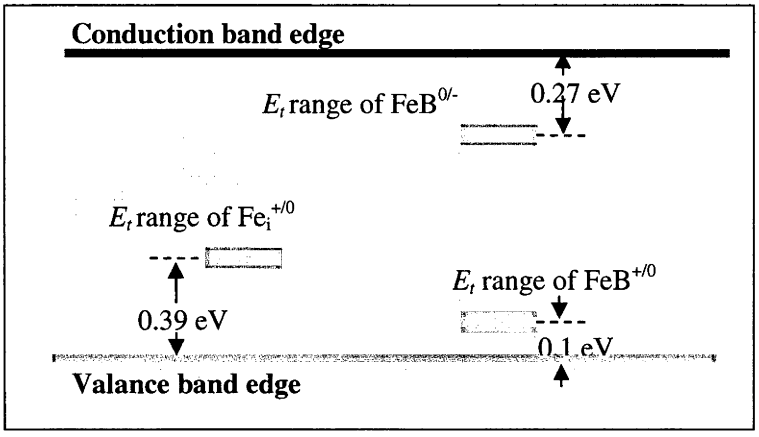

Figure 5.1: Energy level ranges of Fe-related defects in silicon depicting $E_t(Fe_i^{+/0})$, $E_t(FeB^{+/0})$ and $E_t(FeB^{0/-})$.

In *p*-type silicon positively charged Fe_i^+ and Fe_i^{++} is attracted toward negatively charged dopants by virtue of coulombic attraction and forms donor-acceptor pairs, like iron-boron (FeB), iron-aluminum (FeAl), iron gallium (FeGa) or iron-indium (FeIn) pairs, at room temperature (300 K). Fe can also form donor-acceptor pairs with gold in both *n* and *p*-type silicon, forming a donor and an acceptor level [2]. Among these possible donor-acceptor pairs in silicon, the FeB pair is most obvious for boron-doped silicon. Figure 5.1 depicts the E_t of Fe_i^+, Fe_i^{++}, FeB and FeB^+ with the band gap of silicon.

The defect energy E_t of the above mentioned defects has been measured and reported by researchers using different techniques and was found to be quite consistent. However, the reported values for their capture cross sections (σ_n and σ_p) and the dependence of σ_n and σ_p on temperature are inconsistent, as summarized in Table 5.1.

T-dependence of $\sigma_p(Fe_i)$ was first determined by Induskhar *et al.* [4] in 1966 using DLTS followed by Wunstel et al. [5] in 1982 and Brotherton *et al.* [6] in 1984. Their results demonstrated that multi-phonon emission (MPE) capture [7] to be an effective mechanism for hole capture with an activation energy *Ea* which varies from 0.040 to 0.048 eV and the T-independent pre-factor σ_∞ varying from 1.6×10^{-16} to 6.8×10^{-16}. On the other hand $\sigma_n(Fe_i)$ has not been studied as frequently as $\sigma_p(Fe_i)$ by many researchers. The first results

on $\sigma_n(Fe_i)$ at room temperature were published by Collins *et al.* [8] in 1957, followed by Zoth *et al.* [9] in 1990 and Lagowski *et al.* [10] in 1993. Their experiments were based upon surface photo-voltage (SPV) and the photo-dissociation technique and reported different values for $\sigma_n(Fe_i)$ at room temperature. Later, in 1999, Graff [2] presented a T-dependent expression for $\sigma_n(Fe_i)$ in his text by taking the average of reported results from different researchers. However the T-dependent expression presented by Graff [2] does not lead to the same σ_n(Fei) at room temperature published by Zoth *et al.* [9]. Wunstel et al. [5] applied DLTS for temperatures between 50 K and 65 K, followed by Gao *et al.*[11] at the temperature 55 K to measure σ_p(FeB) and published the result, in 1982 and 1991, respectively, neither investigated thermal activation. Lemke *et al.* [12] reported the values of σ_p(FeB) and σ_n(FeB) at 90 K applying DLTS. Later Zoth *et al.* [9] reported σ_n(FeB) at room temperature using DLTS with SPV techniques. Walz *et al.* [13, 14] reported σ_n(FeB) and σ_p(FeB) at room temperature using SPV and the ELYMAT technique. Birkholz *et al.* [15] applied the crossover point (CoP) technique with photoconductance measurements and devices, reporting σ_n(FeB) and σ_n(FeB) for FeB^-.

5.2 Sample details and methodology

Sample details

Boron-doped silicon samples with resistivities 0.6, 1.0, 5.5 and 13 Ω cm are used. The average widths of the samples were 250, 490, 199 and 445 microns respectively. Those samples had been intentionally contaminated with Fe by ion implantation with an implant dose of 1×10^{11} cm^{-2}. After implantation the sample was annealed at 900 °C for one hour in order to obtain uniform distribution of Fe throughout the bulk. The dose is then divided by the width of the wafer to calculate the Fe concentration (N_t) within the bulk. Fe concentration is below the solubility limit of Fe at 900 °C, so that there should be very few Fe atoms in precipitate form. Furthermore, the sample was coated with Plasma-Enhanced Chemical Vapour Deposition (PECVD) SiN_x in order to ensure that the surface recombination was negligible relative to the bulk recombination [16]. Fe atoms also appear in the form of FeB pairs at low temperatures and the fraction of Fe atoms in the form Fe_i and FeB is unknown. The TIDLS procedure to determine $\sigma_p(T)$ and $\sigma_n(T)$ is slightly modified and is presented below.

Table 5.1 Reported results of the electronic properties of Fe related defects in silicon

σ_p (*Fei*)	σ_n (*Fei*)	σ_p (*FeB*)	σ_n (*FeB*)	**Ref and Technique**
$4.54\times10^{-16}\exp(-0.05/k_BT)$	$3.47\times10^{-11}\times T^{-1.48}$	$3.32\times10^{-11}\exp(-0.262/k_BT)$	$5.1\times10^{-9}\times T^{-2.5}$	This work, TIDLS
$6.8\times10^{-16}\exp(-0.04/k_BT)$	----------	----------	----------	[4], TSCAP & DLTS
$5.6\times10^{-16}\exp(-0.048/k_BT)$	----------	----------	----------	[6], DLTS
$1.6\times10^{-16}\exp(-0.043/k_BT)$	----------	----------	----------	[5], DLTS & Hall
$2.8\times10^{-16}\exp(-0.043/k_BT)$	$10^{-10}\times T^{-1.5}$	2.0×10^{-15} at 400 K	1.6×10^{-15}	[1], Average of [6, 9, 11]
$3.9\times10^{-16}\exp(-0.045/k_BT)$	4×10^{-14}	3×10^{-14}	2.5×10^{-14}	[2], Average of[4-6]
----------	----------	5.4×10^{-15} at 90K	1.8×10^{-15} at 90K	[11], DLTS
----------	----------	3×10^{-14}	2.5×10^{-15}	[12] SPV & ELYMAT
----------	----------	1.1×10^{-15}	1.4×10^{-14}	[13], CoP & TIDLS
----------	3.6×10^{-15}	5.5×10^{-15}	2.5×10^{-15}	[14], TIDLS
----------	----------	3×10^{-15}	5×10^{-14}	[15], CoP & IDLS
----------	$\geq 1.5\times10^{-15}$	----------	----------	[8], Hall and Lifetime
----------	2.6×10^{-14}	----------	4×10^{-13}	[9, 10], SPV
*Reported values are for room temperature (300 K) unless otherwise specified				

Methodology for determination of $\sigma_n(Fe_i)$ and $\sigma_p(Fe_i)$

FeB pairs form in boron-doped silicon due to coulombic attraction between a positively charged interstitial Fe (Fe_i^+) and a negatively charged boron atom (B^-). Such a coulombic bond can be broken by the external supply of optical, thermal or electrical energy which dissociates the FeB pairs back to isolated Fe_i^+ and B^- atoms. The temperature at which complete thermal dissociation (T_{CTD}) of FeB pairs occurs is dependent upon the boron (N_A) and Fe concentration in silicon. Figure 5.2 depicts the Arrhenius plot of a boron-doped Fe-contaminated 1.0 Ω cm wafer at $\Delta n = 5 \times 10^{13}$ cm^{-3}, which illustrates T_{CTD} at 235 °C and the effects of Fe_i and FeB on the carrier lifetime. Hence the analysis of effective lifetime measurements at temperatures higher than T_{CTD} gives parameters for Fe_i defects only. $\tau_{n0}(T)$ and $\tau_{p0}(T)$ of Fe_i can be determined by using Equation (2.61) where $p_1(T)$ can be determined by using a known, $E_t = 0.39$ eV [2], from DLTS, by using the model reported by Green *et al.* [17] and $p_0(T)$ from the doping density. $\sigma_n(T)$ and $\sigma_p(T)$ can be calculated from $\tau_{n0}(T)$ and $\tau_{p0}(T)$ respectively by using Equation (2.20) where $v_{thn}(T)$ and $v_{thp}(T)$ can be determined by using a model reported by Green *et al.* [17] and N_t can be determined calculated dividing implant dose by the wafer thickness (W).

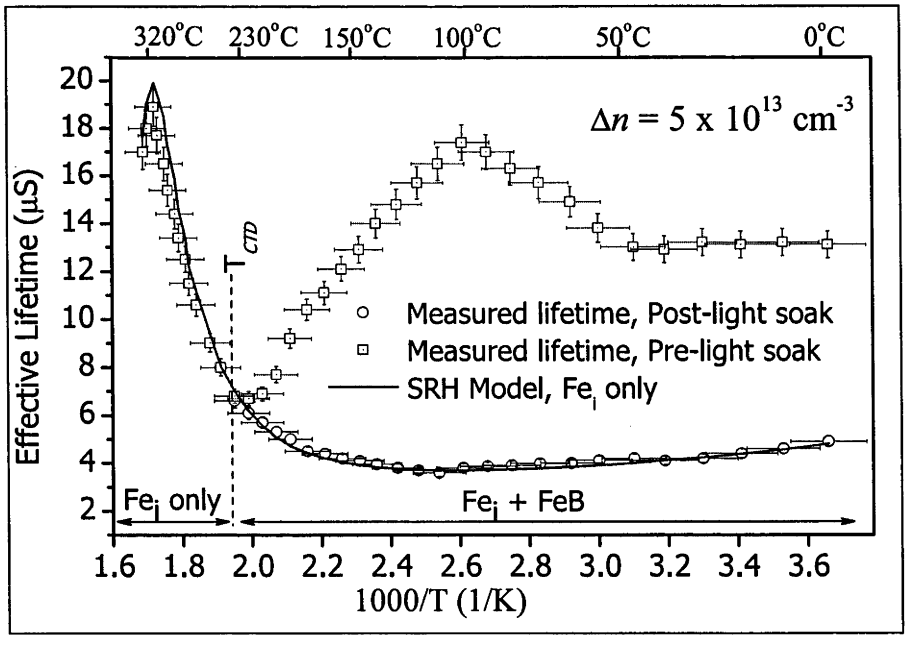

Figure 5.2: Arrhenius plot of 1.0 Ω cm depicting the complete thermal dissociation temperature (T_{CTD}) for FeB pairs at 235 °C and the effect of Fe_i and FeB in silicon.

Methodology for determination of $\sigma_n(FeB)$ and $\sigma_p(FeB)$

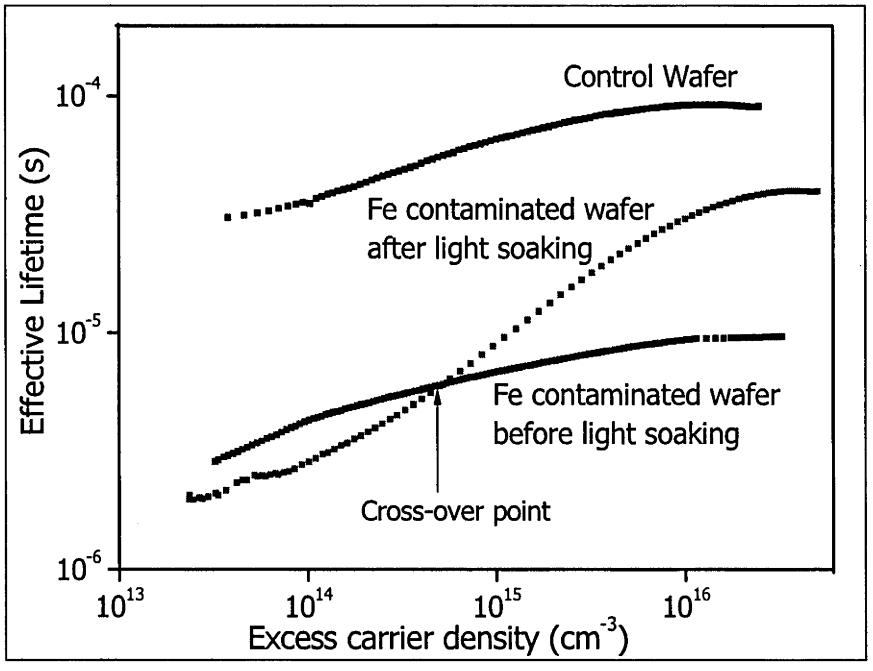

Figure 5.3: Effective lifetime measured for a 1.0 Ω cm sample at 50 °C, depicting the differences in recombination lifetime of an Fe-contaminated wafer with control wafer and cross-over point.

Fe can be present in the form of an Fe_i or FeB defect below T_{CTD}. The concentration of Fe_i or FeB can be altered in boron-doped silicon by dissociating FeB pairs. Despite variations in the density of Fei and FeB, the effective lifetime remains unchanged at a particular excess carrier density known as the characteristic crossover point (CoP) [15, 18]. CoP is depicted in Figure 5.3 for a 1.0 Ω cm wafer at 50 °C. The CoP carrier density (Δn_{CoP}) is independent with a degree of dissociation of FeB pairs and only depends upon the temperature and N_A. Hence at CoP, if we only consider the Shockley-Read-Hall recombination [19, 20], the lifetime (τ_{CoP}) at Δn_{CoP} can be simplified as

$$\frac{1}{\tau_{COP}} = \frac{1}{\tau_{associated}} = \frac{1}{\tau_{dissociated}} = \frac{1}{\tau_{SRH,as(FeB)}} + \frac{1}{\tau_{SRH,as(Fei)}} = \frac{1}{\tau_{SRH,dis(FeB)}} + \frac{1}{\tau_{SRH,dis(Fei)}} \quad (5.1)$$

where τ_{as} denotes the associated and τ_{dis} denotes the dissociated lifetime at the crossover point. Birkholz *et al* [15] solved Equation (5.1) for Δn_{COP} for p-type boron-doped

silicon when $n_1(Fe_i)$, $p_1(Fe_i)$, $p_1(FeB)$ and n_0 can be neglected in comparison to p_0, giving

$$\Delta n_{COP} = \frac{\sigma_n^{-1}(FeB) - \sigma_n^{-1}(Fe_i)}{\sigma_p^{-1}(Fe_i)} p_0 + \frac{\sigma_p(Fe_i)}{\sigma_p(FeB)} N_C \exp\left(-\frac{E_c - E(FeB)}{kT}\right) \quad (5.2)$$

Therefore, from the slope and intercepts of the linear plot of Δn_{COP} versus p_0 at different temperatures, and with the values of $\sigma_n(Fe_i)$, $\sigma_p(Fe_i)$, N_C, and $E_t(FeB)$, T-dependent values for $\sigma_n(FeB)$ and $\sigma_p(FeB)$ can be determined. Figure 5.4 shows a linear plot of Δn_{COP} versus p_0, according to Equation (5.2) for different temperatures where the slopes and intercepts are functions of $\sigma_n(FeB)$ and $\sigma_p(FeB)$.

Experimental details

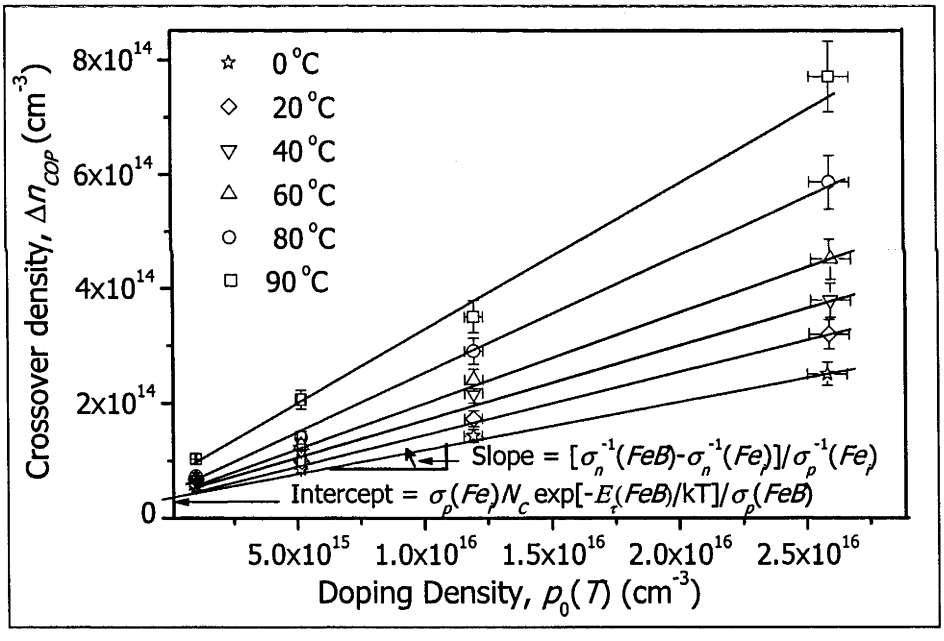

Figure 5.4: Linear plot of Δn_{COP} versus p_0 depicting slope and intercepts as a function of $\sigma_n(FeB)$ and $\sigma_p(FeB)$.

Lifetime measurements were performed on a temperature controlled inductive coil PC based device, described in Chapter 3. T_{CTD} of the sample was achieved by heating the sample (1.0 Ω cm) above 235 °C, which ensures the complete domination of Fe_i defects on the overall recombination process as illustrated in Figure 5.2. Injection-dependent lifetime time measurements for the temperature range 240 to 320 °C were taken and

analyzed according to the procedure proposed in Section 2.5.1 for the determination of $\sigma_n(Fe_i)$ and $\sigma_p(Fe_i)$. The upper limit of the temperature is taken as 320 °C, as intrinsic conduction begins in the sample above this temperature.

A light soaking technique was applied for a partial dissociation of FeB pairs in all four samples in order to determine Δn_{CoP} for different temperatures. Lifetime measurements were taken before (τ_{as}) and after (τ_{dis}) the light soaking for each temperature. Samples were illuminated by a 25 W halogen lamp for two minutes in the T-controlled stage of the PC measurement device for light soaking. All samples were kept in the dark for two hours before taking the next measurement in order to repair a significant fraction of the FeB pairs broken by the light soaking.

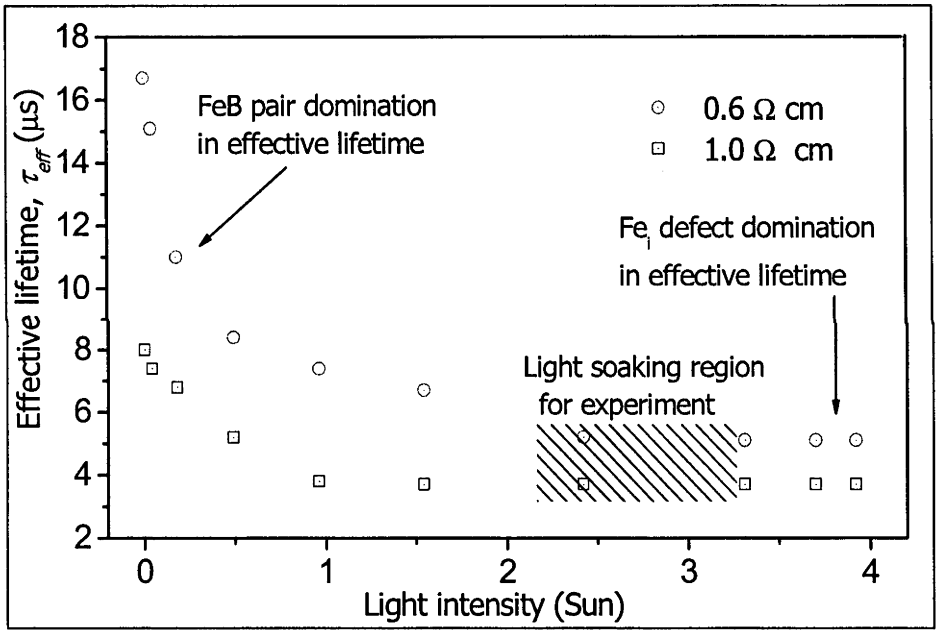

Figure 5.5: Effective lifetime measured after light soaking for 2 minutes on 0.6 and 1.0 Ω cm, B-doped, Fe-contaminated wafers with different light intensities.

The experiment was repeated from 0 to 90 °C at 10 °C steps for all samples. 90 °C is selected as the upper limit for CoP analysis in order to satisfy the condition $n_1(Fe_i)$, $p_1(Fe_i)$, p_1(FeB) and $n_0(T) << p_0(T)$ for all samples under test. Figure 5.5 depicts lifetime measured after light soaking for 2 minutes on 0.6 and 1.0 Ω cm, boron-doped, iron-contaminated wafers with different light soaking intensities. Lifetimes were measured for excess carrier density $\Delta n < \Delta n_{COP}$.

5.3 Capture cross sections of Fe_i

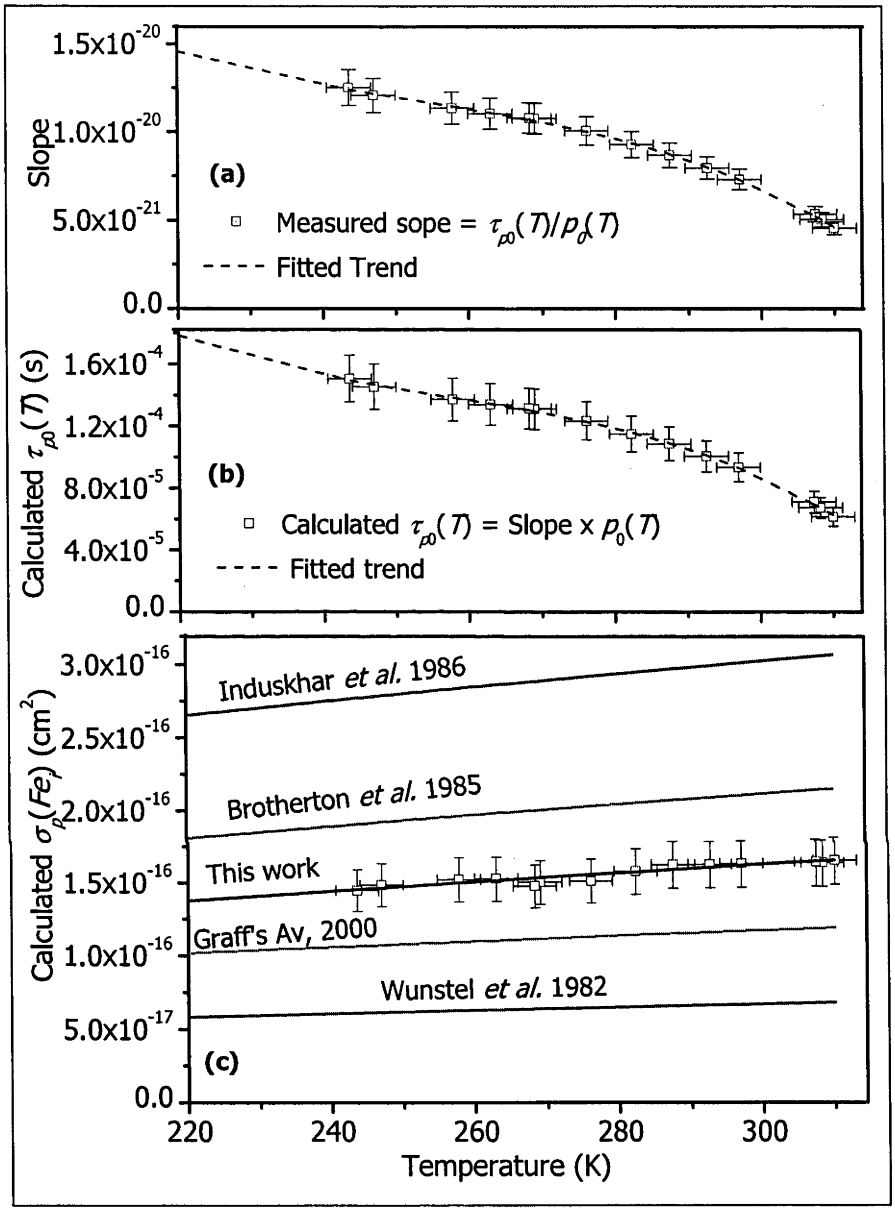

Figure 5.6: Measured slope of the plot τ_{eff} vs Δn (a), calculated $\tau_{p0}(T)$ (b) and calculated $\sigma_p(T)$ with previously reported model (c) of Fe_i defects in silicon for the temperature range 240 to 310 °C.

Figure 5.6 (a) depicts the measured slope, (b) depicts calculated τ_{p0} and (c) depicts calculated $\sigma_p(Fe_i)$ for the temperature range 240 – 310 °C. $\sigma_p(Fe_i)$ found increase with temperature which suggests that MPE is the only effective capture mechanism, consistent with previously reported capture mechanisms [1, 2, 4-6]. However, we find

different values for the activation energy (E_a) of 0.05 ± 0.006 eV and that the T-independent pre-factor (σ_∞) is equal to $4.54 \pm 0.5 \times 10^{-16}$ cm^2. The errors for the results in this work are estimated from the best-fit of the measured data to the equation of the reported capture mechanisms [7, 21, 22]. The MPE capture expression obtained in this work is extended to 220 °C and shown in Figure 5.6 along with expressions reported by others. Where

$$\sigma_{p(Fe_i)} = 4.54 \times 10^{-16} \exp\left(-\frac{0.05}{k_B T}\right) \tag{5.3}$$

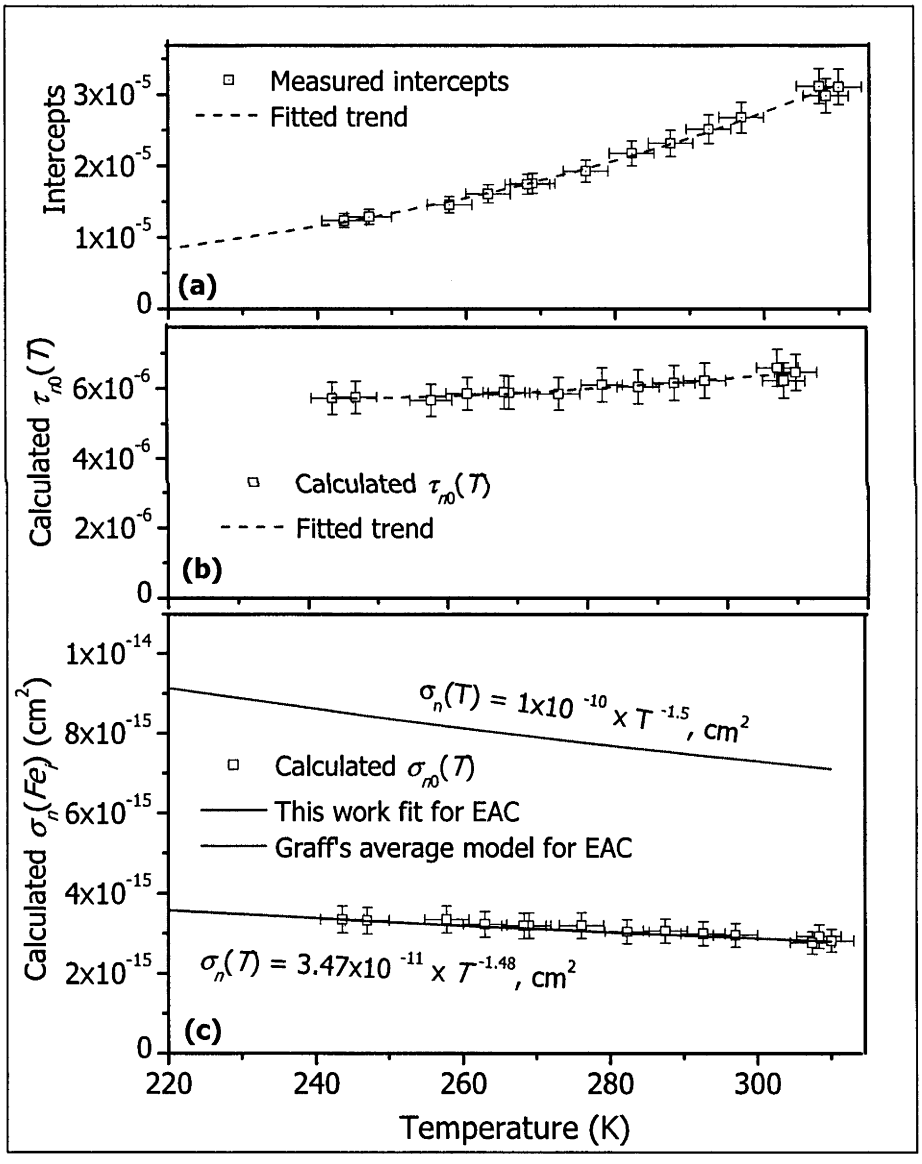

Figure 5.7: Measured intercepts of the plot τ_{eff} vs Δn (a), calculated $\tau_{n0}(T)$ (b) and calculated $\sigma_n(T)$ with previously reported models (c) of Fe_i defects in silicon for the temperature range 240 to 310 °C.

Similarly, Figure 5.7 (a) depicts the measured intercepts, (b) depicts calculated τ_{n0} and (c) depicts calculated $\sigma_p(Fe_i)$ for the temperature range 240 – 320 °C. The measured T-dependent data for $\sigma_n(Fe_i)$ over the temperature range 240 – 320 °C is found to decrease with temperature. Hence the MPE capture mechanism can be ruled out. Instead, the data shows a better fit to the negative power relation to temperature, consistent with the capture mechanism being either cascade capture [21] or excitonic Auger (EA) capture [22]. As the defect level of Fe_i is treated as deep, cascade capture is unlikely in this case. Hence we fitted the measured data for $\sigma_n(Fe_i)$ for the EA capture mechanism to give the T-independent pre-factor, $\sigma_0 = 3.47 \pm 0.5 \times 10^{-11}$ and the correlation exponent, $\alpha = 1.48 \pm 0.02$. A T-dependent expression for $\sigma_n(Fe_i)$ has rarely been reported compared to $\sigma_p(Fe_i)$. Graff [2] reported a T-dependent expression for $\sigma_n(Fe_i)$ by taking average values from various work [6, 9, 12]. Figure 5.7 shows that the expression for $\sigma_n(Fe_i)$ obtained by this work is extended to 220 – 320 °C along with other previously reported values for $\sigma_n(Fe_i)$ at room temperature.

$$\sigma_{n(Fe_i)} = 3.47 \times 10^{-11} \times T^{-1.48} \tag{5.4}$$

5.4 Capture cross sections of FeB

$\sigma_p(FeB)$ and $\sigma_n(FeB)$ are calculated on the basis of T-dependent expressions determined earlier for $\sigma_n(Fei)$ and $\sigma_p(Fei)$ and using the measured slope and intercepts of the linear plot of Δn_{CoP} versus doping density (p_0) for the temperature range 0 – 90 °C. Measured $\sigma_p(FeB)$ was found to increase with temperature over the temperature range 0 – 90 °C and the measured data is comparable with reported data by Brikholz *et al.* [15], however it is less than the values reported by Macdonald *et al.* [23] and Rein *et al.* [24] at room temperature as depicted in Figure 5.8. The T-dependent trend of $\sigma_p(FeB)$ is increasing with temperature. Hence the only possible capture mechanism is MPE capture as shown in Equation (5.5), where $E_a = 0.262 \pm 0.012$ eV and $\sigma_\infty = 3.32 \pm 1.22 \times 10^{11}$ cm^2. Table 5.1 shows the reported values and expressions for $\sigma_p(FeB)$ and $\sigma_n(FeB)$.

$$\sigma_{p(FeB)} = 3.32 \times 10^{-10} \exp\left(-\frac{0.262}{k_B T}\right) \tag{5.5}$$

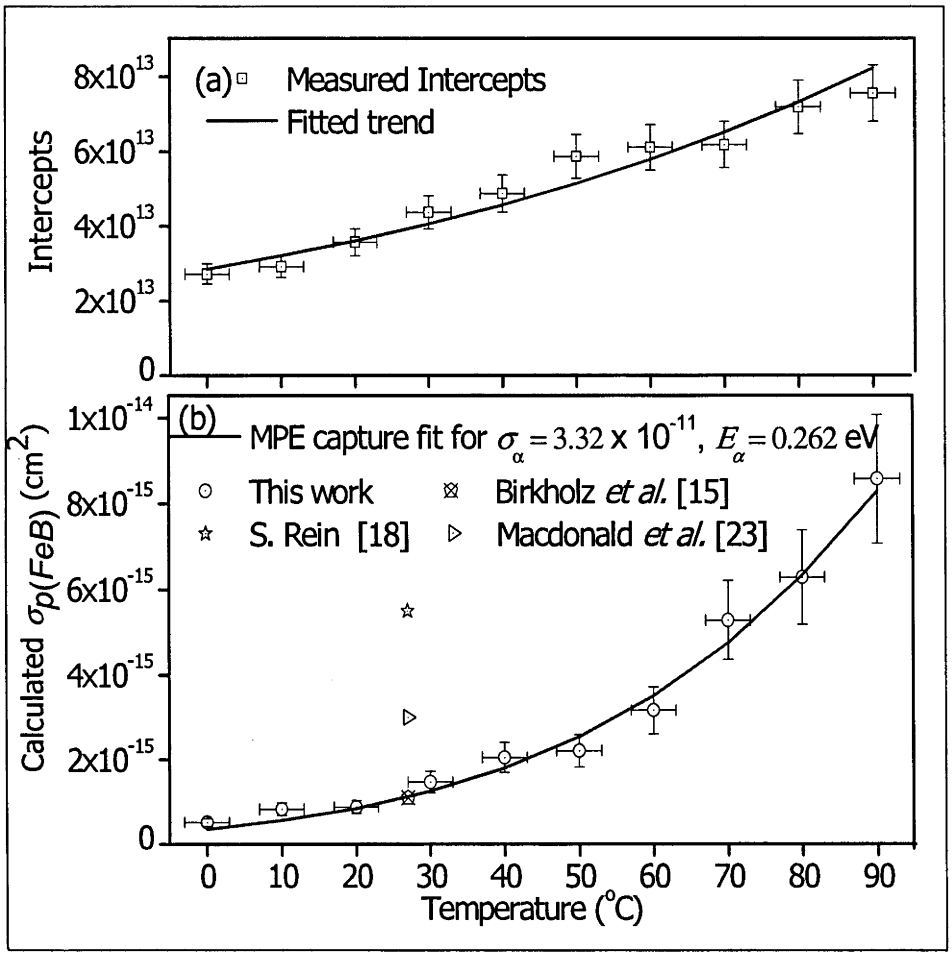

Figure 5.8: (a) Measured intercepts (b) calculated $\sigma_p(T)$ of FeB pairs for 0 – 90 °C with multi-phonon emission capture model fit.

Measured $\sigma_n(FeB)$ was found to decrease with increase in temperature and was comparable to the values reported by Macdonald *et al.* [23] and Rein *et al.* [24] at room temperature. The T-dependent trend of $\sigma_n(FeB)$ resembles the T-dependent trend of $\sigma_n(Fe_i)$ and shows a better fit to the excitonic Auger capture mechanism due to deep centers [22]. Figure 5.9 depicts the plot of excitonic Auger capture with the T-independent pre-factor, $\sigma_0 = 5.1 \pm 1.3 \times 10^{-9}$ and the correlation exponent, $\alpha = 2.5 \pm 0.05$ as

$$\sigma_{n(FeB)} = 5.1 \times 10^{-9} T^{-2.5} \qquad (5.6)$$

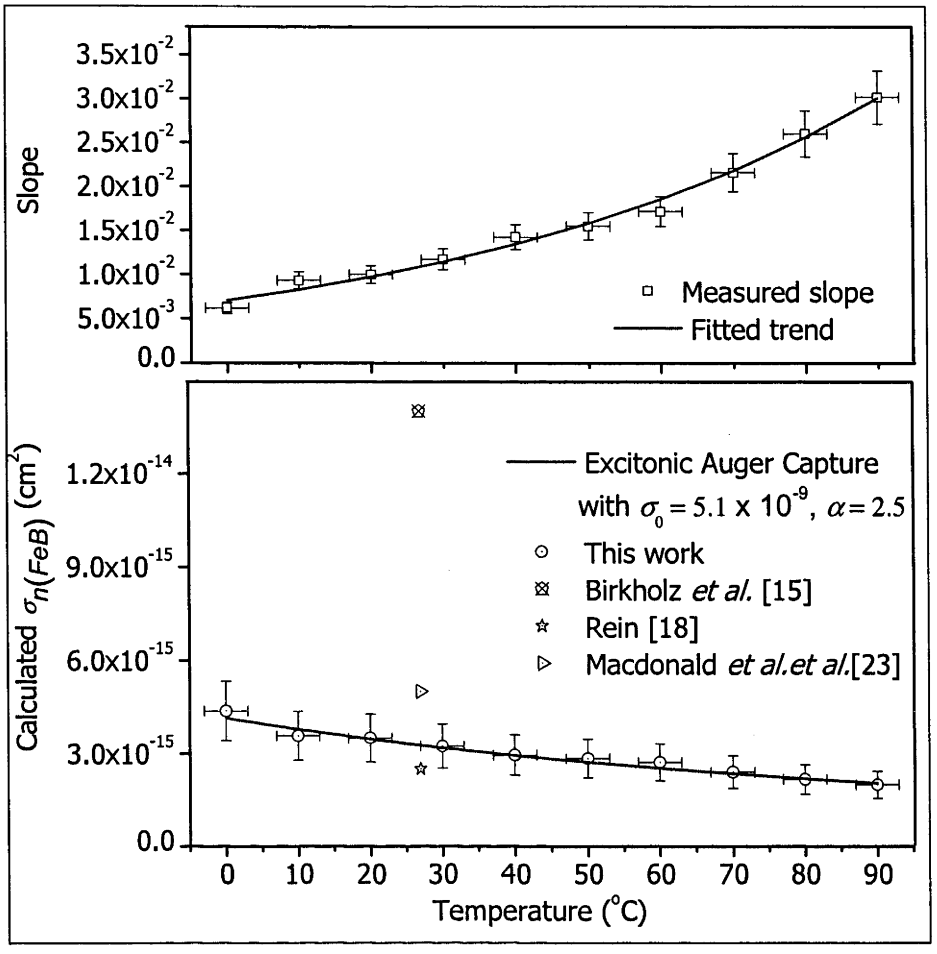

Figure 5.9: Electron capture cross-section of FeB pairs for 0 – 90 °C, measured data and excitonic Auger capture model fit.

5.5 Chapter summary

T-dependent expressions for $\sigma_p(Fe_i)$ and $\sigma_n(Fe_i)$ in crystalline silicon have been measured using a T-controlled PC measurement device and a novel approach in TIDLS. The most likely capture mechanisms for both types of defects are discussed. Measured T-dependent $\sigma_p(Fe_i)$ and $\sigma_n(Fe_i)$ are consistent with previously reported values and expressions through a relatively complex technique (DLTS).

A T-dependent expression for $\sigma_p(FeB)$ and $\sigma_n(FeB)$ had not been reported before, however, the measured value at room temperature shows consistency with reported values. This investigation of a T-dependent expression for $\sigma_p(FeB)$ and $\sigma_n(FeB)$ using lifetime spectroscopy is believed to fill this gap in our knowledge of defect properties of the FeB pair in silicon.

References

[1] A. A. Istratov, H. Hieslmair, and E. R. Weber, "Iron and its complexes in silicon," *Appl Phy A: Mat. Sci & Pro,* vol. 69, pp. 13-44, 1999

[2] K. Graff, *Metal Impurities in Silicon-Device Fabrication*, Second ed. vol. 24. Berlin: Springer, 1999.

[3] F. Beeler, O. K. Andersen, and M. Scheffler, "Theoretical Evidence for Low-Spin Ground States of Early Interstitial and Late Substitutional 3d Transition-Metal Ions in Silicon," *Physical Review Letters,* vol. 55, p. 1498, 1985

[4] H. Indusekhar and V. Kumar, "Properties of iron related quenched-in levels in p-silicon," *Physica status solidi (a),* vol. 95, pp. 269 - 278, 1986

[5] K. Wunstel and P. Wagner, "Interstitial Iron and Iron-Acceptor Pairs in Silicon," *Appl. Phys. A: Mat. Sci. & Pro.,* vol. 27, p. 207, 1982

[6] S. D. Brotherton, P. Bradley, and A. Gill, "Iron and the iron-boron complex in silicon," *JAP,* vol. 57, pp. 1941-1943, 1985.

[7] C. H. Henry and D. V. Lang, "Nonradiative capture and recombination by multiphonon emission in GaAs and GaP," *Phy. Rev. B,* vol. 15, p. 989, 1977

[8] C. B. Collins and R. O. Carlson, "Properties of Silicon Doped with Iron or Copper," *Phy. Rev.,* vol. 108, p. 1409, 1957

[9] G. Zoth and W. Bergholz, "A fast, preparation-free method to detect iron in silicon," *JAP,* vol. 67, pp. 6764-6771, 1990

[10] J. Lagowski, P. Edelman, A. M. Kontkiewicz, O. Milic, W. Henley, M. Dexter, L. Jastrzebski, and A. M. Hoff, "Iron detection in the part per quadrillion range in silicon using surface photovoltage and photodissociation of iron-boron pairs," *Appl. Phys. Lett.,* vol. 63, pp. 3043-3045, 1993.

[11] X. Gao, H. Mollenkopf, and S. Yee, "Annealing and profile of interstitial iron in boron-doped silicon," *Appl Phys Letters,* vol. 59, pp. 2133-2135, 1991.

[12] H. Lemke, "Dotierungseigenschaften von Eisen in Silizium," *Physica status solidi (a),* vol. 64, pp. 215-224, 1981

[13] D. Walz, J. P. Joly, and G. Kamarinos, "On the recombination behaviour of iron in moderately boron-doped p-type silicon," *Appl. Phys. A: Mat. Sci. & Pro,* vol. 62, pp. 345-353, 1996

[14] D. Walz, G. L. Carval, J. P. Joly, and G. Kamarinos, "An in-depth analysis of the ELYMAT technique for characterizing metallic micro contamination in silicon: experimental validation for iron contamination in p-type silicon," *Semicon. Sci. Tech.,* vol. 10, p. 1022, 1995

[15] J. E. Birkholz, K. Bothe, D. Macdonald, and J. Schmidt, "Electronic properties of iron-boron pairs in crystalline silicon by temperature- and injection-level-dependent lifetime measurements," *JAP,* vol. 97, 2005.

[16] A. G. Aberle, *Crystalline Silicon Solar Cells: Advanced Surface Passivation and Analysis*: Centre for Photovoltaic Engineering, University of New South Wales, Sydney NSW 2052, Australia, 1999.

[17] M. A. Green, "Intrinsic concentration, effective densities of states, and effective mass in silicon," *JAP,* vol. 67, pp. 2944-2954, 1990

[18] S. Rein, *Lifetime Spectroscopy - A Method of Defect Characterization in Silicon for Photovoltaic Applications* vol. 85. Berlin: Springer, 2005.

[19] R. N. Hall, "Electron-Hole Recombination in Germanium," *Phy. Rev.,* vol. 87, p. 387, 1952.

[20] W. Shockley and W. T. Read, "Statistics of the Recombinations of Holes and Electrons," *Phys. Rev.,* vol. 87, p. 835, 1952

[21] M. Lax, "Cascade Capture of Electrons in Solids," *Phys. Rev.,* vol. 119, p. 1502, 1960.

[22] A. Hangleiter, "Nonradiative recombination via deep impurity levels in silicon: Experiment," *Phy. Rev. B,* vol. 35, p. 9149, 1987

[23] D. Macdonald, T. Roth, P. N. K. Deenapanray, T. Trupke, and R. A. Bardos, "Doping dependence of the carrier lifetime crossover point upon dissociation of iron-boron pairs in crystalline silicon," *Appl. Phys. Lett.,* vol. 89, p. 142107, 2006.

[24] S. Rein and S. W. Glunz, "Electronic properties of interstitial iron and iron-boron pairs determined by means of advanced lifetime spectroscopy," *JAP,* vol. 98, p. 113711, 2005.

CHAPTER 6

Titanium in silicon

Titanium (Ti) is another common impurity in silicon. Ti can occur as a grown-in impurity during silicon ingot growth, especially in applications for photovoltaics [1]. Ti is less electronegative (1.3 r.u.) than silicon (1.8 r.u.), so it is unlikely for Ti to be segregated out by using an electrochemical segregation technique. Ti can also contaminate the surface of silicon devices during fabrication, such as during sputtering or by mechanical contact in the production line [2]. Such surface contaminations can easily transfer to the bulk during high temperature processes. Once incorporated in a device, in most cases Ti remains dissolved in silicon due to its low diffusivity and form three defect energy levels which acts as recombination centres. Previous research confirmed some of the electrical properties (E_t for all defects and σ of the nearer band gap half as shown in Table 6.1) of Ti-defects in silicon, however σ of the defects lies in the latter band gap half and effective capture mechanisms are yet to be determined. This Chapter presents a T-dependent study of carrier lifetime in Ti-contaminated multi-crystalline silicon wafers, and includes a novel method to measure defect concentration, determination of the segregation coefficient, $\sigma_n(T)$ and the assessment of the effective electron capture mechanism of Ti defects in silicon.

Chapter 6 presents temperature and injection-dependent lifetime measurements performed on deliberately Ti-contaminated, directionally-solidified, *p*-type multi-crystalline silicon wafers. Ti-related defects in silicon and their importance in silicon solar cells are discussed in Section 6.1. This section also lists previous work in characterization of Ti-related defects in silicon. Section 6.2 discusses experimental details and calculation procedures for the identification of active Ti-defect levels and their concentrations. This section presents a lower limit for the effective segregation coefficient for Ti in directionally-solidified multi-crystalline silicon. Section 6.3 presents a procedure for identifying an active Ti-defect level and its concentration. Section 6.4 presents T-dependent value of σ_n for a double donor defect, and analyses this T-dependence in terms of the likely carrier capture mechanism. Section 6.5 presents a lower limit of the segregation coefficient for Ti in multi-crystalline silicon.

6.1 Titanium and its defects in silicon

Ti is incorporated into the silicon lattice in interstitial form, introducing one of three defect energy levels [2](E_t). These defect levels are namely, an accepter (Ti_i^-), a donor (Ti_i^+) and a double donor (Ti_i^{++}), all of which can act as recombination centres. The electronic properties of Ti defect levels in silicon have been studied by several groups, as summarised by [2], with most of them based on deep-level transient spectroscopy (DLTS). Defect energy levels have been determined by DLTS to be E_C - 0.08, E_C - 0.27 and E_V + 0.28 for the accepter, donor and double donor respectively, where E_C and E_V represent the energy levels of the conduction and valance band edges in silicon. These defect energy levels were determined at a particularly low temperature (< 200 K), however a common assumption is that the defect-energy level does not vary with temperature. DLTS has also been employed to determine the electron capture cross section $\sigma_n(T)$ for the acceptor and donor defects, and the hole capture cross section $\sigma_p(T)$ for the double-donor defect, each as a function of temperature [2].

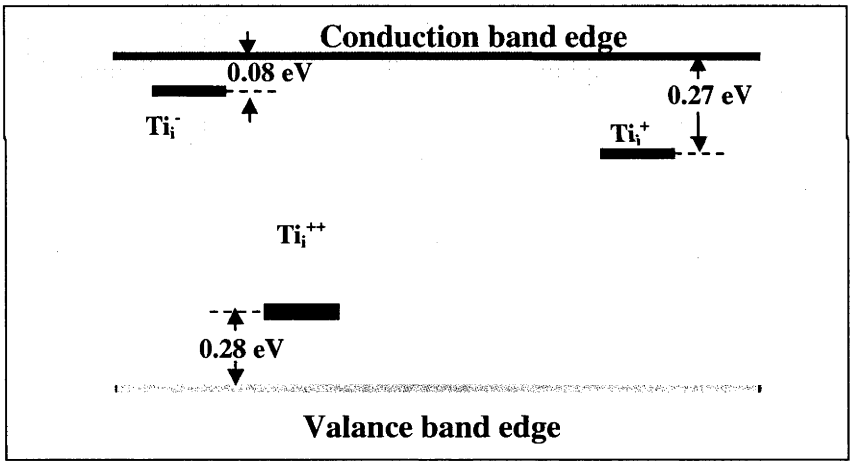

Figure 6.1: Energy level ranges of Ti-related defects in silicon depicting $E_t(Ti_i^-)$, $E_t(Ti_i^+)$ and $E_t(Ti_i^{++})$.

In addition to DLTS, lifetime spectroscopy has been used to characterize Ti defects. Rein [3] employed a mixture of injection-dependent, doping-dependent and T-dependent lifetime spectroscopy to determine E_t and the ratio of the capture cross sections (σ_n/σ_p), also known as the symmetry factor k. More recently, Roth *et al.* [4] performed T-dependent lifetime spectroscopy (TDLS) with injection-dependent lifetime spectroscopy (IDLS) with photoluminescence (PL) lifetime measurements to determine

E_t and k. The value of E_t as determined by Rein (E_V + 0.289 ± 0.005 eV) has close agreement with the double donor level from DLTS [2]. One value of E_t determined by Roth *et al.* (E_C - 0.24 ± 0.03 eV) has fair agreement with the donor level from DLTS, however their second energy level (E_c - 0.49 ± 0.03 eV) does not match any levels detected by DLTS[2]. Note that both Rein[3] and Roth *et al.*[4] calculate σ_n at room temperature from measured k assuming the σ_p at 200 K listed by Graff [2].

Table 6.1 Reported results of the electronic properties of Ti_i in silicon.

Defect	E_t (eV)	σ_p (cm^2)	σ_n (cm^2)	Reference
Acceptor (Ti_i^-)	$E_C - 0.08 \pm 0.01$	----------	3.5×10^{-14}	[2]
	E_C - 0.24 ± 0.03	----------	2.7×10^{-10}	[4]
Donor (Ti_i^+)	$E_C - 0.27 \pm 0.01$	----------	1.3×10^{-14}	[2]
	E_c - 0.49 ± 0.03	----------	3.3×10^{-13}	[4]
Double donor (Ti_i^{++})	$E_V + 0.28 \pm 0.01$	1.9×10^{-17} at 30 °C or $1.5 \times 10^{-16} \exp^{(-0.036/kT)}$	----------	[2]
	$E_V + 0.289 \pm 0.005$	----------	2.3×10^{-16}	[3]
	----------	----------	$9 \times 10^{-14} \exp^{(-0.107/kT)}$	This work

6.2 Sample details and methodology

Sample details

Four Ti-contaminated boron-doped multicrystalline silicon wafers were selected for this experiment. Large-area wafers (12 × 12 cm^2) were taken from 14, 37, 53 and 81% below the top of the ingot, to enable the segregation of Ti along the ingot length to be studied. The nominal resistivity of the samples was 1.0 Ω cm, however the boron concentrations on each sample were determined from dark conductance using the carrier mobility model developed by Regiaani *et al.* [5] at 300 K and it was found to vary slightly due to dopant segregation during crystallization. The concentration of Ti added to the silicon prior to commencement of crystallization [6, 7] was 10 ppma, which equates to approximately 2.9×10^{17} cm^{-3}. One control wafer was selected from the middle of another ingot prepared by the same procedure with similar boron doping, but

without Ti contamination, in order to verify the dominance of the Ti defect on the lifetime measurements.

All wafers were etched and cleaned prior to a phosphorus gettering step which removes fast diffusing interstitial metals such as Fe, which could otherwise partially mask the impact of Ti on the carrier lifetime. After removal of the gettering layers and further cleaning, plasma-enhanced chemical vapour-deposited silicon nitride films were applied to both surfaces, which act to suppress surface recombination. QSSPC [8] measurements were performed at room temperature on one wafer to identify the region which had the highest and most uniform carrier lifetime, and which also fit into the heating and cooling stage of the measurement device mentioned in Chapter 3. This same section (3.5 × 3.5 cm^2) was cut out of each wafer for subsequent analysis. This was necessary to ensure that the recombination is dominated by Ti, and not by crystallographic defects such as dislocation clusters.

Methodology

Three different energy levels of interstitial Ti that may occur in silicon are discussed in Section 6.1 and shown in Figure 6.1. It is essential to first make sure of the dominance of a particular energy level before performing lifetime spectroscopy for defect characterization. Furthermore, Ti impurity was added in the molten state before the crystal growth of the silicon wafer, thus the Ti concentration (N_t) needs to be determined before performing the lifetime analysis for the determination of capture cross section as mentioned in Chapter 2.

The Ti concentration (N_t) can be determined by measuring $\tau_{p0}(T)$ and by applying the simplified version of the SRH equation [9, 10] to measured lifetime data and the known value of $\sigma_p(T)$ of a particular defect energy level and $v_{th}(T)$ in Equation (2.20). Hence, due to unavailability of N_t, a known T-dependent model of $\sigma_p(Ti)$ is used to determine N_t in the sample and then $\sigma_n(T)$ is determined. The measured concentration of Ti on four samples taken from the four different positions of the silicon ingot is then used to calculate the segregation coefficient of Ti in directionally solidified multicrystalline silicon and is presented in Section 6.5.

Experimental details

The injection-dependent lifetimes of the Ti-contaminated wafer taken from the region 53% below the top of the ingot, and the control wafer, which was also from a similar position in the ingot, are depicted in Figure 6.2 for temperatures 0, 100, 150, 200, and 250 °C. The effective lifetime τ_{eff} was measured as a function of the excess carrier density, Δn, for each wafer over the temperature range 0 – 270 °C.

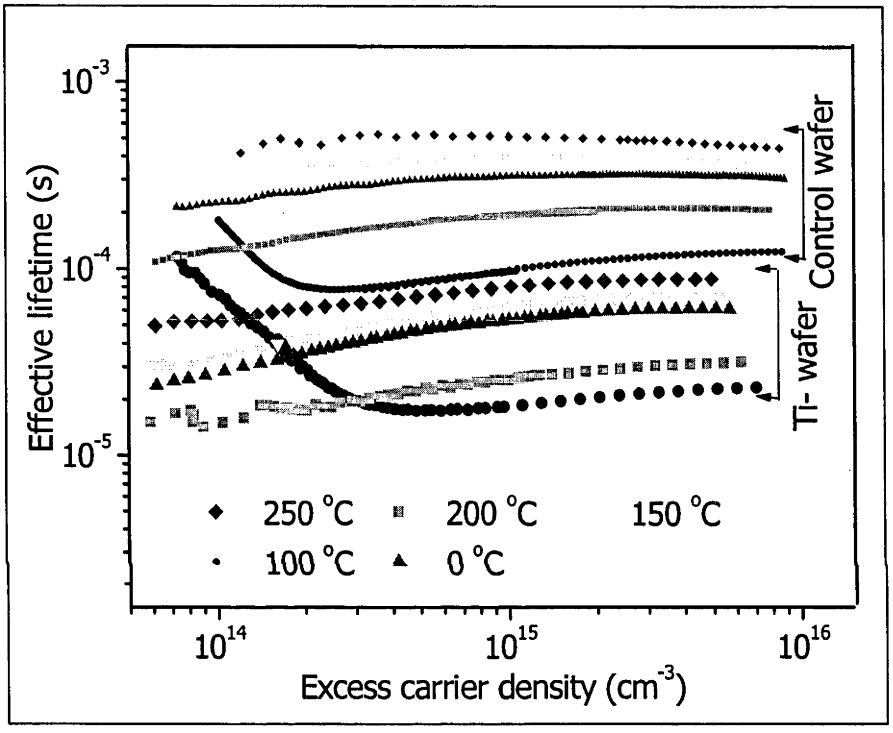

Figure 6.2: Injection-dependent lifetime of a Ti-contaminated wafer and a control wafer.

The effective lifetime of all four wafers and the control wafer was found to increase significantly at lower excess carrier densities, i.e. under Low Level Injection (LLI). This is caused by minority carrier trapping (MCT) for the temperatures below 100 °C [11]. However, for the temperature range above 100 °C, the trapping effect was removed, since the traps become filled with thermally generated carriers [11, 12]. Figure 6.2 shows that the effective lifetime of the Ti-contaminated wafer is only about seven times less than the effective lifetime of the control wafer taken from a similar position in the ingot. Hence the lifetime associated with the Ti defect, τ_{Ti}, was calculated [3] by using

$$\frac{1}{\tau_{Ti}} = \frac{1}{\tau_{Ti-wafer}} - \frac{1}{\tau_{control}} \tag{6.1}$$

where $\tau_{Ti\text{-}wafer}$ is the overall lifetime measured on the Ti-contaminated wafer, and $\tau_{control}$ is the lifetime on the corresponding control wafer taken from a similar position in the ingot.

6.3 Active Ti-defect level and its concentration

Active Ti-defect energy level

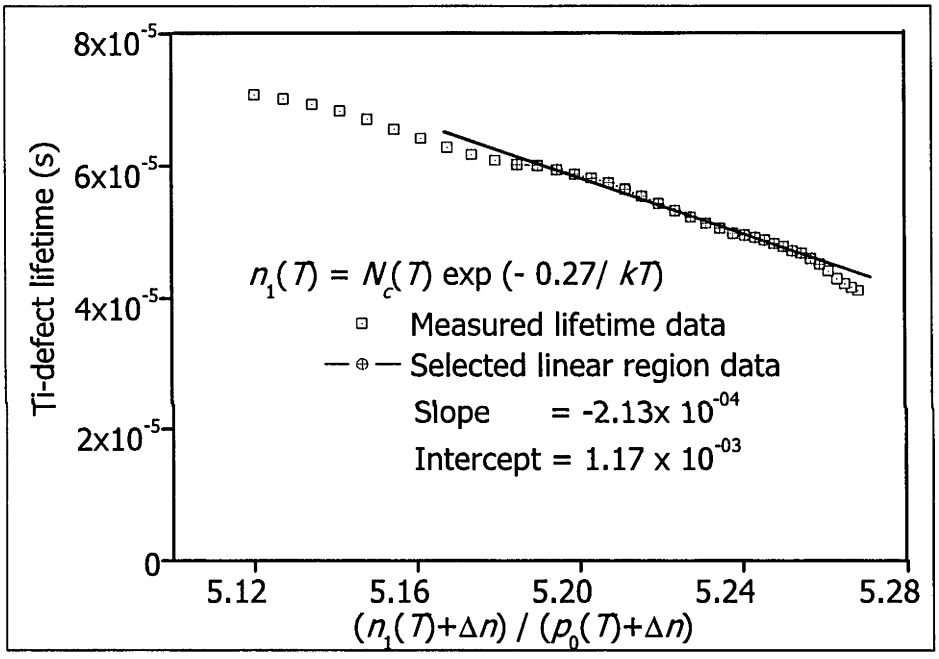

Figure 6.3: Lifetime of Ti-defect wafer versus $(n_1 + \Delta n)/(p_0 + \Delta n)$ for the donor level defect at 200 °C.

The Ti_i^- and Ti_i^+ levels lie in the upper band gap half, making $p_1(T) << p_0(T)$ for all temperatures for a boron-doped silicon wafer. In such situations Equation (2.61) becomes valid, and is re-stated here

$$\tau_{SRH} = \tau_{no} + \tau_{po}\frac{(n_1 + \Delta n)}{(p_0 + \Delta n)} \tag{6.2}$$

Thus, if all inherent assumptions mentioned in Section 2.5.2 are valid, the slope of a plot of τ_{SRH} versus $(n_1 + \Delta n) / (n_1 + \Delta n)$ gives τ_{p0} and the intercept gives τ_{n0}. Such plots of the measured data with n_1 for either donor or acceptor energy levels had negative slopes when T is in the range 140 – 270 °C. Figure 6.3 provides an example of a Ti-wafer at 200 °C when the donor level is considered. Since τ_{p0} cannot be negative, this observation rules out the dominance of energy levels in the upper band gap (Ti_i^- and Ti_i^+).

If instead, the dominant defect is the double donor defect that lies in the lower half of the band gap, $n_1(T)$ is negligible and Equation (2.60) becomes valid and, when Δn is sufficiently less than p_0, τ_{SRH} is expressed as

$$\tau_{SRH} = \frac{\tau_{no}}{p_0}\left(p_1 + p_0\right) + \frac{\tau_{po}}{p_0}\,\Delta n \tag{6.3}$$

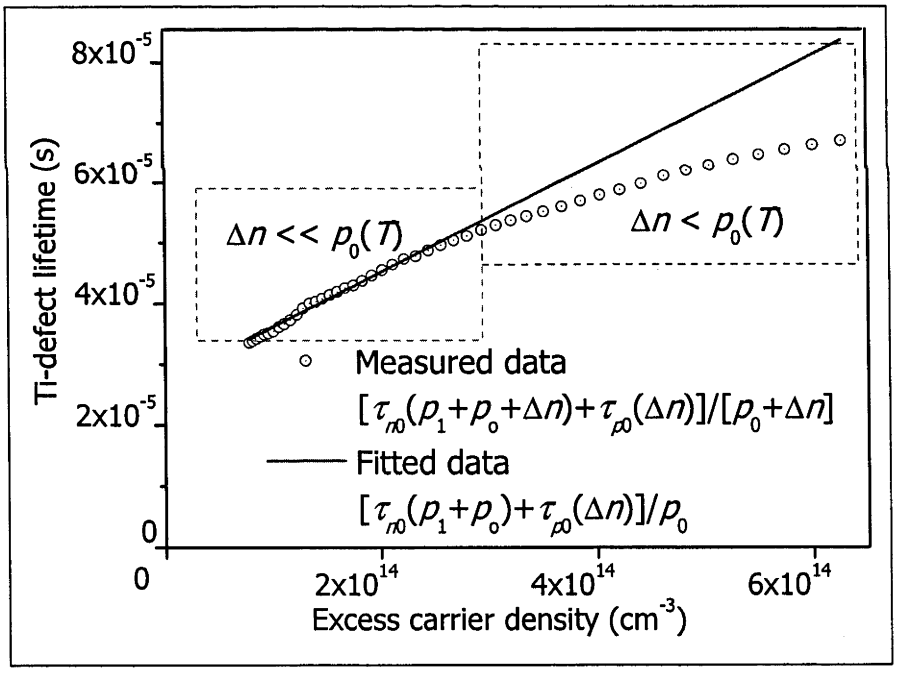

Figure 6.4: Measured lifetime data (Ti wafer at 180 °C) depicting linearity with the fitted model for LLI [$\Delta n << p_0(T)$].

Hence, the slope of a plot of $\tau_{SRH}(\Delta n)$ gives τ_{p0}/p_0 and the intercept gives $(p_1+p_0)\tau_{n0}/p_0$. The measured data and the plotted data for a Ti-wafer is depicted in Figure 6.4 at

180 °C, showing a region in which the assumptions above remain valid, i.e. $\Delta n \leq 3 \times 10^{14}$ cm^{-3}. The slope of the measured lifetime of this sample for different temperatures is depicted in Figure 6.5, showing close agreement with the fitted model for the low injection region.

Ti-density for double donor level

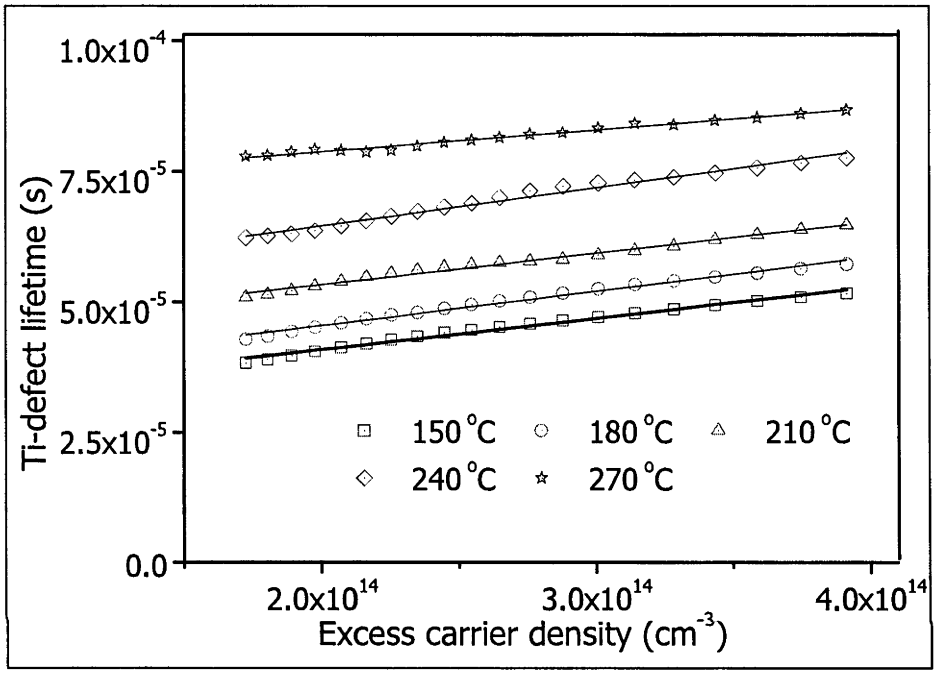

Figure 6.5: Measured carrier lifetime data showing consistency of Ti wafer with fitted model for different temperatures.

The concentration (Nt) of interstitial Ti was determined by assuming that all recombination occurred through its double donor defect energy level, and hence at all temperatures [3]

$$N_T = \frac{1}{\tau_{p0} \times v_{th} \times \sigma_p} = \frac{1}{slope \times p_0 \times v_{th} \times \sigma_p} \tag{6.4}$$

where the slope represents the slope of a plot of $\tau_{SRH}(\Delta n)$ for low injection and the calculation does not require knowledge of σ_n. The calculations were made using $\sigma_p(T) = 1.5 \times 10^{-16} exp(-0.036/kT)$ (cm^2), as determined for the double donor level [2], and the models for $v_{th}(T)$ and $p_0(T)$ given by Green [13] and Rein [3] respectively. N_t is plotted in Figure 6.6, where the uncertainties result from the error in lifetime and in the

least square linear fits. It depicts a constant, N_t, at all temperatures, which supports the technique and the choice of the defect energy level's parameters (E_t and $\sigma_p(T)$) . Note that below 140 °C, there was no clear impact by the Ti-related energy level on the effective lifetime due to lower values of n_1 and p_1, and to carrier trapping. Note that Rein [3] also concluded that the level in the lower half of the band gap (which is the double donor) is dominant for recombination in p-type silicon, by a combination of TDLS and IDLS.

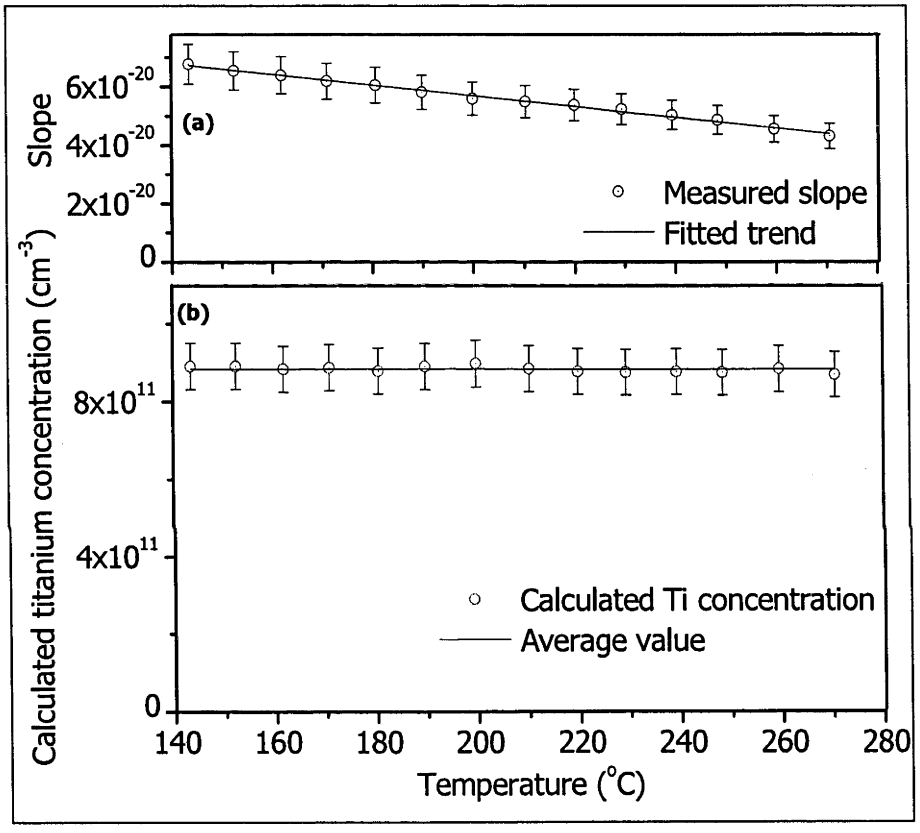

Figure 6.6: Measured slope (τ_{SRH} verses Δn) (a), calculated Ti concentration after lifetime data corrected with the control wafer data (b) for temperature range 145 to 270 °C.

6.4 $\sigma_n(T)$ of Ti_i^{++} defect in silicon

The intercept on the lifetime axis of the plot of $\tau_{eff}(\Delta n)$ gives $(p_1+p_0)\tau_{n0}/p_0$ according to Equation (6.3). Hence, $\tau_{n0}(T)$ can be determined using $p_1(T) = N_v(T) \times exp(-\Delta E_t/k_BT,)$,

the energy level of the double donor and $p_0(T)$. With values of $\tau_{n0}(T)$, N_T and $v_{th}(T)$ the T-dependent value of $\sigma_n(T)$ was calculated and is plotted in Figure 6.7.

The T-dependent trends in $\sigma_n(T)$ associated with various capture mechanisms are listed by Rein [3]. Of these mechanisms, only multiphonon emission (MPE) due to the deep centres [14] yields an increase in $\sigma_n(T)$ with T, consistent with the measured data depicted in Figure 6.7. This suggests that the following mechanisms do not contribute significantly to electron capture at an interstitial Ti defect: photon emission and classical Auger, which have no T dependence; and excitonic Auger capture due to deep centres, cascade capture, and two-stage cascade capture due to the deep coulomb attractive centres [15], all of which decrease with temperature.

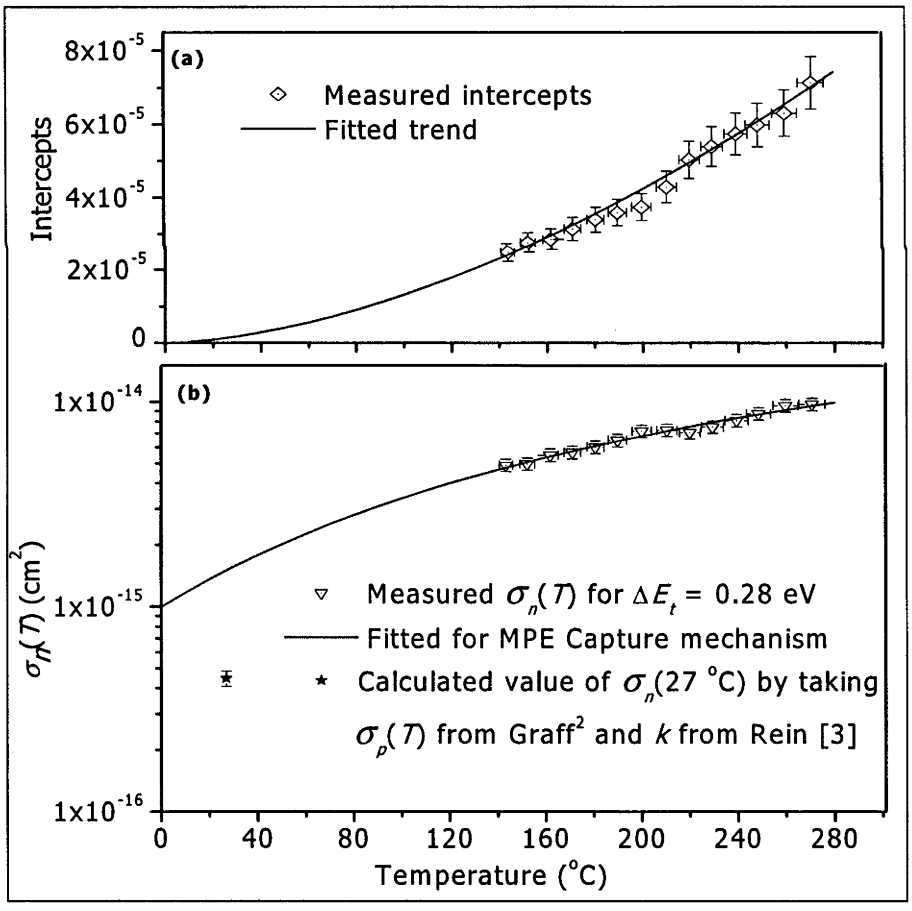

Figure 6.7: Measured intercepts (a) and calculated $\sigma_n(T)$ for Ti^{++} defect in silicon fitted with multi phonon emission capture (MPE) (b).

The electron capture cross section associated with MPE follows the equation [14]

$$\sigma_n(T) = \sigma_\infty \exp\left(\frac{-E_\infty}{k_B T}\right) \tag{6.5}$$

where σ_∞ is the T-independent pre factor and E_∞ is known as activation energy, and where $\sigma_\infty = 9.01 \times 10^{-14}$ cm^2 and $E_\infty = 0.107 \pm 0.01$ eV provide the best fit to the experimental data (plotted in Figure 6.7). Equation (6.5) and these best-fit parameters yield $\sigma_n(300\text{ K}) = 1.5 \times 10^{-15}$ cm^2, which is 3.4 times higher than when calculated from k determined by Rein [3] using $\sigma_p(300\text{ K})$ from Graff [2].

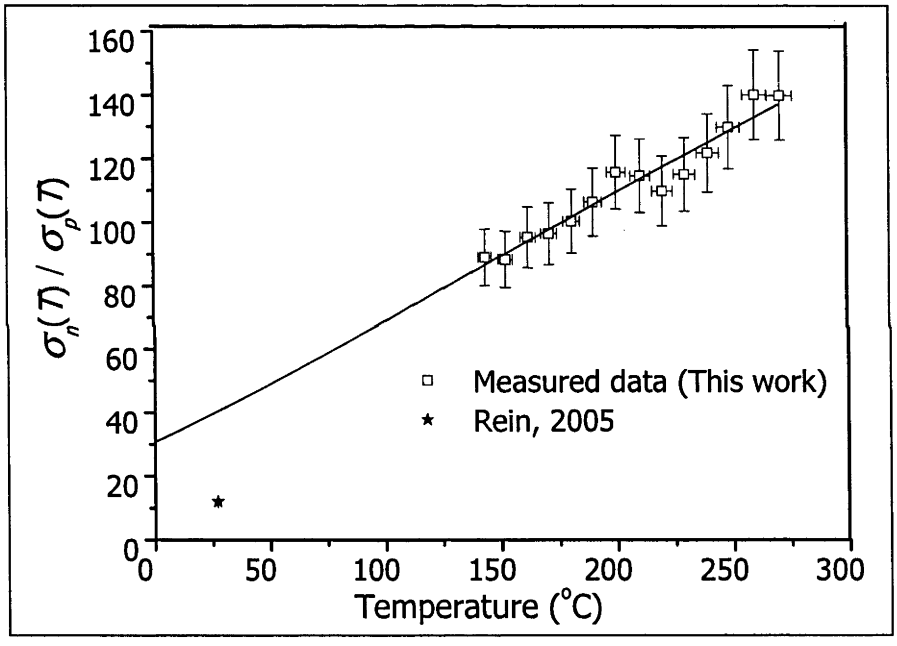

Figure 6.8: Temperature dependence of carrier capture cross section ratio for a double donor level of Ti in silicon.

T-dependent values of the capture cross section ratio $\sigma_n(T)/\sigma_p(T)$ have also been determined, and are plotted in Figure 6.8. The capture cross section ratio was found to increase with temperature because the activation energy for hole capture is less than the activation energy for electron capture, even though both exhibit the same capture mechanism. The T-dependent trend of k gives the value of 40.4 ± 4 at 27 °C, which is 3.4 times higher than the value determined by Rein [3].

6.5 Segregation coefficient of Ti in silicon

A lower limit to the segregation coefficient of Ti in directionally-cast, multi-crystalline silicon was determined by fitting the Scheil equation [16, 17] to the values of N_T along the ingot length as

$$C_S = k_{eff} C_0 (1 - f_s)^{k_{eff}-1} \quad (6.6)$$

where C_s is the concentration of impurities in the solid phase, which is equal to N_t determined in this work, C_0 is the initial concentration in the liquid and f_s is the fraction of solid formed. Ti concentrations on all four wafers were calculated by using Equation (6.6). As there was no control for the wafers taken from the positions 14, 37 and 81% of the ingot, the non-corrected value of Nt has been applied to calculate the segregation coefficient, which gives its lower limit. Furthermore, there are several pre-conditions required for the Scheil model to be valid; a) diffusion in the solid is negligible; b) local equilibrium is maintained at the solid-liquid interface and the curvature effect at the interface is neglected; c) uniform liquid composition; and d) equal solid and liquid densities. As these wafers are prepared by directional solidification and Ti is a slow diffuser, these conditions are believed to be approximately fulfilled in this case. The initial liquid concentration C_0 was 2.9×10^{17} cm^{-3}. The Ti concentrations determined in this work are shown in Figure 6.7 as a function of the position in the ingot from which they came. Also shown is a fit of the Scheil equation. The value of the segregation coefficient that best fits the data is 2.2×10^{-6} with N_t calculated from the lifetime data which was not corrected with the control wafer, and 1.8×10^{-6} with N_t calculated from the lifetime data adjusted with the control wafer. In the second case N_t for one Ti-wafer was calculated and N_t for the other three wafers was adjusted in the same proportion. Note that this is strictly only a lower level limit on the segregation coefficient, as the solid concentrations were determined only for the double donor defect energy level for interstitial Ti. Segregation of metallic impurities on the grain boundaries of multicrystalline silicon can occur as reported by Grovenor [18] and Morita et al. [19]. Rohatgi et al. [20] measured only a small amount of segregated Ti into the grain boundaries of multicrystalline silicon, where this increase with Ti concentration and decrease with an increase in grain diameter [20]. The Ti concentration in the multicrystalline silicon studied here (9×10^{11} cm^3) is more than 100 times smaller than

the Ti concentration in the samples studied by Rohatgi et al., and the nominal grain diameter (1 cm) is more than 10 times larger. Hence the segregation of Ti on the grain boundaries can be neglected in this case. If there are significant quantities of Ti present in other forms (for example as the interstitial acceptor or donor, or as substitutional Ti, or as precipitates), then the segregation coefficient would be larger. This, in fact, could explain the deviation from the Scheil equation for the sample taken from near the top of the ingot.

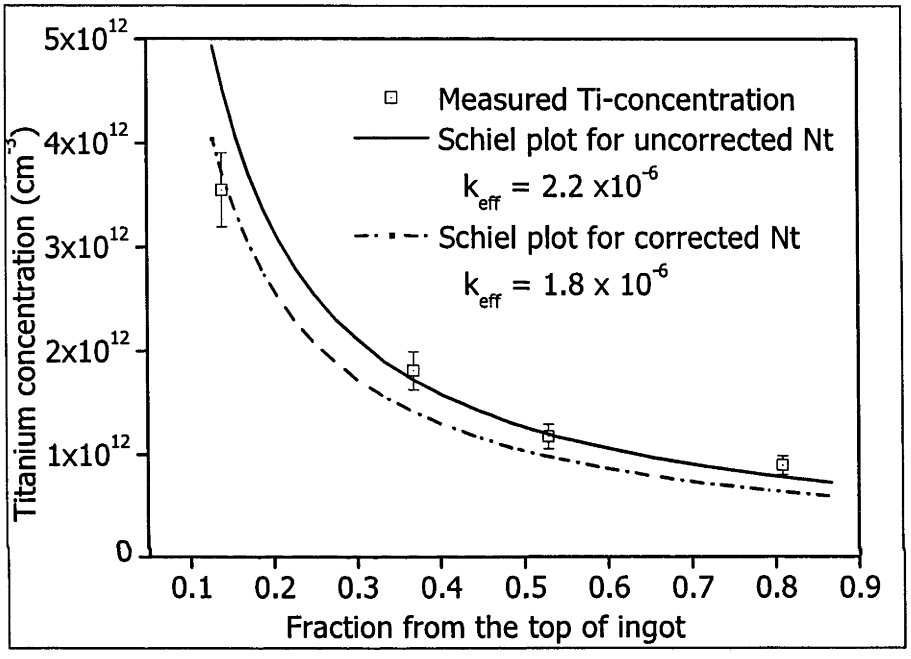

Figure 6.9: Ti concentration for different positions within the ingot plotted with Scheil equation with different k_{eff}.

The segregation coefficient for Ti in single-crystal silicon ingot growth, which is assumed to represent the equilibrium segregation coefficient, has been reported variously as 1.8×10^{-6} [21], 2×10^{-6} [22] and 3.6×10^{-6} [23]. These values are very close to the value determined here. Assuming that there is an insignificant amount of Ti in forms other than the interstitial double donor, this would imply that the segregation of Ti in directionally-solidified multicrystalline silicon proceeds essentially in equilibrium. Recent work has shown that the segregation coefficient of Fe in multicrystalline silicon is also close to the equilibrium value [24].

6.6 Chapter summary

Ti concentrations in multicrystalline silicon wafers were calculated by analysis of injection-dependent carrier lifetime data for different temperatures, in conjunction with the published T-dependent model for $\sigma_p(T)$. Measured lifetime data for the temperature range (140 – 270 °C) were used to calculate the T-dependent value of the electron capture cross section $\sigma_n(T)$ for the double donor level of Ti in silicon. The T-dependent trend for $\sigma_n(T)$ best matched the multi-phonon emission model for carrier capture and when extrapolated gave a comparable value with previously published values of $\sigma_n(T)$ at room temperature. A lower limit for the segregation coefficient of 1.8×10^{-6} for Ti in multicrystalline silicon was determined by using the Scheil model, and indicated that segregation proceeds in equilibrium in this type of ingot growth.

References

[1] T. Buonassisi, A. A. Istratov, M. D. Pickett, M. Heuer, J. P. Kalejs, G. Hahn, M. A. Marcus, B. Lai, Z. Cai, and S. M. Heald, "Chemical natures and distributions of metal impurities in multicrystalline silicon materials," *Progress in Photovoltaics: Research and Applications,* vol. 14, pp. 513-531, 2006.

[2] K. Graff, *Metal Impurities in Silicon-Device Fabrication*, 2nd ed. vol. 24. Berlin: Springer, 1999.

[3] S. Rein, *Lifetime spectroscopy: a method of defect characterization in silicon for photovoltaic applications.* Berlin: Springer, 2005.

[4] T. Roth, M. Rüdiger, W. Warta, and S. W. Glunz, "Electronic properties of titanium in boron-doped silicon analyzed by temperature-dependent photoluminescence and injection-dependent photoconductance lifetime spectroscopy," *J. Appl. Phys,* vol. 104, p. *DOI: 10.1063/1.2996252*, 2008.

[5] S. Reggiani, M. Valdinoci, L. Colalongo, M. Rudan, G. Baccarani, A. D. Stricker, F. Illien, N. Felber, W. Fichtner, and L. Zullino, "Electron and hole mobility in silicon at large operating temperatures. I. Bulk mobility," *IEEE Transactions on Electron Devices 2002,* vol. 49, pp. 490–499, 2002

[6] L. J. Geerligs, P. Manshanden, G. P. Wyers, E. J. Øvrelid, O. S. Raaness, A. N. Waernes, and B. Wiersma, "Specification of solar grade silicon: how common impurities affects the cell efficiency of Mc-Si solar cells " in *20th European Photovoltaic Solar Energy Conference* Barcelona, Sapin, 2005.

[7] L. J. Geerligs, P. Manshanden, I. Solheim, E. J. Øvrelid, and A. N. Waernes, "Impact of common metallurgical Impurities on Mc-Si solar cell efficiency: p-type versus n-type doped ingots " in *21st European Photovoltaic Solar Energy Conference and Exhibition* Dresden, Germany, 2006, pp. 1285 - 1288

[8] R. A. Sinton, A. Cuevas, and M. Stuckings, "Quasi-Steady-State Photoconductance, A New Method for Solar Cell Material and Device Characterization," in *25th IEEE Photovoltaic Specialists Conference*, 1996, pp. 457-460.

[9] W. Shokley and W. T. J. Read, "Statistics of recombinations of holes and electrons," *Phys Rev* vol. 87, pp. 835-842, 1952.

[10] R. N. Hall, "Electron-hole recombination in germanium," *Phys. Rev.,* vol. 87, p. 387, 1952.

[11] D. Macdonald and A. Cuevas, "Trapping of minority carriers in multicrystalline silicon," *Applied Physics Letters,* vol. 74, pp. 1710-1712, 1999.

[12] K. R. McIntosh, B. B. Paudyal, and D. H. Macdonald, "Generalized procedure to determine the dependence of steady-state photoconductance lifetime on the occupation of multiple defects," *Journal of Applied Physics,* vol. 104, p. *DOI:10.1063/1.2999640*, 2008.

[13] M. A. Green, "Intrinsic concentration, effective densities of states, and effective mass in silicon," *Journal of Applied Physics,* vol. 67, p. 2944, 1990

[14] C. H. Henry and D. V. Lang, "Nonradiative capture and recombination by multiphonon emission in GaAs and GaP," *Phys. Rev B,* vol. 15, p. 989, 1977.

[15] R. M. Gibb, G. J. Rees, B. W. Thomas, B. L. H. Wilson, B. Hamilton, D. R. Wight, and N. F. Mott, "A two stage model for deep level capture," *Philosophical Magazine,* vol. 36, pp. 1021-1034 1977.

[16] R. A. Brown and D. H. Kim, "Transient simulations of convection and solute segregation of GaAs growth in gradient freeze furnace," *Journal of Crystal Growth,* vol. 109, pp. 66-74, 1991.

[17] E. Scheil, *Z. Metallkd,* vol. 34, p. 70, 1942.

[18] C. Grovenor, "Grain boundaries in semiconductors," *Journal of Physics C: Solid State Physics,* vol. 18, pp. 4079-4119, 1985

[19] K. Morita and T. Miki, "Thermodynamics of solar-grade-silicon refining," *Intermetallics,* vol. 11, pp. 1111-1117, 2003

[20] A. Rohatgi, R. Hopkins, and J. Davis Jr, "The properties of polycrystalline silicon solar cells with controlled titanium additions, "*IEEE Transactions on Electron Devices,* vol. 28, pp. 103-108, 1981

[21] H. Lemke, "Semiconductor Silicon/1994, edited by H. R. Huff, W. Bergholz, and K. Sumino," in *Semiconductor Silicon*, New Jersey, 1994, p. 695.

[22] J. R. Davis, A. Rohatgi, R. H. Hopkins, P. D. Blais, P. Rai-Choudhury, J. R. McCormick, and H. C. Mollenkopf, "Impurities in Silicon Solar Cells," *IEEE Trans. Electron Devices,* vol. 27, pp. 677-687, 1980.

[23] S. Pizzini, M. Acciarri, and S. Binetti, "From electronic grade to solar grade silicon: chances and challenges in photovoltaics," *physica status solidi (a),* vol. 202, pp. 2928 - 2942, 2005.

[24] R. Kvande, L. J. Geerligs, G. Coletti, L. Arnberg, M. D. Sabatino, E. J. Øvrelid, and C. C. Swanson, "Distribution of iron in multicrystalline silicon ingots," *Journal of Applied Physics,* vol. 104, p. *DOI: 10.1063/1.2956697*, 2008.

CHAPTER 7

Conclusion

This thesis presented a new procedure to analyse injection dependent lifetime data of a semiconductor for explicit determination of the fundamental capture times for electrons and holes (τ_{n0} and τ_{p0}). A T-controlled, inductive-coil, photoconductance-based instrument was developed to measure carrier lifetime as a function of excess carrier density (Δn) suitable for the newly developed characterization procedure. The T-dependent carrier lifetime studies of three common metal impurities in silicon solar cells (Mo, Fe and Ti) were performed to determine electron and hole capture cross sections (σ_n and σ_p) as a function of temperature as well as other electrical properties of the defects.

The proposed characterization technique employs injection-dependent lifetime spectroscopy (IDLS), to determine the slope and intercept of a linear plot of measured minority carrier lifetime (τ_{eff}) with excess carrier density (Δn) at different temperatures. The measured slope was then used to determine the fundamental capture time of the majority carriers (τ_{p0} for p-type and τ_{n0} for n-type). The measured intercept was used to determine the fundamental capture time of the minority carriers (τ_{n0} for p-type and τ_{p0} for n-type), which requires a known value of E_t only above a certain temperature, where that temperature depends upon the depth of E_t in the band gap. The measured $\tau_{n0}(T)$ and $\tau_{p0}(T)$ can then be used to determine $\sigma_n(T)$ and $\sigma_p(T)$ with known values of v_{thn}, v_{thp} and N_t. Alternatively, this technique can be used to determine N_t when either σ_n or σ_p is known. This technique is equally applicable to both p and n-type silicon regardless of the position of E_t in the band gap and is valid below the temperature at which intrinsic conduction begins.

An inductive coil PC measurement instrument (WCT-100) was modified to measure carrier lifetime as a function of excess carrier density for the temperature range -150 to 310 °C. Previously, the WCT-100 had been adapted to operate over a temperature range only from room temperature to 150 °C. The T-dependent calibration of the developed instrument verified that the correlation between photoconductance voltages (V_{PC}) and

sheet conductance (σ_{sq}) of the silicon wafer is nearly linear and independent of temperature.

The proposed characterization technique was implemented to determine $\sigma_n(T)$ and $\sigma_p(T)$ of Mo defects in silicon. Measured $\sigma_n(T)$ and $\sigma_p(T)$ shows the excitonic Auger capture (EA) as an effective capture mechanism, with T-independent coefficients $\sigma_0 = 4.21 \pm 0.4 \times 10^{-8}$, $6.05 \pm 0.8 \times 10^{-14}$ cm^2 and the T-dependent exponents α = 2.95 ± 0.2 and 1.07 ± 0.05 respectively. This indicates that the recombination will be lower with increasing temperature in a solar cell with Mo impurities and the deleterious effect of the Mo impurities is lessened as the temperature increases in both *p* and *n*-types. The capture cross sections ratio $\sigma_n(T)/\sigma_p(T)$ was also found to decrease with temperature. Measured σ_n, σ_p and σ_n/σ_p at room temperature were found to be consistent (within ± 10%) with previously reported values determined by using other techniques.

The measured values of $\sigma_n(T)$ and $\sigma_p(T)$ for interstitial defects of iron (Fe_i) in silicon at different temperatures were found to be consistent with previously reported values. The measured σ_n of Fe_i at different temperature depicts a T-dependent trend that can be better defined with an EA capture mechanism giving the T-independent coefficients, σ_0 = $3.47 \pm 0.5 \times 10^{-11}$ cm^2 and the T-dependent exponent $\alpha = 1.48 \pm 0.02$. Conversely, the T-dependent trend of measured σ_p was better defined by multiphonon emission capture (MPE) with activation energy (E_a) of 0.05 ± 0.006 eV and T-independent pre-factor (σ_∞) equal to $4.54 \pm 0.5 \times 10^{-16}$ cm^2. The measured values for $\sigma_n(T)$ and $\sigma_p(T)$ of iron-boron (FeB) pair defects in silicon at room temperature also depicts consistency with previously reported values. The T-dependent trend of the measured σ_n depicts EA as an effective capture mechanism for electrons in FeB pair defects giving a T-independent pre-factor, σ_0 = $5.1 \pm 1.3 \times 10^{-9}$ cm^2 and the T-dependent exponent, $\alpha = 2.5 \pm 0.05$. Conversely, the T-dependent trend of the measured $\sigma_p(T)$ depicts MPE as an effective capture mechanism for holes in FeB pairs giving $E_a = 0.262 \pm 0.012$ eV and $\sigma_\infty = 3.32 \pm 1.22 \times 10^{11}$ cm^2. This indicates that the lifetime of the minority carriers in *p*-type solar cells with Fe_i or FeB impurities increases with temperature and the detrimental effects of Fe_i or FeB pairs in solar cells are lessened at higher temperatures. On the other hand, the lifetime of the minority carriers in *n*-types solar cells with Fe_i

impurities decreases with temperature and reduces solar cell performance at higher temperatures.

Ti-contaminated boron-doped multicrystalline silicon wafers with a known E_t and T-dependent model for σ_p were used to determine the active Ti concentrations (N_t) in silicon. Measured N_t on the wafers taken from different positions in the ingot were used to determine the segregation coefficient for Ti in silicon. The measured segregation coefficient for multicrystalline silicon was found to be close to the previously reported segregation coefficient for Ti in single-crystal silicon ingot growth, which was assumed to represent the equilibrium segregation coefficient. The T-dependent trend of measured σ_n for double donor defects in silicon depicts MPE as an effective capture mechanism giving $E_\infty = 0.107 \pm 0.01$ eV and $\sigma_\infty = 9.01 \times 10^{-14}$ cm^2. This indicates that the detrimental effect of Ti impurities in solar cell increases with increase in temperature.

Appendix A

Table A1: Parameters of solar cells taken for PC1D simulation

Parameters and Cell type	**A**	**B**	**C**	**D**
Area (cm^2)	1	1	1	1
Thickness (μm)	250	250	200	500
Doping and diffusion				
Background doping	*p*-type	*p*-type	*n*-type	*p*-type
Concentrations(cm^{-3})	1.5×10^{16}	1.5×10^{16}	9.2×10^{14}	1.5×10^{16}
First front diffusion	*n*-type	*n*-type	*p*-type	*n*-type
Concentrations(cm^{-3})	8.1×10^{19}	8.1×10^{19}	9.3×10^{18}	4.5×10^{-19}
Depth (μm)	0.3788	3.788	0.2541	0.1974
Profile	Erfc	Erfc	Erfc	Erfc
Second front diffusion	NA	NA	NA	NA
Front external diffusion	NA	NA	NA	NA
First rear diffusion (cm^{-3})	*p*-type	*p*-type	NA	NA
Peak doping (cm^{-3})	2.1×10^{20}	2.1×10^{19}	NA	NA
Depth factor (□m)	1.781	1.718	NA	NA
Second rear diffusion (cm^{-3})	NA	NA	NA	NA
Rear external diffusion (cm^{-3})	NA	NA	NA	NA
Recombination				
Bulk τ_{n0} (μs)	10^2	10^2	10^2	1
Bulk τ_{p0} (μs)	5×10^2	5×10^2	5×10^2	5×10^2
Front surface s_n, s_p (cms)	10^3,10^3	10^3,10^3	5×10^2,	10^2,10^2
Rear surface s_n, s_p (cms)	10^7,10^7	10^7,10^7	5×10^3,	40, 40
Surface texture				
Front surface	Textured	Textured	Textured	Textured
Angle (degree)	54.74	54.74	54.74	45.74
Depth (μm)	3	3	3	2
Rear surface	Textured	Textured	Textured	NA
Angle (degree)	54.74	54.74	54.74	NA
Depth (μm)	3	3	3	NA
Surface charge	Positive	Positive	Positive	Positive
Front surface (cm^{-2})	10^{12}	10^{12}	10^{12}	10^{11}
Rear surface(cm^{-2})	Neutral	Neutral	Neutral	10^{11}
Contacts definitions				
Emitter contact				
Internal series resistance (Ω)	1	1	0.7	0.2
Distance from surface (μm)	0	0	0	0

Base contact				
Internal series resistance (Ω)	10^{-6}	10^{-6}	10^{-16}	10^{-16}
Distance from surface (μm)	10^{4}	10^{4}	10^{3}	10^{4}
Reflectance				
Front external	Coated	Coated	Coated	Fixed
Broadband reflectance (%)	5	5	0	1
Thickness (nm)	75	75	75	NA
Index	2	2	2	NA
Rear external reflectance (%)	0 (fixed)	0 (fixed)	0 (fixed)	0 (fixed)
Internal reflectance				
Front surface	Diffuse	Diffuse	Diffuse	Diffuse
First bounce (%)	50	50	90	90
Subsequent bounce (%)	50	50	90	90
Rear surface	Diffuse	Diffuse	Specular	Specular
First bounce (%)	50	50	90	90
Subsequent bounce (%)	50	50	90	90

Types of solar cells:

A: Selective Emitter, screen printed, industrial (SunPower)
B: Selective Emitter, screen printed, next generation (SunPower)
C: High efficiency solar cell (SunPower)
D: Passivated emitter with rear locally diffused (PERL) cell

Appendix B

Simplification of the SRH equation for *n*-type silicon

This appendix presents the simplification of the SRH equation for *n*-type silicon which can be used in lifetime spectroscopy. This simplification is analogous to *p*-type silicon as mentioned in Chapter 2. This thesis has presented the results of the experiments performed on *p*-type silicon. However, characterization of *n*-type silicon is equally important as various researches have been performed on *n*-type silicon.

B.1 Preliminary simplification of the SRH equation for *n*-type silicon

The simplified version of the SRH equation allows the determination of the four defect specific parameters τ_{n0}, τ_{p0}, n_1 and p_1, which are related to more fundamental parameters, σ_n, σ_p, N_t and E_t as described in Section 2.2.

The simplified SRH equation mentioned in Section 2.1.3 is re-stated here.

$$\tau_{SRH} = \frac{\tau_{p0}(n_1 + n_0 + \Delta n) + \tau_{n0}(p_0 + p_1 + \Delta n)}{n_0 + p_0 + \Delta n} \tag{B.1}$$

In *n*-type Silicon $p_0 << n_0$ and $p_0 << p_1$ for a certain temperature range (the temperature range is dependent upon N_D and E_t, which is presented in a A.2), hence Equation (B.1) can be written as

$$\tau_{SRH}^{p} = \frac{\tau_{p0}(n_1 + n_0 + \Delta n) + \tau_{n0}(p_1 + \Delta n)}{n_0 + \Delta n} \tag{B.2}$$

In this expression if we subject a condition where excess carrier concentration, $\Delta n << n_0$ and $\Delta n << p_1$, known as low-level injection (LLI), τ_{SRH} can be written as

$$\tau_{SRH}^{LLI,n} = \tau_{p0}\left(1 + \frac{n_1}{n_0}\right) + \tau_{n0}\frac{p_1}{n_0} \tag{B.3}$$

This expression can be subject to two different conditions depending upon the location of E_t in the band gap of the silicon. If we consider E_t in the lower half of the band gap (UBGH), then $n_0 >> n_1$ and Equation (B.3) can be re-written as

$$\tau_{SRH}^{LLI,n} = \tau_{p0} + \tau_{n0} \times \frac{p_1}{n_0}. \tag{B.4}$$

Similarly, if we consider E_t in the upper half of the band gap (LBGH), then $n_0 >> p_1$ and the second part of Equation (B.4) can be neglected and re-written as

$$\tau_{SRH}^{LLI,n} = \tau_{p0}\left(1+\frac{n_1}{n_0}\right) \tag{B.5}$$

This shows that the SRH lifetime of n-type silicon at high temperatures and low injection levels is only dependent upon three defect specific parameters, τ_{p0}, τ_{n0} and p_1, when E_t lies in LPGH and only two, τ_{p0} and n_1, when E_t lies on UBGH of silicon.

B.2 Validity of assumptions for preliminary simplification of the SRH equation

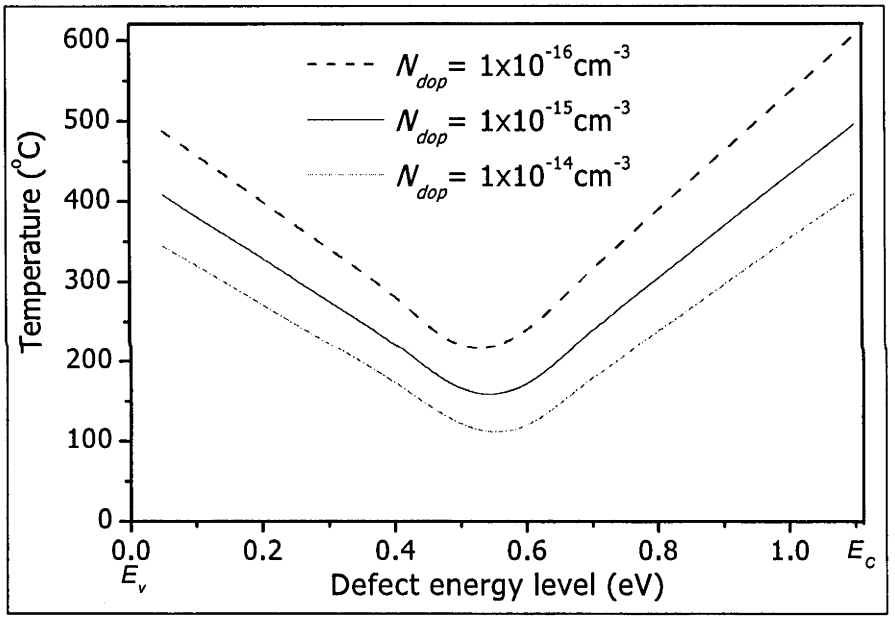

Figure B.1: Minimum temperature required for $p_1(T)$ or $n_1(T)$ >> 0.0001 × $p_0(T)$ or $n_0(T)$ for different doping densities and defect energy levels.

The simplification of the SRH equation for p-type and n-type semiconductor presented in Section 2.4.2 and Annex-A.1 respectively, made the assumptions (a) lifetime is measured at low injection levels ($\Delta n << p_0$, n_0), ($\Delta n << p_1$, n_1) and (b) high temperatures ($p_1 >> p_0$ or $n_1 >> n_0$). These conditions are dependent upon doping density (N_A and N_D), E_t and temperature. This appendix presents the temperature and Δn for different N_A or N_D and E_t and are considered that for a parameter A << B when A is less than 1% of parameter B. The minimum temperatures for which $p_1(T)$, $n_1(T)$ >

0.01 × Δn, where $\Delta n < 0.01 \times p_0(T)$ or $n_0(T) < p_1, n_1$) for different E_t are presented in Table A.1.

Table B.1: Minimum temperature (°C) for which $p_1(T)$, $n_1(T) > 0.01 \times \Delta n$, where $\Delta n < 0.01 \times p_0(T)$ or $n_0(T) < p_1, n_1$) for different E_t

E_t (eV)	N_{DOP}= 1×10^{14} cm^{-3}		N_{DOP} = 1×10^{15} cm^{-3}		N_{DOP} = 1×10^{16} cm^{-3}	
Above E_v	$p_1 >> \Delta n$	$n_1 >> \Delta n$	$p_1 >> \Delta n$	$n_1 >> \Delta n$	$p_1 >> \Delta n$	$n_1 >> \Delta n$
0.05	-230	345	-222	409	-212	488
0.1	-194	321	-181	382	-164	459
0.2	-126	272	-105	330	-77	401
0.3	-63	223	-33	276	6	342
0.4	-1	173	37	222	85	282
0.5	61	122	105	166	168	221
0.6	120	70	172	109	239	158
0.7	179	17	238	51	314	94
0.72	190	6	251	39	329	81
0.75	208	-22	171	21	351	61
0.8	237	-38	303	-9	388	27
0.9	295	-98	368	-71	461	-42
1.0	353	-154	432	-137	534	-117

Appendix C

Simplification of the SRH equation for *n*-type silicon for the new TIDLS procedure

This appendix presents the simplification of the SRH equation for *n*-type silicon for the new TIDLS procedure, which is analogous to the *p*-type presented in Chapter 2. This thesis has implemented the procedures for *p*-type semiconductors as all the experiments were performed in *p*-type silicon. However this procedure can also be implemented for n-type silicon. Appendix C.2 presents the temperature range for different E_t and doping densities for which the assumptions made during the simplification of the SRH equation are valid.

C.1 Simplification of the SRH equation for *n*-type silicon

C.1.1 E_t in the lower half of the band gap (*n*-LBGH)

Simplifications of the SRH equation for an *n*-type wafer with E_t in LBGH can be performed by subjecting it to the following three conditions.

A: Negligible value of $p_0(T)$: $p_0(T)$ can be neglected in comparison to $n_0(T)$ irrespective of the location of E_t for *n*-type silicon for a certain temperature range. The simplified SRH equation can be expressed as

$$\tau_{SRH} = \frac{\tau_{no}(p_1 + p_0 + \Delta n) + \tau_{po}(n_1 + n_0 + \Delta n)}{(n_0 + \Delta n)} \qquad \text{(C.1)}$$

B: Negligible value of $n_1(T)$ and $p_0(T)$: $n_1(T)$ is significantly low in comparison with $n_0(T)$ and $p_0(T)$ is negligible in comparison with $p_1(T)$ when E_t lies in LBGH for a certain range of temperatures. The equation (C.1) can be further simplified as

$$\tau_{SRH} = \frac{\tau_{no}(p_1 + \Delta n) + \tau_{po}(n_0 + \Delta n)}{(n_0 + \Delta n)} \qquad \text{(C.2)}$$

C: Low level injection $p_1(T)$, $n_0(T) >> \Delta n$: For LLI, Δn can be removed from the denominator and numerator in the simplified SRH equation (C.2) and can be re-expressed as,

$$\tau_{SRH}(T)\times n_0(T) = \tau_{no}(T)\times p_1(T) + \tau_{po}(T)\times n_0(T). \quad \text{(C.3)}$$

Hence for a particular temperature and Δn range, when conditions A, B and C are satisfied, the values of $\tau_{p0}(T)$ and $\tau_{n0}(T)$ can be determined by solving two equations for different N_D and using the known value of $p_1(T)$ and $n_0(T)$. However, for the medium level of Δn when $\Delta n << n_0(T)$ but comparable with $p_1(T)$ then the Equation (C.2) can be simplified as

$$\tau_{SRH}(T)\times n_0(T) = \tau_{no}(T)\times \Delta n + \tau_{no}(T)\times p_1(T) + \tau_{po}(T)\times n_0(T) \quad \text{(C.4)}$$

$\tau_{p0}(T)$ and $\tau_{n0}(T)$ can be determined from the slope and the intercept of the linear plot of $\tau_{SRH}(T) \times n_0(T)$. Finally, $\sigma_{p0}(T)$ and $\sigma_{n0}(T)$ can be calculated from $\tau_{p0}(T)$ and $\tau_{n0}(T)$ using known values of $v_{thp}(T)$, $v_{thn}(T)$ and N_t.

C.1.2 E_t in upper band gap half (n-UBGH)

Similar to the other three conditions, simplification of the SRH equation for an n-type wafer with E_t in UBGH can be performed by subjecting it to the following three conditions.

A: Negligible value of $p_0(T)$: $p_0(T)$ can be neglected in comparison with $n_0(T)$ irrespective of the location of E_t for n-type silicon for a certain temperature range. Hence, the equation (B.1) is also valid in this case.

B: Negligible value of $p_1(T) + p_0(T)$: The sum of $p_1(T)$ and $p_0(T)$ is significantly low for n-type silicon when E_t lies in UBGH for a certain range of temperature and Δn. Hence $p_1 + p_0$ ($<< \Delta n$) can be removed from the first part of the numerator in Equation (C.1) and expressed as

$$\tau_{SRH} = \frac{\tau_{no}(\Delta n) + \tau_{po}(n_0 + n_1 + \Delta n)}{(n_0 + \Delta n)} \quad \text{(C.5)}$$

C: Low level injection $n_0(T) >> \Delta n$: For LLI, Δn can be removed from the denominator and numerator in Equation (C.5) and can be re-expressed as

$$\tau_{SRH}(T)\times n_0(T) = \tau_{no}(T)\times \Delta n + \tau_{po}(T)[n_1(T) + n_0(T)] \quad \text{(C.6)}$$

Hence for a particular temperature and Δn range, when conditions A, B and C are satisfied then the slope of the plot $\tau_{SRH}(T) \times n_0(T)$ versus Δn gives $\tau_{n0}(T)$ and offset as $\tau_{p0}(T) \times \{n_1(T) + n_0(T)\}$. As $n_1(T)$ can be calculated for a known E_t and $n_0(T)$ from N_D

and temperature, so $\tau_{p0}(T)$ can be calculated from the offset of the plot. Finally, $\sigma_{p0}(T)$ and $\sigma_{n0}(T)$ can be calculated from $\tau_{p0}(T)$ and $\tau_{n0}(T)$ using known values of $v_{thp}(T)$, $v_{thn}(T)$ and N_t.

In both cases LLI is not mandatory as the Equations (C.2), (C.4) and (C.5) can also be solved for $\tau_{p0}(T)$ and $\tau_{n0}(T)$ with injection-dependent measured lifetime data for a given temperature. However, this condition makes the SRH equation simpler and reduces the measurement errors in $\tau_{p0}(T)$ and $\tau_{n0}(T)$.

Excess carrier density Δn for TIDLS analysis is dependent upon the doping type, doping density, E_t and temperature. Appendix-C.2 summarizes the suitable Δn and T range for TIDLS measurement for different values of doping density and E_t, for both p and n-types of silicon.

C.2 Valid T and Δn range for assumptions in TIDLS analysis

Table C.1: Minimum temperatures (°C) for which $n_1(T) + n_0(T) < 0.01 \times \Delta n$ and $p_1(T) < 0.01 \times p_0(T)$ where $\Delta n < 0.01 \times p_0(T)$ for different N_A and E_t

E_t (eV)	$N_A = 1\times10^{14}$ cm^{-3}		$N_A = 1\times10^{15}$ cm^{-3}		$N_A = 1\times10^{16}$ cm^{-3}	
Above E_v	$n_1+n_0 << \Delta n$	$p_1 << p_0$	$n_1+n_0 >> \Delta n$	$p_1 << p_0$	$n_1+n_0 >> \Delta n$	$p_1 << p_0$
0.05	93	-239	138	-234	195	-228
0.1	93	-195	138	-183	195	-168
0.2	93	-127	138	-107	193	-77
0.3	92.5	-64	137	-34	190	5
0.4	87	-2	125	36	169	84
0.5	53	59	84	104	121	162
0.6	9	119	38	171	69	238
0.7	-35	185	-12	242	16	317
0.8	-81	512	-61	514	-38	524
0.9	-128	1068	-114	1069	-96	1068
1	-177	na	-168	Na	-155	na

For a p-type silicon three assumptions were made to simplify the SRH equation; (a) $n_0(T) << p_0(T)$, (b) $n_1(T) + n_0(T) << \Delta n$ for a defect in LBGH and $p_1(T) << \Delta n$ for a defect in UBGH and (c) low level injection $\Delta n << p_0(T)$. Assumption (a) is only dependent upon the N_A and T. This assumption is valid below 300 °C for $N_A = 1 \times 10^{16}$ cm^{-3}, 250 °C for $N_A = 1 \times 10^{15}$ cm^{-3} and 150 °C for $N_A = 1 \times 10^{14}$ cm^{-3}. Assumption (b) is dependent upon E_t, N_A and T. The temperatures below which this assumption is valid

are listed in Table B.1 for different E_t and N_A. Similarly assumption (c) is valid when Δn is below 1% of N_A and calculations in Table B.1 include this aspect.

In n-type silicon, three assumptions, which are analogous to p-type silicon, were made for simplification of the SRH equation. (a) $p_0(T) << n_0(T)$, (b) $p_1(T) + p_0(T) << \Delta n$ for defects in LBGH and $p_1(T) << \Delta n$ for defects in UBGH and (c) low level injection $n_0(T) >> \Delta n$. Assumption (a) is only dependent upon the N_D and T. This assumption is valid below 300 °C for $N_D = 1 \times 10^{16}$ cm^{-3}, 250 °C for $N_D = 1 \times 10^{15}$ cm^{-3} and 150 °C for $N_D = 1 \times 10^{14}$ cm^{-3}. Assumption (b) is dependent upon E_t, N_D and T. The temperatures below which this assumption is valid are listed in Table C.2 for different E_t and N_D. Similarly assumption (c) is valid when Δn is below 1% of N_D and the calculations in Table B.2 include this aspect.

Table C.2: Minimum temperatures (°C) for which $p_1(T) + p_1(T) < 0.01 \times \Delta n$ and $n_1(T) < 0.01 \times n_0(T)$, where $\Delta n = 0.01 \times n_0(T)$ for different N_D and E_t

E_t (eV)	$N_D = 1\times10^{14}$ cm^{-3}		$N_D = 1\times10^{15}$ cm^{-3}		$N_D = 1\times10^{16}$ cm^{-3}	
Above E_v	$p_1+p_0 << \Delta n$	$n_1 << n_0$	$p_1+p_0 << \Delta n$	$n_1 << n_0$	$p_1+p_0 << \Delta n$	$n_1 << n_0$
0.05	-241	344	-236	408	-231	487
0.1	-212	320	-204	382	-194	458
0.2	-158	271	-144	329	-127	400
0.3	-106	222	-87	275	-64	341
0.4	-55	172	-31	221	-2	281
0.5	-6	121	23	165	60	220
0.6	43	69	77	108	119	157
0.7	85	16	124	50	173	93
0.8	92	-39	136	-10	191	26
0.9	92	-95	137	-72	193	-43
1	92	-155	137	-138	194	-118

Appendix D

Uncertainties in measured lifetimes

Chapter 3 presents the step-by-step measurement of carrier lifetime using photoconductance instrument. Measured lifetimes sustain uncertainties, which are dependent upon the uncertainty of input data, the adopted model and instrument error. This Appendix discusses the effect of each parameter on measured carrier lifetime.

The inductive-coil PC based instrument measures the carrier lifetime of the wafer under test on the basis of the parameters of the test wafer and the different models adopted. The accuracy of the measured data is dependent upon the accuracy of the test wafer parameters and the error associated with the employed physical models. Furthermore, the precision of the instrument is also vital in obtaining better accuracy in the measured data. This section discusses the relative importance of uncertainties in input parameters and the employed models with a review of measurement procedures.

The measured lifetime can be expressed in transient, generalized or steady state forms. The error associated with the measurement of Δn is transferred to the measured lifetime for all three types of lifetimes. Δn is measured as

$$\Delta n(t) = \frac{\Delta \sigma_{sq}(t)}{q \times \mu_s(\Delta n, T) \times W} \tag{D.1}$$

where $\mu_s = (\mu_{pl} + \mu_{nl})$ is the sum of the carrier's mobilities. This shows that the uncertainty of measured Δn is dependent upon the accuracy of the adopted model for μ_s, entered W and measured $\Delta\sigma$.

The uncertainty of the chosen mobility model transfers directly to the measured Δn. Further, the calculation of Δn using the Equation (D.1) is not as straight-forward as it appears, because μ_s is also a function of Δn and its effect on μ_s becomes more significant for higher values ($\Delta n > 10^{15}$ cm^{-3}). The uncertainty in the entered thickness (W) of the test wafer also transfers its uncertainty to measured Δn. However, the measured Δn is further used for calculation of τ_{eff} where Δn needs to be divided by W, hence the uncertainty inherited by W will cancel out. $\Delta\sigma_{sq}(t)$ is calculated from the output voltage V_{OUT} using calibration parameters which may be either linear or quadratic as

$$\Delta\sigma_{sq}(t) = a \times \left[V_{OUT}{}^2(t) - V_{OUT}{}^2(0)\right] + b \times \left[V_{OUT}(t) - V_{OUT}(0)\right] \tag{D.2}$$

where $V_{OUT}(0)$ is the output voltage corresponding to the test wafer prior to illumination. For the linear calibration where $a = 0$, the equation can be written as

$$\Delta\sigma_{sq}(t) = b \times [V_{OUT}(t) - V_{OUT}(0)] = b \times \Delta V \tag{D.3}$$

Hence the uncertainty on measured $\Delta\sigma_{sq}$ is the result of the uncertainties in the calibration coefficients and the measured voltages $V_{OUT}(t)$ and $V(0)$.

This instrument simultaneously measures $V_{OUT}(t)$ and the voltage of a reference cell $V_{ref}(t)$. The value of $V_{ref}(t)$ is used to calculate the photogeneration rate $G(t)$ as,

$$G(t) = \frac{k \times V_{ref}(t)}{W} \tag{D.4}$$

where k (= 38 mA/cm^3 for silicon) is a calibration constant that converts V_{ref} to a generation current density and W is the thickness of the wafer. $G(t)$ is used to calculate τ_{eff} for generalized and steady state forms. Hence the uncertainties of k, $Vref(t)$ and W transferred to $G(t)$ and then to τ_{eff}.

Generalized and transient lifetime measurement employs the time derivative of $\Delta n(t)$ to calculate τ_{eff}. The time derivative of $\Delta n(t)$ can be expressed considering (D.1) and (D.3) for a fixed temperature,

$$\frac{\partial \Delta n(t)}{\partial t} = \frac{V' \times b}{q \times W \times \mu_S(\Delta n)} \left[1 + \frac{\Delta n}{\mu_S(\Delta n)} \frac{\partial \mu_s}{\partial \Delta n} \right]^{-1} \tag{D.5}$$

where V' is the time derivative of ΔV.

Transient measurement of lifetime can be expressed in terms of fundamental parameters by employing (D.5) as,

$$\tau_{eff} = \frac{\Delta n}{\frac{\partial \Delta n(t)}{\partial t}} = -\frac{\Delta V}{V'} \left[1 + \frac{\Delta V \times b}{q \times W \times [\mu_S(\Delta n)]^2} \frac{\partial \mu_s}{\partial \Delta n} \right] \tag{D.6}$$

When μ_s is fixed for a given value of Δn, the second term of Equation (D.6) vanishes and τ_{eff} for transient analysis can be simplified as

$$\tau_{eff} = -\frac{\Delta V}{V'} \tag{D.7}$$

Hence the uncertainty of measured τ_{eff} for transient analysis is equal to the uncertainty of the excess photoconductance decay signal ΔV over the range where μ_s is fixed with T

and Δn. However for the range where μ_s is not fixed with T or Δn the uncertainty of measured τ_{eff} for transient analysis becomes more difficult to calculate as it depends upon uncertainties of ΔV, b, W, μ_s and T.

Steady state analysis can be performed when the rate of change of Δn with t is negligible. τ_{eff} for steady state analysis can be expressed by employing the Equation (D.3)

$$\tau_{eff} = -\frac{b}{qk\mu_s(\Delta n)}\frac{\Delta V}{V_{ref}} \tag{D.8}$$

Hence the uncertainty of measured τ_{eff} for steady state analysis is dependent upon the uncertainties of ΔV, b, k, μ_s, V_{ref} and T for all values of Δn.

In generalized analysis both generation $G(t)$ and rate of decay of Δn are considered. Employing Equations (D.3) and (D.4), τ_{eff} for generalized analysis can be expressed as

$$\tau_{eff} = -\frac{\Delta V}{\frac{qk\mu_s}{b}V_{ref} - V'} \tag{D.9}$$

Among three types of measured lifetimes, transient measurement seems to be less erroneous as the error for transient measurement is dependent upon the ratio of photoconductance voltage and its time derivative (V'). Transient measurement is only suitable for a silicon wafer with a higher lifetime (> 100 μS). Transient measurement of lifetime is not feasible for a sample with a higher recombination rate as the system is unable to detect the Δn signal after the turning off of the flash light.